

Summer 10-15-2009

EXCHANGE BIAS TRAINING EFFECT IN MAGNETICALLY COUPLED BILAYERS

Srinivas Polisetty

University of Nebraska, Lincoln, polisetty.srinivas@gmail.com

Follow this and additional works at: <http://digitalcommons.unl.edu/physicsdiss>



Part of the [Condensed Matter Physics Commons](#)

Polisetty, Srinivas, "EXCHANGE BIAS TRAINING EFFECT IN MAGNETICALLY COUPLED BILAYERS" (2009). *Theses, Dissertations, and Student Research: Department of Physics and Astronomy*. 7.
<http://digitalcommons.unl.edu/physicsdiss/7>

This Article is brought to you for free and open access by the Physics and Astronomy, Department of at DigitalCommons@University of Nebraska - Lincoln. It has been accepted for inclusion in Theses, Dissertations, and Student Research: Department of Physics and Astronomy by an authorized administrator of DigitalCommons@University of Nebraska - Lincoln.

EXCHANGE BIAS TRAINING EFFECT IN MAGNETICALLY COUPLED BILAYERS

by

Srinivas Polisetty

A DISSERTATION

Presented to the Faculty of
The Graduate College at the University of Nebraska
In Partial Fulfillment of Requirements
For the Degree of Doctor of Philosophy

Major: Physics and Astronomy

Under the Supervision of Professor Christian Binek

Lincoln, Nebraska

October, 2009

EXCHANGE BIAS TRAINING EFFECT IN MAGNETICALLY COUPLED BILAYERS

Srinivas Polisetty, Ph.D.

University of Nebraska, 2009

Advisor: Christian Binek

Interfaces in magnetically coupled bilayer heterostructures play a vital role in novel spintronics devices. Particularly, control of the interface spin structure enables the development of progressively down-scalable magnetic read-heads which are of major importance for non volatile magnetic recording media. Exchange bias and its accompanying training effect are fundamental magnetic coupling phenomena taking place at the interfaces of antiferromagnetic/ferromagnetic and hard/soft ferromagnetic bilayers.

Here, in my thesis I present the experimental results of exchange bias training in the prototypical antiferromagnetic/ferromagnetic exchange bias system CoO/Co and the corresponding coupling and aging phenomena in the all ferromagnetic hard/soft bilayer CoPtCrB/CoCr. The latter system provides experimental access to its pinning layer magnetization thereby allowing to measure fundamental properties of exchange bias and its corresponding training phenomenon. A phenomenological theory is best fitted to all experimental training data of antiferromagnetic/ferromagnetic and hard/soft ferromagnetic bilayers evidencing the universality of the theory. My studies are further

extended to the temperature dependence of the exchange bias training effect. Again, excellent agreement between experiment and theory confirms the remarkable universality of the underlying phenomenological approach. Furthermore, the dependence of the exchange bias training on the ferromagnetic film thickness is investigated in a CoO/Co-wedge sample. Scaling behavior with collapse of the temperature and thickness dependent parameters onto a single master curve is presented. Magnetotransport measurements are used for complementary studies of exchange bias in CoO/Co-heterostructures. Here, exchange bias produces a shift of the magnetoresistance curve along the magnetic field axis and an additional asymmetry along the resistance axis. The dynamic non-equilibrium properties of the exchange bias training effect are investigated via the sweep rate dependence of the exchange bias field. A dynamical enhancement of the exchange bias training effect has been observed in both CoO/Co and CoPtCrB/CoCr bilayers with increasing sweep rate of the applied magnetic field. A generalized theory has been developed for the dynamical enhancement studies confirming once more the consistency and universality of the phenomenological approach.

ACKNOWLEDGMENTS

I would like to express my sincere gratitude to all individuals who supported and guided me at every stage throughout my graduate schooling here at University of Nebraska-Lincoln.

Foremost, I am deeply indebted to my supervisor Professor Christian Binek for the continuous support of my Ph.D. study and research, for his patience, motivation, enthusiasm, and immense knowledge in the subject. His guidance helped me all the time during my research in his lab. I could not have imagined having a better mentor for my Ph.D. The stage I have grown today is fully attributed to my supervisor without whom I might have encountered many troubles in pursuing my Ph.D. and surely wouldn't have many publications. I am greatly honored to be the first graduate student under his incredible supervision. I have really enjoyed those long educated discussion sessions we had over the past 5 years and of course without his name I believe this thesis is incomplete.

Besides my supervisor, I would like to thank the rest of my thesis committee: Professor Evgeny Tsymbal, Professor Shireen Adenwalla and Professor Jeff Shield, for their invaluable time, thoughtful and critical reading of this dissertation.

My sincere gratitude goes to my group members: Mr. He Xi, Mr. Tathagata Mukherjee, Mr. Yi Wang, Mr. Will Echtenkamp, Mr. Keith Jones and our ex-post doc Dr. Sarbeswar Sahoo, for the stimulating discussions and for such a wonderful cooperation during all the time in the lab.

In addition, I would also like to thank the following people for helpful discussions, support, and in some cases being very helpful in group study: Dr. Andreas Berger, Prof. Sitaram Jaswal, Prof. Axel Enders, Prof. Korey Sorge, Dr. Andrew Baruth, Dr. Steven Michalski, Dr. J. D. Burton, Dr. Shawn Hilbert, Dr. Marcus Natta, Dr. Ratnakar Palai, Dr. Sha R Valloppilly, Dr. Balamurugan Balasubramanian, Dr. Parashu

Kharel, Mr. Anil Kumar Rajapitamahuni, Mr. Abhijit Mardana, Mr. Tom George, Mr. Shawn Langan, Mr. Kayle DeVaughan, Mr. Dale Johnston, and Mr. Brian Jones.

A special appreciation to all the staff members who made my life smooth in the department: Theresa Sis, Kay Haley, Jenny Becic and Beth Farleigh in the department main office. Verona Skomski and Shelli Krupicka in the MRSEC division. Patty Christen and Joyce McNeil in the business office. Michael J. Jensen, Les Marquart, Keith A. Placek, Pat Pribil and Robert L. Rhynalds for the instrumentation help. Dr. John R. Kelty and Brian Farleigh for their electronic and computer support services.

I also personally thank my present and former roomies: Vineeth Reddy Yeddula, Vijay Musunuru, Gowtham Maranani, Sandeep Lingam, Naresh Arcot, Vishal Seri and Srikanth Mallu. Also, I show special gratitude to my other friends: Varsha Purohit, Rama Krishna Thummalapalli, Krishna Swamy Nallamreddy, Bharat Annapareddy, Ravi Choragudi, Vedvyas Kamarajugadda, Pallavi Vellelacheruvu, Ravi Billa, Manoj Dhuliapala, Mithuna Lingam, Sreedevi Lalithambika, Suhasini Pandharpurkar, Vikram Sivarajan, Sridevi & Dileep Goyal, Anusha Ravula, Manogna Kaluva, etc. You all made my stay very pleasant in Lincoln during my Ph.D. You have been wonderful to me and I cannot forget the fun we had at every instance.

This thesis is meaningless without mentioning my parents, Venakata Lakshmi & Venkata Rangam Polisetty, and my brother, Srikanth Polisetty. Besides my family, other people who know how a difficult time I have gone through in writing my thesis is my fiancée, Sirisha Dupaguntla and her family. Without these people's love, affection and support I do not think I would have reached this stage of my life. I am overwhelmed to dedicate this thesis to my family members. I love you and miss you all.

Finally, I would thank my entire financial supporters for making this thesis successful. My thesis work is mainly supported by "National Science Foundation (NSF) through Grant No. DMR-0547887, the Nebraska Research Initiative (NRI), and the MRSEC program of the NSF through Grant No. DMR-0213808".

TABLE OF CONTENTS

CHAPTER 1

INTRODUCTION	1
1.1. EXCHANGE BIAS	2
1.1.1. PHENOMENOLOGICAL THEORY	4
1.1.2. INTUITIVE PICTURE	10
1.1.3. COERCIVITY ENHANCEMENT	14
1.1.4. POSITIVE EXCHANGE BIAS	16
1.1.5. MICROSCOPIC MODELS	20
1.2. TRAINING EFFECT	28
1.2.1. PHENOMENOLOGICAL THEORY OF EXCHANGE BIAS TRAINING EFFECT IN AF/FM BILAYERS	30
1.2.2. UNIVERSALITY OF THE PHENOMENOLOGICAL THEORY OF THE TRAINING EFFECT	39

CHAPTER 2

SAMPLE PREPARATION METHODS AND EXPERIMENTAL TECHNIQUES	44
2.1. SAMPLE PREPARATION METHODS	44
2.1.1. MAGNETRON SPUTTERING	44
2.1.2. MOLECULAR BEAM EPITAXY	47

2.2. EXPERIMENTAL TECHNIQUES	52
2.2.1. WIDE ANGLE X-RAY DIFFRACTION	52
2.2.2. SMALL ANGLE X-RAY REFLECTIVITY.....	57
2.2.3. ALTERNATING GRADIENT FORCE MAGNETOMETER.....	60
2.2.4. MAGNETO-OPTICAL KERR EFFECT	62
2.2.4.1. EXPERIMENTAL SET-UP	65
2.2.4.2. JONES MATRIX FORMALISM.....	68
2.2.5. SUPERCONDUCTING QUANTUM INTERFERENCE DEVICE.....	99

CHAPTER 3

AF/FM EXCHANGE COUPLED BILAYERS	102
3.1 TEMPERATURE DEPENDENCE OF THE EXCHANGE BIAS TRAINING EFFECT	102
3.1.1. PREPARATION OF THE CoO/Co HETEROSTRUCTURE AND STRUCTURAL CHARACTERIZATION	104
3.1.2. MAGNETIC ANISOTROPY OF Co THIN FILM IN A CoO/Co BILAYER .	106
3.1.3. TRAINING EFFECT IN CoO/Co.....	108
3.1.4. PHENOMENOLOGICAL THEORY OF TEMPERATURE DEPENDENCE OF THE TRAINING EFFECT IN AF/FM BILAYERS	110
3.1.5. TEMPERATURE DEPENDENCE OF THE STRENGTH OF THE TRAINING EFFECT	117
3.2 FERROMAGNETIC THICKNESS DEPENDENCE AND SCALING BEHAVIOR OF THE EXCHANGE BIAS TRAINING EFFECT.....	120

3.2.1. PREPARATION OF A COO/CO-WEDGE SAMPLE AND ITS EXPERIMENTAL DETAILS	122
3.2.2. MAGNETIC CHARACTERIZATION VIA LOCAL MOKE	128
3.2.3. RESULTS OF MAGNETIC MEASUREMENTS	129
3.2.4. SCALING OF THE STRENGTH OF THE TRAINING EFFECT	139

CHAPTER 4

ANTIFERROMAGNETICALLY COUPLED HARD/SOFT FERROMAGNETIC BILAYERS	144
4.1 SPECIFIC SAMPLE PROPERTIES	144
4.2. SAMPLE DESCRIPTION AND MAGNETIC CHARACTERIZATION	147
4.3. TRAINING EFFECT IN COUPLED HARD/SOFT BILAYERS	149
4.3.1. INITIALIZATION OF THE BIAS FIELD	149
4.3.2. THE BIAS FIELD TRAINING EFFECT IN SOFT FERROMAGNET	151
4.3.3. TRIGGERED TRAINING EFFECT BY REVERSAL OF THE FERROMAGNETIC SOFT LAYER	157
4.3.4. STRENGTH OF THE TRAINING EFFECT.....	160
4.3.5. PHENOMENOLOGICAL THEORY OF THE BIAS FIELD TRAINING EFFECT IN ALL FERROMAGNETIC BILAYERS	161
4.4. TEMPERATURE DEPENDENCE OF THE TRAINING EFFECT	168
4.4.1. OVERALL HYSTERESIS LOOPS AT DIFFERENT TEMPERATURES	169
4.4.2. MINOR LOOP HYSTERESIS LOOPS AND ITS TRAINING EFFECT	171

4.4.3.	INTRINSIC COERCIVITY OF THE SOFT MAGNETIC LAYER	174
4.4.4.	THEORY OF TEMPERATURE DEPENDENCE OF THE TRAINING EFFECT IN ALL FERROMAGNETIC BILAYERS	180
4.4.5.	TEMPERATURE DEPENDENCE OF THE CHARACTERISTICS OF THE TRAINING EFFECT	184
4.5.	DYNAMIC ENHANCEMENT OF THE BIAS FIELD TRAINING EFFECT... ..	191
4.5.1.	BROADENING OF THE SOFT LAYER HYSTERESIS	192
4.5.2.	ENHANCED TRAINING EFFECT WITH SWEEP RATES	193
4.5.3.	THEORETICAL APPROACH	195
4.5.4.	SWEEP RATE DEPENDENCE OF THE CHARACTERISTICS OF THE TRAINING EFFECT AND EQUILIBRIUM BIAS FIELD	197
4.5.5.	SWEEP RATE DYNAMICAL ENHANCEMENT IN AF/FM HETEROSYSTEM	199

CHAPTER 5

COMPARISON BETWEEN AF/FM AND HARD/SOFT FERROMAGNETIC BILAYERS	203
--	-----

CHAPTER 6

CONCLUSIONS.....	213
REFERENCES	216

CHAPTER 1

INTRODUCTION

The exchange coupling that occurs at the interface between ferromagnetic (FM) and antiferromagnetic (AF) layers is still an active field of research for several magnetism groups throughout the world due its technological applications in magnetic read heads. Magnetic properties of a FM material are drastically altered in the vicinity of an antiferromagnet giving rise to the phenomenon of exchange bias.

This thesis is organized as follows: Chapter 1 provides an introduction to the effect of exchange bias, including a brief history of different microscopic models and followed by phenomenological theory for the training effect. Chapter 2 describes the experimental methods used to study these effects, including sample preparation and characterization. Chapter 3 and chapter 4 describe experimental results of exchange bias training effect on AF/FM bilayers and hard/soft FM bilayers, respectively. Chapter 5 presents the comparison of experimental results of training effect and corresponding phenomenological theories obtained in AF/FM bilayers and hard/soft FM bilayers. Finally, Chapter 6 gives the summary of my thesis.

1.1. EXCHANGE BIAS

Exchange bias, sometimes referred to as unidirectional or exchange anisotropy, describes a magnetic coupling phenomenon at the interface between ferromagnet and antiferromagnet. When a FM film brought into proximity of an AF pinning layer within the quantum mechanical exchange length, the ferromagnet experiences an exchange induced unidirectional anisotropy.^{1,2,3,4,5,6} The latter reflects its presence most prominently by shifting the FM hysteresis loop along the magnetic field axis. The amount of the shift is quantified by the exchange bias (EB) field, $\mu_0 H_{EB}$. The specific spin structures which give rise to the EB effect need an initialization which can be realized by field-cooling the AF/FM heterostructure to below the blocking temperature, T_b of the antiferromagnet. The blocking temperature is typically, but not necessarily,^{7,8} below the bulk Néel temperature, T_N , and characterizes the onset of AF order in the pinning layer at least on mesoscopic length scales.⁹

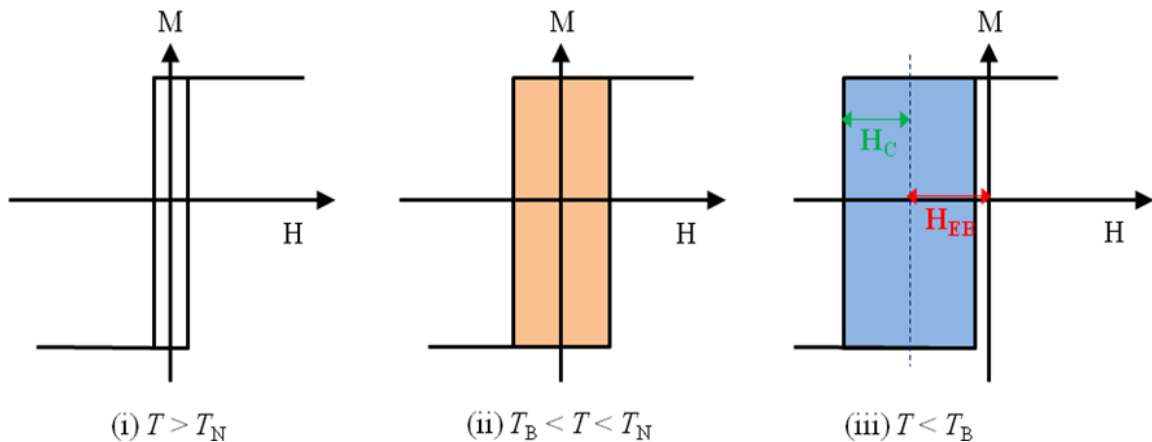


Figure 1.1. Cartoon contrasting hysteresis loops of a ferromagnet (i) at $T > T_N$, (ii) in the vicinity of an antiferromagnet at $T < T_N$ (no exchange bias), (iii) in the vicinity of antiferromagnet at $T < T_B$ showing significant exchange bias and loop broadening effects.

The enhanced hysteresis loop width (or coercivity, H_C) of a ferromagnet is an associated effect of EB in AF/FM heterostructures due to the coupling of the antiferromagnet onto a ferromagnet.^{10,11,12} Figure 1.1 shows the cartoons of hysteresis loops of a ferromagnet at different stages during the initialization process of EB. Fig 1.1 (i) displays the hysteresis loop of a simple ferromagnet above T_N of an antiferromagnet. Having an antiferromagnet adjacent to a ferromagnet does not affect the FM hysteresis loop significantly due to the absence of long range AF correlation above T_N . Hence, the displayed hysteresis loop arises from the intrinsic property of the ferromagnet. Fig 1.1 (ii) displays the FM hysteresis with increased loop width at $T_B < T < T_N$ due to the drag effect generated by the antiferromagnet. Finally, Fig 1.1 (iii) displays a shifted hysteresis loop along the magnetic field axis indicating exchange bias quantified by H_{EB} . The coercivity, H_C also increases due to the increment in a drag effect generated by the antiferromagnet on the ferromagnet.

The exchange bias effect was first discovered in Co/CoO particles by Meiklejohn and Bean in 1956.^{1,2,3} The Co particles revealed a unidirectional magnetic anisotropy and a strictly different hysteresis loop in comparison to the one observed in pure Co material. Since then, exchange bias was observed in many different systems containing AF/FM interfaces such as small particles and inhomogeneous materials,^{13,14,15,16,17,18,19} FM films on AF single crystals^{20,21} and thin films.^{22,23} In addition to AF/FM interfaces, exchange bias and related effects have also been observed in other types of interfaces involving ferrimagnets, *i.e.*, AF/ferrimagnetic,²⁴ ferrimagnetic/FM²⁵ and soft/hard FMs. Enormous

efforts^{26,27,28,29,30,31,32,33,34} resulted in the investigation of microscopic details of the EB effect, however, the origin of EB remains a big controversy up to now. In my thesis I do not enter into the entangled microscopic origin of EB, however, I will provide a macroscopic phenomenological description given by Meiklejohn and Bean, in the next section 1.1.1.

1.1.1. PHENOMENOLOGICAL THEORY

The quantitative description of exchange coupling was introduced initially by Meiklejohn and Bean.^{1,2} The detailed analytical description of this phenomenological theory is nicely written down by Ch. Binek³⁵ in his book on the magnetism of Ising-type Antiferromagnets. Nevertheless, I chose to elaborate those details as they are necessarily relevant to my studies here. Meiklejohn and Bean started from the well-established Stoner-Wohlfarth (SW) free-energy³⁶ expression which describes the coherent hysteretic magnetization-reversal process of single domain particles and magnetic thin films. In order to take into account the interaction between the AF/FM interface moments they added an exchange term which gives rise to additional unidirectional anisotropy energy and finally derived an explicit expression of EB. The detailed analytic description follows:

According to this model, the total free energy per unit area of the AF/FM system is given by $F = F_{FM} + F_{AM} + F_{\text{coupling}}$; where the free energy per unit area of a ferromagnet, $F_{FM} = -\mu_0 H M_{FM} t_{FM} \cos(\theta - \beta) + K_{FM} t_{FM} \sin^2 \beta$, the free energy per unit area of a

antiferromagnet $F_{AF} = -\mu_0 H M_{AF} t_{AF} \cos(\theta - \alpha) + K_{AF} t_{AF} \sin^2 \alpha$ and the coupling term $F_{\text{coupling}} = -J S_{AF} S_{FM} \cos(\beta - \alpha)$. Therefore,

$$F = -\mu_0 H M_{FM} t_{FM} \cos(\theta - \beta) - \mu_0 H M_{AF} t_{AF} \cos(\theta - \alpha) + K_{FM} t_{FM} \sin^2 \beta + K_{AF} t_{AF} \sin^2 \alpha - J S_{AF} S_{FM} \cos(\beta - \alpha). \quad (1-1)$$

Here H is the applied magnetic field and $M_{FM/AF}$, $t_{FM/AF}$, $K_{FM/AF}$ and $S_{FM/AF}$ are the absolute values of total magnetizations, thicknesses, the uniaxial anisotropy constants and interface magnetizations of FM/AF layers, respectively. Note that, here I considered an AF magnetization due to dilute antiferromagnets, for instance, can very well have non zero magnetization.

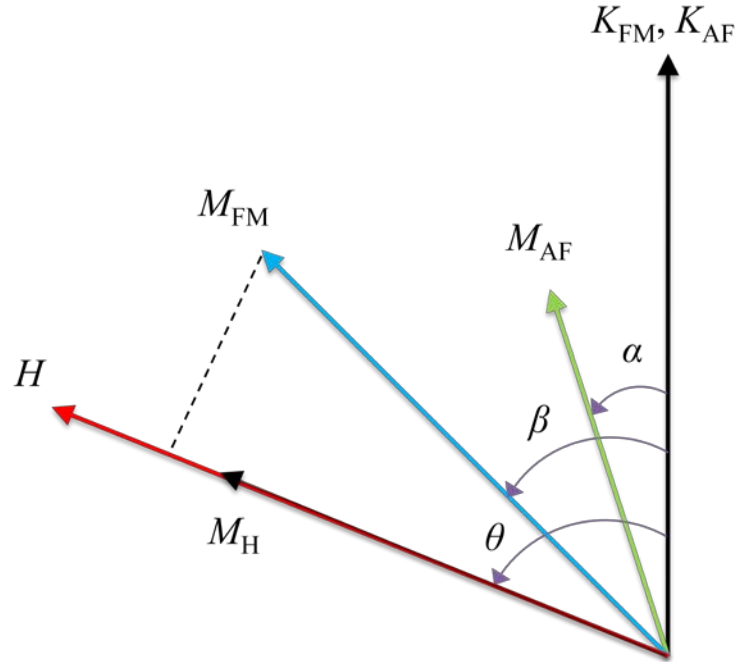


Figure 1.2. Vector diagram showing θ , α and β representing the angles of applied magnetic field H , net AF magnetization M_{AF} and net FM magnetization M_{FM} make with respect to easy axis of the AF and FM designed by the corresponding anisotropy constants $K_{AF/FM}$. M_H is the projection of M_{FM} onto H-axis which is the measured component by magnetometry. (Ref. [35])

The interface magnetizations of AF/FM layers can be interpreted as macroscopic moments because Meiklejohn Bean (MB) approach assumes parallel orientation of all moments during the entire process of coherent rotation. Therefore, the FM spins fulfill the condition $S_i^{FM} = S^{FM} \forall i$, and the interaction of the microscopic spins at the interface can be transformed into an interaction of the macroscopic interface moments according to $\sum_{i,j} S_i^{FM} S_i^{AF} \propto S_{FM} S_{AF}$. These interface magnetizations S_{FM} and S_{AF} are coupled via J , the exchange interaction constant. θ , α and β are the angles made by H , M_{AF} and M_{FM} with the AF/FM anisotropy axis. M_H is the component of M_{FM} projected along the applied magnetic field direction, *i.e.*, $M_H = M_{FM} \cos(\theta - \beta)$ and which is measured for example in a SQUID magnetometer. For the sake of simplicity, it is assumed that K_{FM} and K_{AF} are oriented parallel to the field cooling direction and also do not depend on their respective film thicknesses. Figure 1.2 displays the angles mentioned above between different components.

The bulk magnetization M_{AF} is assumed to be zero. This is a reasonable assumption in the case where the sub lattice magnetizations mutually compensate in the long-range AF ordered state. However, this is no longer the case in diamagnetically diluted AF systems. They are known to decay into a random-field-induced domain state with frozen excess magnetization when cooling to below T_N in an external magnetic field. This mechanism is at least one important possibility to control the appearance of $S_{AF} \neq 0$, at compensated AF surfaces and thus enables EB. At the same time, the excess bulk magnetization, $M_{AF} \neq 0$, of AF domain state may also be important by virtue of the

corresponding Zeeman energy in (1.1). This metastable domain state can also be induced in non-diluted AF pinning layers perhaps due to interface roughness giving rise to both M_{AF} and excess susceptibility.

In the case of infinite anisotropy of the antiferromagnet, the minimization of the free energy demands $\alpha = 0$. However, in reality the antiferromagnet has not fully strong but finite anisotropy. Therefore, a series expansion of Eq. (1-1) with respect to $\alpha = 0$ is reasonable. It reads

$$\begin{aligned}
F \approx & -JS_{AF}S_{FM} \cos \beta - \mu_0 HM_{FM}t_{FM} \cos(\theta - \beta) - \mu_0 HM_{AF}t_{AF} \cos \theta \\
& + K_{FM}t_{FM} \sin^2 \beta + \alpha \left[-JS_{AF}S_{FM} \sin \beta - \mu_0 HM_{AF}t_{AF} \sin \theta \right] \\
& + \alpha^2 \left[K_{AF}t_{AF} + \frac{1}{2}JS_{AF}S_{FM} \cos \beta + \frac{1}{2}\mu_0 HM_{AF}t_{AF} \cos \theta \right]
\end{aligned} \tag{1-2}$$

Now Eq. (1-2) is minimized with respect to α to determine α_{eq} . $\partial F/\partial \alpha = 0$ yields

$$\alpha_{eq} = \frac{JS_{AF}S_{FM} \sin \beta + \mu_0 HM_{AF}t_{AF} \sin \theta}{2K_{AF}t_{AF} + JS_{AF}S_{FM} \cos \beta + \mu_0 HM_{AF}t_{AF} \cos \theta} \tag{1-3}$$

In order to determine H_{c1} and H_{c2} of the FM hysteresis loop, we minimize Eq. (1-2)

with respect to β . $\partial F/\partial \beta = 0$ yields,

$$\begin{aligned}
2K_{FM}t_{FM} \sin \beta \cos \beta + \mu_0 HM_{FM}t_{FM} \sin(\beta - \theta) + JS_{AF}S_{FM} \sin \beta \\
- \alpha JS_{AF}S_{FM} \cos \beta - \frac{1}{2}\alpha^2 JS_{AF}S_{FM} \sin \beta = 0
\end{aligned} \tag{1-4}$$

Now we substitute α_{eq} from Eq. (1-3) into Eq. (1-4) in place of α . Moreover, H_{c1} and

H_{c2} fulfill the conditions $M_H(H_{c1}) = M_H(H_{c2}) = 0$ where $M_H = M_{FM} \cos(\theta - \beta)$ is the

magnetization of M_{FM} pointing parallel to the applied magnetic field as shown in fig 1.2. So in order to obtain explicit expressions for H_{c1} and H_{c2} , we insert limiting conditions of β , *i.e.*, $\beta(M_H = 0) = \theta - \pi/2$ and $\beta(M_H = 0) = \theta - 3\pi/2$, into Eq. (1-4). The EB is then calculated according to $H_{EB} = (H_{c1} + H_{c2})/2$. Although the calculation is straightforward, the results are bit lengthy. In order to simplify the results one has to expand H_{EB} into a Taylor series with respect to $M_{AF} \approx 0$ and $1/K_{AF} \approx 0$ up to first and second order, respectively. Therefore, one obtains:

$$\mu_0 H_{EB} = -\frac{JS_{AF}S_{FM} \cos \theta}{M_{FM}t_{FM}} - \left(\frac{JS_{AF}S_{FM} \cos \theta}{16K_{AF}^2 M_{FM}^2 t_{AF}^2 t_{FM}^2} \left(\begin{array}{l} -4JK_{AF}M_{AF}S_{AF}S_{FM}t_{AF}^2 + J^2M_{FM}S_{FM}^2S_{AF}^2t_{FM} \\ + JK_{FM}M_{AF}S_{AF}S_{FM}t_{FM}t_{AF} - JS_{AF}S_{FM} \cos 2\theta \\ + 3JK_{FM}M_{AF}S_{AF}S_{FM}t_{FM}t_{AF} \cos 4\theta \end{array} \right) \left(\begin{array}{l} -4JK_{AF}M_{AF}t_{AF}^2 \\ + 3JS_{AF}S_{FM}M_{FM}t_{FM} \\ + 4K_{FM}M_{AF}t_{FM}t_{AF} \end{array} \right) \right) \quad (1-5)$$

In the limit of infinite anisotropy of antiferromagnet, Eq. (1-5) becomes

$$\mu_0 H_{EB} = -\frac{JS_{AF}S_{FM} \cos \theta}{M_{FM}t_{FM}} \quad (1-6)$$

If the magnetic field is applied along the easy axes of ferromagnet and antiferromagnet, *i.e.* $\theta=0$, Eq. (1-6) becomes,

$$\mu_0 H_{EB} = -\frac{JS_{AF}S_{FM}}{M_{FM}t_{FM}} \quad (1-7)$$

Eq. (1-7) is the master formula for the qualitative description of the exchange bias for many scenarios. Eq. (1-7) exhibits the well known dependence of $\mu_0 H_{EB}$ on the FM thickness t_{FM} , on the magnetization of FM layer M_{FM} , and interface magnetizations of the ferromagnet and the antiferromagnet, S_{FM} and S_{AF} . The inverse thickness dependence of the FM film has been confirmed in countless investigations including my studies in section [3.2.3] which reflects the true interface nature of the effect. However, note that MB approach does not provide the microscopic origin of S_{FM} and in particular S_{AF} . Nevertheless the simple MB formula at least points out the necessity of interface magnetization, in particular on the AF side of interface in order to obtain finite EB. This basic confirmation as well as the simplicity of the MB approach makes it a favorable first approach in order to interpret experimental data. In the view of this simplicity it is surprising that most of the experimental facts are at least qualitatively described within the framework of MB approach. It has often been claimed that the MB expression is an invalid oversimplification which overestimates the experimental observed EB field typically by more than an order of magnitude.^{37,38,39} Note that the MB expression was developed based on a consideration of smooth interfaces between antiferromagnet and ferromagnet as well as uniform FM magnetization rotation during applied magnetic field reversal. But, in reality neither the interfaces are smooth nor uniform FM rotation takes place. However, the MB approach still remains a useful description with even quantitative predictive power.

The above view on the MB expression suggests that, when interpreting the phenomenological input parameters of the MB approach properly, Eq. (1-7) has applicability which is independent of quite a number of system specific details. However,

one has to realize the fact that the results based on phenomenological approach are of course not appropriate to provide system specific values. Needless to say that Eq. (1-7) says nothing about the system specific values of the AF interface magnetization S_{AF} and the interaction parameter J . It is one of the challenging tasks of experiments and microscopic theories to explain why for instance S_{AF} is crucial in obtaining EB. The MB description in its phenomenological interpretation does not address these questions nor does it address the question about the value of J properly. It is therefore not a flaw of the MB approach when unrealistic values for S_{AF} for instance are used which consequently overestimate the EB fields.

1.1.2. INTUITIVE PICTURE

MB approach is the first one to explain the existence of the loop shifts in exchange coupled AF/FM materials. Note that the phenomenological MB approach provides an intuitive picture to understand EB on a macroscopic level. Conversely, in this section I give an intuitive picture of microscopic spin details of AF/FM bilayers in order to explain the FM loop shift (EB) and broadening effects (coercivity enhancement).

Figure 1.3 shows spin configuration of ferromagnet and antiferromagnet before and during different stages of EB.^{31,32} Note that there is always an interaction exist between atomic magnetic moments at the interfaces of the ferromagnet and antiferromagnet but it is the thermodynamics which controls if the interaction gives rise to unidirectional anisotropy. If a sufficiently large magnetic field is applied at a

temperature $T_N < T < T_C$ of a ferromagnet, all spins in the ferromagnet will align parallel to H , *i.e.*, the ferromagnet is saturated. On the other hand, the antiferromagnet does not establish long range order and, therefore, pinning is absent between antiferromagnet and ferromagnet. Therefore the hysteresis loop of a ferromagnet is symmetric with respect to H - and M -axes as shown in Fig 1.3(1). Afterwards, the AF/FM bilayer is field-cooled through T_N , and the magnetic order is established in the antiferromagnet. Now, the lowering of temperature activates the pinning between the interface spins of the ferromagnet and the antiferromagnet. Hence, the first monolayer of spins in the antiferromagnet will tend to align (anti)parallel to the spins in the ferromagnet in the case of (anti)ferromagnetic exchange coupling at the interface. As a result an uncompensated spin configuration at the interface (only one sublattice of the antiferromagnet is present at the interface) leading to a finite net magnetization of this monolayer. The next monolayer of the antiferromagnet will automatically align antiparallel to the previous layer as to complete the AF order and so on as shown in Fig 1.3(2). This gives rise to a zero net magnetization in the antiferromagnet. Note that an uncompensated spin structure at the interface of the antiferromagnet is not a general result of an ideal smooth surface. Moreover specific surface structures such as (100) or (011) can also influence the possibility of uncompensated or compensated surface at the interface of AF.

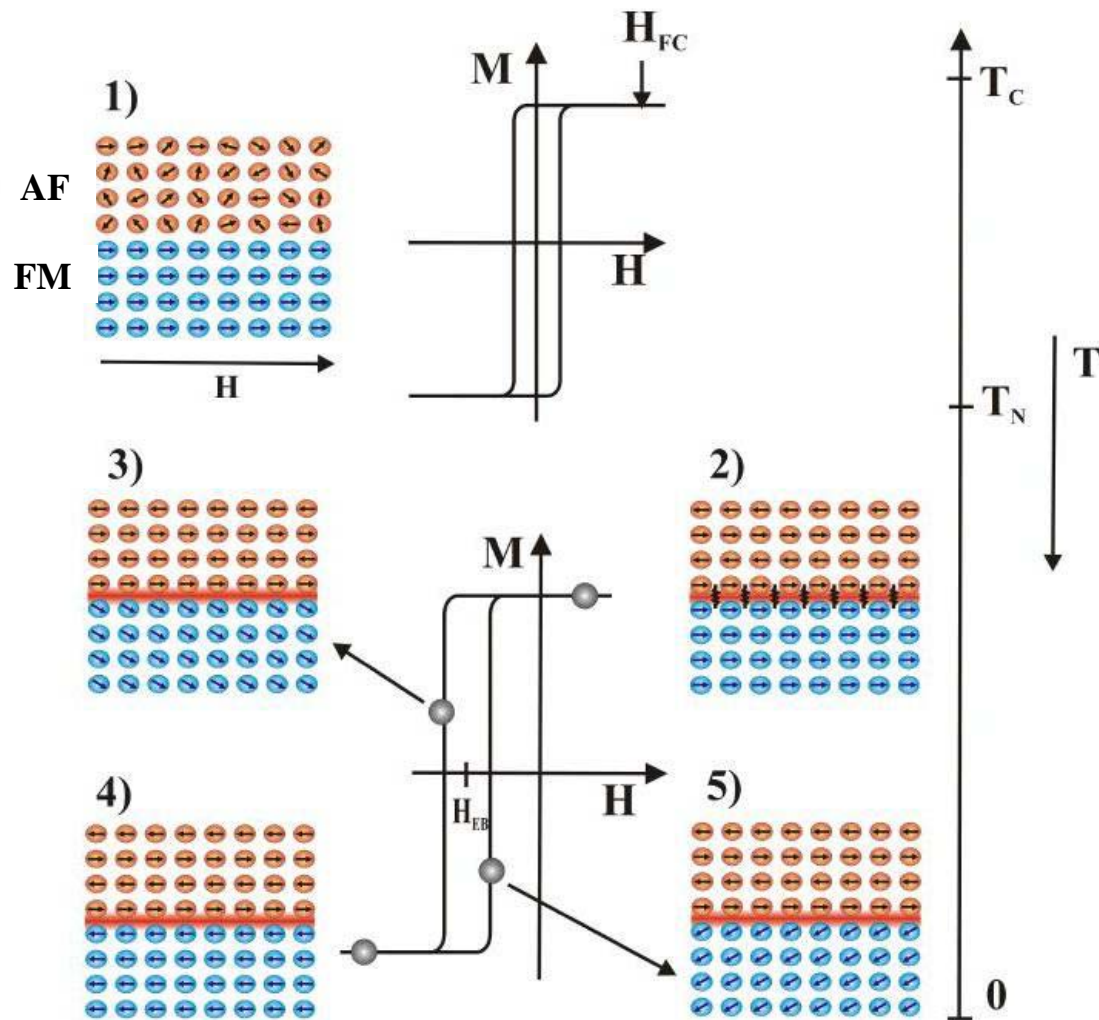


Figure 1.3. Phenomenological model of exchange bias for an AF/FM bilayer. 1) The spin configuration at a temperature $T_N < T < T_C$ (of the FM). AF layer is in a paramagnetic state while the FM layer is ordered. Its magnetization curve (top-right) is centered on zero value of the applied field. Panel 2) is the spin configuration of the antiferromagnet and ferromagnet after field cooling the system through T_N of the antiferromagnet in a positive applied magnetic field. Panel 3) represents the saturated state at the negative applied fields. Panel 4) and 5) show the configuration of the spins during the positive magnetization, assuming that this takes place through in-plane rotation of the FM spins. The center of magnetization curve is displaced at negative values of the applied field by H_{EB} . [Courtesy: Ref (32)]

When reversing the magnetic field, the FM spins will try to follow the applied magnetic field (Fig. 1.3(3)). Being coupled to the antiferromagnet, which is considered to

be rigid, it takes a stronger force and therefore a stronger external field to overcome this coupling and to rotate the FM spins (Fig 1.3(4)). Thus, the magnetic field required to reverse the magnetization in the ferromagnet is then increased when compared to the case of at $T > T_N$. Conversely, when the magnetic field is reversed back to positive values, the rotation of spins in the ferromagnet will be easier than compared to the case of $T > T_N$, since the interaction with the spins in the antiferromagnet favors magnetization reversal of the ferromagnet (Fig 1.3(5)). The ferromagnet behaves as if there was an extra (internal) biasing field, therefore, the magnetization of the ferromagnet easily rotated into positive saturation. A torque is acting on the FM spins for all other angles, except the stable direction which is along the field cooling direction (unidirectional anisotropy). As a result, the magnetization curve is shifted to negative values of the applied field. It is assumed that both the ferromagnet and the antiferromagnet are in a single domain state and that they will remain single domains during the rotation of magnetization process. Moreover, in this simple description the AF spins are considered to be rigid and fixed to the field cooling direction during the entire process.

Although this simple intuitive picture gives a microscopic idea of exchange bias, there is little quantitative understanding of these phenomena. Moreover, the role of the many different parameters involved in exchange bias, such as anisotropy, roughness, spin configuration, is far from being understood. Considering all these facts finally, a clear understanding of exchange bias at the microscopic level is still lacking. The major experimental and theoretical insights in recent years point out that only a fraction of the AF interface magnetization remains stationary during the FM magnetization reversal. It is

this stationary or irreversible fraction S_{AF}^{irr} of the AF interface magnetization that should be used in the MB expression to estimate realistic EB field values.

1.1.3. COERCIVITY ENHANCEMENT

The shift of the FM hysteresis loop along the magnetic field axis is often accompanied by an EB induced loop broadening.^{10,40,41} This effect is not included in the MB description. The understanding of this loop broadening makes it necessary to consider the role of the loosely coupled majority fraction of AF interface spins. The magnetic moment of these loose spins is not irreversible but follows to some extent the magnetization reversal of the adjacent ferromagnet giving rise to a drag effect that broadens the FM hysteresis. So this reversible fraction S_{AF}^{rev} of the interface magnetization of the antiferromagnet is indeed responsible for the enhanced coercivity while the irreversible fraction part S_{AF}^{irr} creates EB loop shift.

More quantitatively based on mean-field arguments it has been predicted that the FM coercivity, H_C , is related to the AF interface susceptibility, $\chi_{AF}^{(1)}$, as follows,⁴²

$$\mu_0 H_C = \frac{\mu_0 H_C^\infty + J_{\text{int}}^2 \chi_{AF}^{(1)} / t_{FM}}{1 + J_{\text{int}} \chi_{AF}^{(2)} / t_{FM}}. \quad (1-8)$$

Here t_{FM} is the FM film thickness, $\mu_0 H_C^\infty = \mu_0 H_c(t_{FM} \rightarrow \infty)$ is the FM bulk coercivity and $\chi_{AF}^{(2)}$ is susceptibility of the antiferromagnet that follows applied magnetic field. In

accordance with the MB approach $\chi_{AF}^{(2)}$ can be assumed to be zero at low temperature. Loosely coupled spins are particularly sensitive to either exchange or applied magnetic fields and, thus, increase the AF interface susceptibility and by that the FM coercivity according to Eq. (1-8). Note that, the EB effect is characteristically reduced when the blocking temperature T_B is approached from $T < T_B$. While loosely coupled moments flip easier when their antiferromagnet neighboring spins lost long range order. Nevertheless a drag effect on the adjacent ferromagnet film is still present above T_B and even above the Néel temperature, T_N , of the AF pinning layer allowing for the persistence of loop broadening above T_N .

In general it is observed that the coercivity decreases with increasing temperature and continues to reduce further above T_B .^{10,43} On the other hand experimentally it is also observed in several systems that the coercivity increases with increasing temperatures and reaches to a maximum at T_B , and start to decrease in the limit of $T_B < T < T_N$.^{12,44,45} This can be correlated to temperature dependence of AF susceptibility. Above T_B , both bulk and interface susceptibilities of the antiferromagnet follow expected Curie-Weiss type behavior, therefore coercivity decreases with increasing temperature. A strongest enhancement in coercivity is observed in the region around T_B where the AF surface spin structure exhibits maximum frustration. This is the point where some fraction of the AF surface spins splits into regions or domains, which are aligned with applied cooling field and rest are in the original AF-coupled configuration. On the other hand, when temperature decreases further below T_B , the correlation between AF bulk susceptibility and H_C vs. T does not hold anymore and it becomes apparent that the T -dependence of the AF interface susceptibility deviates from the bulk behavior. Now this interface

susceptibility of the antiferromagnet is responsible for decrement of the enhancement of the coercivity with the reduction of temperature in accordance with Eq. (1-8).

1.1.4. POSITIVE EXCHANGE BIAS

Almost all hysteresis loops shown in the literature are shifted oppositely to the field cooling direction giving rise to negative EB when applied cooling field is positive. Eq. (1-7) also predicts that the sign of the exchange bias to be negative. Note that the manifestation of EB required field-cooling the EB heterostructure through T_N . Surprisingly, the effects of the cooling field amplitude of EB are rarely reported.⁴⁶ This perhaps due to generally H_{EB} does not depend markedly on the applied cooling field. However, in some systems such as FeF_2/CoPt , FeF_2/Fe and MnF_2/Fe , the EB field changes with the magnitude of the cooling field.⁴⁷ The most striking feature is that for very large cooling fields the hysteresis loop shifts in the same direction as the cooling field, *i.e.*, positive EB.^{47,48} This is contrary to what is observed for small cooling fields or what is observed in other systems.

It is important to note that there is no net EB shift observed when the systems are cooled in zero fields from a demagnetized state of the FM layer. However, when an AF/FM bilayer is zero field-cooled from a remanent state, the EB behavior is present. The magnitude of the cooling field needed to obtain a positive shift depends strongly on the microstructure of the sample, and thus the coupling at the interface. Different theoretical models have been proposed to explain this effect based on the existence of an

AF-coupling at the interface between the FM and AF layers.^{48,49,50} If the coupling at the AF/FM interface is FM, usually it is assumed to have no substantial effect of the cooling field.

In general, positive EB is a rather unusual case but sometimes observed in systems where the interface exchange interaction is AF. At the same time, the freezing field applied during the field-cooling procedure is strong enough to overcome the exchange interaction on cooling the system to below the blocking temperature.^{5,47,48,51,52} Inspection of Fig. 1.4 illustrates intuitively that the measurement of the EB field in a single freezing field is not an appropriate tool to determine the sign of the interface coupling, J . In fact, independent of the sign of J , field cooling allows setting the EB field at negative as well as positive values.⁵³ These details and the specific case of positive EB are discussed in Ref. [5] with the help of the spin structures displayed in Fig. 1.4. Note that all insets in the figure show the spin configurations of ferromagnet and antiferromagnet after initialization of EB below T_B and followed by the complete hysteresis loops of ferromagnets in a positive strong magnetic field. Therefore, the spins of the ferromagnets point in positive field direction in all four insets.

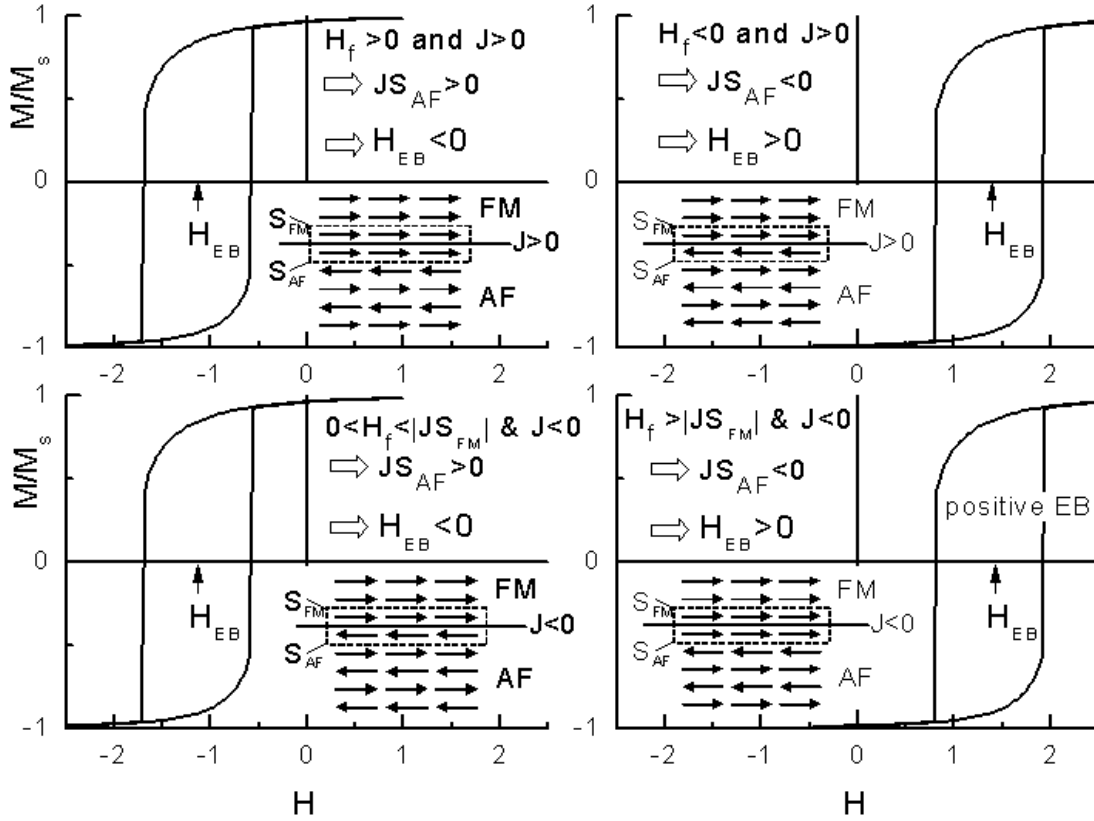


Figure 1.4. Hysteresis loops of an ideal EB heterosystem with FM interface coupling $J > 0$ (upper left and right frames) and AF interface coupling $J < 0$ (lower left and right frames). For $J > 0$ (upper frames) negative (positive) EB fields H_{EB} are indicated by arrows and achieved by field-cooling in a freezing field $H_f > 0$ ($H_f < 0$). For $J < 0$ (lower frames) field-cooling in $0 < H_f < |JS_{FM}|$ creates a regular negative EB field while field-cooling in $H_f > |JS_{FM}|$ gives rise to a positive EB fields which is the fingerprint of the positive EB effect. The frozen AF spin structure and the FM spin structure during the field-cooling process are depicted by arrows. The ideal interface is indicated by a solid line, AF and FM interface spins are marked by boxes (dashed lines). (This figure is from Ref [5])

The two upper frames of Fig. 1.4 show sketches of hysteresis loops after field-cooling an EB heterostructure with FM interface coupling $J > 0$ in positive (left upper frame) and negative (right upper frame) freezing fields H_f . When applying H_f at $T > T_N$ no AF long range order has established and pinning is absent. Hence, the FM top layer is free to align parallel to H_f giving rise to $S_{FM} > 0$ in $H_f > 0$ and $S_{FM} < 0$ in $H_f < 0$. This

state of S_{FM} affects the orientation of the AF interface magnetization which establishes on cooling to below T_{N} . The coupling energy $JS_{\text{AF}}S_{\text{FM}}$ together with the Zeeman energy controls the orientation of S_{AF} . In the case $J > 0$ both, the exchange interaction and the Zeeman energy favor parallel alignment of S_{AF} and S_{FM} such that $JS_{\text{AF}} > 0$ for $H_{\text{f}} > 0$ and $JS_{\text{AF}} < 0$ for $H_{\text{f}} < 0$. Since S_{FM} follows the overall magnetization of the FM layer during a hysteresis loop it is the sign of the stationary product JS_{AF} that determines the sign of the EB field in accordance with Eq. (1-7). Hence, in the case of $J > 0$ negative and positive EB fields are achieved in positive and negative freezing fields, respectively. Obviously, the positive EB field shown in the upper right frame has nothing in common with the phenomenon of positive EB.

The more intricate scenario appears in the case of AF exchange coupling $J < 0$. Both of the two lower frames of Fig. 1.4 show sketches of hysteresis loops after field-cooling an EB heterostructure with AF interface coupling in positive freezing fields. The lower left frame displays the situation of field-cooling in a moderate magnetic field $0 < H_{\text{f}} < |JS_{\text{FM}}|$. Again, when applying H_{f} at $T > T_{\text{N}}$ there is no pinning effect and the FM top layer aligns parallel to $H_{\text{f}} > 0$ giving rise to $S_{\text{FM}} > 0$. The coupling energy $JS_{\text{AF}}S_{\text{FM}}$ favors now antiparallel alignment of S_{AF} relative to $S_{\text{FM}} > 0$. The product $JS_{\text{FM}} < 0$ can be interpreted as an exchange field acting on the AF interface magnetization S_{AF} on cooling. At the same time, S_{AF} has potential or Zeeman energy in the applied freezing field $H_{\text{f}} > 0$ which favors $S_{\text{AF}} > 0$. However, as long as $0 < H_{\text{f}} < |JS_{\text{FM}}|$ is fulfilled, the interface exchange energy overcomes the Zeeman energy resulting in $S_{\text{AF}} < 0$ and, hence, $JS_{\text{AF}} > 0$ giving rise to a regular negative EB field despite $J < 0$.

The situation changes, however, in the case of large positive freezing fields $H_f > |JS_{FM}|$. Now the Zeeman energy overcomes the AF interface coupling giving rise to a parallel alignment of S_{AF} and S_{FM} during the field-cooling process. Hence, $JS_{AF} < 0$ results in a positive EB field in accordance with Eq. (1-7). The latter scenario displayed in the lower right frame of Fig. 1.4 describes the “positive EB effect”. Out of all situations displayed in Fig. 1.4, only here a positive freezing field gives rise to a positive EB field due to *AF interface coupling*. Of course one can repeat the same arguments above for the analogous situation of negative EB fields when field-cooling took place in negative freezing fields. Similar to freezing magnetic field, temperature can also create positive exchange bias after cooling the sample in specific magnetic field as discussed in Ref. [54].

1.1.5. MICROSCOPIC MODELS

Exchange bias is an interface phenomenon. Microscopically the EB phenomenon depends on a large number of system specific details such as structural and magnetic interface roughness, anisotropies of the ferromagnet and antiferromagnet constituents, film thicknesses of the ferromagnet and the antiferromagnet and magnetic history to name just a few. A large number of theoretical models have been proposed and compete to explore the origin of the EB effect. However, almost all theories make at some point a crucial assumption concerning the interface magnetic structure, in particular the interface magnetization of the AF to explain the microscopic details of the EB. Here in this section I present all those different historical microscopic theoretical models and their

corresponding experimental confirmation. Ref [26,31,32] also provide a very good knowledge on several established theories/models of EB so far.

A more reasonable estimate for H_{EB} is obtained by allowing a planar domain wall to form at the interface with the unfavorable FM orientation. This domain wall can in principle be either in the antiferromagnet or in the ferromagnet. However, this domain formation with a domain wall parallel to the interface, *i.e.*, planar domain wall formation, is expected initially on the side of the antiferromagnet.

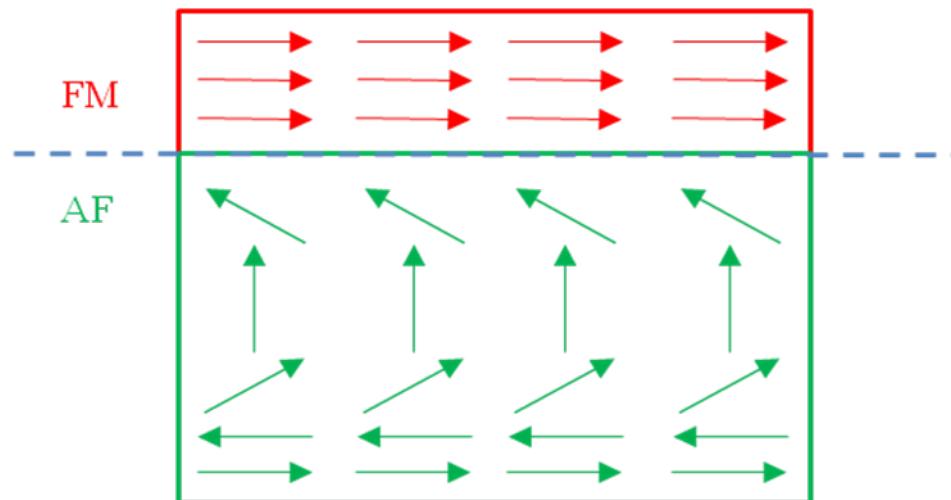


Figure 1.5. Planar AF domain wall (courtesy: Ref [31])

Marrows et al., however, showed that a stable and substantial EB shift can be achieved even for very thin AF layers in which planar domain walls cannot be accommodated.⁵⁵ *Kouvel* and *Néel* first recognized the possibility of obtaining exchange anisotropy with AF partial domain walls (Néel domain wall) that are parallel to the interface as shown in Figure 1.5. More importantly this partial domain wall concept

became pretty famous and was the basis for the following theoretical models to incorporate Néel wall formation as a way to reduce the observed magnitude of EB.^{56,57} However, Kouvel and Néel could not account for the size of these domains and as a result they could not predict the magnitude of the EB field. While *Mauri's* model⁵⁸ had assumed an atomically perfect uncompensated interface. *Malozemoff*^{39,59} assumes that the chemical roughness or alloying at the interface which is present for any realistic bilayer system, causes lateral variation of the exchange field acting on the FM and AF bilayers. The resultant random field causes the antiferromagnet to break up into magnetic domains with domain walls perpendicular to the interface due to the energy minimization as shown in Fig. 1.6. Therefore, Malozemoff was able to estimate some realistic value for H_{EB} .

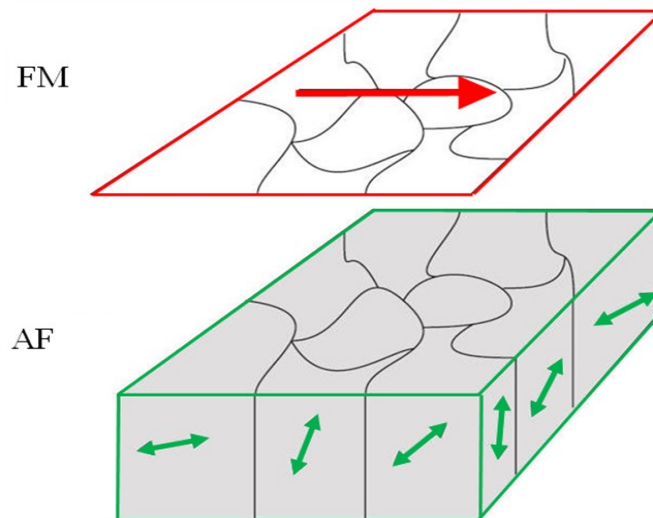


Figure 1.6. Perpendicular AF domain walls. [Ref. 31]

Where all previous models assumed perfectly uncompensated interfaces, *Koon* presented a microscopic explanation of EB in thin films with compensated AF/FM interfaces. He introduced a perpendicular coupling (spin-flop) of the bulk FM moments relative to the AF magnetic easy axis (see Figure 1-7). Furthermore, he proposed that the magnetic moments in the AF interface layer adopt a small canting angle relative to the AF bulk easy axis, with a component opposite to the cooling field direction.

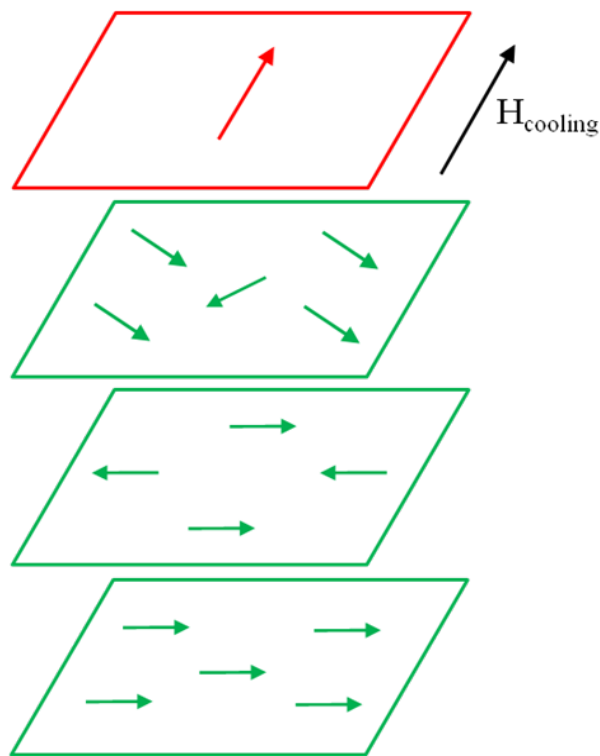


Figure 1.7. Perpendicular coupling between AF/FM layers, with spins canting in the first AF layer. [Ref. 31]

Shulthess and *Butler* demonstrated that *Koon's* model does not actually predict the existence of H_{EB} , but only some enhancement of H_C .⁶⁰ A canted interface magnetic structure is not sufficient to generate EB. *Shulthess* and *Butler* showed that *Malozemoff's*

random interface field and Koon's perpendicular magnetic arrangement can be combined together to provide a meaningful explanation for EB. The quantitative results depend on the nature and concentration of the interface defects. Experimentally, the relation between surface roughness and EB is a complex issue. *Moran et al.*⁶¹ showed that interface disorder increases H_{EB} in the permalloy/CoO system. *Leighton et al.* also reported in the Fe/FeF₂ system, the rougher the interface the larger H_{EB} , but at the same time opposite situation is also occurred in the very similar Fe/MnF₂ system.

Another approach for compensated AF interfaces is the one proposed by *Kiwi et al.*, which explains the effects of the interface coupling in terms of an incomplete domain structure formation in a ferromagnet during the field cooling process.^{62,63} The magnetic structure obtained from the proposition of the ferromagnet is qualitatively compatible with experimental results obtained by *Ball et al.*⁶⁴ The model by *Kiwi et al.* is based on the assumption that the AF compensated interface monolayer freezes into a canted magnetic structure. This model also provides an explanation for positive EB, *i.e.*, a strong cooling magnetic field polarizes the AF spins in the opposite direction in comparison to a low magnetic field cooling procedure, resulting in $H_{EB} > 0$.

Uncompensated moments may originate from domain walls, grain boundaries or defects. The anisotropy of each grain might be different due to local defects and, therefore, the width of domain walls might vary as well. Therefore, extensive theoretical work on polycrystalline samples was presented by *Stiles and McMichael*. In their model the ferromagnet interacts with independent AF grains.^{65,66,67} Each grain is in a single, stable AF state, although a partial AF domain wall parallel to the interface can be created

by coupling to the ferromagnet. When the AF layer is too thin, the AF domain wall formation cannot be completed. Therefore this model postulates that some grains have a critical angle such that when the partial domain wall is wound up to an angle greater than the postulated critical angle, the AF order becomes unstable. The stable grains give rise to unidirectional anisotropy, while the unstable grains result in increasing of the coercivity. A spiraling AF spin structure, as predicted by the models of Mauri, Koon, Schulthess and Butler, and Stiles and McMichael, was experimentally confirmed by *Yang et al.* for permalloy/FeMn/Co trilayers.⁶⁸

Takano et al. proposed that EB originates mainly as a consequence of uncompensated interfacial spins in the antiferromagnet.⁶⁹ They showed that the temperature dependence of the remanent moment due to the uncompensated spins is similar to the temperature dependence of H_{EB} , concluding that both effects are closely related to each other. On the other hand, *Parker et al.* argued that the interfacial, uncompensated spins are of chemical origin.⁷⁰ They found that the interfacial exchange coupling between an AF CoO layer and a FM metal film (Co, Fe, Ni, and Permalloy) occurs via direct exchange between metal atoms and not by super exchange interaction that might be expected at a metal/oxide interface. *Ohldag et al.* detected these pinned interfacial spins in Co/NiO films by measuring element specific hysteresis loops using X-ray magnetic circular dichroism (XMCD).⁷¹ The uncompensated interfacial Ni spins follow the FM Co spins as is clearly revealed by the Ni hysteresis loops. Furthermore, the Ni loops exhibit a small vertical loop shift, originating from pinned interfacial spins. They reported the pinned, uncompensated interfacial spins constitute only 4% of one

monolayer and which are speculated to be located at the grain boundaries. They have also observed unpinned interfacial Ni spins as the source of the increased coercivity.⁷²

Stamps presented a theory, where an interface region between ferromagnet and antiferromagnet is defined in such a way that roughness and imperfection effects can be treated.⁷³ In this theory, the EB is controlled by pinning of partial (Néel) domain walls at the interface. Different amounts of energy stored in the partial wall during forward and reverse paths of the magnetization loop, results in asymmetric hysteresis. On the other hand, *Suess et al.* showed that a bilayer with perfectly compensated interfaces, free of defects and other structural imperfections within grains, can still exhibit EB. The effect of EB shift and coercivity are explained by lateral Néel domain wall formation between exchange-coupled grains in the antiferromagnet.⁷⁴

Nowak et al. has revitalized Malozemoff approach and finally proposed a domain state model for a FM layer coupled to a diluted AF layer.^{75,76} The idea behind this particular model is the antiferromagnet is diluted by non-magnetic defects throughout the entire volume of the antiferromagnet (not just at the interface). This particular antiferromagnet when is field-cooled below the Néel temperature in the presence of the exchange field of the ferromagnet, the disorder in the antiferromagnet together with the homogeneous magnetic field act as a random field on the AF order parameter. This creates the random field domain state in the antiferromagnet. The resulting domains walls in antiferromagnet are pinned at the defects, thus forming a metastable state that becomes frozen during field-cooling. These and only these are the random field domains which carry a remanent magnetization since they develop during a field-cooling process in

which the antiferromagnet is in contact with a saturated ferromagnet. This magnetization provides the biasing field to the ferromagnet, causing the shift of the FM hysteresis loop. Several issues related to EB, such as the dependence of EB on dilution, the role of the AF film thickness,^{77,78} and temperature dependence were successfully discussed within the framework of this domain state model. The structure and stability of the domains in the interface monolayer, which provide the bias field, are strongly influenced by the bulk domain structure.⁷⁹ Calculations using the domain state model are able to describe all features appearing in the data acquired for the IrMn/Co system.⁸⁰ From numerical investigations of the domain state model it was found that asymmetric magnetization reversal in AF/FM multilayers depends on the angle between the FM, AF easy axis and the applied magnetic field.⁸¹

Finally, theoretical difficulties in explaining the interconnection between exchange bias and coercivity are partly explained by Radu *et al.*^{32,82} Radu considered a magnetic state of the interface between the FM and AF layer which is magnetically disordered behaving similar to a spin glass system. The proposed AF/FM interface has both frozen-in uncompensated AF spins that are responsible for the EB shift while low anisotropy interfacial reversible AF spins contribute to the coercivity enhancement.

Microscopic details of the interface between antiferromagnet and ferromagnet play important role in order to understand the origin of EB. However, all models make at some point a crucial assumption concerning this interface; in particular all assumptions are on the interface magnetization of the antiferromagnet. Therefore, it is indeed difficult to compare different types of AF/FM bilayers with one universal theory or model. One

might have to make a distinction between various models when describing systems with compensated or non-compensated interfaces and systems with weak or strong anisotropies. By now it is apparent that the AF and FM domain formations and defects in the crystal structure are also essential parameters in estimating the EB effect in addition to interface roughness. From this summary of various theoretical models and experimental investigations of the EB effect, we have learned that there is no commonly applicable, predictive theory that can fully explain the possibility of interface magnetization in the antiferromagnet. Eventually most of all these theories and models come back to explain specific values of S_{AF} entering the Meiklejohn Bean expression in predicting the value of exchange bias.

1.2. TRAINING EFFECT

The earlier sections provided an intuitive understanding of exchange bias effect; and its phenomenological and historic microscopic theories were presented. This section describes the exchange bias training effect with the basis of phenomenological theory. The later part of the section explains universality of the presented phenomenological theory by fitting it to all possible exchange bias systems.

After EB has been established in AF/FM heterosystem, consecutive hysteresis loops performed on this system can result in a monotonic reduction of EB. This effect is quantified by $\mu_0 H_{EB}$ vs. n and known as training effect (TE), where n labels the number of hysteresis loops cycled after preparation of the initial state of EB via the field-cooling

procedure.^{8,32,83,84,85,86,87,88,89} It is widely accepted that the training effect is related to the unstable state of the AF layer and/or interface between the antiferromagnet and ferromagnet prepared by field cooling procedure. However, it is not yet well established what mechanisms are dominantly contributing to the training effect.

Néel discussed the training effect as a tilting of the magnetization of the AF domains. Micromagnetic simulations within the domain state model show that the hysteresis curve of the ferromagnet is not closed after a complete loop.^{75,90} The reduced magnetization is directly related to a partial loss of the magnetization in the AF domains, which further leads to a decreased exchange bias. Hoffmann argues that only biaxial or higher AF symmetry can lead to training effects, reproducing important features of the experimental data, while simulation with uniaxial AF symmetry show no difference between the first and second hysteresis loops. Experiments performed by polarized neutron reflectivity (PNR) and Kerr Microscopy also support the irreversible changes taking place at the AF/FM interface and in the antiferromagnet which are responsible for the training effect.^{91,92,93} Radu *et al*, presented experimental evidence for a mechanism reducing S_{AF} and, hence, the EB-field decreased by several orders of magnitude in a potentially uncompensated Py/CoO EB heterostructure.⁹⁴ Moreover, they suggested that the experimental values of the training effect can be fitted with a purely empirical expression of double-exponential.

Alternatively, Binek derived a phenomenological description for the training effect in AF/FM bilayers based on Landau-Khalatnikov (LK) approximation which expresses interface magnetization of the antiferromagnet in its order parameter.⁹⁵

Analytical calculations in the framework of non-equilibrium thermodynamics leads to a recursive relation accounting for the dependence of the H_{EB} field on n . Subsequently I show the details of the derivation for training effect in AF/FM bilayers.

1.2.1. PHENOMENOLOGICAL THEORY OF EXCHANGE BIAS TRAINING EFFECT IN AF/FM BILAYERS

Training of the EB refers to changes of the order parameter of the pinning layer from a non-equilibrium initial state of increased free energy into a state of reduced free energy via a discrete sequence of intermediate states. This phenomenological view has its own microscopic correspondence in spin configurational changes of the pinning layer from a non-equilibrium configuration towards a quasi-equilibrium state which is indeed triggered by the consecutive magnetic hysteresis loops of the pinned layer. These spin configurational changes in the pinning layer can be local involving uncorrelated single spin flips but they can as well involve collective mesoscopic domain rearrangements. In general, the pinning layer and pinned layers are antiferromagnet and ferromagnet, respectively for a regular EB system. However, the concept of training has much broader^{43,96,97} applicability; therefore, the pinning layers can include ferrimagnets, spinglasses or magnetically hard ferromagnets to name just a few examples.

The simplest MB expression [Eq. (1-7)] does not directly address the phenomenon of EB training. However, it correlates the exchange bias field with the AF interface magnetization S_{AF} . The latter can and typically does change during successively

cycled hysteresis loops of the FM layer such that $S_{AF} = S_{AF}(n)$ gives rise to an n -dependence in $\mu_0 H_{EB}$ according $\mu_0 H_{EB}(n) = \sigma S_{AF}(n)$. Here σ is independent of the loop index n and is given by $\sigma = -JS_{FM}/(M_{FM}t_{FM})$ according to MB expression of Eq. (1-7).

The precise analysis of the derivation involving $\mu_0 H_{EB}(n) = \sigma S_{AF}(n)$ and mapping it directly onto training effect of EB based on Landau-Khalatnikov (LK) equation⁹⁸ has already developed in Ref [95] with adequate detail. However, I mention those details briefly here as those are hub of my further theoretical modeling and corresponding experimental studies mentioned in chapter 3 and chapter 4 of this thesis.

According Ref [95], the LK equation reads

$$\xi \dot{S}_{AF} = -\frac{\partial \Delta F}{\partial S_{AF}}. \quad (1-9)$$

The Eq. (1-9) is a dynamical equation that provides relaxation in the pinning layer towards its equilibrium state. Here ξ is phenomenological damping constant and \dot{S}_{AF} is the time derivative of interface magnetization of S_{AF} and ΔF is the change in the free energy of the pinning layer.

The left hand side of Eq. (1-9) represents the time derivative of AF interface magnetization S_{AF} . Note that, it is an experimental fact that the S_{AF} does not change continuous in time, instead it is altered every time only when a magnetization reversal of the ferromagnet takes place. There might be a relaxation in the antiferromagnet in the

time interval between two consecutive hysteresis loops of the ferromagnet, however, it is insignificant in comparison to the change in S_{AF} during reversal of the ferromagnet.

Therefore, one has to discretize \dot{S}_{AF} as follows,

$$\dot{S}_{AF} = \frac{S_{AF}(n+1) - S_{AF}(n)}{\tau}. \quad (1-10)$$

Here $S_{AF}(n)$ and $S_{AF}(n+1)$ are the AF interface magnetizations of successive n^{th} and $(n+1)^{\text{th}}$ hysteresis loops of the ferromagnet and τ is a characteristic time taken to measure one hysteresis loop of the ferromagnet.

If we assume $\Delta F(\delta S_{AF}) = \Delta F(-\delta S_{AF})$, a series expansion of ΔF up to fourth order in δS_n reads

$$\Delta F = \frac{1}{2} \tilde{a} \delta S_n^2 + \frac{1}{4} \tilde{b} \delta S_n^4 + O(\delta S_n^6). \quad (1-11)$$

Here $\delta S_n = S_{AF}(n) - S_{AF}^e$ and $S_{AF}^e = \text{Lim}_{n \rightarrow \infty} S_{AF}(n)$. The latter describes quasi-equilibrium interface magnetization of the antiferromagnet after infinite number of magnetic reversal of the pinned layer. In general $O(\delta S_n^6)$ are negligible here due to smallness of $|\delta S_n|$. Note that any positive or negative deviation in δS_n of the AF interface magnetization reflects in its free energy according to Eq. (1-11).

From Eq. (1-9), (1-10) and (1-11) one can write

$$\tilde{\xi} (S_{AF}(n+1) - S_{AF}(n)) = -\delta S_n (\tilde{a} + \tilde{b} \delta S_n^2), \quad (1-12)$$

where $\tilde{\xi} = \xi/\tau$. In the case of strictly monotonic decrease of $|S_{AF}(n)|$, $\tilde{a} > 0$ causes necessarily an asymptotic decay of the type $S_{AF}(n) \propto e^{-\tilde{a}n} + S_{AF}^e$ in the limit $n \rightarrow \infty$, when finally $\delta S_n \gg \delta S_n^3$. Exponential relaxation, which is generically faster than any potential decay, is typically observed, when spin correlation becomes negligible. But in the case of exchange bias, however, a large AF spin correlation is essential in order to pin the FM layer during its magnetization reversal. Exchange bias and the training effect disappear only above the blocking temperature where antiferromagnet spin correlation significantly levels off. Hence, non-exponential relaxation has to be expected below the blocking temperature. Therefore, this condition gives rise to $\tilde{a} = 0$.

Note that, the above mentioned description provides the absence of the second order dependence (from Eq. (1-11)) of the free energy on S_{AF} using the experimental observation as an input. However, this argument can be justified and derived by using mean-field approach as well. We know at $T < T_N$, the free energy of the pinning layer has two pronounced minima at $\eta = \pm\eta_e$, where $\eta = (m_1 - m_2)/2$ describes primary order parameter of the antiferromagnet, while the magnetization $m = (m_1 + m_2)/2$ describes secondary order parameter. Here $m_{1,2}$ are the normalized sublattice magnetizations. Due to these two pronounced minima of $\pm\eta_e$, ΔF of the pinning layer can be expanded in harmonic approximation, *i.e.*,

$$\Delta F = \alpha(T)(\eta - \eta_e)^2 \quad (1-13)$$

with $\alpha(T)$ as temperature-dependent expansion coefficient. On the other hand, mean-field theory provides the relation between the primary and secondary order parameters. From mean-field theory one obtains η is an even function of m in the vicinity of the equilibrium value $m=0$, which reads

$$\eta = \eta_e + \frac{1}{2} \left. \frac{\partial^2 \eta}{\partial m^2} \right|_{m=0} m^2 + \dots, \quad (1-14)$$

substitution of the expression (1-14) and from $\delta S_{AF} \propto m$ into (1-13) yields,

$$\Delta F \propto \alpha(T) \left(\left. \frac{\partial^2 \eta}{\partial m^2} \right|_{m=0} \right)^2 (\delta S_{AF})^4 \quad (1-15)$$

i.e., $\Delta F \propto (\delta S_{AF})^4$, which is precisely consistent with above mentioned description of appearance of *only* fourth order dependence of the free energy on S_{AF} giving rise to $\tilde{a}=0$ in Eq. (1-11).

Therefore, Eq. (1-12) simplifies to,

$$S_{AF}(n+1) - S_{AF}(n) = -\frac{\tilde{b}}{\tilde{\xi}} \delta S_n^3 \quad (1-16)$$

The expression (1-16) has close analogy with the phenomenon of critically slowing down.⁹⁹ One may speculate that the close analogy between critical slowing down and the training effect originates from the physics of large spin fluctuations, which play an important role in the case of both phenomena.

Now, the substitution of $\delta S_n = S_{AF}(n) - S_{AF}^e$ and $\mu_0 H_{EB}(n) = \sigma S_{AF}(n)$ into Eq.

(1-16), give rise to an implicit equation:

$$\mu_0 H_{EB}(n+1) - \mu_0 H_{EB}(n) = -\gamma \left(\mu_0 (H_{EB}(n) - H_{EB}^e) \right)^3. \quad (1-17)$$

Here $\gamma = \tilde{b}/\sigma^2 \tilde{\xi}$ The Eq. (1-17) represents the phenomenological expression of the training effect in AF/FM bilayers. The fitting parameters γ and H_{EB}^e are the results of fits involved Eq. (1-17) to the experimental data. Figure 1.8 shows fits (black solid squares) of Eq. (1-17) to the experimental data (open solid circles).

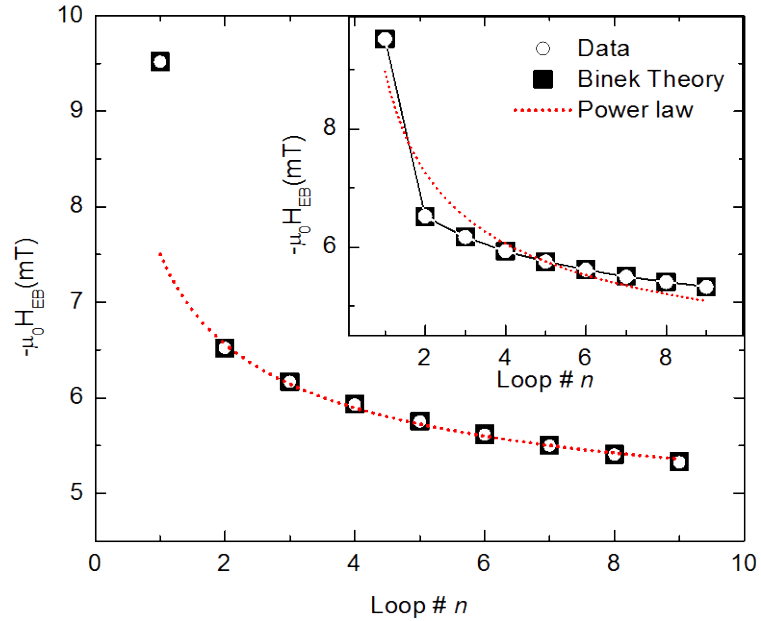


Figure 1.8. Training effect $\mu_0 H_{EB}$ versus n (open solid circles) of a NiO/Fe heterostructure (Ref. 96) and the corresponding results of the best fits of Eq. (1-17) for $n \geq 1$ in solid black squares. Dotted red line shows the best fit of Eq. (1-18) to the data for $n > 1$. The result of the fit is extrapolated down to $n=1$ in order to indicate the breakdown of the power-law behavior at $n=1$. [Inset] shows again the experimental data (open circles) as reference, while the squares display the result of the best fit of implicit sequence (1-17) to the entire data set for $n \geq 1$. The straight lines connecting the squares are a guide to the eyes only. Dotted red line is a best fit of Eq. (1-18) to the entire experimental data.

The fit shows perfect agreement with the data. This concludes that the experimental data satisfactorily described for $\tilde{a}=0$, which asymptotically corresponds to the Power-law.^{83,100} The latter expression is the first empirical expression suggested for the training effect as loop index n , which reads

$$\mu_0 H_{EB}(n) = \mu_0 H_{EB}^e + \frac{\kappa}{\sqrt{n}}, \quad (1-18)$$

where κ is an experimental constant. This expression follows well with the experimental dependence of the EB field for $n \geq 2$, as shown in Fig 1.8 by red colored dotted line. The extrapolation of the fit to $n=1$ indicates the breakdown of the power-law behavior at $n=1$. However, the inclusion of first point in the fit of Eq. (1-18) for $n \geq 1$ make the fit inaccurate as shown in the inset of Fig. 1.8 by dotted red line.

Subsequently I show that the asymptotic behavior of Eq. (1-17) in the limit of large n eventually produces power-law behavior of the training effect in accordance with Eq. (1-18).

In limit of large n , $\sqrt{n+1} \approx \sqrt{n} + \frac{1}{2\sqrt{n}}$. Now substitution of Eq. (1-18) into Eq. (1-17)

with this approximation produces,

$$\mu_0 H_{EB}^e + \frac{\kappa}{\left(\sqrt{n} + \frac{1}{2\sqrt{n}}\right)} - \left(\mu_0 H_{EB}^e + \frac{\kappa}{\sqrt{n}}\right) = -\gamma \left(\mu_0 H_{EB}^e + \frac{\kappa}{\sqrt{n}} - \mu_0 H_{EB}^e\right)^3.$$

The above equation is simplified to,

$$\frac{\sqrt{n} - \left(\sqrt{n} + \frac{1}{2\sqrt{n}} \right)}{\sqrt{n} \cdot \left(\sqrt{n} + \frac{1}{2\sqrt{n}} \right)} = -\gamma \frac{\kappa^2}{n^{3/2}}$$

But in the limit of large n , the denominator $\sqrt{n} \cdot \left(\sqrt{n} + \frac{1}{2\sqrt{n}} \right)$ becomes n . Therefore,

$$\frac{1}{2n^{3/2}} = \gamma \frac{\kappa^2}{n^{3/2}} \quad (1-19)$$

Note that both left and right hand sides of Eq. (1-19) have the same power of n . This evidences the asymptotic behavior of Eq. (1-17) in the limit of large n giving rise to Eq. (1-18). In other words, Eq. (1-17) contains the power law but in contrast to the latter is also applicable at low n down to $n=1$. From Eq. (1-19) one obtains the relation between κ and γ , which reads

$$\gamma = \frac{1}{2\kappa^2} \quad (1-20)$$

From Fig. 1.8 it is clearly shown that Binek's proposed implicit expression (1-17) provides the best fit in comparison to power-law decay (1-18). The implicit equation (1-17) is the "only" theoretical model so far and can be successfully fit to the training behavior of different systems. This concludes the accomplishment in deriving the equation of the training effect based on phenomenological approach.

Note that a large values of γ refer to small absolute training effects where the absolute strength of the training effect is quantified according to

$\mu_0(H_{EB}(n = \text{const}) - H_{EB}^e)$. It becomes obvious when rearranging the terms in Eq. (1-17) into,

$$\gamma = \frac{\mu_0(H_{EB}(n) - H_{EB}(n+1))}{(\mu_0(H_{EB}(n) - H_{EB}^e))^3} \quad (1-21)$$

A large value of γ requires a small value of the denominator, which means small deviations from the equilibrium EB field. In other words, the strength of the training effect is weaker for large value of γ . However reaching T_B , the absolute training effect has to become zero where the EB effect itself is zero for all n . On the other hand, small values of γ correspond to large absolute training effects which are, however, spread over a larger number of cycles. The limiting value of $\gamma = 0$ at $T = 0$ is a special case where $\mu_0(H_{EB}(n) - H_{EB}^e)$ remains finite and same for all n , which means the system is frozen where $\mu_0(H_{EB}(n) - H_{EB}(n+1)) = 0$. This makes perfect sense due to the fact that the lack of thermal excitations, no change of the EB field that is thermally assisted and the system is unable to reach the equilibrium value $\mu_0 H_{EB}^e$ on consecutive hysteresis loops, n . However, note that it does not mean that the EB field is zero.

Eq. (1-17) has mainly been applied to cases where the $\mu_0 H_{EB}$ shows a gradual n -dependence. In the literature it has been suspected that the expression (1-17) may not be able to fit step-like training effect where all dynamics or relaxation in the AF pinning layer happens only between first and second hysteresis loops of the ferromagnet. This is of course not correct and the Fig 1.9(c) of the next section evidences the fact that the phenomenological expression (1-17) also successfully explains the step-like behavior of

the training effect. This is in strong contrast to recent interpretations¹⁰¹ of Eq. (1-17). It is straightforward to show, that

$$\gamma = \frac{1}{\left(\mu_0 H_{EB}(n=1) - \mu_0 H_{EB}^e\right)^2} \quad (1-22)$$

gives rise to pure step-like characteristics of $\mu_0 H_{EB}$ vs. n . Defining a steepness parameter C as $C = (H_{EB}(n=1) - H_{EB}(n=2)) / (H_{EB}(n=1) - H_{EB}^e)$ which quantifies the characteristics of the training behavior one can show $\gamma = C / (\mu_0 H_{EB}(n=1) - \mu_0 H_{EB}^e)^2$ where $0 \leq C \leq 1$. $C=1$ resembles step-like behavior, while $C < 1$ gives rise to gradual behavior of $\mu_0 H_{EB}$ vs. n for $n > 2$.

1.2.2. UNIVERSALITY OF THE PHENOMENOLOGICAL THEORY OF THE TRAINING EFFECT

The earlier section provides the phenomenological based exchange bias training effects expression (1-17) for AF/FM heterosystems. However, meanwhile we have observed that Eq. (1-17) is also applicable to a variety of distinct systems that are structurally, chemically and magnetically diverse. Here in this section we present the results from all those dissimilar systems such as regular EB heterostructures, exchange spring type HL/SL bilayers, FM/ferrimagnetic systems, nanocomposites, small FM precipitates in an AF host matrix, systems with intrinsic phase separation and many more.^{4,43,83,96,97,102,103,104,105,106,107,108}. All of the examples mentioned above are

quantitatively described by the phenomenological theory of the training effect based on Eq. (1-17). Figure 1.9 displays some of the examples mentioned above.

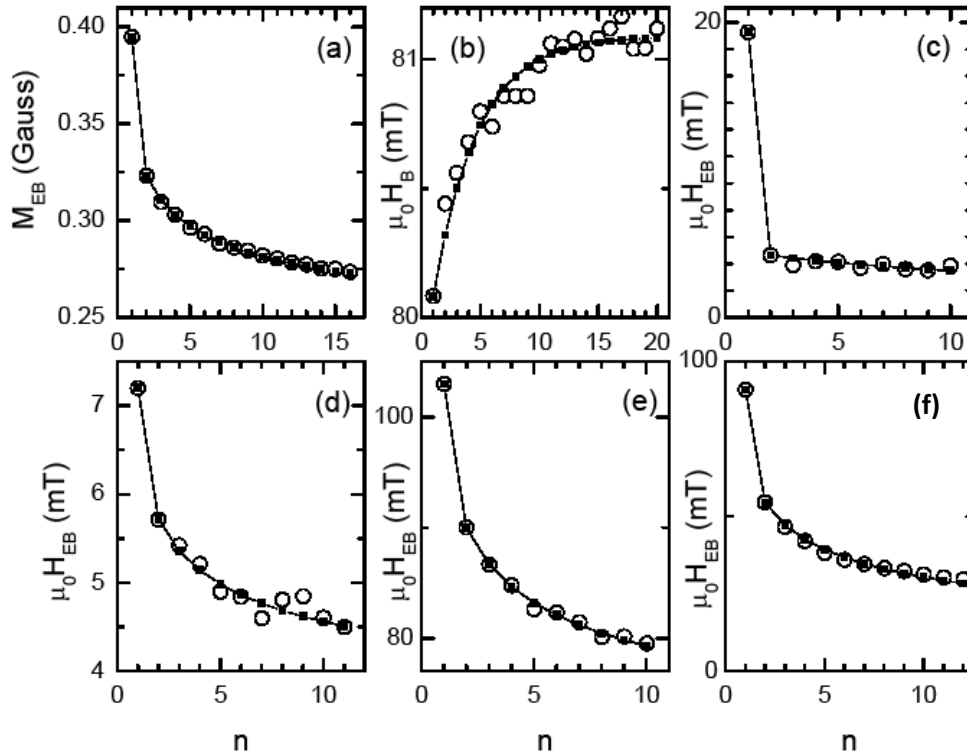


Figure 1.9. Training effect $\mu_0 H_{EB}$ vs. loop # n for different EB systems. (a) FM nanodomains embedded in the charge ordered antiferromagnet, (b) FM hard/soft bilayers, (c) Co/CoO heterostructure, (d) FM precipitates surrounded spinglass matrix, (e) Layered cobaltite $Sr_{1.5}Pr_{0.5}CoO_4$, (f) Layered cobaltite $La_{1-x}Sr_xCoO_3$.

We recall data from original references and exhibit them in Fig. 1.9 consistently by open circles. Solid squares in Fig. 1.9 (a) and (c)-(f) represent two-parameter fits of Eq. (1-15). The data shown in Fig. 1-9 (b) originates from all FM hard/soft bilayer system and are therefore best fitted with an expression analogue to Eq. (1-17). The details of deriving this expression from discretized LK equation are mentioned in chapter 4. All of

the best fits displayed here have been generated by us to ensure comparability between the various data sets. It is obvious to get interested in knowing the system specific parameters such as a function of temperature or layer thickness for instance.^{109,110,111} Therefore, chapter 3 and chapter 4 are solely dedicated for this purpose. Here we provide specific details of all those systems mentioned above in Figure 1.9

Fig. 1.9 (a) shows a training effect of the FM nanodomains embedded in the charge ordered AF manganite $\text{Pr}_{1/3}\text{Ca}_{2/3}\text{MnO}_3$. Data has been digitized from Ref. [97] and are best fitted with Eq. (1-17) showing excellent agreement.

Fig. 1.9 (b) shows data from the FM hard/soft bilayer discussed in Ref. [112]. The theory fits are results of an explicit expression that analogous to Eq. (1-17). Chapter 4 discusses the phenomenological description in obtaining this expression.

Fig. 1.9 (c) refers to data from Ref. [111] measured locally on a wedged but otherwise regular EB Co/CoO heterostructure with the help of the magneto-optical Kerr effect. The sample specifications are mentioned in the chapter 3. A remarkable steep training behaviour with a very pronounced decent of the EB field between the first and the second loop is again perfectly described by Eq. (1-17). The potential of Eq. (1-17) to describe step-like training characteristics has been doubted in the literature although it is straightforward to show that it is inherent to the implicit sequence given by Eq. (1-17). We will discuss this point in chapter 3 in detail.

Fig. 1.9 (d) shows data from Ref. [102] obtained from the perovskite cobaltite $\text{La}_{1-x}\text{Sr}_x\text{CoO}_3$ where spontaneous phase separation creates interfaces between FM

precipitates and a surrounding spinglass matrix. The data shown here refer to $x=0.18$. Despite the exotic nature of this sample's intrinsic EB effect, the two parameter fit of Eq. (1-17) describes the n -dependence of the EB field perfectly within the noise level of the data.

Fig. 1.9 (e) and (f) show data of two other phase separating systems, the layered cobaltite $\text{Sr}_{1.5}\text{Pr}_{0.5}\text{CoO}_4$ and again the cobaltite $\text{La}_{1-x}\text{Sr}_x\text{CoO}_3$ studied by a different group and in the lower doping regime $x=0.12$. The experimental data is obtained from Ref. [103] and Ref. [107] and convincingly fitted with the help of Eq. (1-17), respectively.

By now it is obvious that the successful application of the Eq. (1-17) to structurally, chemically and magnetically dissimilar systems clearly evidences the fact that the phenomenological theory is universal and applicable to all systems independent of their specific details. Note that a systematic refinement of Eq. (1-17) is simple when generalizing the harmonic approximation of the free energy as outlined in Ref. [113]. So far we are not aware of any EB training data which cannot be described by Binek's postulated phenomenological theory. The phenomenological approach of the training effect and in particular Eq. (1-17) has been sometimes misinterpreted as an inapplicable approach for EB training effect based on microscopically motivated arguments. Note that Eq. (1-17) is developed based on neither microscopic details nor specifications of a particular EB system. This is indeed a general misconception in perceiving the phenomenological models. Sometimes the microscopic motivated arguments are accompanied by introducing alternative fitting functions. It is like comparing 'pears' with

'apples'. Ref. [4] discusses these arguments and contrasts them against the general background of phenomenology.

CHAPTER 2

SAMPLE PREPARATION METHODS AND EXPERIMENTAL TECHNIQUES

This chapter contains two sub-sections. The first section describes the sample preparation techniques such as magnetron sputtering and Molecular Beam Epitaxy. The second section deals with different structural and magnetic characterization techniques I have used throughout my research work. The structural characterization includes methods of wide angle X-ray diffraction and small angle X-ray reflectivity. The magnetic properties are characterized with the help of an Alternating Gradient Force Magnetometer, a Superconducting Quantum Interference Device, and Longitudinal-Magneto Optical Kerr Effect. By using Jones matrix formalism, we identified two optimized Kerr configurations and confirm their superior performance experimentally.

2.1. SAMPLE PREPARATION METHODS

2.1.1. MAGNETRON SPUTTERING

Sputtering is a physical process that can be seen as throwing steel balls at a concrete wall. Upon impact, the ball tears away fragments of the concrete. In sputtering, the steel balls are ionized atoms and the wall is a surface of the material to be sputtered, called a target. The sputtering takes place in an evacuated chamber which contains a

substrate and the target of the film material to be sputtered. Typically Ar gas is introduced and then ionized inside the chamber. The accelerated positive Ar ions finally bombard the negatively maintained target. If the kinetic energy of the Ar ions is sufficient, then the surface atoms are sputtered from the target.¹¹⁴ In our case the kinetic energy of the Ar ion is 3×10^{-17} J. Since the chamber is maintained at low pressures ($\sim 6.7 \times 10^{-3}$ mbar during sputtering), the liberated material settles on everything in the chamber, mainly onto the substrate which is grounded.^{115,116,117}

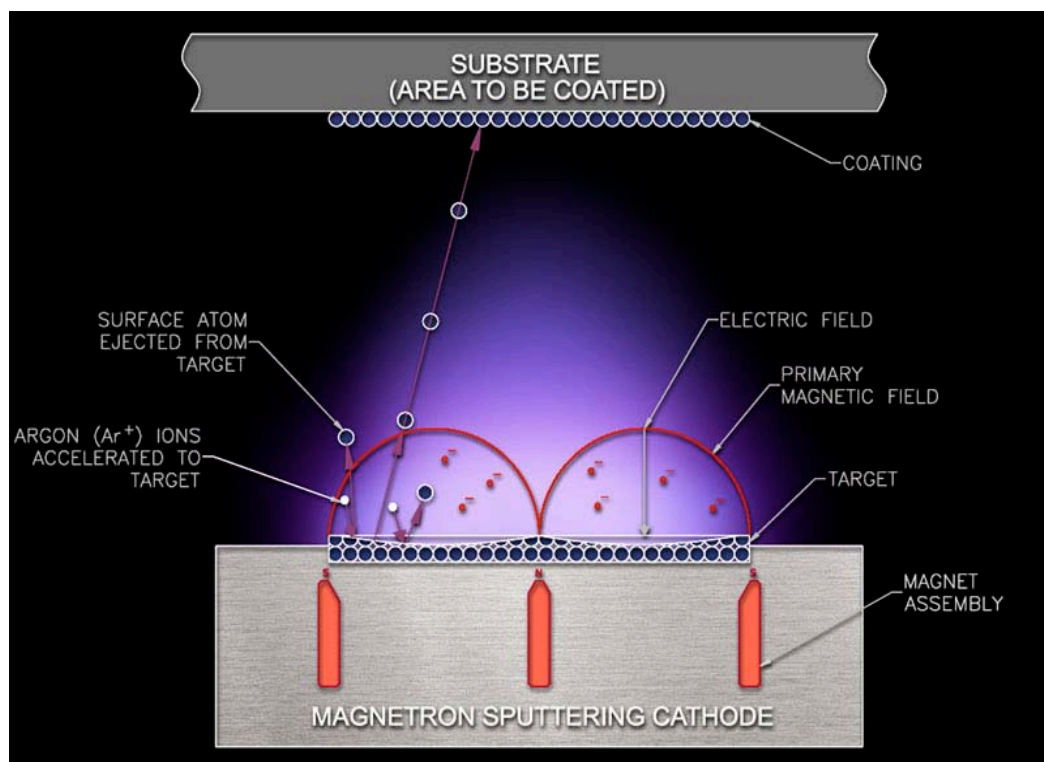


Figure 2.1. The side view of magnetron sputtering inside the growth chamber. The target is connected to negative electrode. The knocked out atoms by electrons are directed towards a substrate which is grounded. Purple color background is plasma of electron and Ar⁺ atoms.¹¹⁸

In magnetron sputtering, magnets are placed behind or aside to the target, as shown in figure 2.1, to improve the growth rates of deposited material. These magnets confine the escaping electrons in the immediate vicinity of the target. Since the electric and magnetic fields are perpendicular to each other, the electrons produced during the collisions propagate in helical orbits due to Lorentz force and are constrained above the targets, efficiently enhancing the further ionization of Ar atoms. As a result, the ion current of Ar hitting the target increases by an order of magnitude over conventional sputtering systems, resulting in faster deposition rates even at lower pressures.

Sputtering is a method of depositing metal films, insulators and alloys onto a substrate. In case of depositing insulators, one has to use RF-sputtering to avoid the positive space-charge between target and substrate. Our samples were fabricated in a homemade DC magnetron sputtering system that has been prepared based on different components received from the 3M and Varian. The growth chamber has been pumped down with one cryo-pump (1.0×10^{-7} mbar) backed by a mechanical pump (5.0×10^{-3} mbar). Substrates were clamped on a water cooled holder which can hold 12 samples per sputtering run. The rotational position of the sample holder is controlled by a stepper motor connected to a PC. The chamber has been pumped down for roughly 14 hours until the desired base pressure is reached and then sputtering was performed in Ar atmosphere of pressure $\sim 6.7 \times 10^{-3}$ mbar.^{29,119}

2.1.2. MOLECULAR BEAM EPITAXY

Molecular beam epitaxy (MBE) is a potential layer by layer deposition technique of growing high quality thin films. This technique was invented in 1960s at Bell laboratories by J. R. Arthur and Alfred Y. Cho.^{120,121,122,123} The word “epitaxy” refers to method of depositing a monocrystalline film on a monocrystalline substrate. Basically there are two forms of epitaxy: the first one is ‘homoepitaxy’, where a single-crystalline film is deposited on a substrate of the same material, and the second one is ‘heteroepitaxy’, where a crystalline film grows onto a crystalline substrate or film of another material.

The principle underlying MBE growth is relatively simple in comparison to sputtering: it consists essentially of atoms or clusters of atoms, which are produced by heating up a solid source. They then migrate in an ultra-high vacuum (UHV) environment and impinge directly on a substrate, where they can diffuse and eventually incorporate into the growing film. Despite the conceptual simplicity, a great technological effort is required to produce systems that yield the desired quality in terms of material purity, uniformity and interface control and, also achieving the epitaxial growth of the film is a gigantic challenge. MBE is a proper technique when some particular requirements are needed such as abruptness of the film surfaces, control over the interfaces and doping profiles. Typically, MBE deposition takes place in UHV ($<10^{-8}$ mbar) and at slower deposition rates (typically less than $3^{\circ}\text{A}/\text{sec}$) in comparison to sputtering, which may allow the possibility of epitaxial growth of film. Finally, the UHV environment in MBE may also provide the use of electron diffraction probes such as Reflecting High Energy

Electron Diffraction (RHEED) without any differential pumping system attached RHEED gun.

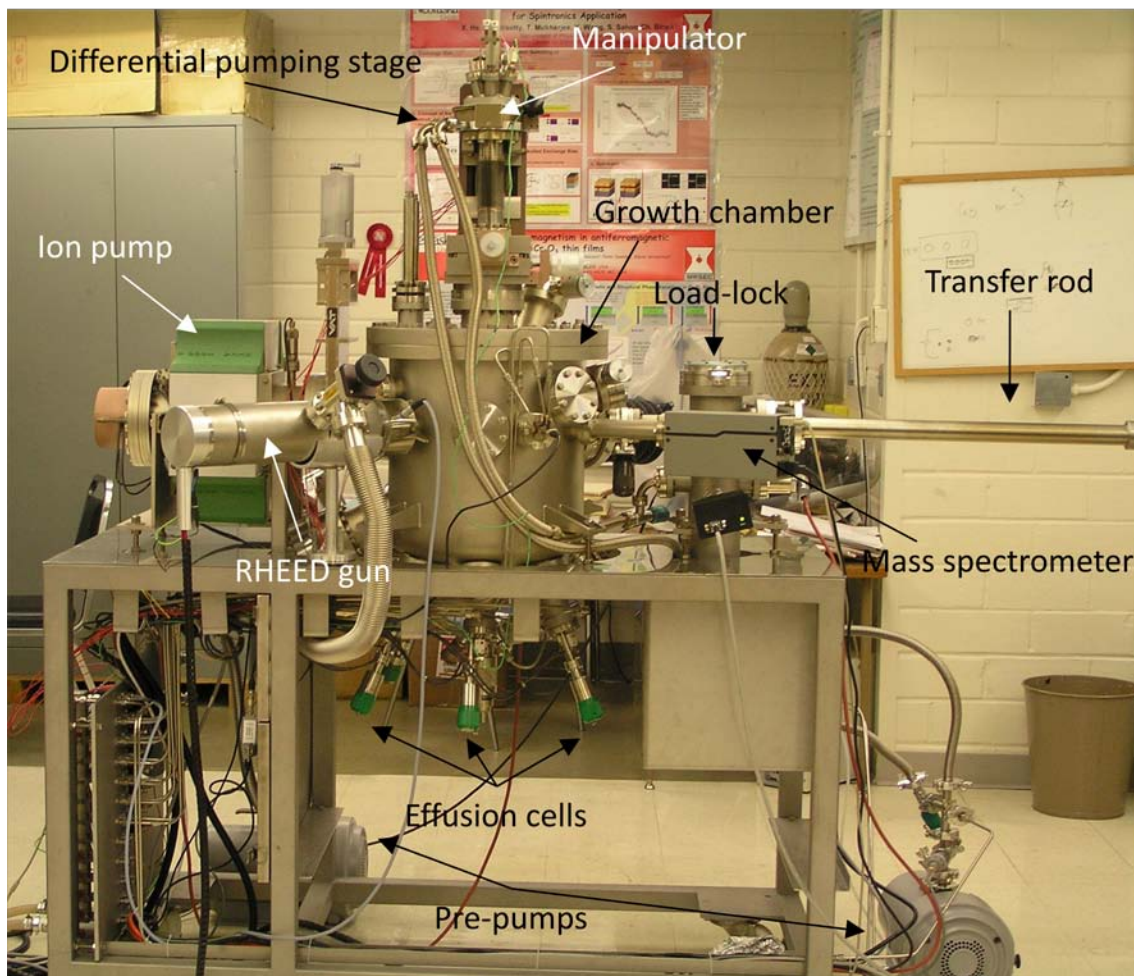


Figure 2.2. A Snap shot of our present Molecular Beam Epitaxy apparatus. Two backing pumps (at the bottom), two turbo molecular pumps (not visible), an ion pump (on the left hand side) and the titanium flash (not visible) are used in pumping down the pressure of the growth chamber. A transfer rod (on the right) transfers the sample from the load-lock chamber to the manipulator of the growth chamber. A differential pumping rotational stage is helpful in mounting the sample and also in aligning sample for getting RHEED pattern. Pressure gauges (not visible) are connected to both growth and load-lock chamber separately. Four effusion cells and one e-beam evaporator are located at the bottom of the growth chamber are utilized in evaporating Co, Pd, Cr, Fe and Ni, respectively. A wobble stick is located on the other side of the growth chamber (not visible) to cover the sample before deposition. In addition to a quartz crystal monitor (not visible) and a RHEED gun is also assembled to growth chamber for monitoring layer-by-layer growth of thin films during the deposition. Additionally this system has baking unit (not shown) to bakeout the whole chamber and further reduces the pressure. A mass spectrometer is also connected to growth chamber to monitor the gasses present inside the growth chamber during all the time. Soon we are planning connect sputtering ion gun to clean the substrates thoroughly before we evaporate thin films on to it.

Figure 2.2 is the snapshot of our present MBE apparatus. During the initial period of my Ph.D work, I have spent my time in assembling different components of the MBE that are transported from Createc. Our MBE System SY050 is a custom designed machine used for growing of epitaxial layers on custom designed sample holders of 1 inch in size. The system is fully bakeable, to achieve lowest base pressure of typical value 5×10^{-11} mbar for crystal growth. The detailed block diagram of our MBE shown in figure 2.3 reveals the connections between different existing components in MBE. Here, I am going to discuss these different components in detail.

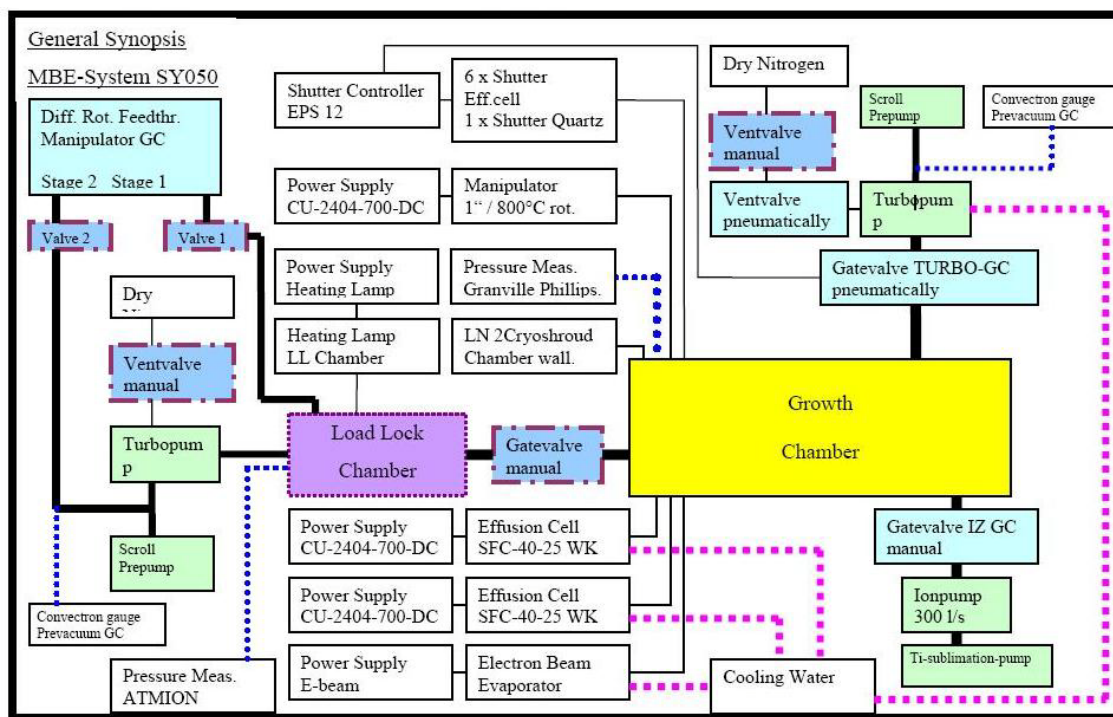


Figure 2.3. Block diagram of Molecular Beam Epitaxy SY050 from Createc

The Growth Chamber: A 16-inch UHV chamber that is equipped with 4 effusion cells (Createc), an electron-beam evaporator (Oxford Scientific), a manipulator (Createc), two gate valves (VAT, Inc), Reflection High Energy Electron Diffraction (RHEED) gun, an infrared heat-coil and windows for observing transfer, a cryoshroud for the chamber wall, water cooling units for the effusion cells and a Bayard Alpert (BA) ionization gauges (Varian) for vacuum measurement. A water-cooled Quartz crystal microbalance (McVac) monitors the *in-situ* growth rate. A quadrupole mass spectrometer (Stanford Research systems) monitors the residual gases present in the growth chamber. The growth chamber is pumped down by an ion pump (Varian) with the help of integrated Ti sublimation (Varian) pump. The growth chamber is isolated from a load-lock chamber by means of a manual gate valve (VAT, Inc). All the components of the growth chamber are able to resist bake-out temperatures of up to 200°C for extended periods of time, which are necessary to minimize out-gassing from the internal walls.

The Load-Lock Chamber: It allows loading a 1-inch wafer holder. It is connected directly to the growth chamber through a gate valve. The load-lock chamber is pumped down with a water-cooled turbo molecular pump (Varian) and a dry scroll pre-pump (Varian) to achieve very fast high vacuum ($\sim 10^{-9}$ mbar). One infrared heating lamp allows removing the water from mounted wafer holders just after pump down. A Bayard Alpert type gauge (Atmion) monitors UHV conditions of the chamber. The transfer rod helps in transferring samples from load-lock into growth chamber and back. A Residual Gas Analyzer (RGA) is connected to load-lock chamber which provides the information on constituents present inside the growth chamber.

The pumping system: It is the combination of pre-pumps, turbo molecular pumps, ion pump and Ti-sublimation. The growth chamber is connected to a turbo molecular pump ($\sim 10^{-9}$ mbar) via RHEED gun (Specs). An oil free pre-pump (1.3×10^{-3} mbar) serves the purpose of backing pump to a turbo pump. Once the vacuum in the growth chamber reaches $\sim 10^{-9}$ mbar, then ion-pump starts working and brings down the pressure to $\sim 10^{-10}$ mbar. Later on Ti-sublimation pump sublimates once in 4-8 hours for one minute and lowers the pressure down to 5×10^{-11} mbar. The whole process of reaching 10^{-10} mbar from atmospheric pressure takes usually 1.5 days and reaching 10^{-11} mbar takes few more days. The load-lock chamber is separately connected to a turbo molecular pump with backing oil-free pump and is isolated from growth chamber by a gate valve. Both load-lock and growth chambers are separately connected with pressure gauges.

Effusion cells: These are the key components of an MBE system, because they provide an excellent flux stability and uniformity in thin film growth. Furthermore, they should withstand the highest temperatures for the longest periods. Therefore a careful choice of elements, materials and geometry must be taken. Our chamber has four effusion cells and one electron beam gun for depositing Cobalt, Palladium, Iron, Chromium and Nickel, respectively. Cobalt and Palladium are placed in high temperature effusion cell crucible made of Beryllium Oxide, BeO ($T_{\max}=1800\text{C}$). Iron and Chromium are placed in single filament effusion cells and the crucibles are made of Pyrolytic Boron Nitrite (PBN) ($T_{\max}=1400\text{C}$). All effusion cells are equipped with thermocouples and which are connected to PID controllers to readout the temperatures of effusion cells. Nickel is placed in electron beam gun. All effusion cells including the electron-beam evaporator are water cooled during all the time.

The Manipulator: It is designed for heating and cooling the sample substrate. A Tungsten wire is used as a filament to heat the wafer holder while a cryostat is used to cool the substrate wafer. A two-stage differential pumping system is included to provide rotational freedom and limited translational freedom for the manipulator. X-, Y- and Z-adjustments of the manipulator helps in mounting the sample holder and most importantly plays crucial role on getting RHEED pattern on screen.

2.2. EXPERIMENTAL TECHNIQUES

The basic structural characterization of the grown sample is done using wide angle X-ray diffraction (XRD). It provides the information of the crystal structure in grown thin film heterostructures. In addition, a small angle X-ray reflectivity (XRR) is also performed on heterostructures to verify the thicknesses of different existing constituents. The XRR scans also provide an idea of surface roughness. In addition, pole figure scans are performed to evidence single-crystalline structure in the thin films.

2.2.1. WIDE ANGLE X-RAY DIFFRACTION

To describe the atomic arrangements in a given crystal, a probing sensor that can interact with atoms is required. Under this category X-rays are one of the best probing sources with the wavelength around one Angstrom which is equivalent to inter atomic distances.

Our XRD measurements are carried out on both a Rigaku D/Max-B Diffractometer and Bruker-AXS D8 Discover High-Resolution Diffractometer with HI-STAR area detector. X-rays are produced in an X-ray tube that consists of a source of electrons and two metallic electrodes. A voltage between these electrodes (typically tens of thousands of volts) accelerates electrons rapidly towards the anode. This bombardment of electrons on the anode with a sufficiently high energy produces X-rays, consisting of a superposition of continuous and characteristic spectra. The continuous spectrum is produced by the rapid deceleration of electrons striking the anode; collisions with nuclei produce deflections of the beam electrons radiating X-ray photons (Bremsstrahlung radiation) which are not of our interest. On the other hand, if an electron bombarding the anode has enough energy, it can knock an electron out of the K -shell (usually done with Cu target, but holds true for other materials), leaving the anode atom in an excited state. One of the outer electrons (in the L, M, N, \dots shells) falls into the vacancy in the K -shell, emitting a photon and producing one of the characteristic lines ($K_\alpha, K_\beta, K_\gamma, \dots$), depending on where the electron come from. Note that the K_α -line is the strongest among others. Due to the spin-orbit coupling, the energy levels of the shells (except K -shell) split into fine structure of the spectral lines. In particular, the L -shell split into three sublevels. Out of these three levels, the transition is possible between only two sublevels of L -shell onto K -level due to the selection rules. This gives rise to doublet of K_{α_1} and K_{α_2} , with slightly different energies. The intensity of ratios of $K_{\alpha_1} : K_{\alpha_2} = 10:5$, showing that only the core shell electrons are necessary for consideration.^{124,125,126,127,128} The Cu- K_{α_1} -line with wave length 0.1541 nm is used for our X-ray measurements here.

Now, the produced X-ray photons collide with electrons in atoms and scatter away with same/different wavelengths. If the wavelength of these scattered X-rays does not change, the process is called elastic scattering or Thompson scattering. These are the X-rays that are measured in diffraction experiments, as the scattered X-rays that carry information about the electron distribution in materials. On the other hand, when X-ray photons collide with loosely bound electrons in the atoms, some of the energy of X-ray photon is used in providing kinetic energy for the free electron. Therefore, the scattered X-ray photon has different energies/wavelengths than incident X-ray photon gives rise to inelastic or Compton scattering. Note that in case of Compton scattering, the phase of the scattered X-ray has no fixed relation to the incident beam. Therefore, inelastic scattering is indeed incoherent scattering which will go as undesired background in the diffraction pattern.^{124,125,126,127,128}

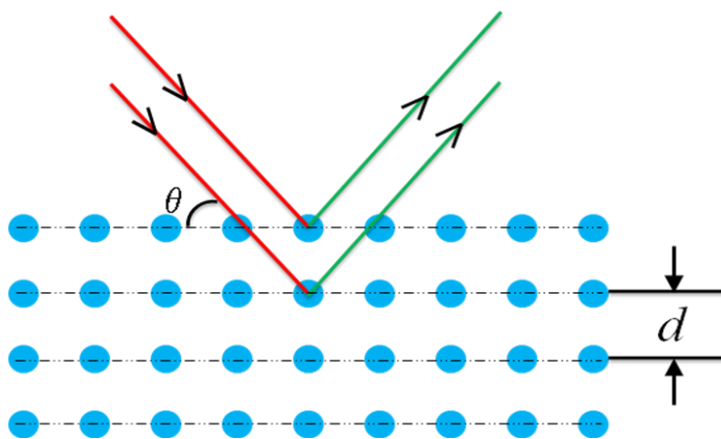


Figure 2.4. Graphical representation of the diffraction by parallel planes of atoms (separated by a distance d) in a crystal. The incident X-ray makes an angle θ with lattice plans. If the path difference between successive planes ($2d \sin\theta$) is equal to integral value of wavelength ($n\lambda$) of the X-ray then constructive interference will be obtained.

Diffracted waves from different atoms interfere with each other and the resulting intensity is strongly modulated. If the atoms are arranged in a periodic fashion, as in crystals, the diffracted waves will consist of sharp interference maxima with the same symmetry as in the distribution of atoms. Measuring the diffraction pattern, therefore, allows us to deduce the distribution of atoms in a material. However, the phase information gets lost because only intensities from scattered X-ray photons are measured in XRD but not the electric fields.

Let us consider a crystalline solid where all atoms are arranged in a periodic pattern. The atoms, represented by blue spheres in the figure 2.4, can be viewed as forming different sets of planes in the crystal. When a beam of monochromatic X-rays fall onto this periodic structure, the incident X-rays will be scattered by the atoms in all directions. But for some of the incident directions the scattered X-ray beams will be specularly reflected by any one plane of atoms and the reflected rays from successive adjacent planes will interfere constructively. For those two X-ray beams to constructively interfere, the path difference between them must be an integral number of the wavelength. Therefore, for a given set of lattice planes with an inter-plane distance of d_{hkl} , the condition for a diffraction to occur can be simply written as

$$n\lambda = 2d_{hkl} \sin \theta \quad (2-1)$$

The Eq. (2-1) is also known as the Bragg's law, after W.L. Bragg and his father, W.H. Bragg proposed it. Here λ is the wavelength of the X-ray, θ is the scattering angle, and n is an integer representing the order of the diffraction peak.

The most useful method for describing diffraction phenomena in a crystal is done with the help of “reciprocal lattice”. The fact that the diffracting Bragg patterns are inherently three dimensional, one can remove a dimension from the problem by representing each plane as a vector which is defined as perpendicular distance from the origin of a unit cell to the first plane in the family (hkl), *i.e.*, $\vec{G}_{hkl} = \frac{2\pi}{d_{hkl}} \hat{n}$, where \hat{n} is the unit vector normal to the plane. Now the reciprocal lattice vectors can be constructed from the primitive vectors as shown elsewhere.^{124,127} The primitive vectors in reciprocal lattice are

$$\vec{b}_1 = 2\pi \frac{\vec{a}_2 \times \vec{a}_3}{\vec{a}_1 \cdot (\vec{a}_2 \times \vec{a}_3)}, \quad b_2 = 2\pi \frac{\vec{a}_3 \times \vec{a}_1}{\vec{a}_1 \cdot (\vec{a}_2 \times \vec{a}_3)}, \quad b_3 = 2\pi \frac{\vec{a}_1 \times \vec{a}_2}{\vec{a}_1 \cdot (\vec{a}_2 \times \vec{a}_3)}.$$

here $\vec{a}_1, \vec{a}_2, \vec{a}_3$ are the primitive vectors of the crystal lattice. $\vec{b}_1, \vec{b}_2, \vec{b}_3$ are the primitive vectors in corresponding reciprocal lattice which are related by $\vec{G}_{hkl} = v_1 \vec{b}_1 + v_2 \vec{b}_2 + v_3 \vec{b}_3$, where \vec{G}_{hkl} is the reciprocal lattice vector and v_1, v_2, v_3 are the integers. The corresponding Bragg’s condition for the reciprocal lattice is given by:

$$\vec{K} - \vec{K}_0 = 2\pi \vec{G}_{hkl} \quad (2-2)$$

Where \vec{K}_0 and \vec{K} are the unit wave vectors of incident and diffracted X-ray beams.

It is important to point out that although we have used atoms as scattering points in this example, Bragg's Law applies to scattering centers consisting of any periodic distribution of electron density. In other words, the law holds true if the atoms are

replaced by molecules or collections of molecules, such as colloids, polymers, proteins and virus particles all of which are made out of atoms of course.

2.2.2. SMALL ANGLE X-RAY REFLECTIVITY

X-rays are one among the best probe sensor to realize the electron density at the surface and thereby obtain information about the surface roughness, thin film thickness and density of the material.^{124,125,126,127,128} The technique involves measuring the reflected X-ray intensity as a function of incidence angle over a range of angles close to the critical angle for total reflection. Above this critical angle the specularly reflected intensity (i.e. with symmetric incident and reflected angles) decreases, with a form that is dependent on the roughness of the interface. This can then be analyzed to obtain the electron density profile of the interface normal to the surface. A typical reflectivity profile is shown figure 2.5.

In general, the X-ray reflectivity is limited to small angles of incidence where it is possible to consider the electron density as a continuum. In this approximation, the reflection can be treated as a classical problem of reflection of an electromagnetic wave at an interface. The reflection coefficient in amplitude is obtained by writing the continuity of the electric field and of the magnetic field. The reflectivity which is the modulus square of this coefficient can be formulated in the case of X-rays as^{29,129}

$$R(\theta) = rr^* = \left| \frac{\theta - \sqrt{\theta^2 - \theta_c^2 - 2i\beta}}{\theta + \sqrt{\theta^2 - \theta_c^2 - 2i\beta}} \right|^2 \quad (2-3)$$

where β is the absorption coefficient and θ_C is the critical angle. These details are found elsewhere.^{29,129} In the case infinitely thick sample with a perfectly flat interface, one sees the expected Fresnel reflectivity.

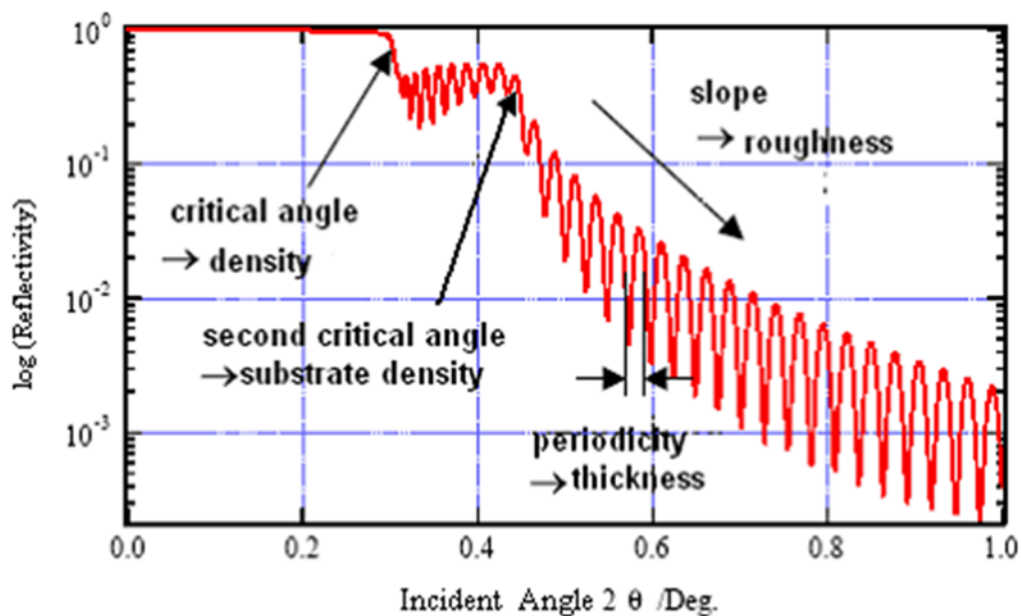


Figure 2.5. A typical XRR profile with indications of the critical angle, the second critical angle, slope and periodicity of fringes, which correspond to the density of thin film and density of the substrate, surface roughness, and thickness, respectively.¹³⁰

In the case of thin films, low angle X-ray diffraction gives insight into the thickness for single film, repeated bilayers and even more complicated thin-film structures like superlattices. A change in material density (at an interface between two materials) leads to a change in the index of refraction, which will lead to reflection and transmission of the X-rays from the top surface of the thin film. The transmitted X-ray once again reflects from the bottom of the surface thin film and interferes with initially

reflected X-ray from the top surface. The path difference between these X-rays satisfies the Bragg condition given by

$$n\lambda = 2t \sin \theta \quad (2-4)$$

where t is the distance between the two interfaces (thickness of a given thin film) and θ is angle of incident.

Typically, XRR involves a complicated fitting function that has been used to fit experimental data. A software package called Leptos, which incorporates X-ray scattering models and numerical methods into the package involving these complex functions. This software allows for the analysis of extremely complicated heterostructure materials, and can factor in density changes, interface roughness and instrument resolution that are difficult to analyze directly. Assuming a grazing incidence angle, the average scattering (the atoms are no longer considered discrete at small angles but a continuous electron density) is measured and gives an index of refraction based on the electron density. Finally, in repeated bilayer structures, it is also possible to determine bilayer thickness based on a superlattice peak. For a particular angle 2θ , the contributions from the interference pattern in reflectivity for a repeated bilayer add up to give a peak. The intensity of this peak increases with an increasing number of bilayers. This superlattice peak satisfies the Bragg condition for the bilayer thickness which is given by

$$t = \frac{n\lambda}{2\sin\theta}, \quad (2-5)$$

where n implies that there are multiple order superlattice peaks (the order of peaks gives insight into interface roughness between bilayers). Using an off-specular technique, where θ and 2θ have an offset (usually between 0.1 to 1 degrees), one can remove the thickness oscillations and left with only the Fresnel reflectivity curve accompanied by the superlattice peaks. This approach is an extremely accurate method for determining film thicknesses.

2.2.3. ALTERNATING GRADIENT FORCE MAGNETOMETER

The Alternating Gradient Force Magnetometer (AGFM)¹³¹ is an integral method that measures the bulk magnetic moment in a thin magnetic film. In the AGFM, a sample of typically 1 to 3 mm square is mounted on a vertical extension rod, which is along z -axis as shown figure 2.6. The top end of this rod is attached to the piezoelectric element which is rigidly clamped. This piezoelectric transducer oscillates when the sample is subjected to an alternating magnetic field gradient superimposed on the DC field of an electromagnet, which is along x -axis. The force due to negative gradient of the Zeeman potential energy on a magnetized sample produces a bending moment on the piezoelectric element, which generates a voltage proportional to the force on the sample. The output from the piezoelectric element is sensitively detected at the frequency of the gradient field.

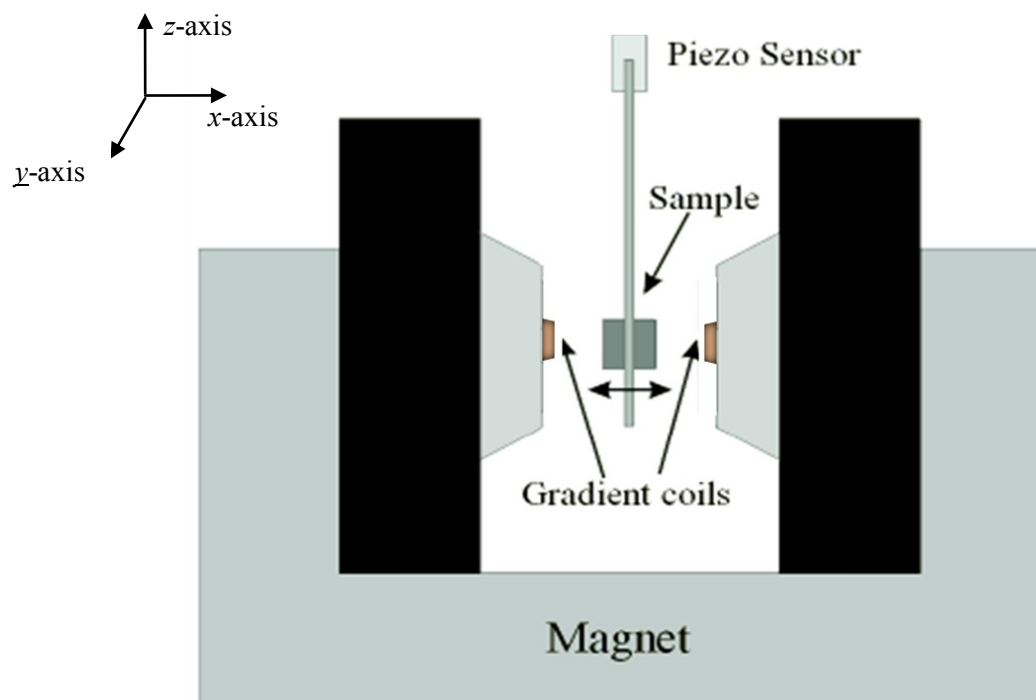


Figure 2.6. Schematic of the Alternating Gradient Force Magnetometer

This technique is considered as force technique, which measures the force on a magnetized sample in the presence of a magnetic field gradient. The piezoelectric sample holder of the AGFM, which is fragile and expensive, operates at its resonance frequency, which depends on the mass of the sample/substrate combination. Therefore, each new sample requires tuning to its resonance frequency. If the magnetic moment is very low, automatic tuning does not work out and the user has to do it manually. Even with careful manual tuning of a low moment sample, the saturation moment was found to vary by more than 5% over 10 consecutive measurements. It is necessary to make sure that the measured sample is always calibrated, placed in the same location and is of the same size compared to the calibrated sample to avoid strong deviations from the actual magnetic

moment. When measuring samples with smaller coercivity $\sim 10\text{mT}$, it is important to reduce the magnitude of gradient field in order to improve the signal-to-noise ratio.

All of our room temperature measurements were made using a Princeton Magnetics MicroMag Model 2900 AGFM. The AGFM is sensitive to about 10^{-10} A.m^2 and can be applied a maximum external magnetic field of 1.35 T. This system can measure thin film samples in two modes: The applied magnetic field perpendicular and parallel to the film.

2.2.4. MAGNETO-OPTICAL KERR EFFECT

When a linearly polarized monochromatic light falls on a magnetized surface, then reflected and transmitted light become elliptically polarized and the polarization axis is tilted by an angle. These Magneto-Optical effects were first discovered by Michael Faraday (Faraday effect: An effect observed in transmission through a material) and J. C. Kerr (Kerr effect: An effect observed on reflection from a material). Often there is some confusion in referring to the Kerr effect in reflection from materials that are not optically opaque and where radiation may travel through the material and back again several times; eventually appearing on the side of reflection as a multiply reflected beam. In case of these materials, the properties that give rise to effects referring both Kerr and Faraday effects. In general, it is convenient to refer change in polarization of reflected light as Kerr effects and change in polarization of transmitted light as Faraday effects.

In general, the magneto-optic Kerr effect (MOKE) is categorized by three different set-ups as shown below in figure 2.7.

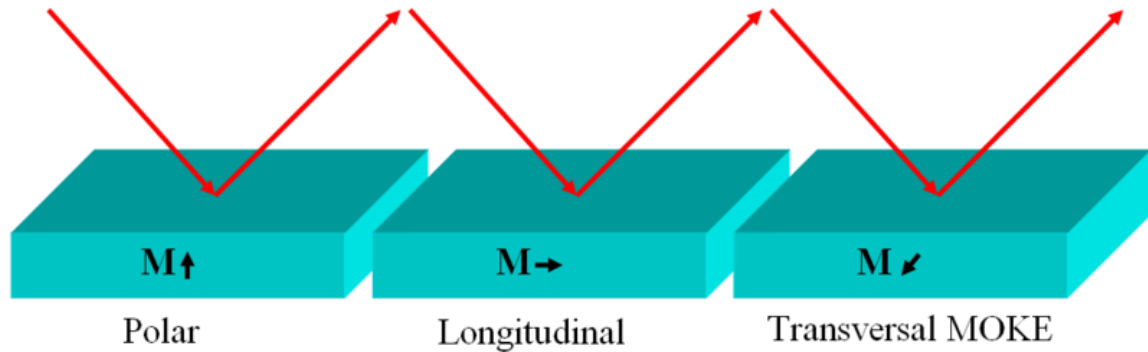


Figure 2.7. All three basic MOKE configurations: Polar, Longitudinal and Transverse MOKE set-ups. The red lines are incident and reflected light in pointed arrow direction. The black colored arrows are directions of applied magnetic field on the thin-film samples.¹³²

Following the path of the light beam from its starting place to the photo detector the setup involves a monochromatic light source which can be realized, *e.g.*, by a stable laser diode. The latter provides a monochromatic, nearly parallel light beam of roughly linearly polarized light. Further elements are a polarizer (P), the magnetic sample (S), a photo-elastic modulator (O), an analyzer (A) and the photo-detector (D). Since the Kerr rotation angle θ_K and ellipticity ε_K are typically small, *i.e.*, $\sim 10^{-3}$ rad, optimization of the signal-to-noise (S/N) ratio is very crucial. In order to achieve an optimum S/N ratio, appropriate placements and orientations of the optical components are crucial. By now, a great variety of MOKE methodologies, both experimentally and analytically, have been developed. However, a systematic investigation of the S/N ratio, both experimentally and theoretically, for all possible configurations of optical elements is still lacking.^{133,134,135,136,137,138,139,140,141}

Therefore, in this section, we analyze a large variety of commonly used arrangements of the optical elements where the position and relative orientations of different optical elements have been systematically changed. We use a modulation technique allowing the application of phase sensitive detection methodology by means of a lock-in amplifier. Although the modulation technique is in principle widely employed,^{142,143,144,145,146} there can be various arrangements of the optical components which yield similar but not identical results from the point of view of S/N optimization.

In particular, experiments studying the evolution of magnetic properties involving the magnetic history of subsequently cycled loops, *e.g.*, aging phenomena like the training of the exchange bias effect, cannot just average loops to increase the S/N. Therefore an S/N-optimized configuration is mandatory. By using Jones matrix formalisms we identify two optimized Kerr configurations and confirm their superior performance experimentally. We also emphasize the fact that when simultaneously measuring the first and second harmonics these appropriate optimized configurations discussed in detail below should be used. Our theoretical conclusions are experimentally confirmed by measuring hysteresis loops on a Co/CoO bilayer sample and calculating the corresponding S/N ratios for each configuration. Although we present those results involving only the case of longitudinal MOKE (due to in-plane easy axis of Co) which utilizes *s*-polarized light; the analyses can easily be extended to the cases of polar and transverse MOKE as well as for *p*-polarization state.

2.2.4.1. EXPERIMENTAL SET-UP

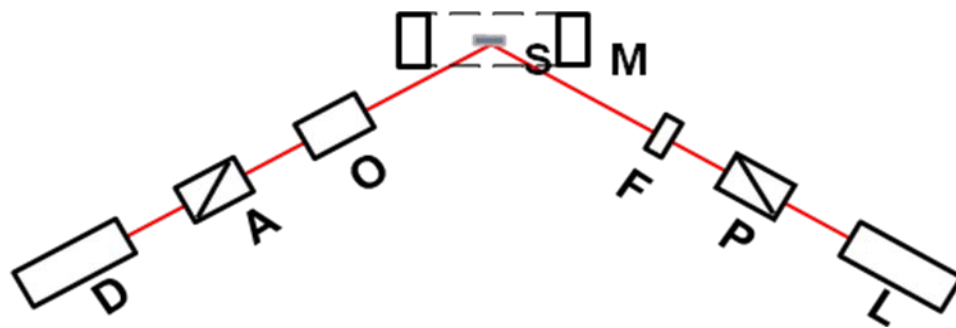
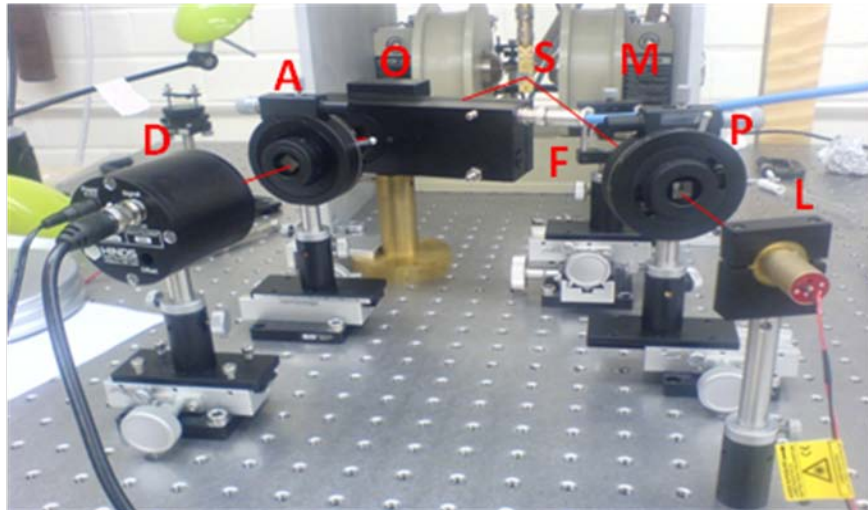


Figure 2.8. (Top) A photograph of the MOKE measurement setup in longitudinal geometry. *L*: laser, *P*: polarizer, *F*: focusing lens, *M*: magnet pole, *S*: sample, *O*: photo elastic modulator, *A*: analyzer, *D*: detector. *P*, *F*, *A*, and *D* are mounted on rotating stages *RS*. (Bottom) A schematic of the longitudinal MOKE.

Figure 2.8 shows a photograph of our MOKE measurement setup and its corresponding schematic drawing. It starts with a solid state laser diode of wavelength $\lambda=670$ nm and an output power of 5 mW. The latter produces a nearly linearly polarized beam allowing for *s*-polarized (electric field vector oscillating perpendicular to the plane of incidence in accordance with the German word *senkrecht* meaning perpendicular) or *p*-

polarized (electric field vector oscillating in the plane of incidence) configurations. Subsequently, we discuss *s*-polarized incoming light only. In our setup, due to geometrical constraints of the magnet given the laser beam makes only an angle of about 20° with the normal of the sample surface. This is significantly below the Brewster angle $\theta_{BR} \approx \arctan(n_2/n_1) = 63^\circ$ when using $\text{Re}(n_2) = 2$ for Co metal and $n_1 = 1$ for air. At the latter, the reflection of *p*-polarized light is minimized while the longitudinal Kerr rotation of *s*-polarized light increases linearly with increasing angle of incidence up to $\approx \theta_{BR}$.^{147,148} The laser beam then passes through a Glan-Thompson polarizer (Edmund Optics) with an extinction coefficient of 10^{-5} which produces high degree of polarization. A lens of focal length $f = 350$ mm and diameter of $D = 25$ mm is used to focus the light beam onto the sample surface. The reflected beam is periodically modulated between left and right circularly polarized light by the photo-elastic modulator (PEM-90, Hinds Instruments). Modulation takes place with a frequency of 50 kHz and phase amplitudes of $\varphi_0 = 108^\circ$

and $\varphi_0 = 175^\circ$ which maximize¹⁴⁹ the Bessel-function $J_1(\varphi) = \sum_{m=0}^{\infty} \frac{(-1)^m}{m!(m+1)!} \left(\frac{\varphi}{2}\right)^{2m+1}$ and

$J_2(\varphi) = \sum_{m=0}^{\infty} \frac{(-1)^m}{m!(m+2)!} \left(\frac{\varphi}{2}\right)^{2m+2}$ for first and second harmonic measurements,

respectively, as shown in Figure 2.9.

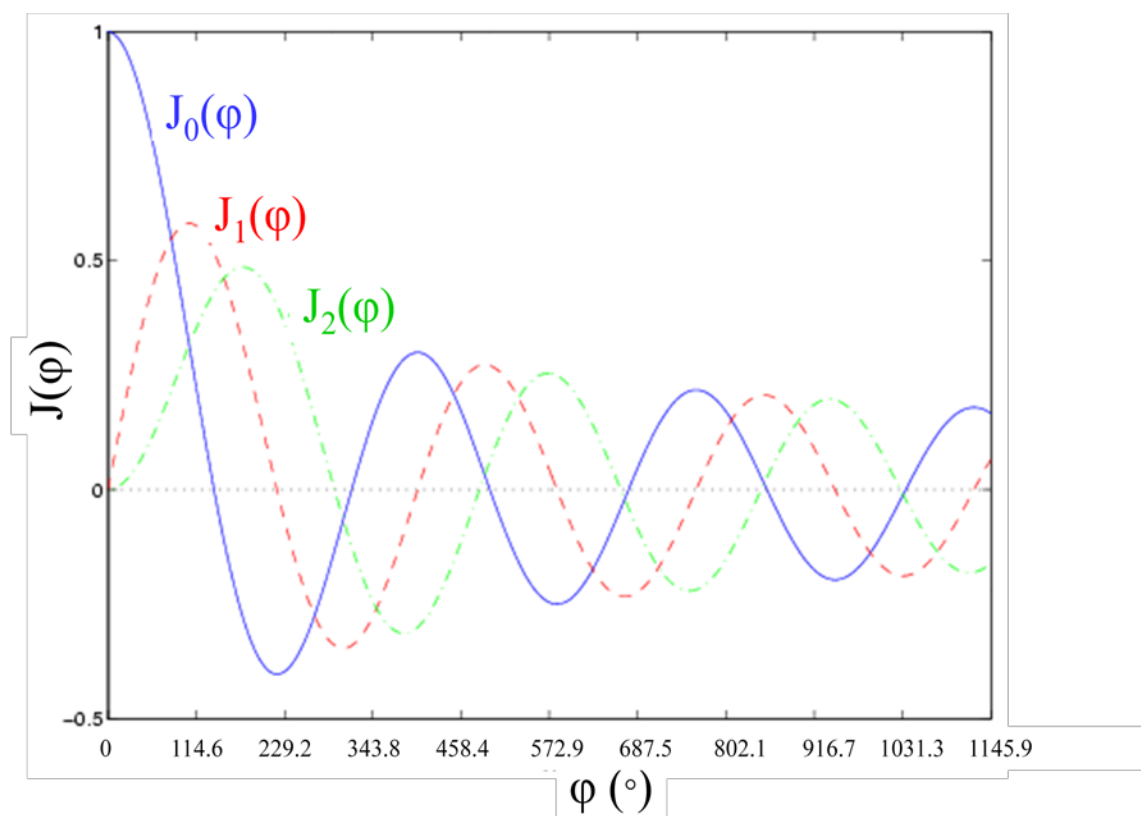


Figure 2.9. Zero (blue), first (red) and second (green) harmonics of Bessel function which maximize at 0, 108 and 175°, respectively.

The modulation signal is used as reference signal for a lock-in amplifier (Stanford Research Systems, SR830 DSP). The beam then transmits through an analyzer and is finally detected by a photo-sensitive fast responding diode (DET-100, Hinds Instruments) providing the input signal to the lock-in amplifier.

An electromagnet (GMW 3470) powered by a bipolar power supply (Kepco, BOP 36-12M) generates magnetic fields that is calibrated by a Hall sensor (model 5080, Sypris Instruments). The sample is mounted on a cryostat (Janis Research, CCS-350H) specimen holder, where the temperature can be varied between 10 K and 475 K. The

versatile designs of the electromagnet and cryostat allow studying a wide variety of magnetic properties in longitudinal, polar and transverse geometries. Moreover, Faraday effect and magneto-transport measurements can also be realized. The magnetic field control, intensity measurements and subsequent data collection were coordinated with self-written LabVIEW-7 (National Instruments) programs. The magnet power supply and the lock-in were controlled with the computer via a GPIB card.

2.2.4.2. JONES MATRIX FORMALISM

The MOKE describes the change of the polarization states of light when reflected at a magnetic material. Thereby linearly polarized light experiences a rotation of the polarization plane (Kerr rotation θ_K) and a phase difference between the electric field components perpendicular and parallel to the plane of the incident light (Kerr ellipticity ε_K). These two quantities are connected to form Kerr angle:

$$\phi_K = \theta_K + i\varepsilon_K \quad (2-6)$$

In a macroscopic description of MOKE the interaction of the magnetic sample with the electromagnetic field is represented by the dielectric tensor. The off-diagonal elements of the tensor are linearly dependent on the magnetization and describe the magneto-optic contributions, which occur through different absorption of left and right circular polarized light. The diagonal elements describe optical reflectivity. First and second harmonics of the reflected light intensity are related to the off-diagonal elements $r_{sp/ps}$ of the sample's dielectric tensor and determine θ_K and ε_K .

In the following, we describe the principle of MOKE with polarization modulation technique in terms of the Jones matrix method.¹⁵⁰ Each optical component in Figure 2.8 can be expressed by a Jones matrix. All angles are relative to the plane of incidence unless otherwise noted. The matrices of the polarizer (P) and analyzer (A) with major transmission axes oriented at angles β and α , respectively, with the plane of incidence are

$$\underline{P} = \begin{bmatrix} \cos^2 \beta & \sin \beta \cos \beta \\ \sin \beta \cos \beta & \sin^2 \beta \end{bmatrix} \quad (2-7)$$

$$\underline{A} = \begin{bmatrix} \cos^2 \alpha & \sin \alpha \cos \alpha \\ \sin \alpha \cos \alpha & \sin^2 \alpha \end{bmatrix} \quad (2-8)$$

The matrix describing the magnetic sample is expressed as

$$\underline{M}_S = \begin{bmatrix} \tilde{r}_p & \tilde{r}_{ps} \\ \tilde{r}_{sp} & \tilde{r}_s \end{bmatrix} \quad (2-9)$$

where the diagonal terms, $\tilde{r}_p = r_p e^{i\delta_p}$ and $\tilde{r}_s = r_s e^{i\delta_s}$, are independent of magnetization and are identified as usual Fresnel reflection coefficients. The off-diagonal cross terms account for the magneto-optic Kerr effect and are symmetric, i.e., $\tilde{r}_{ps} = -\tilde{r}_{sp} = r_{ps} e^{i\delta_{ps}} = -r_{sp} e^{-i\delta_{sp}}$ and δ_i are the corresponding phase angles. The photo-elastic modulator (O) with its axes oriented at 0 and 90° is represented by the matrix

$$\underline{M}_{PEM} = \begin{bmatrix} e^{i\frac{\varphi}{2}} & 0 \\ 0 & e^{-i\frac{\varphi}{2}} \end{bmatrix}, \quad (2-10)$$

here $\varphi = \varphi_0 \sin \omega t$ is the periodic retardation of the modulator. The subsequent analysis requires a Fourier decomposition of $\cos(\varphi(t))$ and $\sin(\varphi(t))$ which reads

$$\cos(\varphi) = J_0(\varphi_0) + 2 \sum_{m=1}^{\infty} J_{2m}(\varphi_0) \cos(2m\omega t) \quad \text{and} \quad \sin(\varphi) = 2 \sum_{m=0}^{\infty} J_{2m+1}(\varphi_0) \sin[(2m+1)\omega t].$$

Here $J_k(\varphi_0)$ are Bessel functions of argument φ_0 and order k .

The electric field amplitude of the reflected beam at the photo-detector can be represented by a vector equation,

$$\begin{bmatrix} E_p \\ E_s \end{bmatrix}^r = \underline{\underline{A}} \underline{\underline{O}} \underline{\underline{S}} \underline{\underline{P}} \begin{bmatrix} E_p \\ E_s \end{bmatrix}^i \quad (2-11)$$

where \underline{E}^i is the amplitude of incident light. E_p and E_s are the E -vector amplitudes in the direction parallel and perpendicular to the plane of incidence, while $\underline{\underline{A}}$, $\underline{\underline{O}}$, $\underline{\underline{S}}$, and $\underline{\underline{P}}$ are the matrices representing analyzer (A), photo elastic modulator (O), sample (S), and polarizer (P) respectively.

The signal intensity measured at the detector is given by

$$I \propto |E^r|^2. \quad (2-12)$$

The S/N ratio is obtained from the ratio of the average signal $|I_{avg}^{sat}|$ obtained in a field range where the magnetization of the reference sample is in its saturation state to the

$$\text{average noise } \Delta I^{sat} = \frac{1}{\Delta H I_{avg}^{sat}} \int_H^{H+\Delta H} (I^{sat}(H) - I_{avg}^{sat})^2 dH \text{ in a measured hysteresis loop,}$$

$$S / N = \frac{|I_{avg}^{sat}|}{|\Delta I^{sat}|}. \quad (2-13)$$

The primary noise that can be effectively reduced by the modulation technique originates from fluctuations in the polarization of the light caused by fluctuations in the Fresnel reflection coefficients. Note that time dependent misalignments of the light beam with respect to the optical axis are not included in the Jones matrix analysis. Hence, the modulation technique is not effective in noise reduction of mechanical origin. In addition, the efficiency of the modulation technique depends critically on the quality and stability of the modulator. If the latter fluctuates in phase or amplitude the modulation technique can actually add noise to the detected intensity instead of reducing it.

Now we consider various meaningful configurations of our MOKE setup. They are distinguished by the order of placements of the optical components and variation of the polarizer/analyzer orientations with respect to each other and with respect to the retardation axis of the modulator. The laser beam transmits through the optical components in the order given in each configuration. The latter is indicated at the beginning of each configuration subsequently analyzed in detail.

Configuration 1.1:

P transmission axis at 90°, *S*, *O* axes at 0 and 90°, *A* transmission axis at α

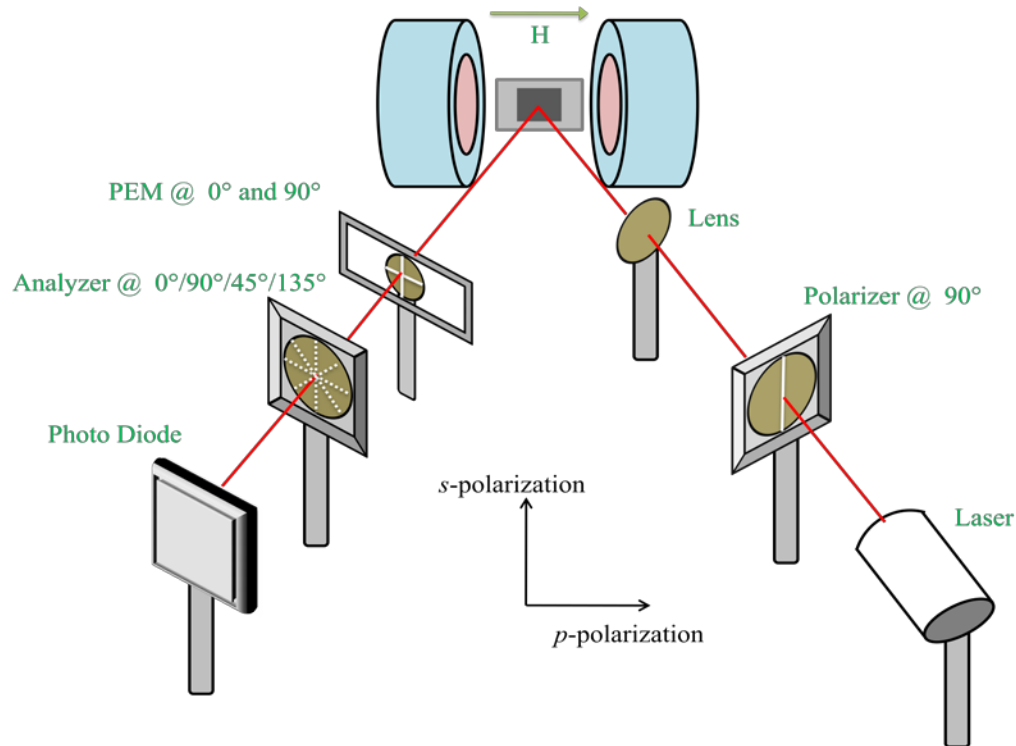


Figure 2.10. A sketch of placement and angles of different optical elements for configuration 1.1

The electric field vector of the reflected light for this configuration following Eq. (2-11) reads

$$\begin{bmatrix} E_p \\ E_s \end{bmatrix} = \begin{bmatrix} \cos^2 \alpha & \sin \alpha \cos \alpha \\ \sin \alpha \cos \alpha & \sin^2 \alpha \end{bmatrix} \begin{bmatrix} e^{i\frac{\varphi}{2}} & 0 \\ 0 & e^{-i\frac{\varphi}{2}} \end{bmatrix} \begin{bmatrix} \tilde{r}_p & \tilde{r}_{ps} \\ \tilde{r}_{sp} & \tilde{r}_s \end{bmatrix} \begin{bmatrix} 0 & 0 \\ 0 & 1 \end{bmatrix} \begin{bmatrix} 0 \\ 1 \end{bmatrix}$$

The intensity is calculated following Eq. (2-11) and given by

$$\begin{aligned} I &\propto r_s^2 \sin^2 \alpha + r_{ps}^2 \cos^2 \alpha + 2J_0(\varphi_0) r_s r_{ps} \cos(\delta_s - \delta_{ps}) \sin \alpha \cos \alpha \\ &+ 4J_1(\varphi_0) \sin \omega t r_s r_{ps} \sin(\delta_s - \delta_{ps}) \sin \alpha \cos \alpha \\ &+ 4J_2(\varphi_0) \cos 2\omega t r_s r_{ps} \cos(\delta_s - \delta_{ps}) \sin \alpha \cos \alpha \\ &+ \text{higher order terms} \end{aligned}$$

Now let's analyze the variation of intensity with different α as shown below.

Case 1, $\alpha = 0$

$$I \propto r_{ps}^2$$

Case 2, $\alpha = 90^\circ$

$$I \propto r_s^2$$

Case 3, $\alpha = 45^\circ$

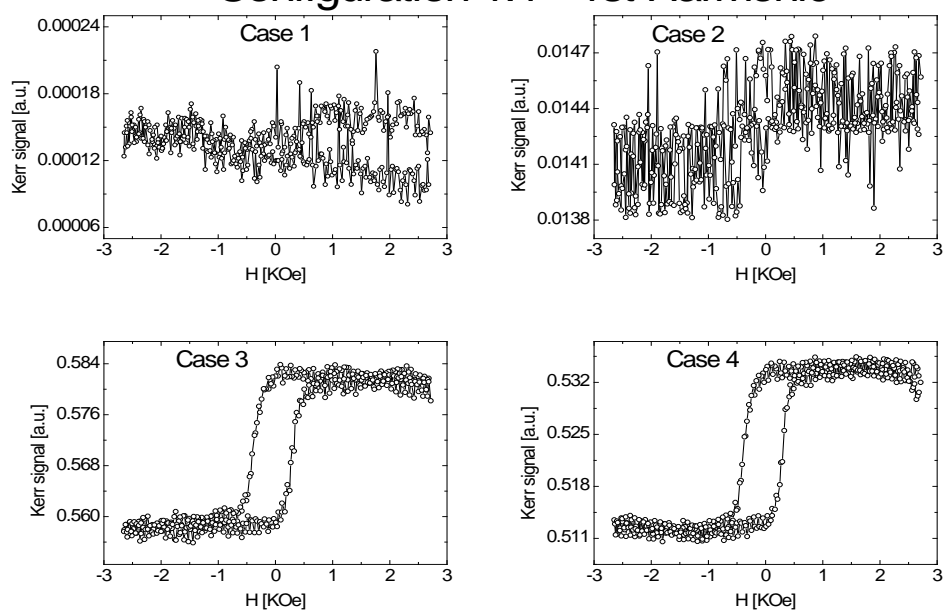
$$\begin{aligned} I \propto & \frac{1}{2}r_s^2 + \frac{1}{2}r_{ps}^2 + J_0(\varphi_0)r_s r_{ps} \cos(\delta_s - \delta_{ps}) \\ & + 2J_1(\varphi_0) \sin \omega t r_s r_{ps} \sin(\delta_s - \delta_{ps}) + 2J_2(\varphi_0) \cos 2\omega t r_s r_{ps} \cos(\delta_s - \delta_{ps}) \\ & + \text{higher order terms} \end{aligned}$$

Case 4, $\alpha = 135^\circ$

$$\begin{aligned} I \propto & \frac{1}{2}r_s^2 + \frac{1}{2}r_{ps}^2 - J_0(\varphi_0)r_s r_{ps} \cos(\delta_s - \delta_{ps}) \\ & - 2J_1(\varphi_0) \sin \omega t r_s r_{ps} \sin(\delta_s - \delta_{ps}) - 2J_2(\varphi_0) \cos 2\omega t r_s r_{ps} \cos(\delta_s - \delta_{ps}) \\ & + \text{higher order terms} \end{aligned}$$

The first and second harmonic Kerr loops measured for various cases in the experimental data is presented in Figure 2.11.

Configuration 1.1 - 1st Harmonic



Configuration 1.1 - 2nd Harmonic

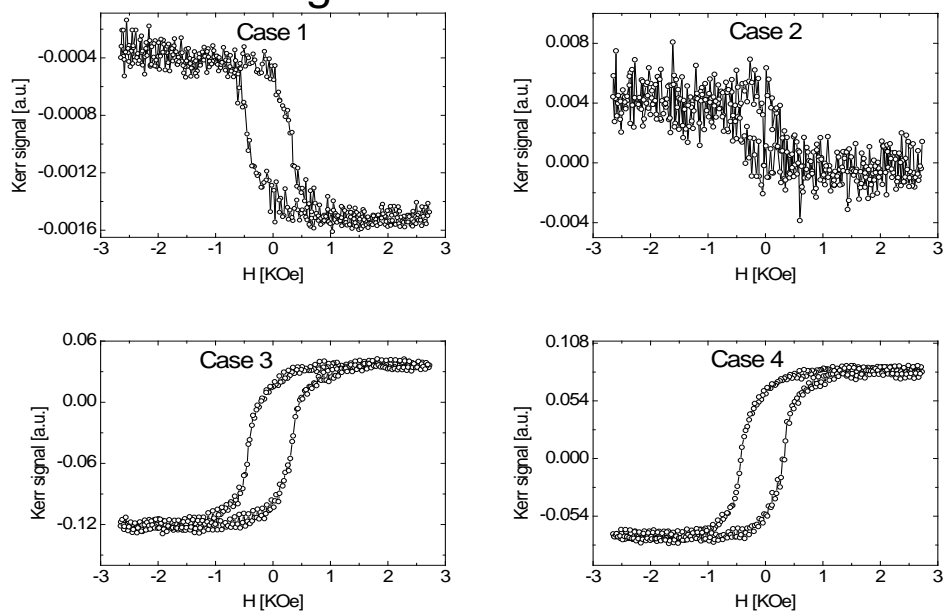


Figure 2.11. First and second harmonics MOKE hysteresis loops obtained in various cases using configuration 1.1.

The fact that no Kerr signal is expected for cases 1 and 2 is corroborated by experimental observation of the measured data; however, misalignment in the optical setup causes unexpected noise in the hysteresis loops for case 1 and 2 of second harmonic. On the other hand, terms containing first and second harmonics for cases 3 and 4 result in signals detected by the lock-in amplifier and, hence, Kerr hysteresis loops. With the help of Eq. (2 - 13), the S/N ratio amounts to 21.7 (first harmonic), 45.9 (second harmonic), and 24.2 (first harmonic), 51.0 (second harmonic) for cases 3 and 4, respectively. The subsequent analysis of various configurations reveals that configuration 1.1, cases 3 and 4, is one of the optimized setup for longitudinal Kerr measurements for the first as well as the second harmonics.

Configuration 1.2:

P axis at 90° , O axes at 0 and 90° , S, A axis at α

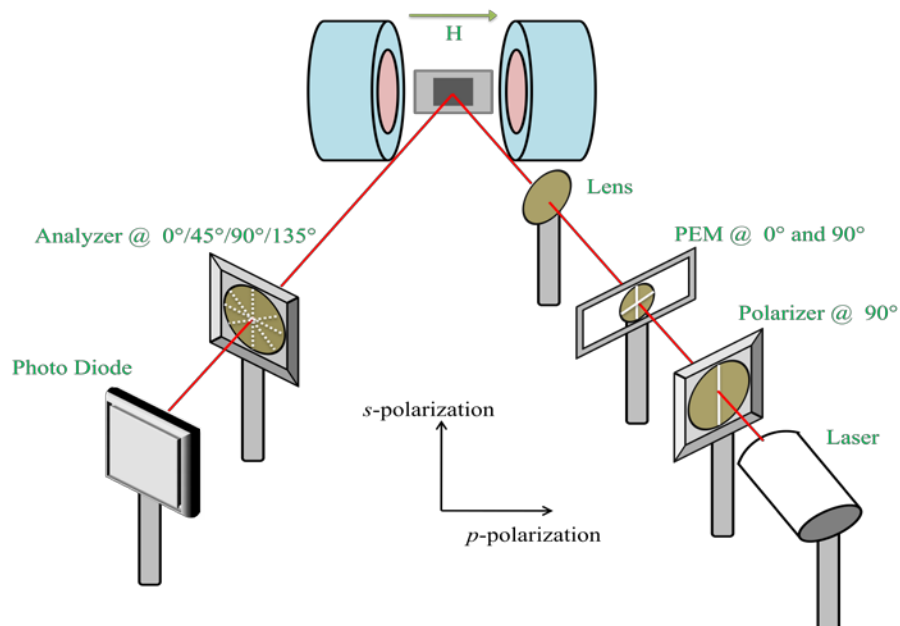


Figure 2.12. A sketch of placement and angles of different optical elements for configuration 1.2

In this case the intensity at the detector is given by

$$I \propto r_s^2 \sin^2 \alpha + r_{ps}^2 \cos^2 \alpha + 2r_s r_{ps} \cos(\delta_s - \delta_{ps}) \sin \alpha \cos \alpha$$

Analyze the variation of intensity with different α is shown below.

Case 1, $\alpha = 0$

$$I \propto r_{ps}^2$$

Case 2, $\alpha = 90^\circ$

$$I \propto r_s^2$$

Case 3, $\alpha = 45^\circ$

$$I \propto \frac{1}{2} r_s^2 + \frac{1}{2} r_{ps}^2 + r_s r_{ps} \cos(\delta_s - \delta_{ps})$$

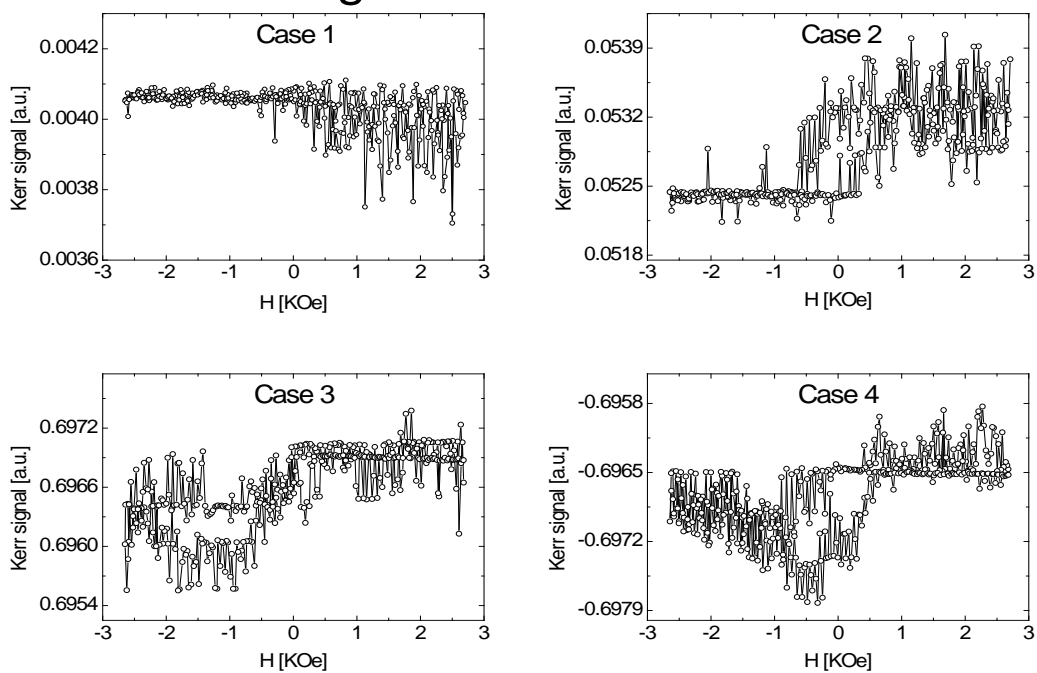
Case 4, $\alpha = 135^\circ$

$$I \propto \frac{1}{2} r_s^2 + \frac{1}{2} r_{ps}^2 - r_s r_{ps} \cos(\delta_s - \delta_{ps})$$

The loops measured in this configuration are displayed in figure 2.13 for completeness.

As predicted by the theory, no hysteresis loop was observed experimentally due to absence of any time dependence of the signal.

Configuration 1.2 - 1st Harmonic



Configuration 1.2 - 2nd Harmonic

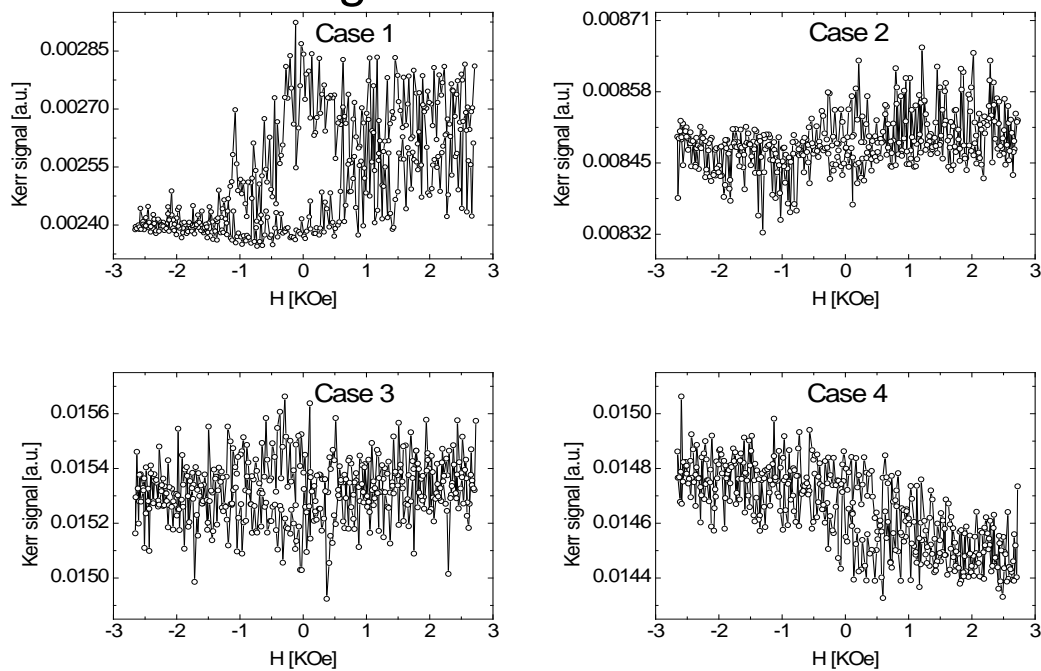


Figure 2.13. First and second harmonics MOKE hysteresis loops obtained in various cases using configuration 1.2.

Configuration 2.1:

P axis at 45° , S , O axes at 0 and 90° , A axis at α

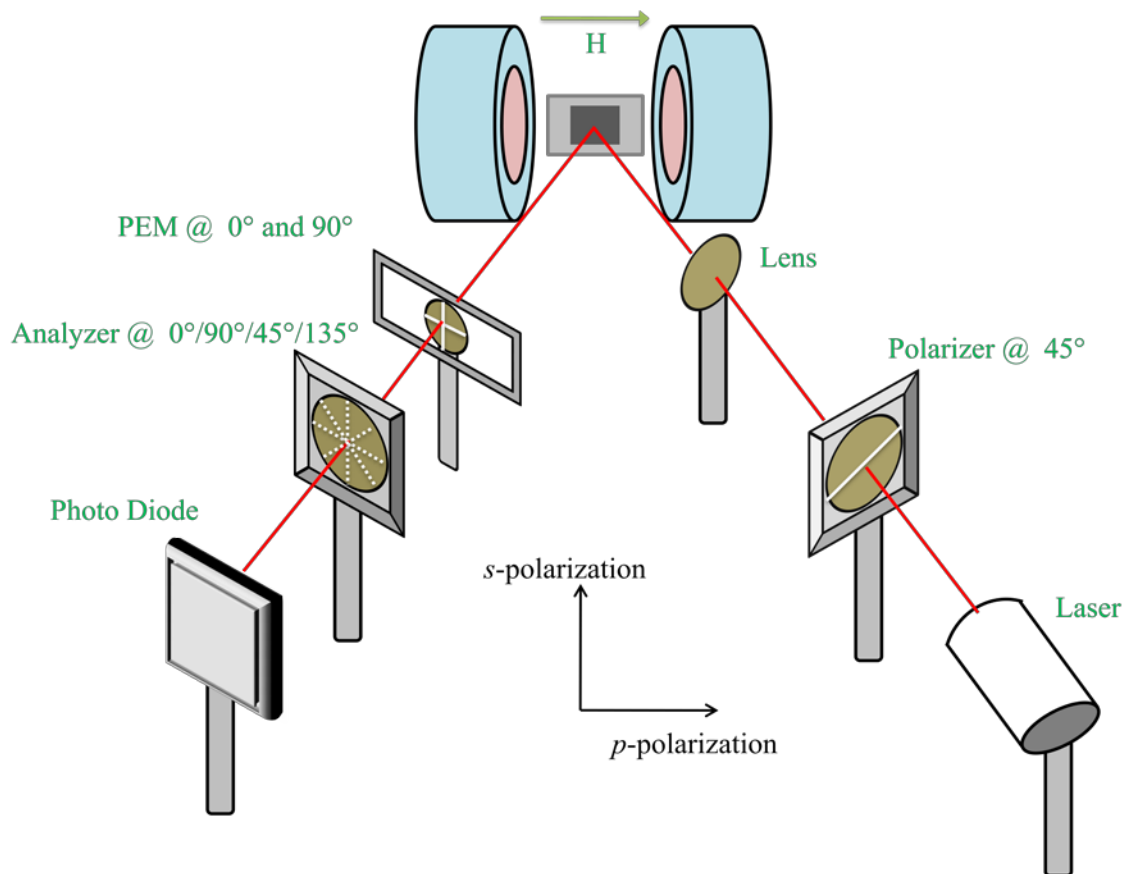


Figure 2.14. A sketch of placement and angles of different optical elements for configuration 2.1

The calculated intensity for this configuration is

$$\begin{aligned}
I \propto & \frac{1}{4}r_p^2 \cos^2 \alpha + \frac{1}{4}r_s^2 \sin^2 \alpha + \frac{1}{4}r_{ps}^2 + \frac{1}{2}r_p r_{ps} \cos(\delta_p - \delta_{ps}) \cos^2 \alpha \\
& - \frac{1}{2}r_s r_{ps} \cos(\delta_s - \delta_{ps}) \sin^2 \alpha \\
& + \frac{1}{2}J_0(\varphi_0)[r_p r_s \cos(\delta_p - \delta_s) \sin \alpha \cos \alpha - r_p r_{ps} \cos(\delta_p - \delta_{ps}) \sin \alpha \cos \alpha + \\
& r_s r_{ps} \cos(\delta_s - \delta_{ps}) \sin \alpha \cos \alpha - r_{ps}^2 \sin \alpha \cos \alpha] \\
& - J_1(\varphi_0) \sin \omega t [r_p r_s \sin(\delta_p - \delta_s) \sin \alpha \cos \alpha - r_p r_{ps} \sin(\delta_p - \delta_{ps}) \sin \alpha \cos \alpha - \\
& r_s r_{ps} \sin(\delta_s - \delta_{ps}) \sin \alpha \cos \alpha] \\
& + J_2(\varphi_0) \cos 2\omega t [r_p r_s \cos(\delta_p - \delta_s) \sin \alpha \cos \alpha - r_p r_{ps} \cos(\delta_p - \delta_{ps}) \sin \alpha \cos \alpha + \\
& r_s r_{ps} \cos(\delta_s - \delta_{ps}) \sin \alpha \cos \alpha - r_{ps}^2 \sin \alpha \cos \alpha] \\
& + \text{higher order terms}
\end{aligned}$$

Case 1, $\alpha = 0$

$$I \propto \frac{1}{4}r_p^2 + \frac{1}{4}r_{ps}^2 + \frac{1}{2}r_p r_{ps} \cos(\delta_p - \delta_{ps})$$

Case 2, $\alpha = 90^\circ$

$$I \propto \frac{1}{4}r_s^2 + \frac{1}{4}r_{ps}^2 - \frac{1}{2}r_s r_{ps} \cos(\delta_s - \delta_{ps})$$

Case 3, $\alpha = 45^\circ$

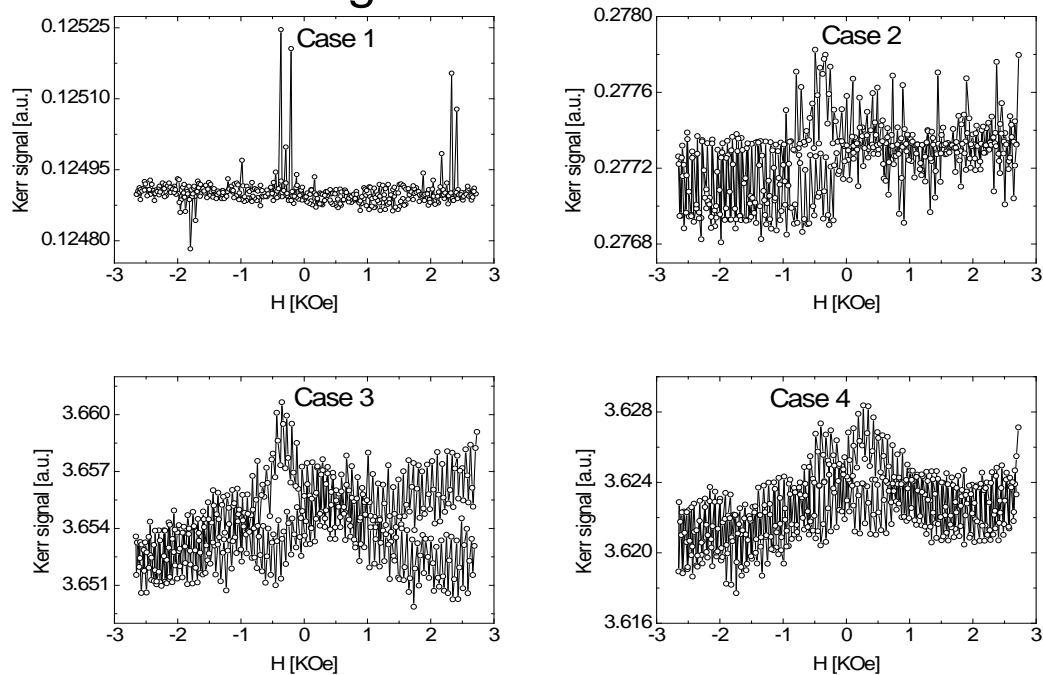
$$\begin{aligned}
I \propto & \frac{1}{8}r_p^2 + \frac{1}{8}r_s^2 + \frac{1}{4}r_{ps}^2 + \frac{1}{4}r_p r_{ps} \cos(\delta_p - \delta_{ps}) - \frac{1}{4}r_s r_{ps} \cos(\delta_s - \delta_{ps}) \\
& + \frac{1}{4}J_0(\varphi_0)[r_p r_s \cos(\delta_p - \delta_s) - r_p r_{ps} \cos(\delta_p - \delta_{ps}) + r_s r_{ps} \cos(\delta_s - \delta_{ps}) - r_{ps}^2] \\
& - \frac{1}{2}J_1(\varphi_0) \sin \omega t [r_p r_s \sin(\delta_p - \delta_s) - r_p r_{ps} \sin(\delta_p - \delta_{ps}) - r_s r_{ps} \sin(\delta_s - \delta_{ps})] \\
& + \frac{1}{2}J_2(\varphi_0) \cos 2\omega t [r_p r_s \cos(\delta_p - \delta_s) - r_p r_{ps} \cos(\delta_p - \delta_{ps}) + r_s r_{ps} \cos(\delta_s - \delta_{ps}) - r_{ps}^2] \\
& + \text{higher order terms}
\end{aligned}$$

Case 4, $\alpha = 135^\circ$

$$\begin{aligned}
 I &\propto \frac{1}{8}r_p^2 + \frac{1}{8}r_s^2 + \frac{1}{4}r_{ps}^2 + \frac{1}{4}r_p r_{ps} \cos(\delta_p - \delta_{ps}) - \frac{1}{4}r_s r_{ps} \cos(\delta_s - \delta_{ps}) \\
 &- \frac{1}{4}J_0(\varphi_0)[r_p r_s \cos(\delta_p - \delta_s) - r_p r_{ps} \cos(\delta_p - \delta_{ps}) + r_s r_{ps} \cos(\delta_s - \delta_{ps}) - r_{ps}^2] \\
 &+ \frac{1}{2}J_1(\varphi_0)\sin\omega t [r_p r_s \sin(\delta_p - \delta_s) - r_p r_{ps} \sin(\delta_p - \delta_{ps}) - r_s r_{ps} \sin(\delta_s - \delta_{ps})] \\
 &- \frac{1}{2}J_2(\varphi_0)\cos 2\omega t [r_p r_s \cos(\delta_p - \delta_s) - r_p r_{ps} \cos(\delta_p - \delta_{ps}) + r_s r_{ps} \cos(\delta_s - \delta_{ps}) - r_{ps}^2] \\
 &+ \text{higher order terms}
 \end{aligned}$$

The experimental details are presented Figure 2.15.

Configuration 2.1 - 1st Harmonic



Configuration 2.1 - 2nd Harmonic

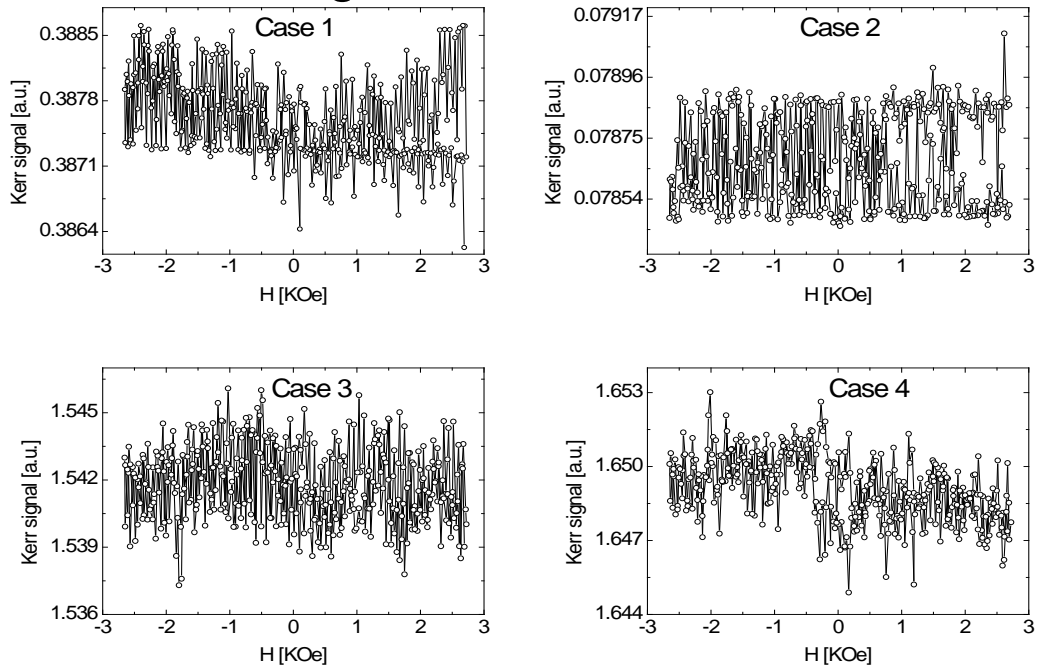


Figure 2.15. First and second harmonics MOKE hysteresis loops obtained in various cases using configuration 2.1.

The loops recorded in this configuration do not display any clear hysteresis. The low quality of the loops originates from the fact the diagonal elements r_p and r_s dominate both harmonics such that the magnetic information in the off-diagonal elements is masked.

Configuration 2.2:

P axis at 45° , O axes at 0 and 90° , S , A axis at α

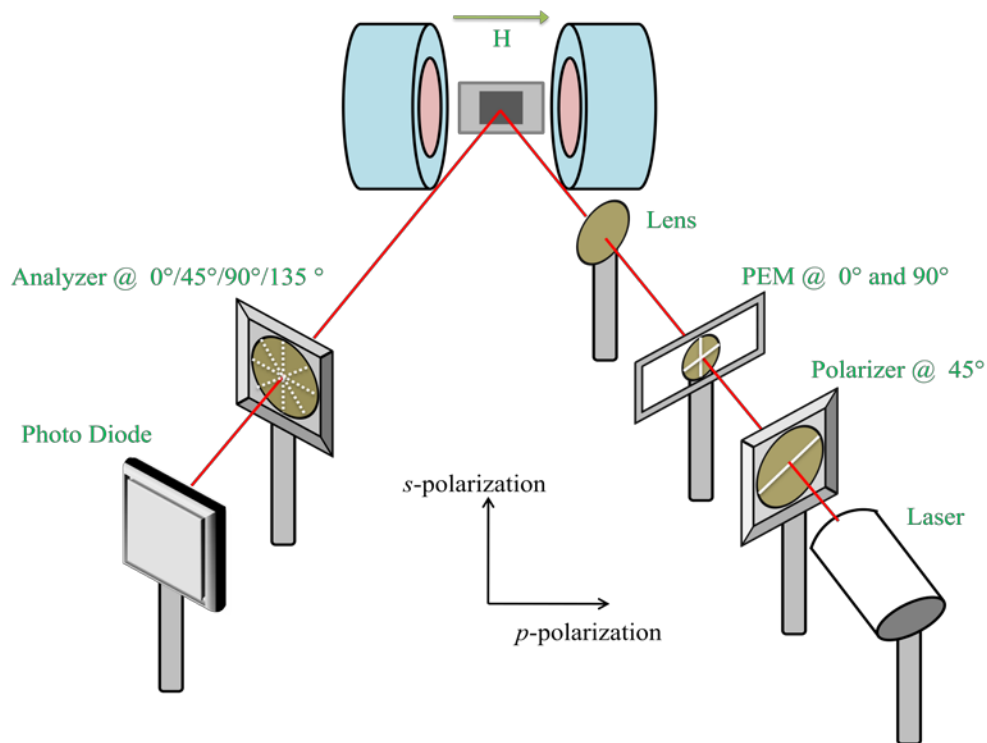


Figure 2.16. A sketch of placement and angles of different optical elements for configuration 2.2

The calculated intensity is given by

$$\begin{aligned}
 I \propto & \frac{1}{4}r_p^2 \cos^2 \alpha + \frac{1}{4}r_s^2 \sin^2 \alpha + \frac{1}{4}r_{ps}^2 - \frac{1}{2}r_p r_{ps} \cos(\delta_p - \delta_{ps}) \sin \alpha \cos \alpha \\
 & + \frac{1}{2}r_s r_{ps} \cos(\delta_s - \delta_{ps}) \sin \alpha \cos \alpha + \frac{1}{2}J_0(\varphi_0)[r_p r_s \cos(\delta_p - \delta_s) \sin \alpha \cos \alpha + \\
 & r_p r_{ps} \cos(\delta_p - \delta_{ps}) \cos^2 \alpha - r_s r_{ps} \cos(\delta_s - \delta_{ps}) \sin^2 \alpha - r_{ps}^2 \sin \alpha \cos \alpha] \\
 & - J_1(\varphi_0) \sin \omega t [r_p r_s \sin(\delta_p - \delta_s) \sin \alpha \cos \alpha + r_p r_{ps} \sin(\delta_p - \delta_{ps}) \cos^2 \alpha + \\
 & r_s r_{ps} \sin(\delta_s - \delta_{ps}) \sin^2 \alpha] + J_2(\varphi_0) \cos 2\omega t [r_p r_s \cos(\delta_p - \delta_s) \sin \alpha \cos \alpha + \\
 & r_p r_{ps} \cos(\delta_p - \delta_{ps}) \cos^2 \alpha - r_s r_{ps} \cos(\delta_s - \delta_{ps}) \sin^2 \alpha - r_{ps}^2 \sin \alpha \cos \alpha] \\
 & + \text{higher order terms}
 \end{aligned}$$

Case 1, $\alpha = 0$

$$I \propto \frac{1}{4}r_p^2 + \frac{1}{4}r_{ps}^2 + \frac{1}{2}J_0(\varphi_0)r_p r_{ps} \cos(\delta_p - \delta_{ps}) - J_1(\varphi_0)\sin \omega t r_p r_{ps} \sin(\delta_p - \delta_{ps}) \\ + J_2(\varphi_0)\cos 2\omega t r_p r_{ps} \cos(\delta_p - \delta_{ps}) + \text{higher order terms}$$

Case 2, $\alpha = 90^\circ$

$$I \propto \frac{1}{4}r_s^2 + \frac{1}{4}r_{ps}^2 - \frac{1}{2}J_0(\varphi_0)r_s r_{ps} \cos(\delta_s - \delta_{ps}) - J_1(\varphi_0)\sin \omega t r_s r_{ps} \sin(\delta_s - \delta_{ps}) \\ - J_2(\varphi_0)\cos 2\omega t r_s r_{ps} \cos(\delta_s - \delta_{ps}) + \text{higher order terms}$$

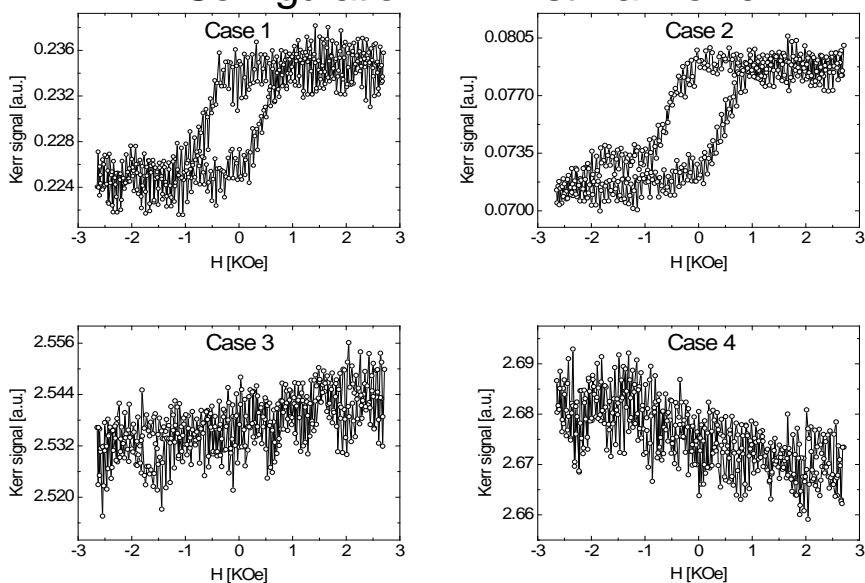
Case 3, $\alpha = 45^\circ$

$$I \propto \frac{1}{8}r_p^2 + \frac{1}{8}r_s^2 + \frac{1}{4}r_{ps}^2 - \frac{1}{4}r_p r_{ps} \cos(\delta_p - \delta_{ps}) + \frac{1}{4}r_s r_{ps} \cos(\delta_s - \delta_{ps}) \\ + \frac{1}{4}J_0(\varphi_0)[r_p r_s \cos(\delta_p - \delta_s) + r_p r_{ps} \cos(\delta_p - \delta_{ps}) - r_s r_{ps} \cos(\delta_s - \delta_{ps}) - r_{ps}^2] \\ - \frac{1}{2}J_1(\varphi_0)\sin \omega t [r_p r_s \sin(\delta_p - \delta_s) + r_p r_{ps} \sin(\delta_p - \delta_{ps}) + r_s r_{ps} \sin(\delta_s - \delta_{ps})] \\ + \frac{1}{2}J_2(\varphi_0)\cos 2\omega t [r_p r_s \cos(\delta_p - \delta_s) + r_p r_{ps} \cos(\delta_p - \delta_{ps}) - r_s r_{ps} \cos(\delta_s - \delta_{ps}) - r_{ps}^2] \\ + \text{higher order terms}$$

Case 4, $\alpha = 135^\circ$

$$I \propto \frac{1}{8}r_p^2 + \frac{1}{8}r_s^2 + \frac{1}{4}r_{ps}^2 + \frac{1}{4}r_p r_{ps} \cos(\delta_p - \delta_{ps}) - \frac{1}{4}r_s r_{ps} \cos(\delta_s - \delta_{ps}) \\ - \frac{1}{4}J_0(\varphi_0)[r_p r_s \cos(\delta_p - \delta_s) - r_p r_{ps} \cos(\delta_p - \delta_{ps}) + r_s r_{ps} \cos(\delta_s - \delta_{ps}) - r_{ps}^2] \\ + \frac{1}{2}J_1(\varphi_0)\sin \omega t [r_p r_s \sin(\delta_p - \delta_s) - r_p r_{ps} \sin(\delta_p - \delta_{ps}) - r_s r_{ps} \sin(\delta_s - \delta_{ps})] \\ - \frac{1}{2}J_2(\varphi_0)\cos 2\omega t [r_p r_s \cos(\delta_p - \delta_s) - r_p r_{ps} \cos(\delta_p - \delta_{ps}) + r_s r_{ps} \cos(\delta_s - \delta_{ps}) - r_{ps}^2] \\ + \text{higher order terms}$$

Configuration 2.2 - 1st Harmonic



Configuration 2.2 - 2nd Harmonic

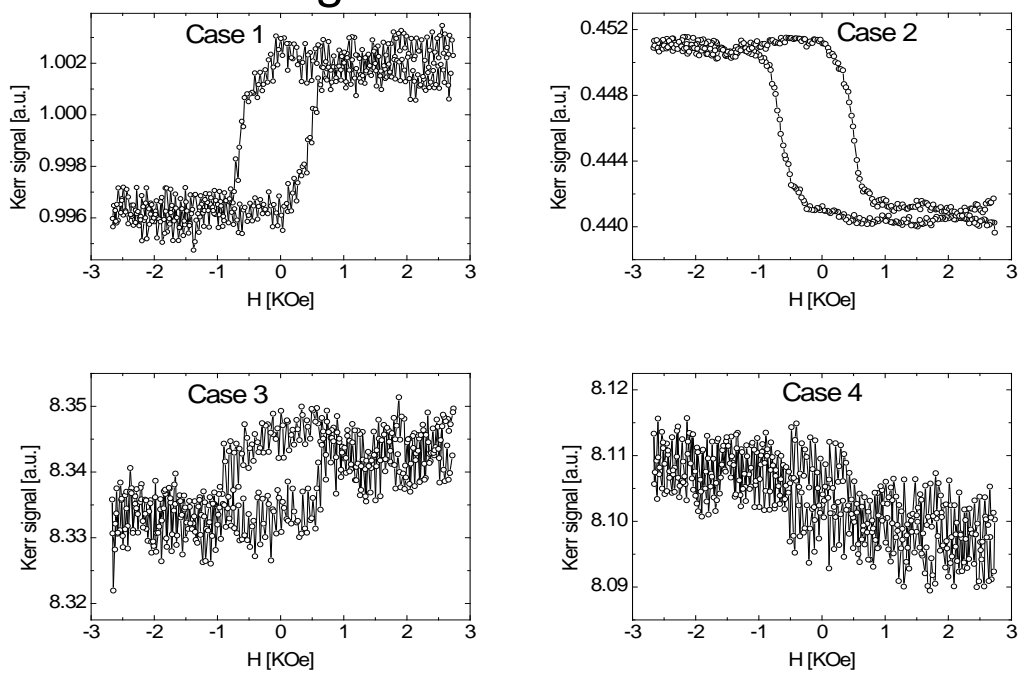


Figure 2.17. First and second harmonics MOKE hysteresis loops obtained in various cases using configuration 2.2.

The calculated intensity has a similar structure as configuration 1.1; therefore, the present configuration can also be used as an ideal configuration for both first and second harmonics. However, the experimental S/N values are comparatively smaller than configuration 1.1 perhaps due to misalignment in optics set-up while measuring magnetic hysteresis loop.

Configuration 3.1

P axis at 90° , S , O axes at 45° and 135° , A axis at α

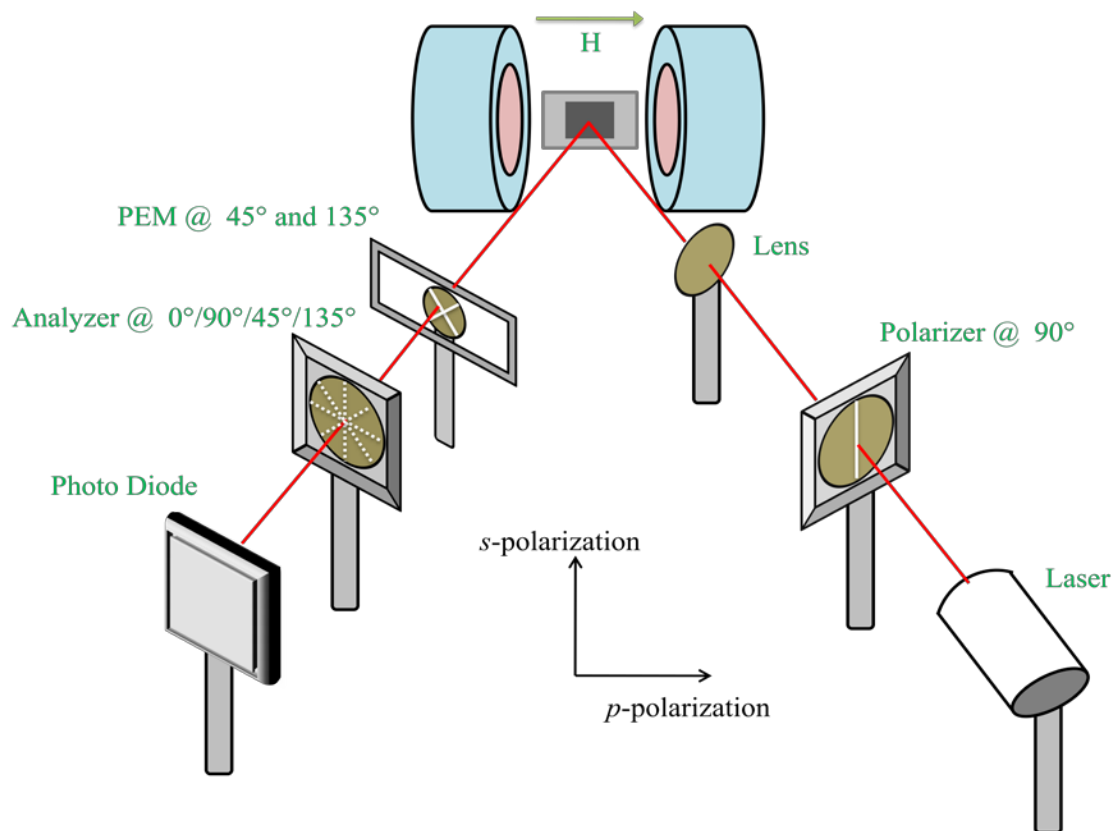


Figure 2.18. A sketch of placement and angles of different optical elements for configuration 3.1

The calculated intensity in this configuration is given by

$$\begin{aligned}
 I \propto & \frac{1}{2}r_s^2 + \frac{1}{2}r_{ps}^2 + r_s r_{ps} \cos(\delta_s - \delta_{ps}) \sin 2\alpha - \frac{1}{2}J_0(\varphi_0)(r_s^2 - r_{ps}^2) \cos 2\alpha \\
 & - 2J_1(\varphi_0) \sin \omega t r_s r_{ps} \sin(\delta_s - \delta_{ps}) \cos 2\alpha - J_2(\varphi_0) \cos 2\omega t (r_s^2 - r_{ps}^2) \cos 2\alpha \\
 & + \text{higher order terms}
 \end{aligned}$$

Case 1, $\alpha = 0$

$$\begin{aligned}
 I \propto & \frac{1}{2}r_s^2 + \frac{1}{2}r_{ps}^2 - \frac{1}{2}J_0(\varphi_0)(r_s^2 - r_{ps}^2) - 2J_1(\varphi_0) \sin \omega t r_s r_{ps} \sin(\delta_s - \delta_{ps}) \\
 & - J_2(\varphi_0) \cos 2\omega t (r_s^2 - r_{ps}^2) + \text{higher order terms}
 \end{aligned}$$

Case 2, $\alpha = 90^\circ$

$$\begin{aligned}
 I \propto & \frac{1}{2}r_s^2 + \frac{1}{2}r_{ps}^2 + \frac{1}{2}J_0(\varphi_0)(r_s^2 - r_{ps}^2) + 2J_1(\varphi_0) \sin \omega t r_s r_{ps} \sin(\delta_s - \delta_{ps}) \\
 & + J_2(\varphi_0) \cos 2\omega t (r_s^2 - r_{ps}^2) + \text{higher order terms}
 \end{aligned}$$

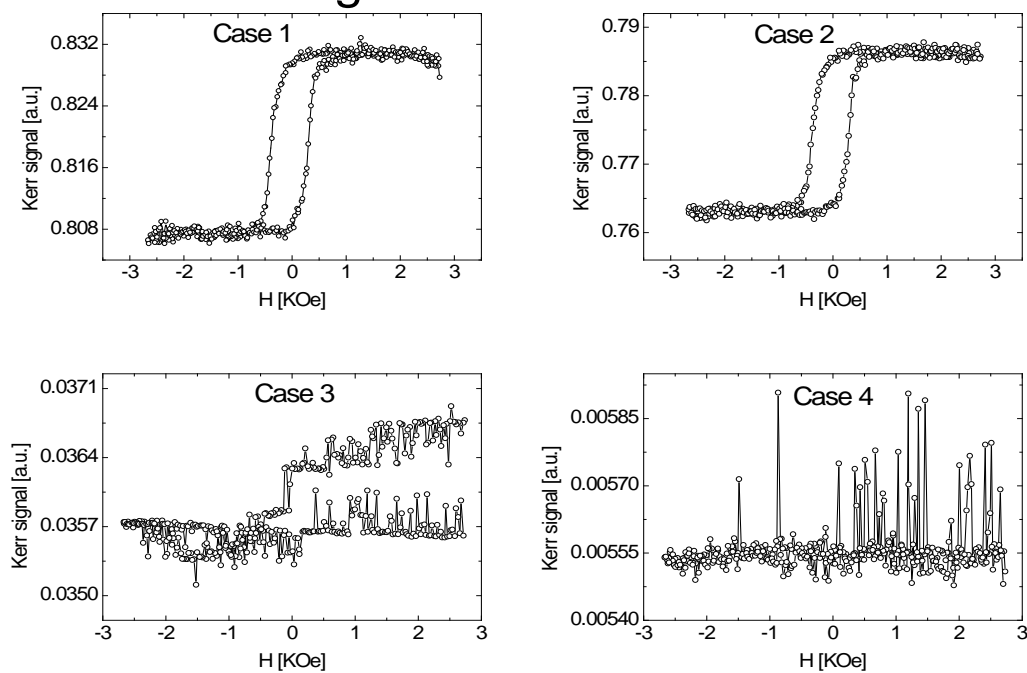
Case 3, $\alpha = 45^\circ$

$$I \propto \frac{1}{2}r_s^2 + \frac{1}{2}r_{ps}^2 + r_s r_{ps} \cos(\delta_s - \delta_{ps})$$

Case 4, $\alpha = 135^\circ$

$$I \propto \frac{1}{2}r_s^2 + \frac{1}{2}r_{ps}^2 - r_s r_{ps} \cos(\delta_s - \delta_{ps})$$

Configuration 3.1 - 1st Harmonic



Configuration 3.1 - 2nd Harmonic

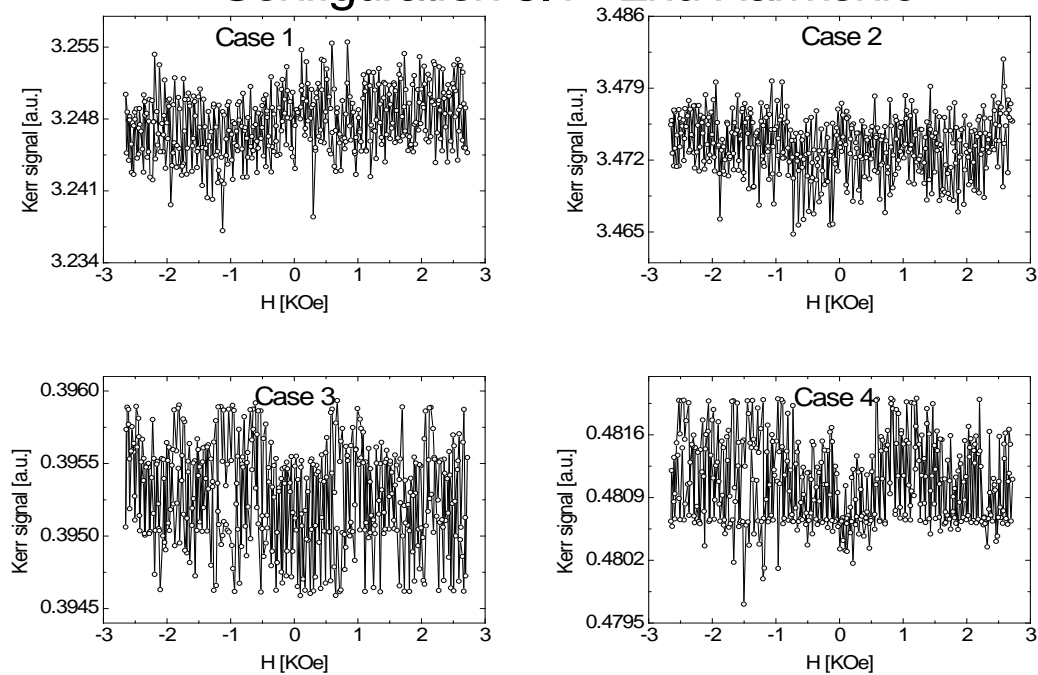


Figure 2.19. First and second harmonics MOKE hysteresis loops obtained in various cases using configuration 3.1.

It is noticed that cases 1 and 2 for the first harmonic give rise to high S/N such as 36.6 and 47.2, respectively in agreement with the theoretical analysis. In addition the theory predicts that the second harmonic signal will be reduced by a factor of 2 with respect to the first harmonic signal. This is qualitatively confirmed by the low quality loops of Figure 2.19. This configuration reflects an asymmetric situation and is, hence, not suitable for the simultaneous measurement of both harmonics.

Configuration 3.2

P axis at 90° , *O* axes at 45° and 135° , *S*, *A* axis at α

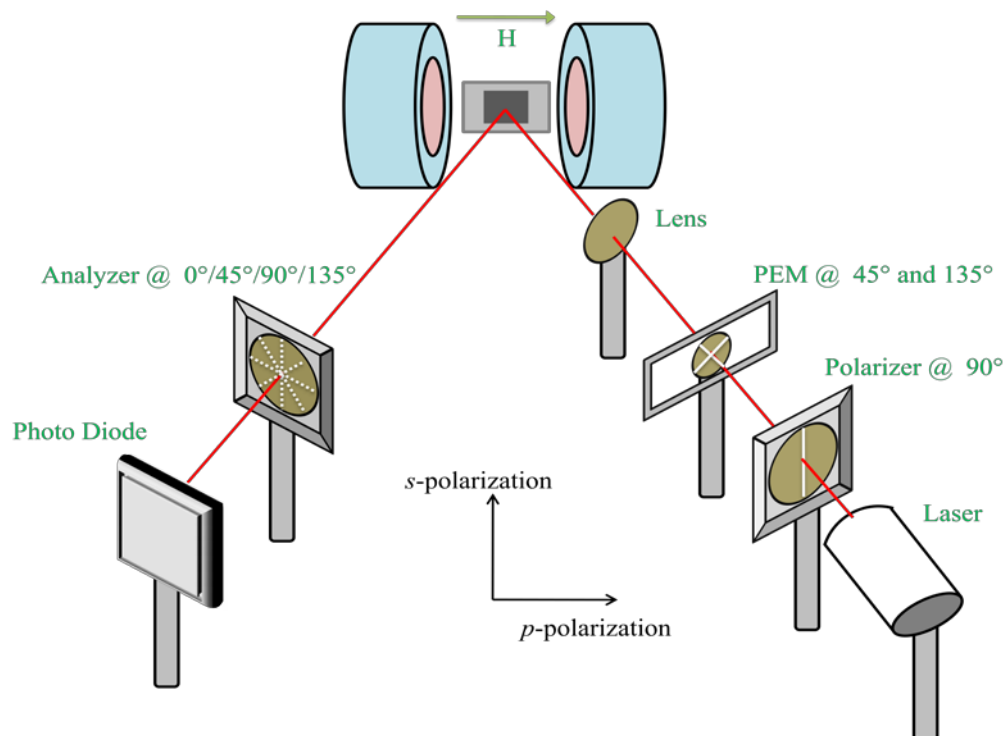


Figure 2.20. A sketch of placement and angles of different optical elements for configuration 3.2

The calculated intensity in this configuration is given by

$$\begin{aligned}
I = & \frac{1}{2}r_p^2 \cos^2 \alpha + \frac{1}{2}r_s^2 \sin^2 \alpha + \frac{1}{2}r_{ps}^2 - r_p r_{ps} \cos(\delta_p - \delta_{ps}) \sin \alpha \cos \alpha \\
& + r_s r_{ps} \cos(\delta_s - \delta_{ps}) \sin \alpha \cos \alpha - \frac{1}{2}J_0(\varphi_0)[r_p^2 \cos^2 \alpha - r_s^2 \sin^2 \alpha \\
& - r_{ps}^2 \cos 2\alpha - 2r_p r_{ps} \cos(\delta_p - \delta_{ps}) \sin \alpha \cos \alpha + 2r_s r_{ps} \cos(\delta_s - \delta_{ps}) \sin \alpha \cos \alpha] \\
& - 2J_1(\varphi_0) \sin \omega t [r_p r_s \sin(\delta_p - \delta_s) \sin \alpha \cos \alpha + r_p r_{ps} \sin(\delta_p - \delta_{ps}) \cos^2 \alpha \\
& + r_s r_{ps} \sin(\delta_s - \delta_{ps}) \sin^2 \alpha] - J_2(\varphi_0) \cos 2\omega t [r_p^2 \cos^2 \alpha - \\
& r_s^2 \sin^2 \alpha - r_{ps}^2 \cos 2\alpha - 2r_p r_{ps} \cos(\delta_p - \delta_{ps}) \sin \alpha \cos \alpha \\
& + 2r_s r_{ps} \cos(\delta_s - \delta_{ps}) \sin \alpha \cos \alpha] + \text{higher order terms}
\end{aligned}$$

Case 1, $\alpha = 0$

$$\begin{aligned}
I \propto & \frac{1}{2}r_p^2 + \frac{1}{2}r_{ps}^2 - \frac{1}{2}J_0(\varphi_0)(r_p^2 - r_{ps}^2) - 2J_1(\varphi_0) \sin \omega t r_p r_{ps} \sin(\delta_p - \delta_{ps}) \\
& - J_2(\varphi_0) \cos 2\omega t (r_p^2 - r_{ps}^2) + \text{higher order terms}
\end{aligned}$$

Case 2, $\alpha = 90^\circ$

$$\begin{aligned}
I \propto & \frac{1}{2}r_s^2 + \frac{1}{2}r_{ps}^2 + \frac{1}{2}J_0(\varphi_0)(r_s^2 - r_{ps}^2) - 2J_1(\varphi_0) \sin \omega t r_s r_{ps} \sin(\delta_s - \delta_{ps}) \\
& + J_2(\varphi_0) \cos 2\omega t (r_s^2 - r_{ps}^2) + \text{higher order terms}
\end{aligned}$$

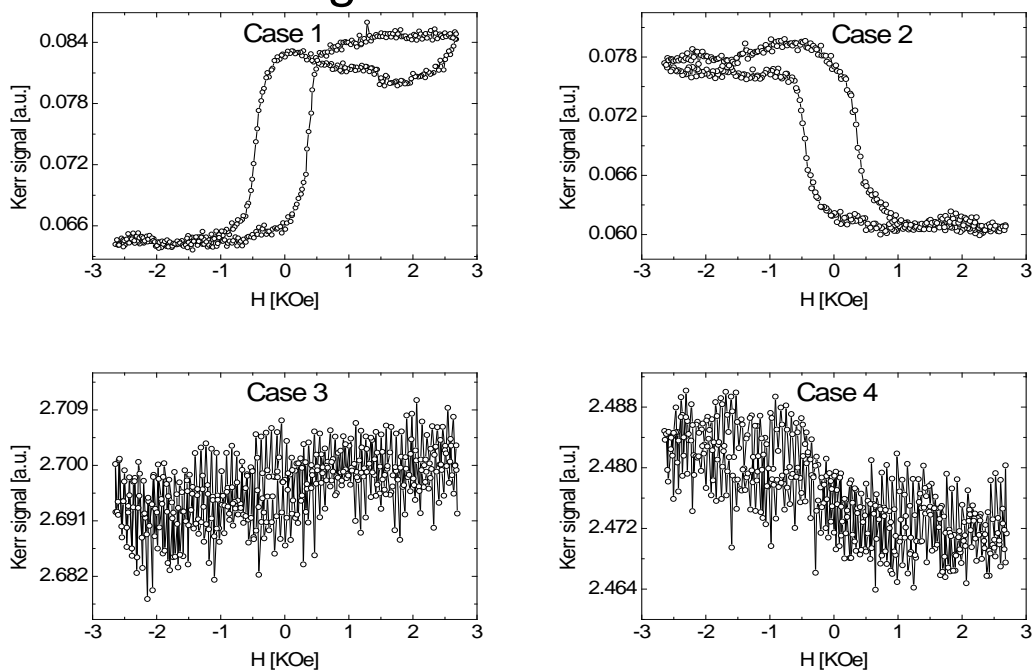
Case 3, $\alpha = 45^\circ$

$$\begin{aligned}
I \propto & \frac{1}{4}r_p^2 + \frac{1}{4}r_s^2 + \frac{1}{2}r_{ps}^2 - \frac{1}{2}r_p r_{ps} \cos(\delta_p - \delta_{ps}) + \frac{1}{2}r_s r_{ps} \cos(\delta_s - \delta_{ps}) \\
& - \frac{1}{4}J_0(\varphi_0)[r_p^2 - r_s^2 - 2r_p r_{ps} \cos(\delta_p - \delta_{ps}) + 2r_s r_{ps} \cos(\delta_s - \delta_{ps})] \\
& - J_1(\varphi_0) \sin \omega t [r_p r_s \sin(\delta_p - \delta_s) + r_p r_{ps} \sin(\delta_p - \delta_{ps}) + r_s r_{ps} \sin(\delta_s - \delta_{ps})] \\
& - \frac{1}{2}J_2(\varphi_0) \cos 2\omega t [r_p^2 - r_s^2 - 2r_p r_{ps} \cos(\delta_p - \delta_{ps}) + 2r_s r_{ps} \cos(\delta_s - \delta_{ps})] \\
& + \text{higher order terms}
\end{aligned}$$

Case 4, $\alpha = 135^\circ$

$$\begin{aligned}
 I \propto & \frac{1}{4}r_p^2 + \frac{1}{4}r_s^2 + \frac{1}{2}r_{ps}^2 + \frac{1}{2}r_p r_{ps} \cos(\delta_p - \delta_{ps}) - \frac{1}{2}r_s r_{ps} \cos(\delta_s - \delta_{ps}) \\
 & - \frac{1}{4}J_0(\varphi_0)[r_p^2 - r_s^2 + 2r_p r_{ps} \cos(\delta_p - \delta_{ps}) - 2r_s r_{ps} \cos(\delta_s - \delta_{ps})] \\
 & + J_1(\varphi_0) \sin \omega t [r_p r_s \sin(\delta_p - \delta_s) - r_p r_{ps} \sin(\delta_p - \delta_{ps}) - r_s r_{ps} \sin(\delta_s - \delta_{ps})] \\
 & - \frac{1}{2}J_2(\varphi_0) \cos 2\omega t [r_p^2 - r_s^2 + 2r_p r_{ps} \cos(\delta_p - \delta_{ps}) - 2r_s r_{ps} \cos(\delta_s - \delta_{ps})] \\
 & + \text{higher order terms}
 \end{aligned}$$

Configuration 3.2 - 1st Harmonic



Configuration 3.2 - 2nd Harmonic

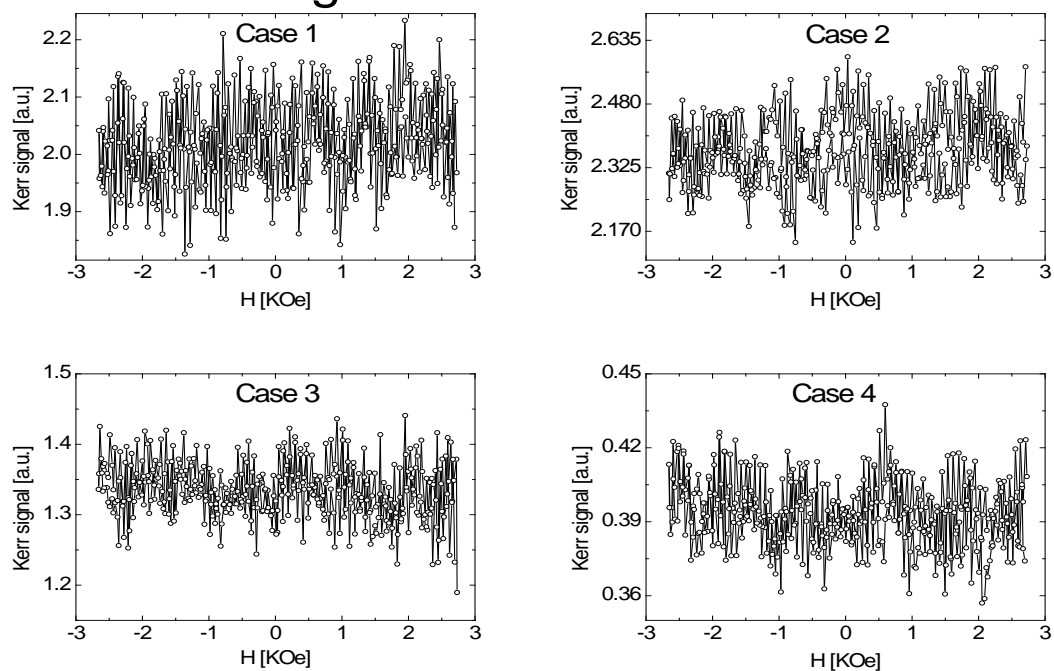


Figure 2.21. First and second harmonics MOKE hysteresis loops obtained in various cases using configuration 3.2.

This configuration shows the same asymmetry between the first and second harmonic as configuration 3.1 and is, hence, not ideal.

Configuration 4.1

P axis at 45° , S , O axes at 45° and 135° , A axis at α

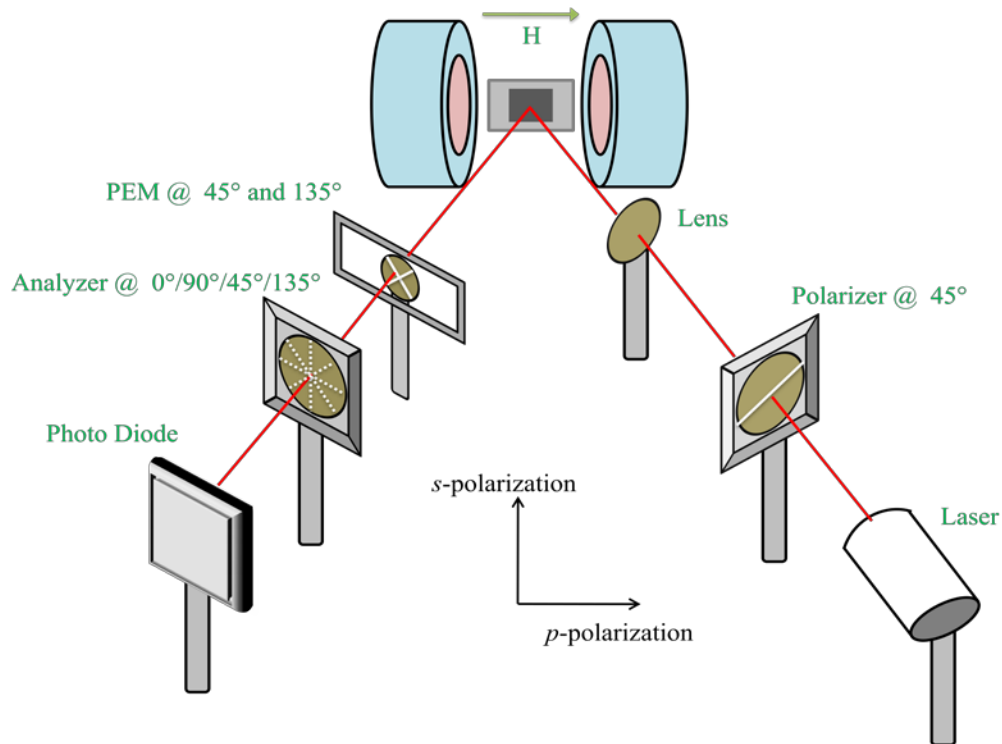


Figure 2.22. A sketch of placement and angles of different optical elements for configuration 4.1

The calculated intensity in this configuration is given by

$$\begin{aligned}
 I \propto & \frac{1}{8}r_p^2 + \frac{1}{8}r_s^2 + \frac{1}{4}r_{ps}^2 + \frac{1}{4}r_p r_{ps} \cos(\delta_p - \delta_{ps}) - \frac{1}{4}r_s r_{ps} \cos(\delta_s - \delta_{ps}) \\
 & + \frac{1}{2}r_p r_s \cos(\delta_p - \delta_s) \sin \alpha \cos \alpha - \frac{1}{2}r_p r_{ps} \cos(\delta_p - \delta_{ps}) \sin \alpha \cos \alpha + \\
 & \frac{1}{2}r_s r_{ps} \cos(\delta_s - \delta_{ps}) \sin \alpha \cos \alpha - \frac{1}{2}r_{ps}^2 \sin \alpha \cos \alpha \\
 & + \frac{1}{8}J_0(\varphi_0)[r_p^2 \cos 2\alpha - r_s^2 \cos 2\alpha + 2r_p r_{ps} \cos(\delta_p - \delta_{ps}) \cos 2\alpha + \\
 & 2r_s r_{ps} \cos(\delta_s - \delta_{ps}) \cos 2\alpha] \\
 & + \frac{1}{2}J_1(\varphi_0) \sin \omega t [r_p r_s \sin(\delta_p - \delta_s) \cos 2\alpha - r_p r_{ps} \sin(\delta_p - \delta_{ps}) \cos 2\alpha - \\
 & r_s r_{ps} \sin(\delta_s - \delta_{ps}) \cos 2\alpha] \\
 & + \frac{1}{4}J_2(\varphi_0) \cos 2\omega t [r_p^2 \cos 2\alpha - r_s^2 \cos 2\alpha + 2r_p r_{ps} \cos(\delta_p - \delta_{ps}) \cos 2\alpha + \\
 & 2r_s r_{ps} \cos(\delta_s - \delta_{ps}) \cos 2\alpha] \\
 & + \text{higher order terms}
 \end{aligned}$$

Case 1, $\alpha = 0$

$$\begin{aligned}
I &\propto \frac{1}{8}r_p^2 + \frac{1}{8}r_s^2 + \frac{1}{4}r_{ps}^2 + \frac{1}{4}r_p r_{ps} \cos(\delta_p - \delta_{ps}) - \frac{1}{4}r_s r_{ps} \cos(\delta_s - \delta_{ps}) \\
&+ \frac{1}{8}J_0(\varphi_0)[r_p^2 - r_s^2 + 2r_p r_{ps} \cos(\delta_p - \delta_{ps}) + 2r_s r_{ps} \cos(\delta_s - \delta_{ps})] \\
&+ \frac{1}{2}J_1(\varphi_0) \sin \omega t [r_p r_s \sin(\delta_p - \delta_s) - r_p r_{ps} \sin(\delta_p - \delta_{ps}) - r_s r_{ps} \sin(\delta_s - \delta_{ps})] \\
&+ \frac{1}{4}J_2(\varphi_0) \cos 2\omega t [r_p^2 - r_s^2 + 2r_p r_{ps} \cos(\delta_p - \delta_{ps}) + 2r_s r_{ps} \cos(\delta_s - \delta_{ps})] \\
&+ \text{higher order terms}
\end{aligned}$$

Case 2, $\alpha = 90^\circ$

$$\begin{aligned}
I &\propto \frac{1}{8}r_p^2 + \frac{1}{8}r_s^2 + \frac{1}{4}r_{ps}^2 + \frac{1}{4}r_p r_{ps} \cos(\delta_p - \delta_{ps}) - \frac{1}{4}r_s r_{ps} \cos(\delta_s - \delta_{ps}) \\
&- \frac{1}{8}J_0(\varphi_0)[r_p^2 - r_s^2 + 2r_p r_{ps} \cos(\delta_p - \delta_{ps}) + 2r_s r_{ps} \cos(\delta_s - \delta_{ps})] \\
&- \frac{1}{2}J_1(\varphi_0) \sin \omega t [r_p r_s \sin(\delta_p - \delta_s) - r_p r_{ps} \sin(\delta_p - \delta_{ps}) - r_s r_{ps} \sin(\delta_s - \delta_{ps})] \\
&- \frac{1}{4}J_2(\varphi_0) \cos 2\omega t [r_p^2 - r_s^2 + 2r_p r_{ps} \cos(\delta_p - \delta_{ps}) + 2r_s r_{ps} \cos(\delta_s - \delta_{ps})] \\
&+ \text{higher order terms}
\end{aligned}$$

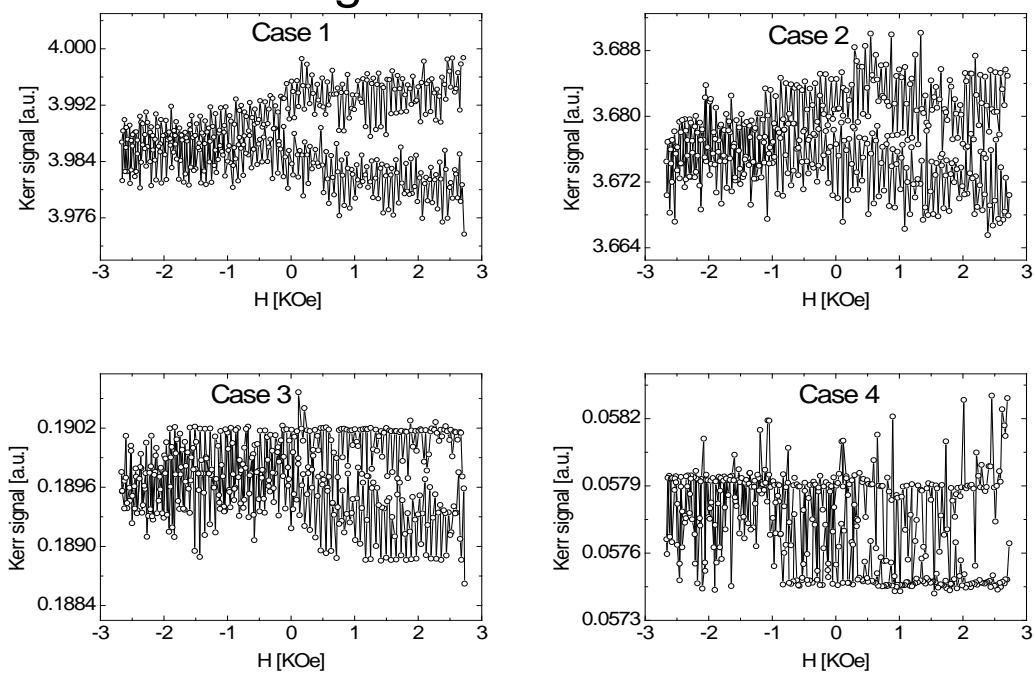
Case 3, $\alpha = 45^\circ$

$$I \propto \frac{1}{8}r_p^2 + \frac{1}{8}r_s^2 + \frac{1}{4}r_p r_s \cos(\delta_p - \delta_s)$$

Case 4, $\alpha = 135^\circ$

$$I \propto \frac{1}{8}r_p^2 + \frac{1}{8}r_s^2 + \frac{1}{2}r_{ps}^2 - \frac{1}{4}r_p r_s \cos(\delta_p - \delta_s) + \frac{1}{2}r_p r_{ps} \cos(\delta_p - \delta_{ps}) - \frac{1}{2}r_s r_{ps} \cos(\delta_s - \delta_{ps})$$

Configuration 4.1 - 1st Harmonic



Configuration 4.1 - 2nd Harmonic

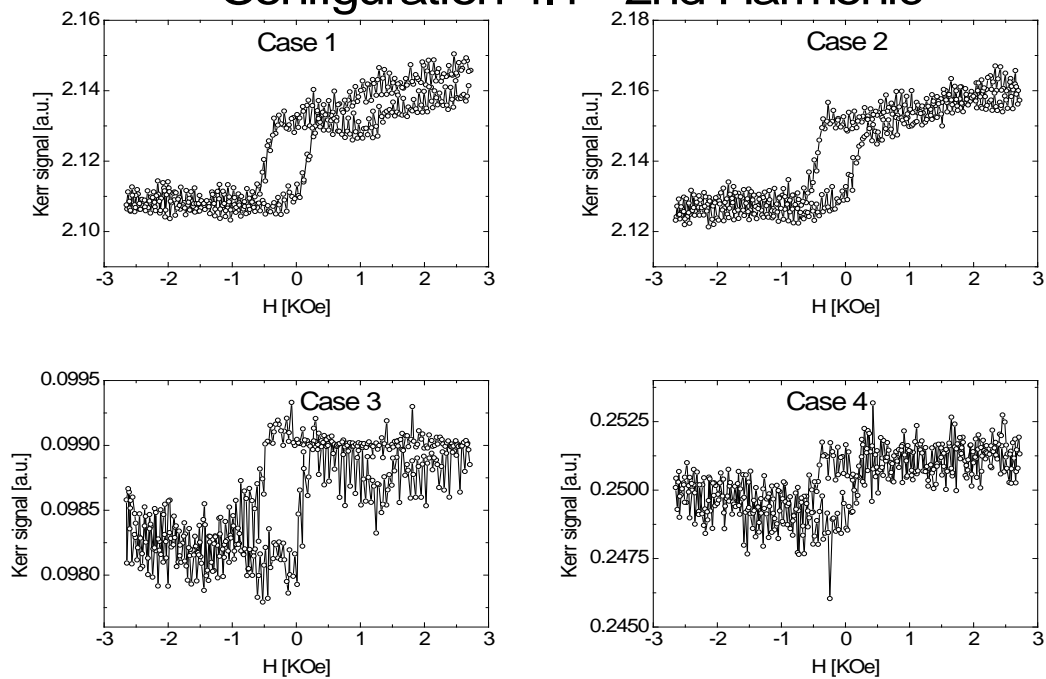


Figure 2.23. First and second harmonics MOKE hysteresis loops obtained in various cases using configuration 4.1.

Configuration 4.1 combines the disadvantages of reduced harmonic signals and the masking of the magnetic information by the diagonal elements making it non-ideal situation.

Configuration 4.2

P axis at 45° , O axes at 45° and 135° , S, A axis at α

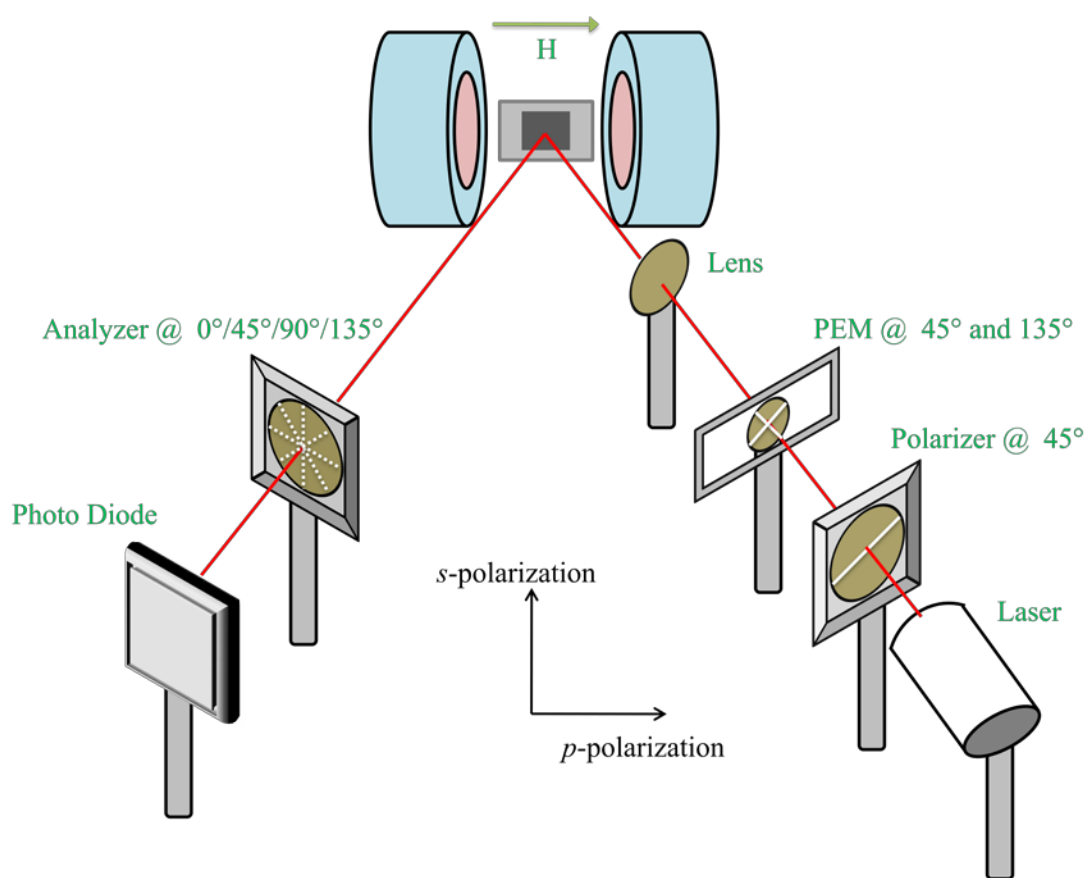


Figure 2.24. A sketch of placement and angles of different optical elements for configuration 4.2

The calculated intensity in this configuration is given by

$$\begin{aligned}
 I \propto & \frac{1}{4}r_p^2 \cos^2 \alpha + \frac{1}{4}r_s^2 \sin^2 \alpha + \frac{1}{4}r_{ps}^2 - \frac{1}{2}r_{ps}^2 \sin \alpha \cos \alpha + \frac{1}{2}r_p r_s \cos(\delta_p - \delta_s) \sin \alpha \cos \alpha \\
 & + \frac{1}{2}r_p r_{ps} \cos(\delta_p - \delta_{ps}) \cos^2 \alpha - \frac{1}{2}r_p r_{ps} \cos(\delta_p - \delta_{ps}) \sin \alpha \cos \alpha - \frac{1}{2}r_s r_{ps} \cos(\delta_s - \delta_{ps}) \sin^2 \alpha + \\
 & \frac{1}{2}r_s r_{ps} \cos(\delta_s - \delta_{ps}) \sin \alpha \cos \alpha
 \end{aligned}$$

Case 1, $\alpha = 0$

$$I \propto \frac{1}{4}r_p^2 + \frac{1}{4}r_{ps}^2 + \frac{1}{2}r_p r_{ps} \cos(\delta_p - \delta_{ps})$$

Case 2, $\alpha = 90^\circ$

$$I \propto \frac{1}{4}r_s^2 + \frac{1}{4}r_{ps}^2 - \frac{1}{2}r_s r_{ps} \cos(\delta_s - \delta_{ps})$$

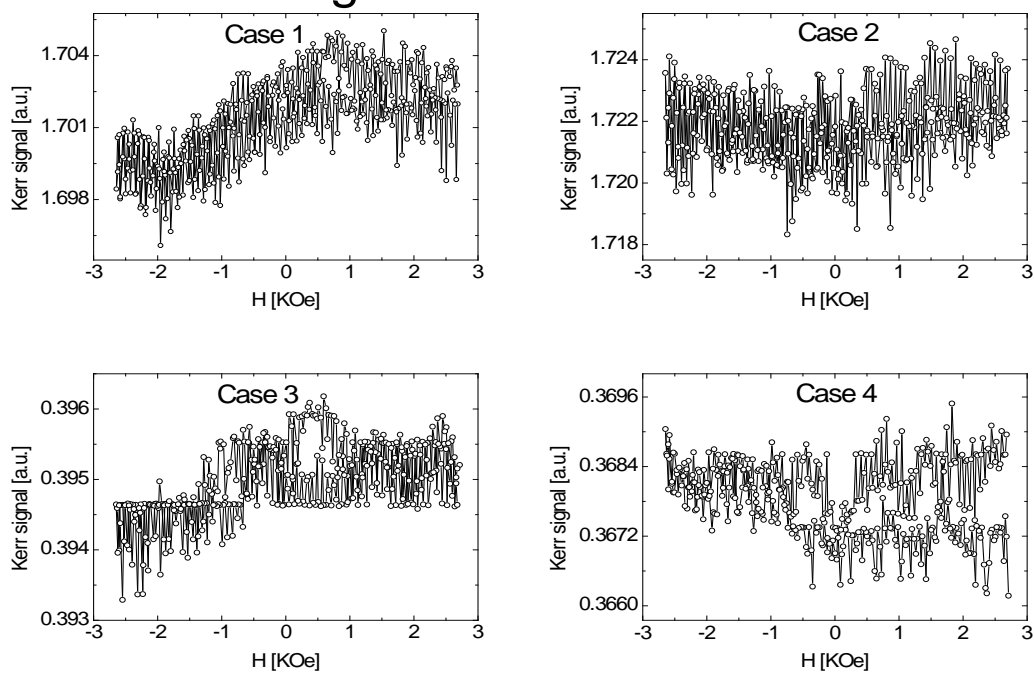
Case 3, $\alpha = 45^\circ$

$$I \propto \frac{1}{8}r_p^2 + \frac{1}{8}r_s^2 + \frac{1}{4}r_p r_s \cos(\delta_p - \delta_s)$$

Case 4, $\alpha = 135^\circ$

$$I \propto \frac{1}{8}r_p^2 + \frac{1}{8}r_s^2 + \frac{1}{2}r_{ps}^2 - \frac{1}{4}r_p r_s \cos(\delta_p - \delta_s) + \frac{1}{2}r_p r_{ps} \cos(\delta_p - \delta_{ps}) - \frac{1}{2}r_s r_{ps} \cos(\delta_s - \delta_{ps})$$

Configuration 4.2 - 1st Harmonic



Configuration 4.2 - 2nd Harmonic

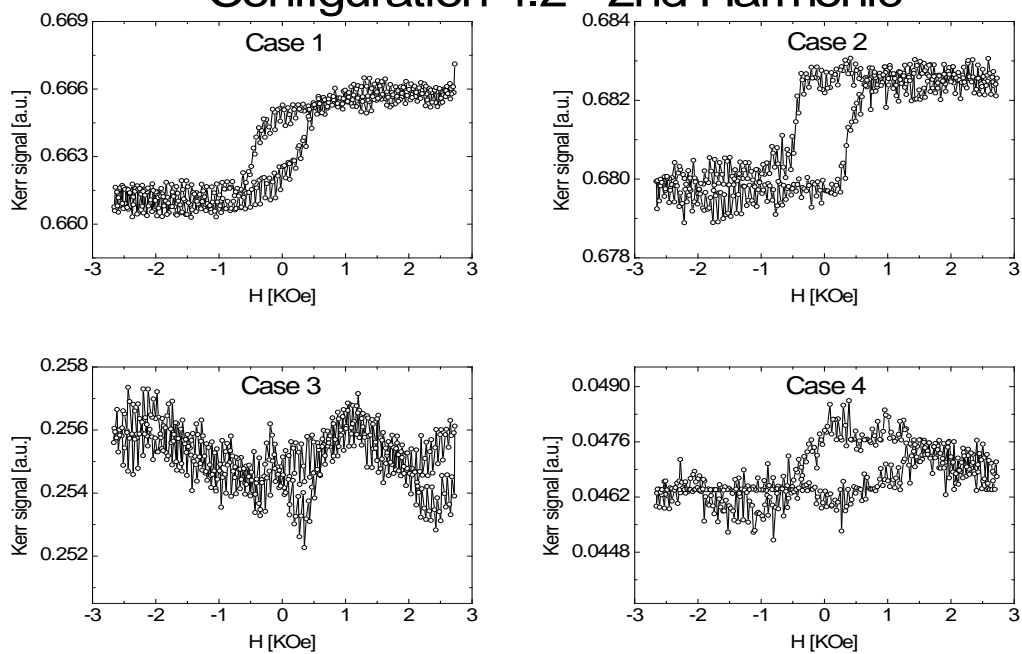


Figure 2.25. First and second harmonics MOKE hysteresis loops obtained in various cases using configuration 4.2.

The theoretical calculation of intensity suggests the absence of any signal, which is in good agreement with our experimental findings, however, misalignments of the optical elements may give rise to a very poor hysteresis loops for the cases 1 and 2 of second harmonic.

All these findings are tabulated below.

<i>Configurations</i>		<i>1st harmonic</i>	<i>2nd harmonic</i>
<i>Config.</i> <i>1.1</i>	Case 3	21.7	45.9
	Case 4	24.2	51.0
<i>Config.</i> <i>2.2.</i>	Case 1	6.7	9.5
	Case 2	1.2	26.9
<i>Config.</i> <i>3.1.</i>	Case 1	36.6	N/A
	Case 2	47.2	N/A
<i>Config.</i> <i>3.2.</i>	Case 1	51.2	N/A
	Case 2	37.3	N/A

Table 1. The calculated S/N ratio values for meaning configurations

From these studies, we can conclude¹⁵¹ that the various configurations give rise to different Kerr signals. Some of them have either optimized first or second harmonic signals. Others show reduced signal to noise ratios due to large field independent contributions originating from the diagonal elements of the dielectric tensor. The

optimized setups (*configuration 1.1*) and (*configuration 2.2*) stand out to be the best ones by maximizing the signal of the *first* and the *second* harmonics and are free from nonmagnetic background contributions.

2.2.5. SUPERCONDUCTING QUANTUM INTERFERENCE DEVICE

Superconducting Quantum Interference Device (SQUID) is one of the most sensitive ways of measuring magnetic properties. In particular, this method allows directly determining the overall magnetic moment of a sample in absolute units. SQUID combines the physical phenomena of flux quantization and Josephson tunneling. If two superconductors are separated by an insulating film, it is found that an electric current can tunnel from one side of the junction to the other. Following the equations established by Brian David Josephson in 1962, the electrical current density through a weak electric contact between two superconductors depends on the phase difference $\Delta\phi$ of the two superconducting wave functions. This effect is known as Josephson effect. Moreover, the time derivative of $\Delta\phi$ is correlated with the voltage across this weak contact. In a superconducting ring with one (so-called *RF-SQUID*, fig. 2.26., blue) or two (*DC-SQUID*) weak contacts, $\Delta\phi$ is additionally influenced by the magnetic flux Φ through this ring. Therefore, such a structure can be used to convert magnetic flux into an electrical voltage.

The magnetic signal from the sample is obtained via a superconducting pick-up coil. This coil, together with a SQUID antenna (red in fig. 2.26.), is part of a whole

superconducting circuit transfers the magnetic flux from the sample to RF-SQUID device which is located away from the sample. This device acts as a magnetic flux-to-voltage converter (blue in fig. 2.26.). This voltage is then amplified and read out by the magnetometer's electronics (green in fig. 2.26.).

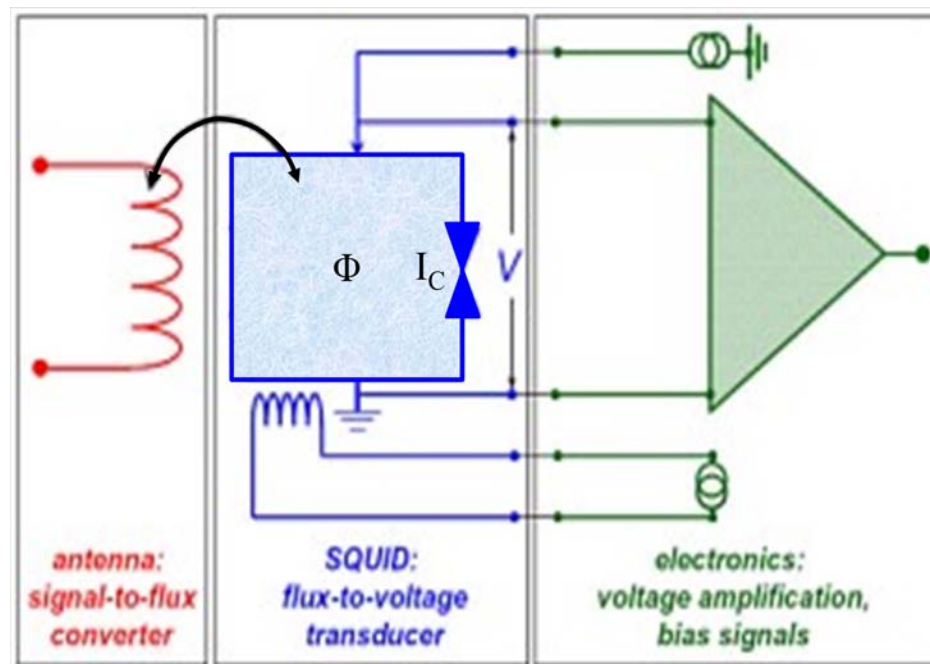


Figure 2.26. Equivalent circuit of SQUID = flux-to-voltage converter

When the sample is moved up and down it produces an alternating magnetic flux in the pick-up coil which leads to an alternating output voltage of the SQUID device. By locking the frequency of the readout to the frequency of the movement (RSO, reciprocating sample oscillation), the magnetometer system can achieve extremely high sensitivity for ultra small magnetic signals as described above.¹⁵²

We operate a commercial SQUID magnetometer system from Quantum Design, San Diego (magnetic properties measurement system MPMS XL-7). The sample is located in the center of a superconducting solenoid producing magnetic fields up to 7 Tesla. The sample space is filled with helium at low pressures. Our SQUID can operate at the temperature range from 2 to 400 K with sweep rates of 0.001 to 10K/min. The sensitivity of the system is 10^{-8} emu or 10^{-11} J/T in RSO mode. The whole system is fully computer-controlled and operated 24 hours a day. Measuring sequences can be programmed in advance and will be executed automatically.

CHAPTER 3

AF/FM EXCHANGE COUPLED BILAYERS

In this chapter I discuss the experimental results of exchange bias training in coupled CoO/Co bilayer thin films. Simultaneous studies of temperature and FM thickness dependence of the exchange bias and training effect reveal universal scaling of the exchange bias training effect. All experimental results are consistent with the phenomenological theory based on the Landau-Khalatnikov equation. The end section of this chapter discusses magnetoresistance measurements on CoO/Co bilayer heterostructures with special emphasis on the question how exchange bias impacts the magnetoresistance of the bilayer.

3.1 TEMPERATURE DEPENDENCE OF THE EXCHANGE BIAS TRAINING EFFECT

Non-equilibrium systems provide some of the most challenging problems of modern statistical mechanics.^{153,154} Relaxation phenomena is one of the major branches of non-equilibrium phenomena among others. Their complexity becomes more apparent when comparing the complete characterization of a dynamical state with its corresponding steady state. The latter is determined by the few variables that describe the equilibrium state while temporal derivatives and gradients are inherent to the dynamical

state. The training of the EB effect is one^{66,84,85,86,87,155,156} of the several other available non-equilibrium relaxation phenomena. The fact that the exchange bias training is not continuous but triggered provides special opportunities to study non-equilibrium physics in contrast to those processes that take place continuously in time. In this chapter, an analytic theory is presented and certain model properties of this non-equilibrium problem of statistical physics are emphasized.

From chapter 1 it is a known fact that there is not a unique microscopic theory of exchange bias but many which explain the origin of interface magnetization of the antiferromagnet which enters the MB formula. On the other hand, the training effect seems to be universal which has already been evidenced in varieties of systems. Therefore, a phenomenological theory for the training effect is developed which is independent of microscopic details. This is possible due to the fact that the structure of the free energy that enters the dynamical equation is so general applicable for all types of systems. In chapter 1, I have shown the derivation of a phenomenological implicit sequence (1-17) for the training effect that was derived by Binek from a discretized Landau-Khalatnikov (LK) equation. Note that γ entered in implicit expression (1-17) is an essential temperature-dependent parameter which reads,

$$\gamma = \frac{\mu_0(H_{EB}(n) - H_{EB}(n+1))}{(\mu_0(H_{EB}(n) - H_{EB}^e))^3} \quad (3-1)$$

In section (1.2.1) I have shown implicit sequence (1-17) has capacity to produce step-like behavior of training effect for which γ becomes,

$$\gamma = \frac{1}{\left(\mu_0 H_{EB}(n=1) - \mu_0 H_{EB}^e\right)^2} \quad (3-2)$$

The major objective of this section is to experimentally understand the temperature dependence of γ which characterizes of $\mu_0 H_{EB}$ vs. n behavior.

3.1.1. PREPARATION OF THE CoO/Co HETEROSTRUCTURE AND STRUCTURAL CHARACTERIZATION

The experimental data are obtained from a CoO/Co heterostructure, which has been fabricated by DC sputtering of Co on top of the single-crystal substrate of α -Al₂O₃. The substrate is placed in acetone container and thoroughly cleaned with the help of sonicator before it is mounted on a sample holder. The whole chamber was pumped down to a base pressure of 1.3×10^{-7} mbar before sputtering Co. Sputtering took place at an Ar pressure of 6.7×10^{-3} mbar after pre-sputtering the Co target for 10 mins. The Co film was deposited at a rate of 0.2 nm/s for $t=500$ sec. The natural CoO thin film has been formed on top of Co after bringing Co thin film into ambient conditions.

Figure 3.1 shows the results of the wide angle X-ray diffraction of (a) the substrate, (b) the entire heterostructure before, and (c) after annealing. The latter heat treatment took place under vacuum condition of 2.7×10^{-7} mbar at a temperature $T=1000$ K for $t=4$ hrs. Figure 3.1 (a) shows the θ - 2θ scan of the crystalline α -Al₂O₃ substrate. The polished surface of the substrate platelet of 0.5 mm thickness corresponds to the α -

plane cut in accordance with the strong ($h00$) reflexes for $h=2$ and 4 and a weaker reflex for $h=3$.

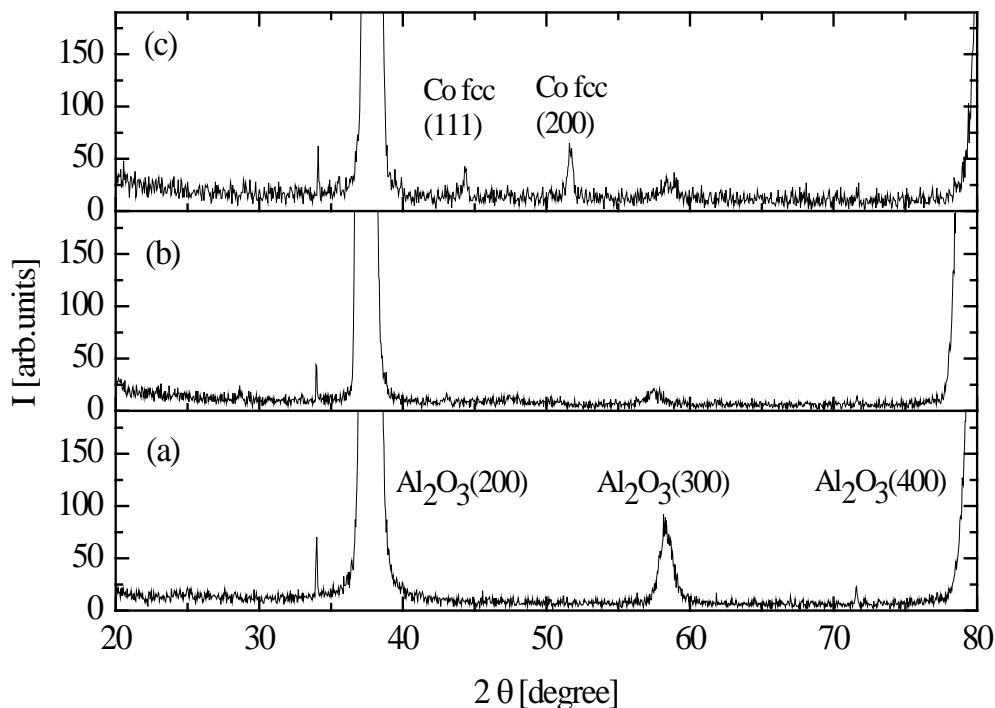


Figure 3.1. θ - 2θ X-ray analysis of the (a) α -Al₂O₃ substrate, (b) the Al₂O₃/Co/CoO heterostructure as prepared, (c) and after annealing for 4 hrs at $T=1000$ K. All scans show the dominant (200) and (400) peaks of the single-crystalline Al₂O₃ substrate and its weaker (300) peak. There is no significant additional peak in the prepared structure (b). After annealing (c) two additional peaks are observed and assigned as (111) and (200) peaks of fcc Co.

Before annealing, there is no clear signature of the sputtered Co film as shown in Fig. 3.1 (b). However, after annealing, two additional peaks are observed which are assigned as (111) and (200) peaks of Co in an fcc structure as shown in Fig. 3.1 (c). The latter result can be compared with the structural analysis Ref. [157], where epitaxially

grown Co on top of the a -plane of an Al_2O_3 single crystal. Here, neutron reflectometry shows a pronounced Co fcc (111) peak, but no indication of a (200) peak. In contrast to the strong planar anisotropy in the epitaxially grown samples of Ref. [157], our sputtered samples show virtually no in-plane anisotropy as discussed later in section 3.1.2. We believe the structural difference alters the properties of the magnetic anisotropy in the sample. Note that the X-ray data in Fig. 3.1 (c) show no indications of a CoO surface layer which, however, reveals its presence in the magnetic data via the EB effect.

3.1.2. MAGNETIC ANISOTROPY OF CO THIN FILM IN A COO/CO BILAYER

The ratio of the remanent magnetic moment m_r and the saturation moment m_s is displayed in figure 3.2 for various angles $0 \leq \Phi \leq 2\pi$ between the applied planar magnetic field and a fixed direction in the sample plane. Within the small uncertainty level, the data of m_r/m_s vs. Φ fall on an invariable line. This implies the absence of an easy anisotropy axis in the plane in our CoO/Co sample. The solid line represents the best linear fit to the data set and indicates a small scattering around the constant value $m_r/m_s=0.22$. The inset of Fig. 3.2 shows a typical magnetic hysteresis of the heterostructure measured at room temperature with the help of an AGFM. In accordance with the diamagnetic susceptibility of the Al_2O_3 substrate, a linear background has been determined and subtracted from each curve before analyzing the m_r to m_s ratio.

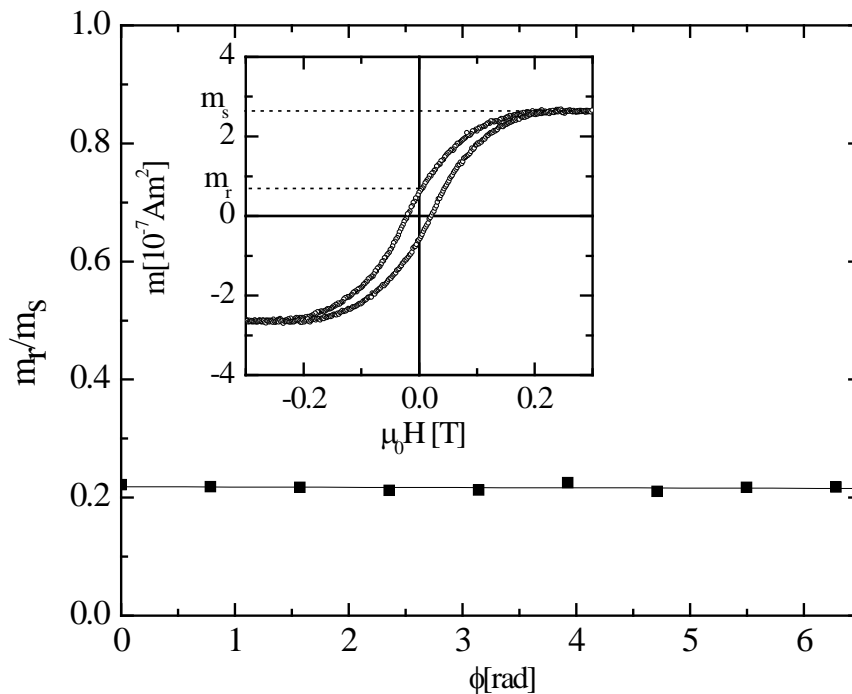


Figure 3.2. The value of m_r/m_s of the remanent and the saturation magnetic moment for various in-plane orientations $0 \leq \Phi \leq 2\pi$ of the magnetic field. Squares are the experimental data of m_r/m_s determined from hysteresis loops of $\text{Al}_2\text{O}_3/\text{Co}/\text{CoO}$ measured from different orientations by alternating gradient force magnetometry at room temperature. A solid line is the best straight line fit. The inset shows a typical loop measured at one particular orientation Φ . Dashed lines indicate the remanent and the saturation magnetic moment, respectively.

With the conclusion that there is no preferred anisotropy axis in sputtered CoO/Co , the low temperature hysteresis loops are measured for a fixed but arbitrary direction of the sample with the in-plane magnetic field. Further details of sample magnetic characterization are discussed in the section 3.1.3.

3.1.3. TRAINING EFFECT IN CoO/Co

A SQUID has been used in order to measure the consecutively cycled magnetic hysteresis loops. Each set of 6-10 consecutive loops are measured after field cooling the sample from $T=320$ K to the target temperatures $T=5, 25, 50, 65, 75, 80, 105,$ and 120 K in the presence of an applied in-plane magnetic field of $\mu_0 H = 0.3$ T. The strength of this cooling field secures saturation of the Co film at a minimal perturbation of the natural AF CoO pinning layer. The training effect at fixed temperature is analyzed with the help of a best fit of Eq. (1-17). The experimental data obtained from SQUID and corresponding theoretical fittings are shown in Fig. 3.3.

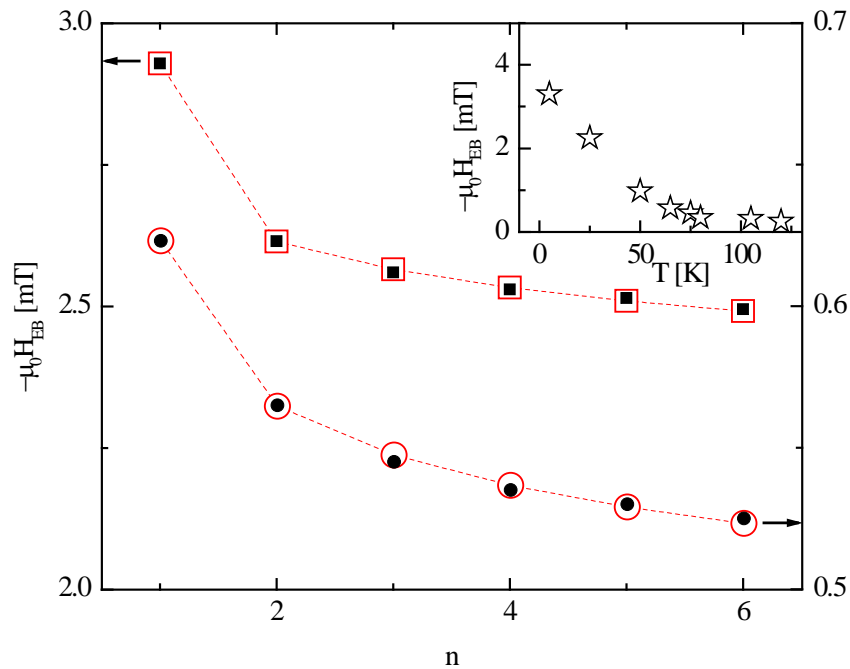


Figure 3.3. Training effect $\mu_0 H_{EB}$ versus n for $T=25$ (open squares) and 75 K (open circles) and the corresponding results of the best fits of Eq. (1-17). Note the different scales for $T=25$ and 75 K, assigned by arrows. The dotted lines have no meaning, they are just eye guiding. Inset shows the equilibrium EB field $\mu_0 H_{EB}^e$ vs. T which results from fitting of Eq. (1-17) to various data sets at $5 \leq T \leq 120$ K.

The training effect $\mu_0 H_{EB}$ vs. n for $T=25\text{K}$ (solid squares) and 75K (solid circles) and corresponding results of the best fits from Eq. (1-17) are shown as open squares and open circles for $T=25\text{K}$ and 75K , respectively. The two-parameter fits yield γ and $\mu_0 H_{EB}^e$, which are the results from the fits of implicit sequence of Eq. (1-17) to the experimental data of $\mu_0 H_{EB}$ vs. n . The dotted lines are just eye guiding lines and have no physical meaning. The data shows a well known enhanced training effect between the first and second loops as described in Ref. [89], for example. The inset of Fig. 3.3 shows $\mu_0 H_{EB}^e$ vs. T , where $\mu_0 H_{EB}^e$ is the extrapolation of $\mu_0 H_{EB}(n)$ for $n \rightarrow \infty$. Incidentally, we found a change of the sign of the EB field to positive values at $T=150\text{K}$, which is very similar to the behavior observed in Ref. [157]. However, the tiny absolute value of the EB field did not allow us to perform a reliable analysis of the training effect. It is surprising that we could, however, measure and analyze training effects for absolute values $\mu_0 H_{EB} \leq 0.5\text{mT}$ (see Fig. 3.3, right axis).

It is indeed crucial to apply the same method of analysis for all hysteresis loops; therefore, there is a necessary to mention the methodology that I followed to extract the values of EB field from the experimental hysteresis loops. A linear fit of the magnetization data at $0.51 < \mu_0 H < 0.6\text{T}$ of the down branch of the loop has been used to determine the linear background involved in the SQUID measurements. Note that the background is temperature dependent and has been determined individually for each loop. After background subtraction, I determined the left and right coercive fields

$\mu_0 H_{c1,2}$ from linear fits, involving data points in a symmetric interval of width $\Delta(\mu_0 H) = 30$ mT in the vicinity of the intercepts of the loop with the field axis and evaluated the value of EB from $\mu_0 H_{EB} = \mu_0 (H_{c1} + H_{c2})/2$

In the next section I focus on interesting derivation of temperature dependence of the training effect in terms of $\gamma = \gamma(T)$ based on mean-field approximation.

3.1.4. PHENOMENOLOGICAL THEORY OF TEMPERATURE DEPENDENCE OF THE TRAINING EFFECT IN AF/FM BILAYERS

In the framework of the fluctuation theory of phase transition, it is a standard approach to expand the free energy with respect to the primary order parameter η in the vicinity of the equilibrium order parameter, $\eta_e \neq 0$.¹⁵⁸ This ansatz is in contrast to the usual Landau expansion, which holds close to the critical temperatures where $\eta_e \approx 0$. We follow here the ideas similar to the fluctuation approach in order to tackle the EB problem because EB takes place at $T < T_B$, where the pinning layer is in its AF phase. The primary order parameter $\eta = (m_1 - m_2)/2$ describes the AF order of the pinning layer, while the magnetization $m = (m_1 + m_2)/2$ of the AF layer becomes a secondary order parameter. Here $m_{1,2}$ are the normalized sublattice magnetizations, which are assumed to have Ising symmetry for simplicity. At $T < T_N$, the free energy has pronounced minima,

$\pm\eta_e$. The field cooling process decides either of the sign of η_e . Therefore, it is reasonable to expand the free energy in harmonic approximation around η_e as shown in Fig. 3.4.

$$\Delta F = \alpha(T)(\eta - \eta_e)^2 \quad (3-3)$$

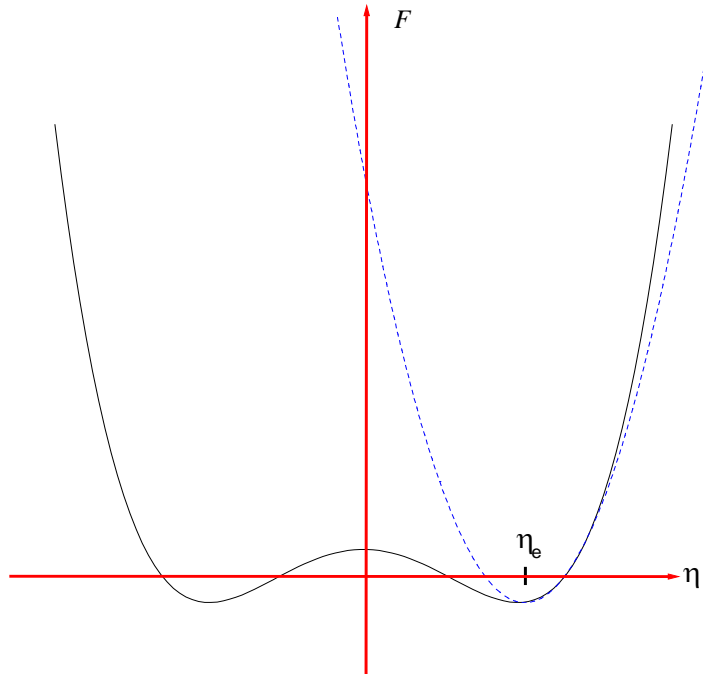


Figure 3.4. Landau-type free energy (solid line) of the AF pinning layer at $T < T_B$ and the harmonic approximation around $\eta = \eta_e$ (dashed blue color)

where $\alpha(T)$ is a temperature-dependent expansion coefficient. Eq. (3-3) is consistent with the Landau-type equation for $T \rightarrow T_N$,

$$\Delta F = \frac{\tilde{a}}{2}\eta^2 + \frac{\tilde{b}}{4}\eta^4 \quad (3-4)$$

The relation between coefficients $\alpha(T)$ in Eq. (3-3), \tilde{a} , and \tilde{b} can be simply obtained by differentiating Eq. (3-4) and substituting in Taylor series of $\Delta F(\eta)$ in the vicinity of η_e .

The math details follow,

$$F(\eta) = F(\eta_e) + \frac{\partial F}{\partial \eta} \Big|_{\eta=\eta_e} (\eta - \eta_e) + \frac{1}{2} \frac{\partial^2 F}{\partial \eta^2} \Big|_{\eta=\eta_e} (\eta - \eta_e)^2$$

The first and second derivatives of free energy are obtained from Eq. (3-4). Therefore, the above equation becomes,

$$\Delta F(\eta) = \tilde{b} \eta_e^2 (\eta - \eta_e)^2$$

Comparing the above equation with Eq. (3-3), one obtains $\alpha(T) = \tilde{b} \eta_e^2$. Figure 3.4 shows the Landau-type free energy of the AF pinning layer below its blocking temperature and the idea of harmonic approximation in the vicinity of equilibrium order parameter sketched in dotted blue line.

Mean-field theory provides a relation between the primary and secondary order parameters η and m .¹⁵⁹ In zero applied and zero staggered magnetic field there is no induced magnetization and, hence, we obtain $m = 0$ in equilibrium. The self-consistent mean-field equations derived in Ref. [159] provide,

$$\eta = \frac{\sinh \left[\frac{2\eta(J + J')}{K_B T} \right]}{\cosh \left[\frac{2m(J - J')}{K_B T} \right] + \cosh \left[\frac{2\eta(J + J')}{K_B T} \right]} \quad (3-5)$$

where J and J' are related to the number of nearest and next nearest neighbors z and z' and the nearest and next-nearest neighbor interactions \tilde{J} and \tilde{J}' according to $J = z\tilde{J}$ and $J' = z'\tilde{J}'$. $\tilde{J} > 0$ and $\tilde{J}' < 0$ describe AF nearest and the next nearest interactions, while $\tilde{J} < 0$ and $\tilde{J}' > 0$ are FM interactions.

In the framework of the mean-field approximation, the critical temperature depends on J and J' according to $T_N = (J + J')/K_B$ while details of the lattice symmetry are neglected. Inspection of Eq. (3-5) shows that η is an even function of m and, therefore, a series expansion of η with respect to m in the vicinity of $m=0$ is possible,

$$\eta = \eta_e + \frac{1}{2} \left. \frac{\partial^2 \eta}{\partial m^2} \right|_{m=0} m^2 + \dots \quad (3-6)$$

where $\eta_e = \eta(m=0)$. Substitution of the expansion (3-6) into Eq. (3-3) yields,

$$\Delta F = \frac{\alpha(T)}{4} \left[\left(\frac{\partial^2 \eta}{\partial m^2} \right)_{m=0} \cdot m^2 \right]^2,$$

with $\alpha(T) = \tilde{b} \eta_e^2$ and $m \propto \delta S_{AF}$, one obtains,

$$\Delta F \propto \left[\eta_e \left(\frac{\partial^2 \eta}{\partial m^2} \right)_{m=0} \right]^2 (\delta S_{AF})^4 \quad (3-7)$$

From the and Eq. (1-17), we know $\gamma = \frac{\tilde{b}}{\sigma^2 \tilde{\xi}}$, where $\tilde{b} = \left[\eta_e \left(\frac{\partial^2 \eta}{\partial m^2} \right)_{m=0} \right]^2$ is a

temperature dependent coefficient in front of 4th order of δS_{AF} in free energy of Eq. (1-

15). Here, σ is proportionality constant and $\tilde{\xi} = \frac{\xi}{\tau}$ (Refer section 1.2.1 for additional details). Finally, the temperature dependence of γ in the framework of above theory is given by,

$$\gamma(T) \propto \left[\eta_e(T) \left(\frac{\partial^2 \eta(m, T)}{\partial m^2} \right)_{m=0} \right]^2 \quad (3-8)$$

$\gamma = \gamma(T)$ requires the calculation of $\left[\left(\frac{\partial^2 \eta(m, T)}{\partial m^2} \right)_{m=0} \right]^2$ and an approximation for $\eta_e(T)$ which holds in a wide temperature range. $\left[\left(\frac{\partial^2 \eta(m, T)}{\partial m^2} \right)_{m=0} \right]^2$ is calculated via twofold implicit differentiation of Eq. (3-5). Subsequently I show some math details in obtaining this second order derivate of η .

From Eq. (3-5) it follows $\eta = f(\eta(m), m)$. So, the first derivative of η with respect to m gives,

$$\frac{\partial \eta}{\partial m} = \frac{\partial f}{\partial \eta} \frac{\partial \eta}{\partial m} + \frac{\partial f}{\partial m}$$

Now, the second derivative of η with respect to m can be obtained by taking derivative of above equation with respect to m ,

$$\frac{\partial^2 \eta}{\partial m^2} = \frac{\partial^2 f}{\partial \eta \cdot \partial m} \frac{\partial \eta}{\partial m} + \frac{\partial^2 f}{\partial \eta^2} \left(\frac{\partial \eta}{\partial m} \right)^2 + \frac{\partial f}{\partial \eta} \frac{\partial^2 \eta}{\partial m^2} + \frac{\partial^2 f}{\partial m^2}$$

Recall $\left. \frac{\partial \eta}{\partial m} \right|_{m=0} = 0$. This simplifies the above equation and gives rise to,

$$\left. \frac{\partial^2 \eta}{\partial m^2} \right|_{m=0} = \frac{\left. \frac{\partial^2 f}{\partial m^2} \right|_{m=0}}{1 - \left. \frac{\partial f}{\partial \eta} \right|_{m=0}}. \text{ Therefore, Eq. (3-8) becomes, } \gamma(T) \propto \left(\eta_e(T) \cdot \frac{\left. \frac{\partial^2 f}{\partial m^2} \right|_{m=0}}{\left. \frac{\partial f}{\partial \eta} \right|_{m=0}} \right)^2. \text{ The}$$

derivates $\left. \frac{\partial^2 f}{\partial m^2} \right|_{m=0}$ and $\left. \frac{\partial f}{\partial \eta} \right|_{m=0}$ can be evaluated from Eq. (3-5) which gives rise to,

$$\gamma(T) = C \left(\frac{\eta_e(T) \tanh \left[\frac{T_N \eta_e(T)}{T} \right]}{T \left\{ T \left(1 + \cosh \left[\frac{2T_N \eta_e(T)}{T} \right] \right) - 2T_N \right\}} \right)^2 \quad (3-9)$$

Here C becomes a fitting parameter which summarizes various phenomenological parameters while $\eta_e(T)$ is given by the solution of Eq. (3-5) for $m=0$. At $T \ll T_N$, where $\eta_e(T) \rightarrow 1$, the approximation reads $\eta_e(T) \approx \tanh(2T_N/T)$ and is indicated by red color line as shown in Figure 3.5. This approximation can be easily derived by substituting $m=0$ and $\eta_e(T) \rightarrow 1$ in Eq. (3-5). On the other hand, in the limit $T \rightarrow T_N$, where $\eta_e(T) \rightarrow 0$, the equivalent approximation reads $\eta_e(T) \approx (T/T_N) \sqrt{3(T_N - T)/T_N}$. The latter approximation converges to Landau-type approximation for $T/T_N \rightarrow 1$ as shown in Fig (3.5) by green color line. This approximation in the limit $T \rightarrow T_N$ can be obtained by series expansion of Eq. (3-5) in the limit of $\eta_e(T) \rightarrow 0$.

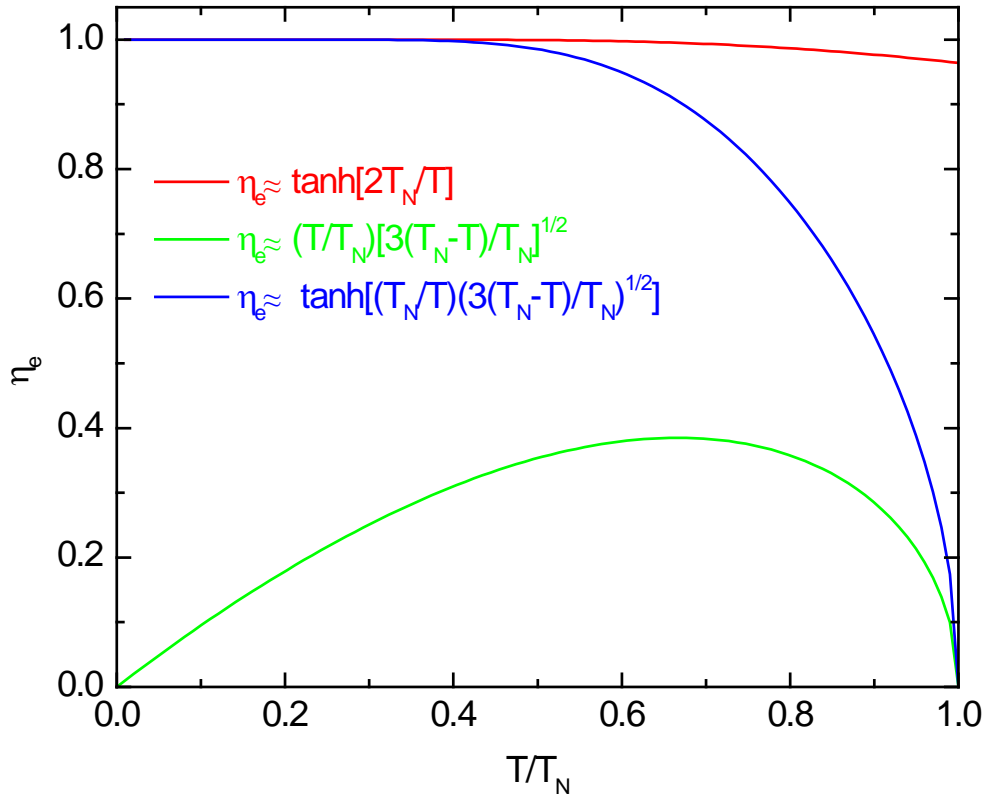


Figure 3.5. Curves of η_e vs. T/T_N for three cases. (i) Red color line shows the approximation of η_e for $T \ll T_N$. (ii) Green color line is the approximation of η_e in the limit of $T \rightarrow T_N$. (iii) Blue color line shows Landau approximation for η_e that fulfills cases (i) and (ii).

Note that these both approximations are valid for their limiting cases of $T \ll T_N$ and $T \rightarrow T_N$, respectively. However, an interpolating ansatz is essential for the description of the temperature dependence of the AF order parameter between $T=0$ and T_N . Therefore, the following simple analytic approximation provides that particular unique solution for the Eq. (3-5) which fulfils both limiting cases,

$$\eta_e(T) \approx \tanh\left(\frac{T_N}{T} \sqrt{3(T_N - T)/T_N}\right). \quad (3-10)$$

Eq. (3-10) is an useful explicit second order approximation of $\eta_e(T)$ for all $0 < T \leq T_N$. Blue color line in Fig (3.5) shows the curve of Eq (3-10) in the interval of $0 < T \leq T_N$. Note that this expression can generate $\eta_e(T)$ of both cases mentioned above. Combining Eqs. (3-9) and (3-10) provides an explicit fitting function for the experimental values of γ . The Néel temperature T_N in Eq. (3-9) is replaced by the blocking temperature $T_B = 186$ K [Ref. 157], at which EB completely vanishes. Therefore Eq. (3-9) becomes a one parameter fitting function for $\gamma(T)$ which reads,

$$\gamma(T) \approx C \left(\frac{\tanh\left(\frac{T_B}{T} \sqrt{3(T_B - T)/T_B}\right) \cdot \tanh\left[\frac{T_B}{T} \cdot \tanh\left(\frac{T_B}{T} \sqrt{3(T_B - T)/T_B}\right)\right]}{T \left\{ T \left(1 + \cosh\left(\frac{2T_B}{T} \cdot \tanh\left(\frac{T_B}{T} \sqrt{3(T_B - T)/T_B}\right)\right)\right) - 2T_B \right\}} \right)^2 \quad (3-11)$$

The following discussion shows experimental results of $\gamma(T)$ and corresponding theoretical fits of Eq. (3-11).

3.1.5. TEMPERATURE DEPENDENCE OF THE STRENGTH OF THE TRAINING EFFECT

Fig. 3.3 shows the results of the training effect at various temperatures $5 < T < 120$ K and successful theoretical fits of Eq. (1-17). The theoretical fit provides a fitting

parameter γ that varies systematically with the temperature. Figure 3.6 shows the results obtained from the subsequent fitting procedures of Eq. (1-17) to all data sets $\mu_0 H_{EB}$ vs n involving more than 50 successive hysteresis loops at every temperature. Circles show the resulting γ vs T behavior, which quantifies the temperature dependence of the training effect. The line represents the one parametric best fit of Eq. (3-11) to the data and is a strong confirmation of the qualitative correctness of the theory outlined before.

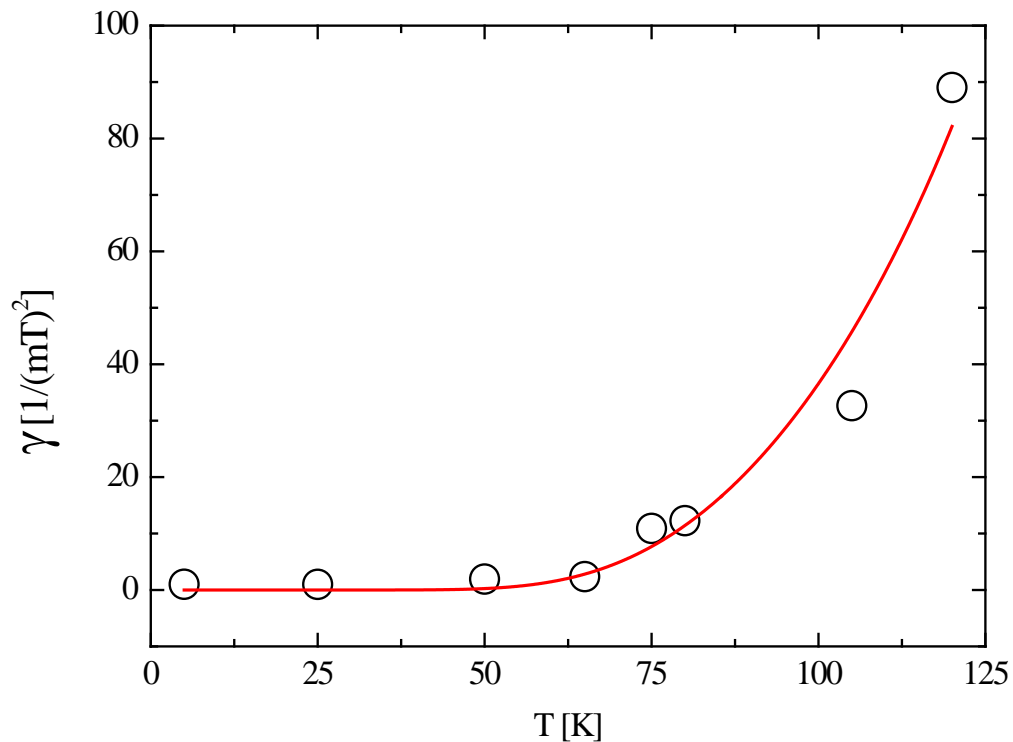


Figure 3.6. γ vs T obtained from fitting procedures of Eq. (1-17) to $\mu_0 H_{EB}$ vs n data for temperatures $5 \leq T \leq 120$ K. The line is a one parameter best fit of Eq. (3-11) to γ vs T .

Note that γ increases with increasing temperature implying small absolute training effects, $\mu_0(H_{EB}(n = cons) - H_{EB}^e)$ at high temperatures, which is also apparent from Fig. 3.3. Note that the value of γ increases continuously until T reaches T_B . However, at T_B the absolute training effect becomes zero due to zero EB for all n . On the other hand, small values of γ occurs at low temperatures that correspond to large absolute training effects which spread over a larger number of cycles. The fit in Fig 3.6 yields $\gamma = 0$ at $T = 0$, which is a special case where the system is frozen where $\mu_0[H_{EB}(n) - H_{EB}(n+1)] = 0$ due to the lack of thermal excitations. Therefore, no change in EB is expected and the system is unable to reach the equilibrium value H_{EB}^e on consecutive hysteresis loops, n . However, this does not mean that the EB field is zero.

In summing up, a phenomenological theory of temperature dependence of training effect in exchange-bias heterostructures is presented. The theory is applied to the training effect in a magnetic Co/CoO heterostructure. Individual training effects are measured by consecutive cycling hysteresis loops at various temperatures $5 \leq T \leq 120$ K. The success of the thermodynamic approach is a strong confirmation of a recently derived implicit sequence of training effect, which allows describing $\mu_0 H_{EB}$ vs n for $n \geq 1$ in diverse systems. It is a challenging task for the future time to find a microscopic theory of the training effect. Even if it turns out that there is no simple unique microscopic theory for the EB effect, the training might be a universal property. The predictions made here allow for further experimental tests. For instance, the relation between the AF interface magnetization and the EB field suggest that γ increases with the square of the FM layer thickness (will be studied in next section of this chapter) and decreases inversely

proportional to the square of the FM interface magnetization. Both parameters are experimentally accessible.

3.2 FERROMAGNETIC THICKNESS DEPENDENCE AND SCALING BEHAVIOR OF THE EXCHANGE BIAS TRAINING EFFECT

The most frequently studied size effect in EB systems is given by the $1/t_{\text{FM}}$ -dependence of the EB field on the FM film thickness t_{FM} .^{10,157,160,161,162} The inverse FM thickness dependence reveals the interface nature of the EB effect and reflects the origin of EB as a competition between the Zeeman energy of the FM layer and AF/FM interface coupling energy. Nevertheless, the detailed microscopic understanding of the interface is still elusive. However, under the assumption of homogeneous magnetization along the FM film normal, the Zeeman energy will increase linearly with t_{FM} independent of the specific nature of the interface coupling energy.

This section of chapter 3 sheds light on the t_{FM} -dependence of the EB training effect and, in particular, its scaling behavior. Training, which describes the decrease of the EB field with subsequently cycled hysteresis loops of the ferromagnet, can be understood in the framework of triggered spin configurational relaxation of the AF pinning layer. This general view includes deviations of the AF spins from their easy axes and, hence, from the AF ground-state of the pinning layer. Recently such deviations and

reorientations of spins between easy axes have been evidenced as a microscopic origin for large training effects and asymmetry in EB in systems like CoO/Co where more than one easy axis exists.^{112,163} Since in this general sense training originates from changes of the spin structure of the AF pinning layer towards its equilibrium configuration, it is not apparent at all that a variation of the FM thickness could affect the EB training effect. Therefore, a closer look reveals the need of studying the FM thickness dependence of the EB training effect.

EB is an interface phenomenon and the EB fields follow $\mu_0 H_{EB} \propto 1/t_{FM}$ dependence. If this simple $1/t_{FM}$ -dependence holds for every individual hysteresis loop of a training sequence according to $\mu_0 H_{EB}(n) \propto 1/t_{FM}$, where n is the hysteresis loop # in a training sequence, then one may conclude that the n -dependent evolution of the AF interface magnetization is independent of t_{FM} . Note, that such a finding is not apparent considering the fact that the antiferromagnet acts on the ferromagnet by changing its coercivity where a counter reaction of some sort has to be expected.^{35,164} In addition, even the simple $1/t_{FM}$ -dependence of $\mu_0 H_{EB}(n)$ leaves a non-trivial fingerprint in the characteristics of the training sequence allowing for a unique cross-check of the recently introduced theoretical approach. Furthermore, this sub-chapter also presents scaling of the crucial parameter involved in the fits of $\mu_0 H_{EB}$ vs. n data and its collapse on a FM thickness and temperature dependent master curve. The latter provides excellent evidence for the universality of underlying phenomenological description of the EB training effect.

3.2.1. PREPARATION OF A COO/CO-WEDGE SAMPLE AND ITS EXPERIMENTAL DETAILS

The deposited Co thin film is a wedge with thickness gradient along the length of the substrate of *c*-plane Al₂O₃. The-state-of-art MBE is used to grow this film. Deposition takes place under ultra high vacuum (UHV) conditions at a base pressure of 5.0×10^{-11} mbar and the substrate is maintained at a temperature of 573 K. An average thickness gradient of 3 nm to 28 nm over 1 cm lateral distance was achieved by partially opening the shutter of the effusion cell and projecting the truncated beam of the profile onto the substrate. Unlike other step wedges where sample growth was controlled by using motored shutter movement attached to the substrate,^{157,160,165} we exploit shutter control of the Co effusion cell allowing for the growth of a “continuous” Co wedge. Although the latter process sounds trivial, in fact it is a very intricate process and requires several attempts to capture only the truncated beam profile on to the substrate.

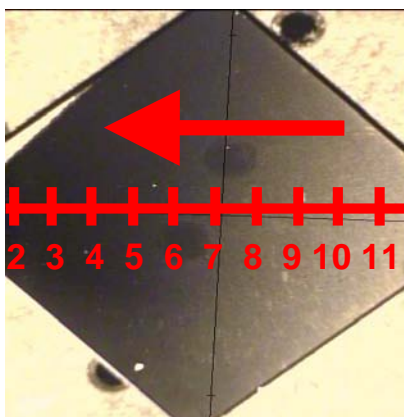


Figure 3.7. A digital photo of the Co wedge shaped thin film. The arrow points in the direction of thickness gradient. The scale defines the position on the sample.

Fig. 3.7 shows an optical micrograph of the sample revealing the lateral change of optical transparency and hence, resembling the thickness gradient of the wedge. The latter is indicated by an arrow. The numbers indicate individual positions, x , of different thicknesses along the wedge.

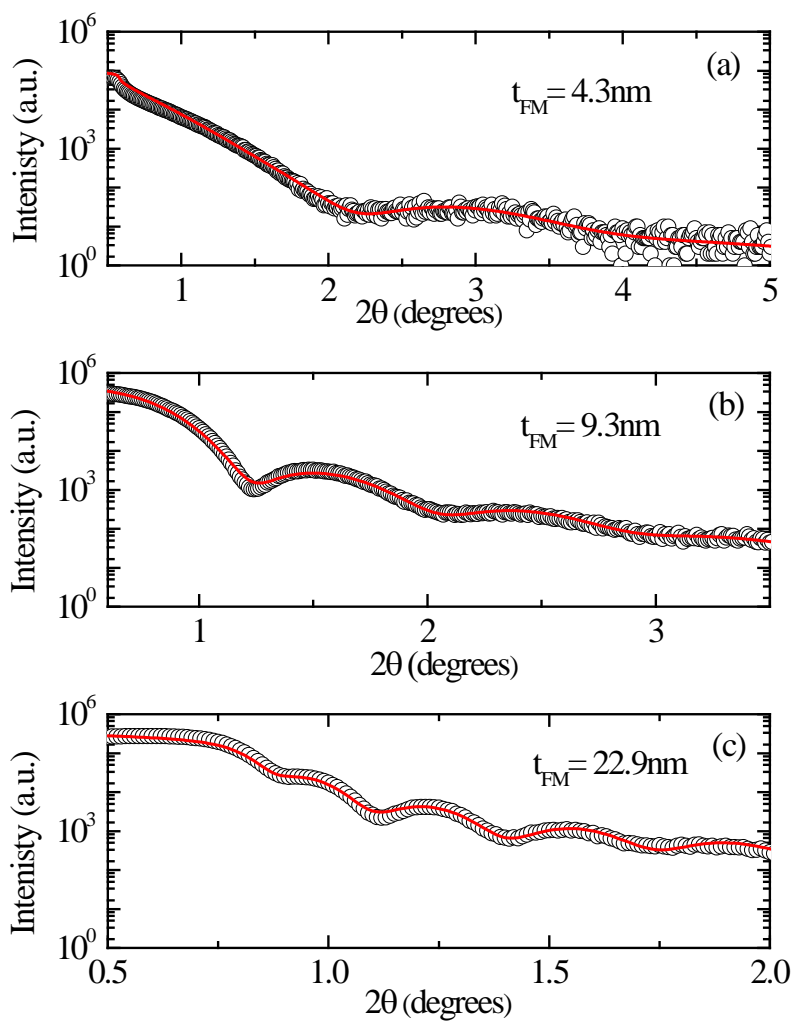


Figure 3.8. Small angle x-ray reflectivity data (circles) for three different thicknesses (a) 4.3 nm, (b) 9.3 nm, and (c) 22.9 nm obtained from best fits (red lines) using the LEPTOS-2 software program.

Local thicknesses at different positions, x , along the sample have been measured by small angle XRR using collimated X-rays with a lateral resolution of about $\delta x \approx 0.5$ mm in the direction of the gradient while the grazing incidence of the X-rays gives rise to a spatial average normal to the gradient. Note that this direction represents constant Co thickness as shown in Fig 3.7 in accordance with the growth technique. Fig. 3.8. (a), (b), and (c) show three typical XRR θ - 2θ scans taken at different positions. Best fits (lines) reveal the thicknesses $t_{FM}(x_1 = 10\text{mm}) = 4.3$ nm, $t_{FM}(x_2 = 6\text{mm}) = 9.3$ nm and $t_{FM}(x_3 = 2\text{mm}) = 22.9$ nm, respectively.

Since the wedge resembles the projected flux profile of the partially closed Co effusion cell onto the sapphire substrate, the local Co thickness is a nonlinear function of the lateral position x . In order to obtain a quantitative relation $t_{FM} = t_{FM}(x)$ which allows for continuous thickness interpolation, the locally measured thickness data are fitted to an empirical profile $t(x)$. The latter has been modeled with the help of a Fermi-type function $t(x) = A / (e^{(x-x_0)/w} + 1)$. It is an empirical approach replacing the cosine law of an ideal point like Knudsen cells where constant flux is realized on spherical surfaces touching the evaporation point.¹⁶⁶ Here, however, we take advantage of the perturbation of the flux induced by a shutter. Collision of Co atoms leaving the cell gives rise to momentum transfer and, hence, to a broadening of the geometrically sharp shadow. The broadening is modeled by the width, w , entering the profile function $t(x)$. The unperturbed Co evaporation rate in the center of the flux profile was monitored by a calibrated quartz crystal and found to be $2t(x_0)/\tau = 0.02\text{nm/s}$. The sapphire substrate has been exposed to the Co evaporation profile for $\tau = 10^4$ sec calibrating $A = 2t(x_0)$ as $A =$

200 nm. The two remaining parameters x_0 and w adjust the onset and steepness of the flux drop from maximum unperturbed flux down to zero flux for $x \gg x_0$. Best fitting yields $x_0 = -6.91$ mm and $w = 4.32$ mm. The result of the best fit is displayed as a line in Fig. 3.9 and an enlarged scale in inset of Fig. 3.9, respectively.

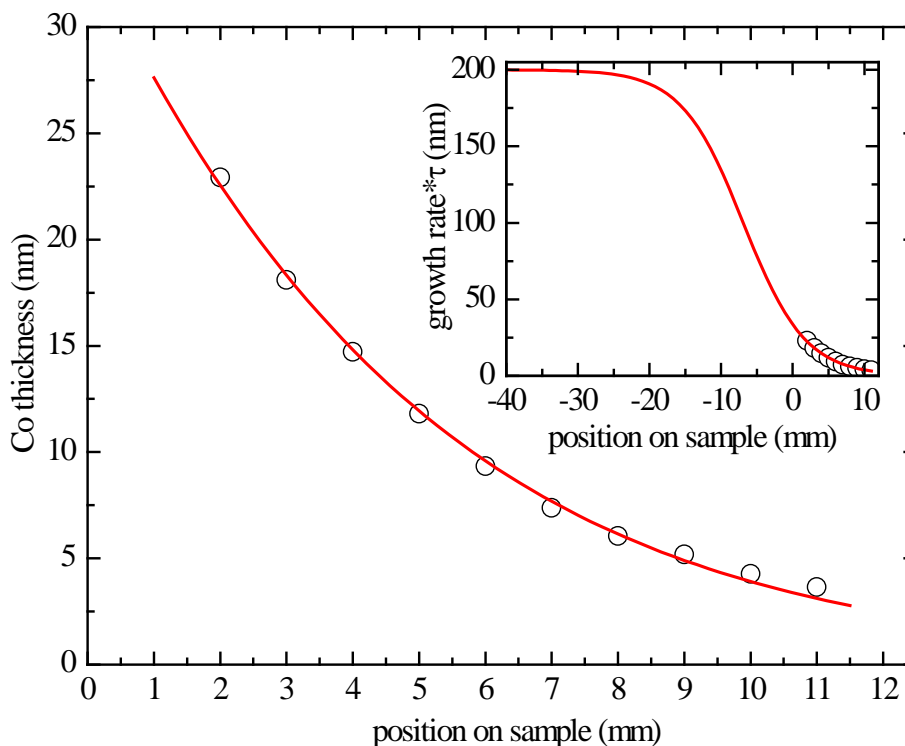


Figure 3.9. Variation of Co thickness with respect to the position, x , on the sample parallel to the thickness gradient. Circles represent local thickness values obtained from x-ray reflectivity. An empirical Fermi-type function is best fitted to the data as shown in red colored line. The inset shows an extrapolation of the empirical Fermi-type flux profile created by the partially shuttered evaporation beam (line) along with the data points (circles).

A constant thickness, $t_{AF} \approx 3$ nm, of naturally formed AF CoO layer has been identified by small angle XRR after atmospheric exposure of the Co wedge. The use of a

single Co wedge ensures that the CoO pinning layer has constant thickness while t_{FM} varies continuously. This has advantages over the preparation of a sequence of individual samples with various Co thicknesses, because the exposure time and various other ill controlled factors influence the thickness of the naturally formed CoO layer. Since we study the t_{FM} -dependence of the EB and its training effect, a constant AF pinning layer thickness is a necessary condition in order to avoid fluctuations in $\mu_0 H_{EB}$ induced by variations in t_{AF} .

Detailed structural characterization of the wedge CoO/Co sample has been performed by θ - 2θ wide angle XRD and pole figure scans using Rigaku D/Max-B diffractometer and Bruker-AXS D8, respectively.

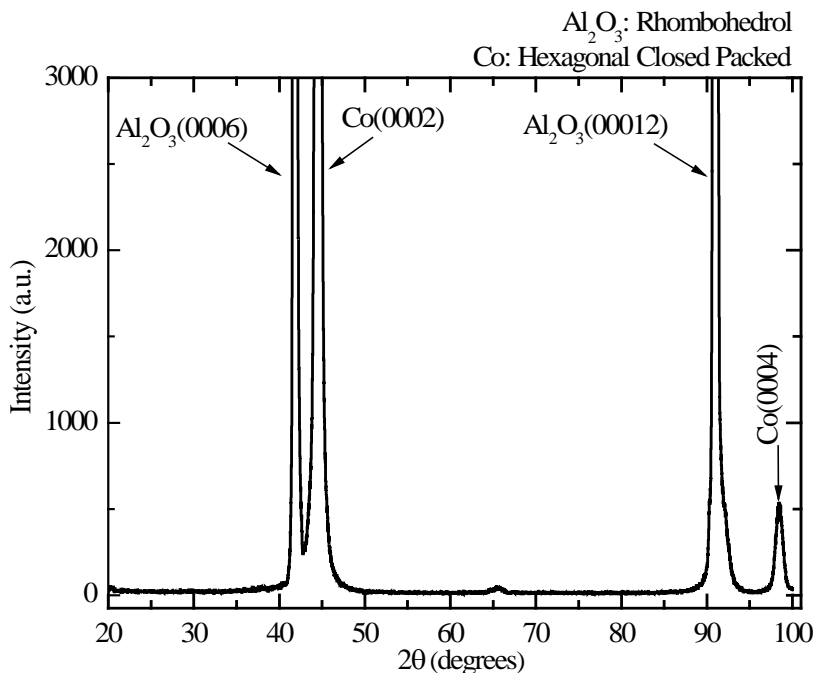


Figure 3.10. X-ray diffraction pattern of the Co/CoO heterostructure deposited on *c*-Al₂O₃ substrate. Single-crystalline peaks of hexagonal Co film.

The XRD pattern of Fig. 3.10 reveals a single-crystalline hexagonal Co film with (0002)-oriented growth on the *c*-Al₂O₃ substrate similar to the results found from deposition on the α -plane of sapphire in Ref. [167]. The corresponding pole figure scan in Fig. 3.11 evidences the six-fold symmetry of the Co film confirming hexagonal growth.

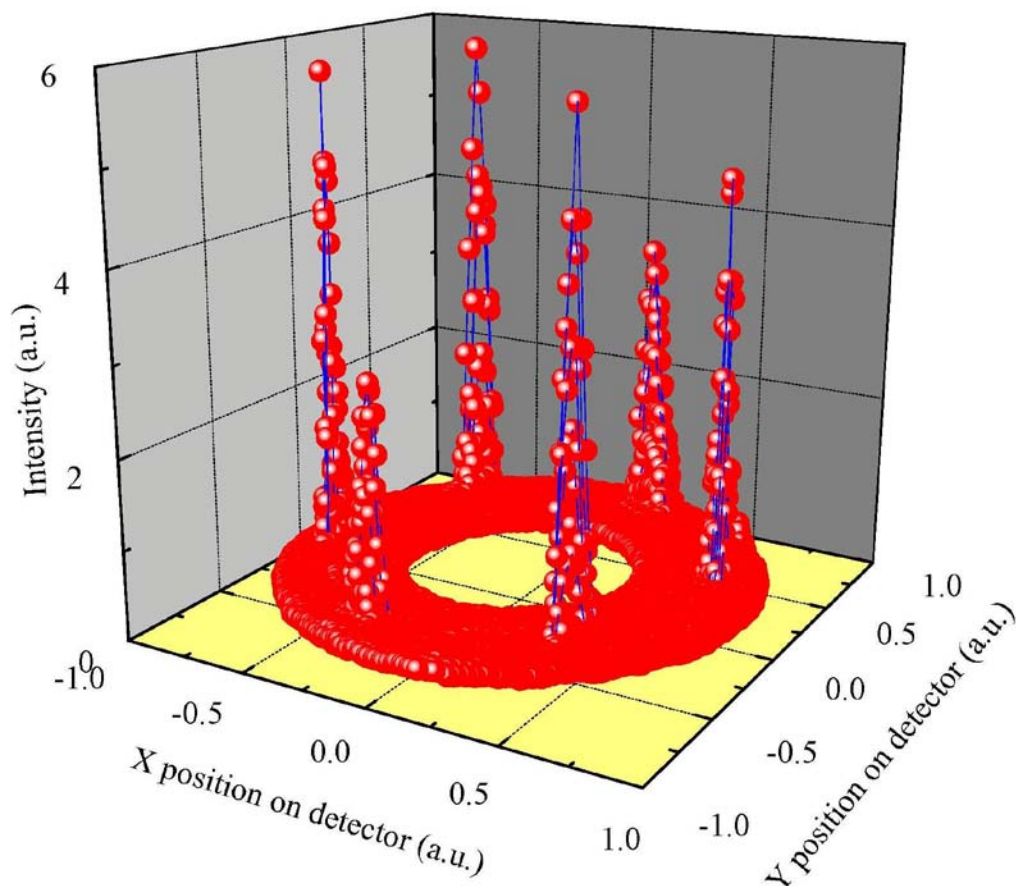


Figure 3.11. 3D pole figure scans performed at $2\theta = 44.2^\circ$ of Co (0002). Peak intensities separated by 60° confirm the hexagonal in-plane symmetry of the Co film.

The pole figure scans were performed at various Co thicknesses along the wedge keeping $2\theta = 44.2^\circ$ of Co (0002) fixed using the 2D detector (HI-STAR). They all reveal identical hexagonal symmetry.

3.2.2. MAGNETIC CHARACTERIZATION VIA LOCAL MOKE

Longitudinal magneto-optical Kerr effect (LMOKE) has been employed to measure the local magnetic hysteresis loops along the thickness gradient of a CoO/Co wedge sample. Magnetic fields $-0.25T \leq \mu_0 H \leq 0.25T$ are applied parallel to the sample surface. LMOKE loops were recorded at various temperatures, $20 \text{ K} \leq T \leq 70 \text{ K}$ after cooling the heterostructure from $T = 320 \text{ K}$ in the presence of in-plane magnetic field of $0.25T$. The *s*-polarized incident laser beam of wavelength $\lambda = 670 \text{ nm}$ makes an angle of about 20° with respect to the normal of the sample surface. Glan-Thompson polarizers are used for polarizing and analyzing the light. A lens of focal length $f = 350 \text{ mm}$ and diameter of $D = 25 \text{ mm}$ is utilized here to focus the light beam onto the particular position on sample surface. The reflected beam is periodically modulated between left and right circularly polarized light by the photo-elastic modulator (PEM). We have used an optimized MOKE setup “configuration 1.1” (based on discussion from 2.2.4. in chapter 2) for all magnetic studies here.

The focused laser beam is scanned across the wedge shaped Co film probing local hysteresis loops. The scan takes place parallel to the thickness gradient. The local thickness is identified from readings of the respective laser spot positions on an mm-

ruler attached to the sample. The diameter of the laser spot is diffraction limited according to the Rayleigh criterion $\Delta l = 1.22 f \lambda / D \approx 11 \mu\text{m}$. Taking into account the limited spatial resolution of the X-ray beam while measuring thicknesses as well as reading errors in the local laser spot position due to parallax, outshining of the airy disk and inaccuracy in the scale attached to the sample we estimate a total uncertainty in the position reading to be $\Delta x < 1 \text{ mm}$. This uncertainty gives rise to a relative thickness uncertainty. With $x_0 = -6.91 \text{ mm}$ and $w = 4.32 \text{ mm}$, $e^{(x-x_0)/w} \gg 1$ holds for all positions $2 \text{ mm} < x < 11 \text{ mm}$ and, hence, $\Delta t / t$ is estimated according to $\Delta t / t = \left| \partial t / \partial x \right| \Delta x / t \approx \Delta x / w \lesssim 23\%$. However, this uncertainty in the Co thickness is corrected to a large extent with the help of the scaling plots as outlined subsequently in the next section 3.2.3.

3.2.3. RESULTS OF MAGNETIC MEASUREMENTS

As we discussed before the investigation of the EB training effect requires initialization of the EB prior to every set of subsequently cycled hysteresis loops. A well defined EB initialization takes place via field cooling the sample from $T=320 \text{ K} > T_N(\text{CoO})=291 \text{ K}$ to target temperature in the presence of an in-plane applied magnetic field of $\mu_0 H=0.25 \text{ T}$. The latter exceeds the saturation field of our Co wedge. Note that the easy axis of Co films with thicknesses $3 \text{ nm} < t_{\text{FM}} < 28 \text{ nm}$ is always in-plane.^{168,169,170} After EB initialization a fixed temperature between $20 \text{ K} < T < T_B = 96.8 \text{ K}$ is stabilized with $\delta T < 10 \text{ mK}$ precision in a closed cycle optical cryostat. Measurements of the local

training effect were performed at a fixed position x by recording 10 subsequently cycled longitudinal Kerr loops in a field interval $-0.25 T < \mu_0 H < 0.25 T$. The EB shift $\mu_0 H_{EB} = \mu_0 (H_{c1} + H_{c2}) / 2$ of the hysteresis loop is determined for each individual loop from the coercive fields $H_{c_{1,2}}$ by linear best fits in the region of zero magnetization $M(H_{c_1}) = M(H_{c_2}) = 0$.

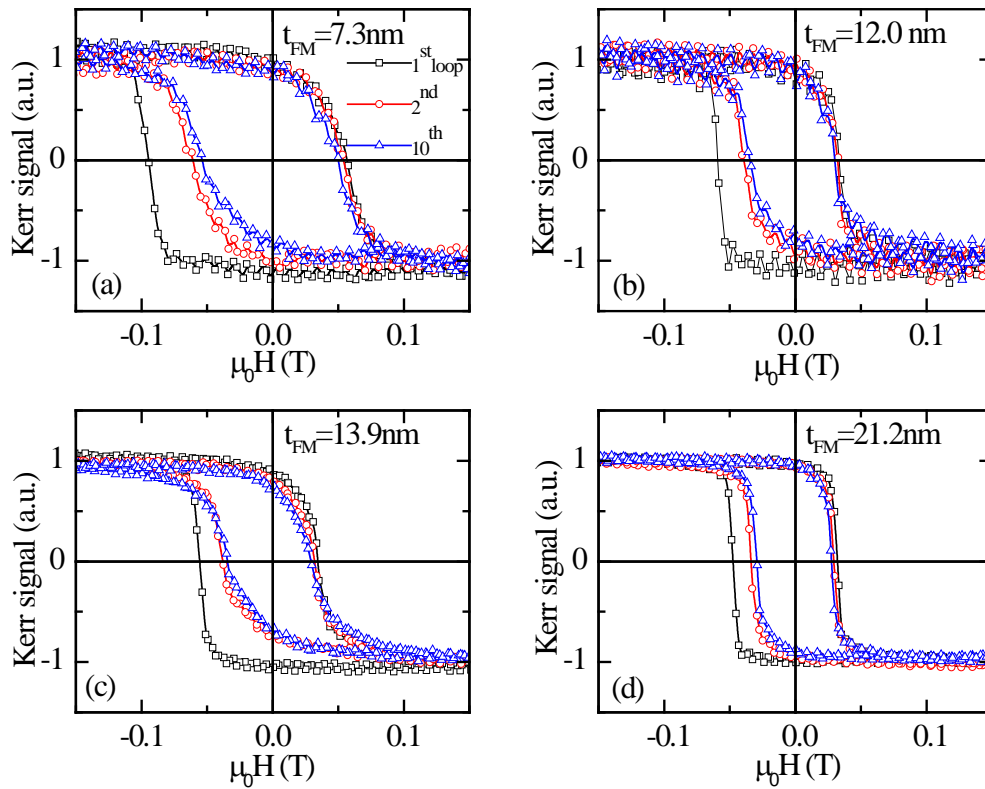


Figure 3.12. Normalized Kerr magnetic hysteresis loops measured at $T=50K$ within a training sequence: first loop (squares), second loop (circles), and tenth loop (triangles) for four different Co thicknesses, (a) 7.3 nm, (b) 12.0 nm, (c) 13.9 nm, and (d) 21.2 nm.

Figure 3.12 (a)-(d) show the hysteresis loops of the 1st (squares), 2nd (circles) and 10th (triangles) for CoO(\sim 3nm)/Co(t_{FM}). Measurements take place at various positions corresponding to the nominal thicknesses $t_{\text{FM}} = 7.3, 12.0, 13.9$ and 21.2 nm at $T=50$ K after EB initialization, respectively. Fig. 3.12 shows a pronounced EB and its accompanied training effect as well change in the loop width $\mu_0 H_c = \mu_0(H_{c2} - H_{c1})$. Fig. 3.13 (a)-(d) shows decay of EB with loop number, $\mu_0 H_{\text{EB}}$ vs. n , resulting from Fig 3.12, at $T=50$ K for all four different nominal thicknesses.

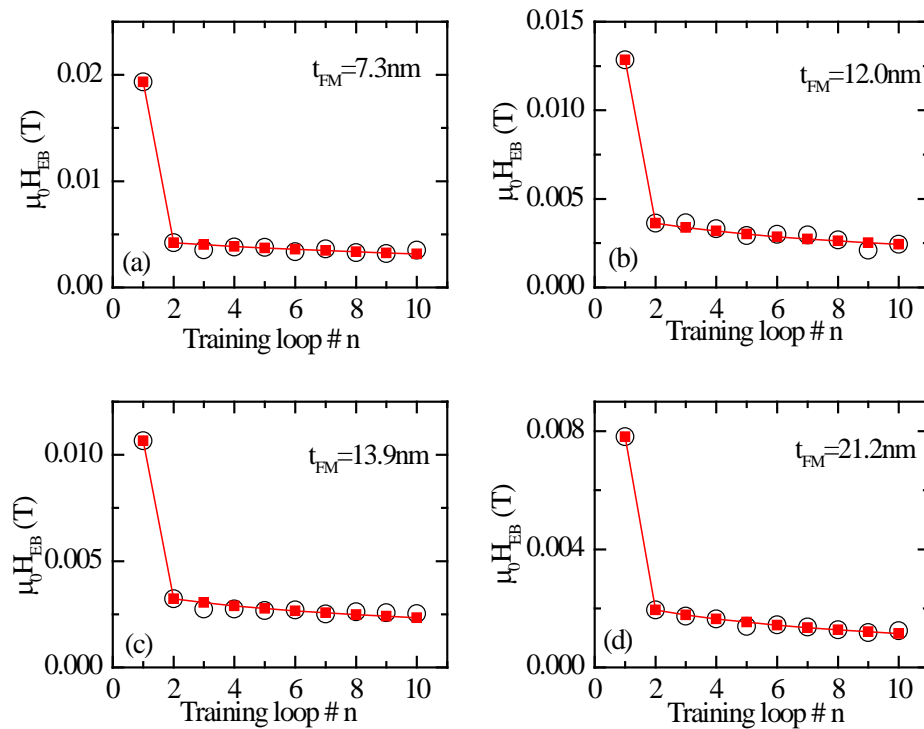


Figure 3.13. Training effect of the exchange bias $\mu_0 H_{\text{EB}}$ vs. loop# n (circles) and the corresponding best fits according to Eq. (1-17) (squares) for the same Co thicknesses as displayed in Fig. 5 measured at $T=50$ K. Lines are guide to the eye only.

Circles are the experimental data while red colored squares are obtained from the best fit of the implicit Eq. (1-17). The lines have no physical meaning; they are just eye guiding lines. From Fig. 3.13, it is obvious to see approximately 80% of the training dynamics takes place between the first and second training loops while the remaining 20% decay gradually with increasing number of loops. In addition to the above displayed data at $T = 50$ K, training sequences of 10 subsequent loops have been measured and best fitted with Eq. (1-17) for all nominal Co thicknesses $t_{FM} = 7.3, 12.0, 13.9$ and 21.2 nm at other various temperatures $T = 20, 27, 35, 43, 57, 65$ and 70 K, respectively. The experimental training sequence hysteresis loops for the other temperatures follow similar manners as $T = 50$ K (not shown).

In Fig 3.14 (a), we have plotted EB fields, $\mu_0 H_{EB}(n=1)$ vs. T , of the first loop of a respective training sequence for all measured thicknesses, t_{FM} , and temperatures, T . This graph represents the behavior of the EB with different temperatures and thicknesses.

Apparently, but in the absence of a proper theory, the individual data sets, $\mu_0 H_{EB}(n=1, t_{FM} = 7.3 \text{ nm})$ vs. T (squares), $\mu_0 H_{EB}(n=1, t_{FM} = 12.0 \text{ nm})$ vs. T (circles), $\mu_0 H_{EB}(n=1, t_{FM} = 13.9 \text{ nm})$ vs. T (up triangles) and $\mu_0 H_{EB}(n=1, t_{FM} = 21.2 \text{ nm})$ vs. T (down triangles) follow a linear temperature dependence, respectively. The lines in the graph are the best linear fits to the experimental data.

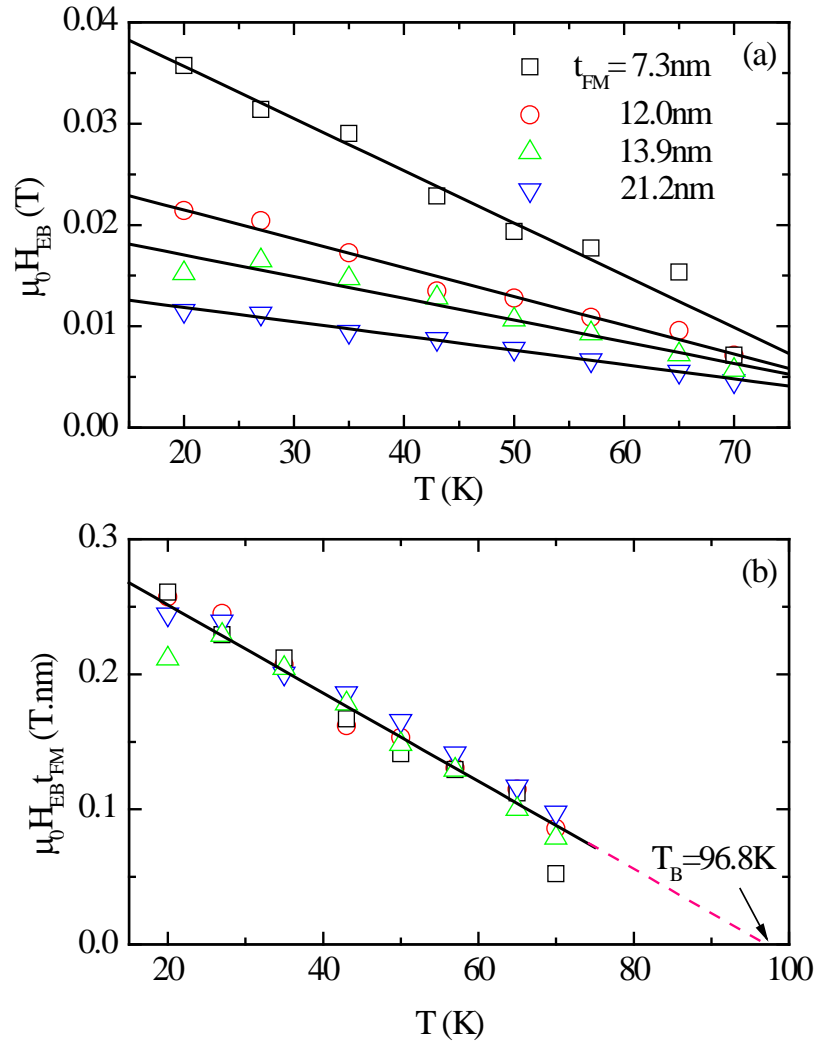


Figure 3.14. (a) Variation of exchange bias $\mu_0 H_{EB}$ vs. T for Co thickness values 7.3 nm (squares), 12.0 nm (circles), 13.9 nm (up triangles), and 21.2 nm (down triangles). The lines are the best linear fits. (b) The master line $\mu_0 H_{EB} t_{FM}$ vs. T with corresponding scaled data and the blocking temperature $T_B = 96.8$ K marked by an arrow at the intercept of the master line with the T -axis.

In accordance with the Meiklejon Bean expression (1-7), $\mu_0 H_{EB}(n=1)$ follows a $1/t_{FM}$ -dependence. Eq. (1-7) expresses the relation of the EB field to a phenomenological coupling J between the FM and AF interface magnetization S_{FM} and

S_{AF} , and the saturation magnetization M_{FM} of the FM film of thickness t_{FM} . Therefore, scaling according to $\mu_0 H_{EB}(n=1) \times t_{FM}$ vs. T as shown in Fig. 3.14 (b) is naturally expected. Since each individual data set follows empirically a linear T -dependence, data collapse takes place on a virtually linear master curve. The line shows a best fit to the scaled data $\mu_0 H_{EB}(n=1) \times t_{FM}$ vs. T with slope $a = -0.0387$ T nm/K and y-axis intercept $b = 3.3697$ T nm. Its extrapolation towards $\mu_0 H_{EB}(n=1) \times t_{FM} = 0$ determines the blocking temperature $T_B = 96.8$ K, where EB completely disappears. Furthermore, we plotted the scaled graph of EB with respect to the FM thickness, t_{FM} , for all possible temperatures. The results are shown in Fig. 3.15.

Fig. 3.15 (a) shows $\mu_0 H_{EB}(n=1)$ vs. t_{FM} for $T=20$ (squares), 27 (circles), 35 (up triangles), 43 (down triangles), 50 (diamonds), 57 (left triangles), 65 (right triangles) and 70K (hexagons), respectively. As expected, the individual data sets follow the $1/t_{FM}$ -dependence of Eq. (1-7). The lines are best fits to Eq. (1-7) where $P_1 = -JS_{FM}S_{AF}/M_{FM}$ becomes the temperature dependent fitting parameter for each data set. Recalling the fitting parameters a and b of the linear master curve of Fig. 3.14 (b) we create a data collapse according to the scaling $\mu_0 H_{EB}(n=1)/(aT+b)$ vs. t_{FM} . Fig. 3.15 (b) shows the result of this scaling which reflects the $1/t_{FM}$ -dependence of the individual data sets. The master curve of the scaled $\mu_0 H_{EB}(n=1)/(aT+b)$ vs. t_{FM} data is again obtained by a best fit to $g(t_{FM}) = g_0/t_{FM}$ where the unit free fitting parameter reads $g_0 = 0.1051 \pm 0.0025$.

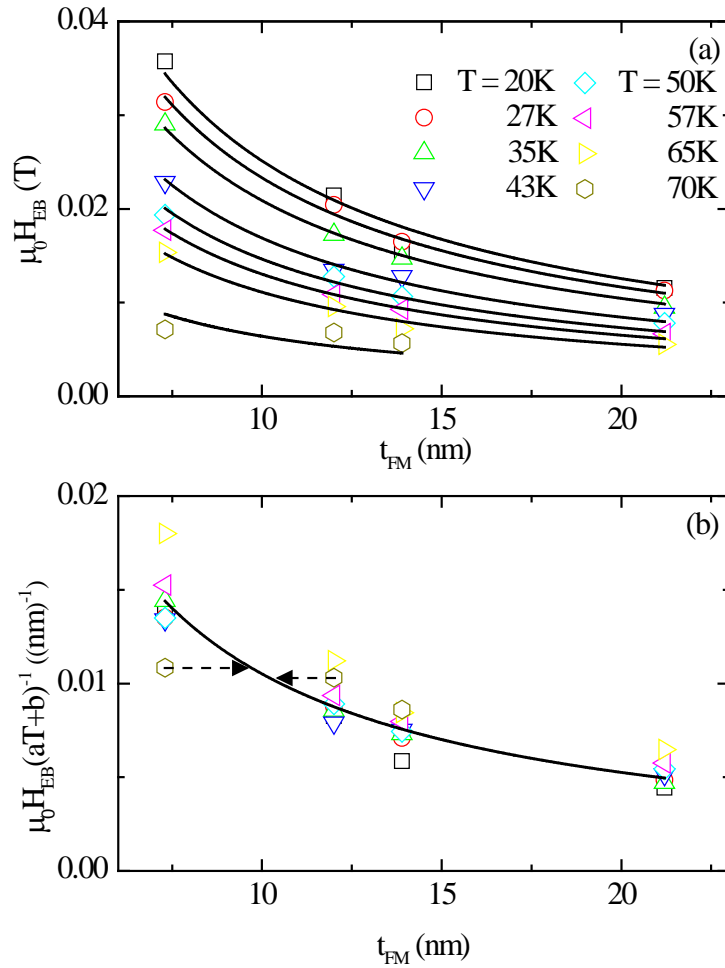


Figure 3.15. (a) Variation of exchange bias $\mu_0 H_{EB}$ vs. ferromagnet thickness t_{FM} at different temperatures. The lines are best fits to Eq. (1-7). (b) Scaled data $\mu_0 H_{EB} \times (aT+b)^{-1}$ vs. t_{FM} (for details regarding a and b see text). The master curve is represented by a best fit (line) of a Meiklejon Bean-type formula to the scaled data. Arrows provide a geometrical interpretation of the thickness correction assigning scaled thickness values to the nominal thicknesses.

As we discussed before, the nominal thicknesses t_{FM} suffer from experimental uncertainties $\Delta t_{FM} / t_{FM}$ of up to 23%. However, the master curve $g(t_{FM})$ of Fig. 3.15 (b) allows for the determination of scaled/corrected thicknesses, t_{FM}^{scaled} . They are to a large extent free from the experimental errors originating from Δx uncertainties. Considering

the quality of our Kerr magnetic loops it is reasonable that the statistical deviations of the data points from the master curve originate from errors in t_{FM} while errors in the EB fields of the first loops are insignificant. Under this consideration t_{FM}^{scaled} is obtained from the relation $g_0 / t_{FM}^{scaled} = \mu_0 H_{EB}(n=1, t_{FM}) / (aT + b)$. Geometrically, this correction procedure describes a shift of the data points along the t_{FM} -axis onto the master curve. This procedure is indicated in Fig. 3.15 (b) by horizontal arrows for two exemplary data points of $T=70$ K (hexagons). The resulting relative corrections $\left| t_{FM}^{scaled} - t_{FM} \right| / t_{FM}$ are within the expected maximum error $\Delta t / t \approx \Delta x / w = 23\%$ associated with the Δx uncertainties. Also, we did confirm the correctness of the nominal thicknesses with the help of a 3D graph of EB as shown below.

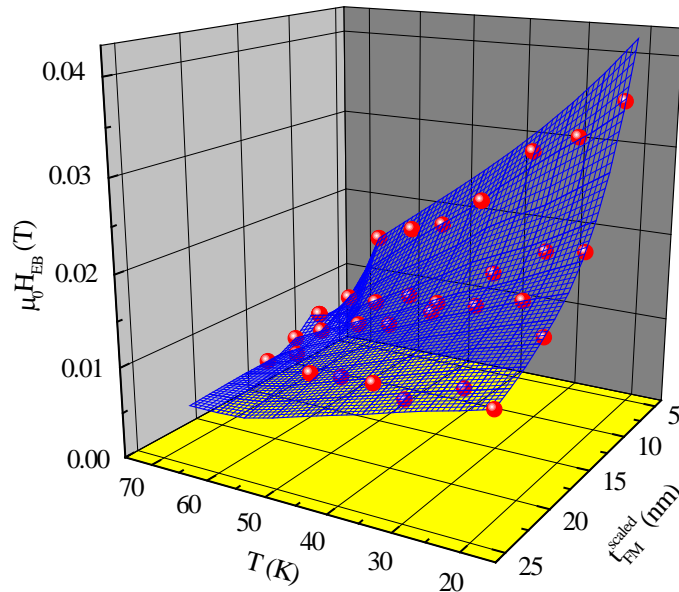


Figure 3.16. 3D plot illustrating the exchange bias $\mu_0 H_{EB}$ vs. (t_{FM}^{scaled}, T) . The spheres are the experimental data and the interpolating grid results from Renka-Cline gridding algorithm.

Fig. 3.16 shows a 3-dimensional plot of $\mu_0 H_{EB}(n=1)$ vs. (t_{FM}^{scaled}, T) for all scaled thicknesses and temperatures. All data points fall on a smoothly curved surface indicating that $\mu_0 H_{EB}(n=1)$ decreases with increasing temperature as well as FM thickness. The smoothness of the interpolating surface indicates that in fact the thickness correction effectively eliminates the errors in the nominal thicknesses t_{FM} . Note, that due to the scaling procedure $t_{FM} \rightarrow t_{FM}^{scaled}$ the $\mu_0 H_{EB}(n=1)$ -data points do not follow iso-thickness lines anymore.

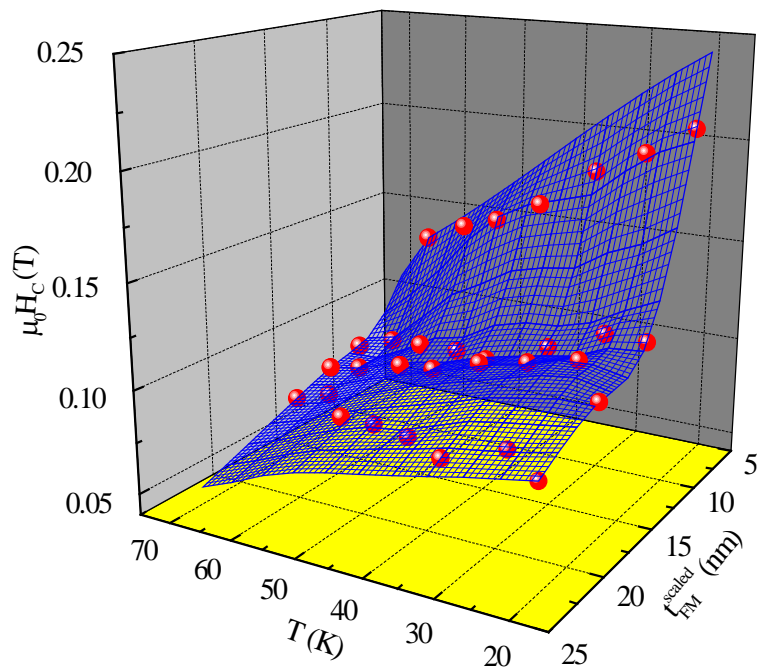


Figure 3.17. 3D plot illustrating the exchange bias $\mu_0 H_C$ vs. (t_{FM}^{scaled}, T) . The spheres are the experimental data and the interpolating grid results from Renka-Cline gridding algorithm.

Fig. 3.17 shows a similar 3-dimensional plot for coercivity $\mu_0 H_c (n=1)$ vs. (t_{FM}^{scaled}, T) , of the first loop of a respective training sequence for all scaled thicknesses and temperatures. The loop width or coercivity is known to increase with decreasing temperature below the EB blocking temperature T_B . Qualitatively this behavior can be understood due to the drag effect the FM interface spins experience on magnetization reversal. In addition, Fig. 3.17 shows an increase of the coercivity with decreasing FM thickness. The decrease in thickness of FM increases the surface-to-volume ratio of the magnetic moment in the FM. Therefore, the effective coupling at the interface between FM and AF enhances which ultimately increases the coercivity on both left and right branches of the FM hysteresis loop. Recently, Scholten *et al.* provided a mean-field solution for the coercivity change in EB heterolayers. It reads

$$\mu_0 H_c(t_{FM}) = \frac{\mu_0 H_c^\infty + J^2 \chi / t_{FM}}{1 + J \chi / t_{FM}} \quad (3-12)$$

where $\mu_0 H_c^\infty = \mu_0 H_c(t_{FM} \rightarrow \infty)$ is the FM bulk coercivity and χ is the temperature dependent magnetic susceptibility of the AF layer at the interface. Individual best fits of Eq. (3-12) to $\mu_0 H_c$ vs. t_{FM}^{scaled} at constant temperature (not shown) indicate $J \chi / t_{FM} \ll 1$ and $\mu_0 H_c^\infty \ll \mu_0 H_c(t_{FM})$ for all studied thicknesses. Therefore an approximate $1/t_{FM}$ -behavior is expected not only for $\mu_0 H_{EB}(n=1)$ but also for $\mu_0 H_c(n=1)$ vs. T . The latter is consistent with the intuitive picture that the coercivity enhancement in EB system is an

interface effect. $1/t_{FM}$ -dependence and more general $(1/t_{FM})^\alpha$ behavior of $\mu_0 H_c(t_{FM})$ has been observed in various EB systems.^{66,}

From Eq. (3-12) and its successful application to the $\mu_0 H_c$ vs. (t_{FM}^{scaled}, T) data it is apparent that the thickness dependence of the FM loop width is related to the AF interface susceptibility. Hence, as a counter effect, one might expect that the AF interface susceptibility/magnetization and, with it, the EB training effect depends on the FM film thickness in a non-trivial $1/t_{FM}^{scaled}$ -manner. Subsequently we evidence, however, that the training effect in our CoO/Co samples reflects only the explicit $1/t_{FM}^{scaled}$ -dependence of Eq. (1-7) implying that the S_{AF} vs. n does not or only insignificantly depend on t_{FM}^{scaled} . We evidence this statement later in section (3.2.4) with the help of the recently introduced implicit sequence [Eq. (1-17)] for the EB training effect.

3.2.4. SCALING OF THE STRENGTH OF THE TRAINING EFFECT

We have plotted a 3-dimensional graph of the characteristic decay rate γ as a function of t_{FM} and T to get a glimpse of the overall γ evolution.

Fig. 3.18 shows a 3-dimensional plot of the crucial fitting parameter γ vs. (t_{FM}^{scaled}, T) . In section 3.1.4, we have derived a mean-field expression for the temperature dependence of γ .

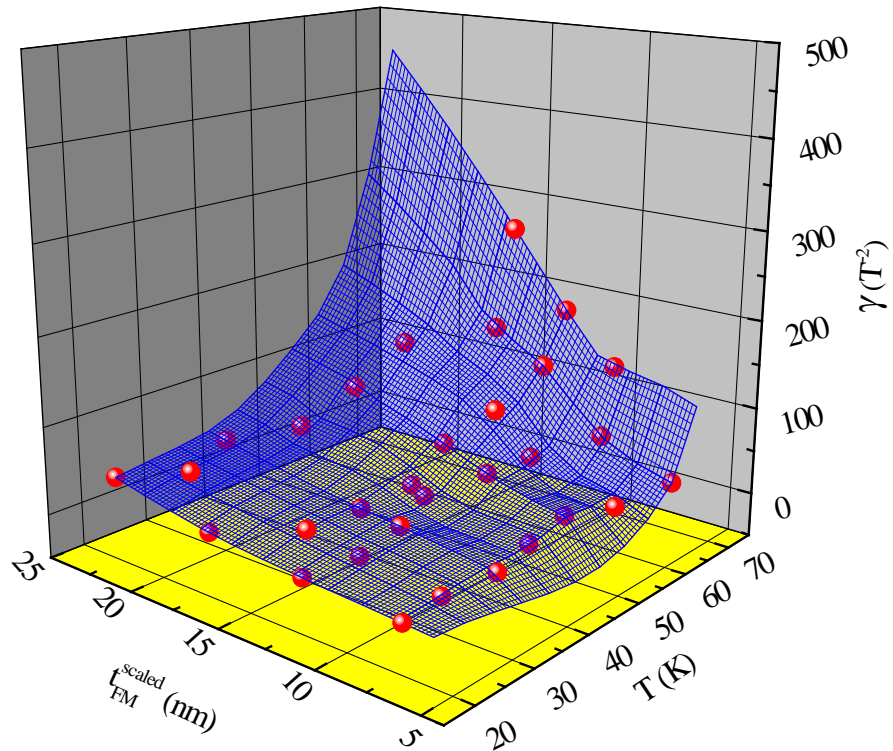


Figure 3.18. 3D plot illustrating fitting parameter γ vs. (t_{FM}^{scaled}, T) . The γ -values are obtained from best fits of the training data to Eq. (1-17). The spheres are the experimental data and the simulated grid results from Renka-Cline gridding algorithm.

In accordance with this result the iso-thickness lines γ vs. T show an increase of γ with increasing temperature (as shown Fig. 3.5). At the same time, the isotherms follow a $\gamma \propto (t_{FM}^{scaled})^2$ behavior. This can be easily seen by substituting MB expression of Eq. (1-7) into implicit expression Eq. (1-17)

Eq. (1-7) reads $H_{EB}(n) = -\frac{JS_{FM}}{\mu_0 M_{FM} t_{FM}} S_{AF}(n)$ and

Eq. (1-17) reads $\gamma = -\frac{\mu_0(H_{EB}(n+1) - H_{EB}(n))}{[\mu_0(H_{EB}^e - H_{EB}(n))]^3}$,

By substituting Eq. (1-7) into Eq. (1-17), we obtain

$$\gamma = (t_{FM}^{scaled})^2 \left(\frac{M_{FM}}{\mu_0 JS_{FM}} \right)^2 \frac{(S_{AF}(n+1) - S_{AF}(n))}{(S_{AF}^e - S_{AF}(n))^3} \propto (t_{FM}^{scaled})^2 \quad (3-13)$$

where S_{AF}^e is the quasi-equilibrium AF interface magnetization achieved in the limit

$n \rightarrow \infty$. Note, $\gamma \propto (t_{FM}^{scaled})^2$ behavior from Eq. (3-13) suggesting a scaling plot $\gamma / (t_{FM}^{scaled})^2$

vs. T . Fig. 3.19 displays this scaling plot which is the essence of our study here. Within the error bars perfect data collapse onto a master curve is achieved. The line is a single parameter fit of Eq. (3-11) using the fixed blocking temperature $T_B=96$ and the error bars are calculated from

$$\Delta \left(\frac{\gamma}{(t_{FM}^{scaled})^2} \right).$$

The fact that data collapse is achieved on the basis $\gamma \propto (t_{FM}^{scaled})^2$ implies

$\mu_0 H_{EB}(n) \propto 1/t_{FM}^{scaled}$ and, therefore, $S_{AF}(n)$ are independent of t_{FM}^{scaled} [according to Eq.

(1-7), (1-17) and Eq. (3-13)]. In other words, $\gamma \propto (t_{FM}^{scaled})^2$ is a direct consequence of

$S_{AF}(n)$ being independent of t_{FM}^{scaled} . It is not transparent from the beginning until it has been proven now.

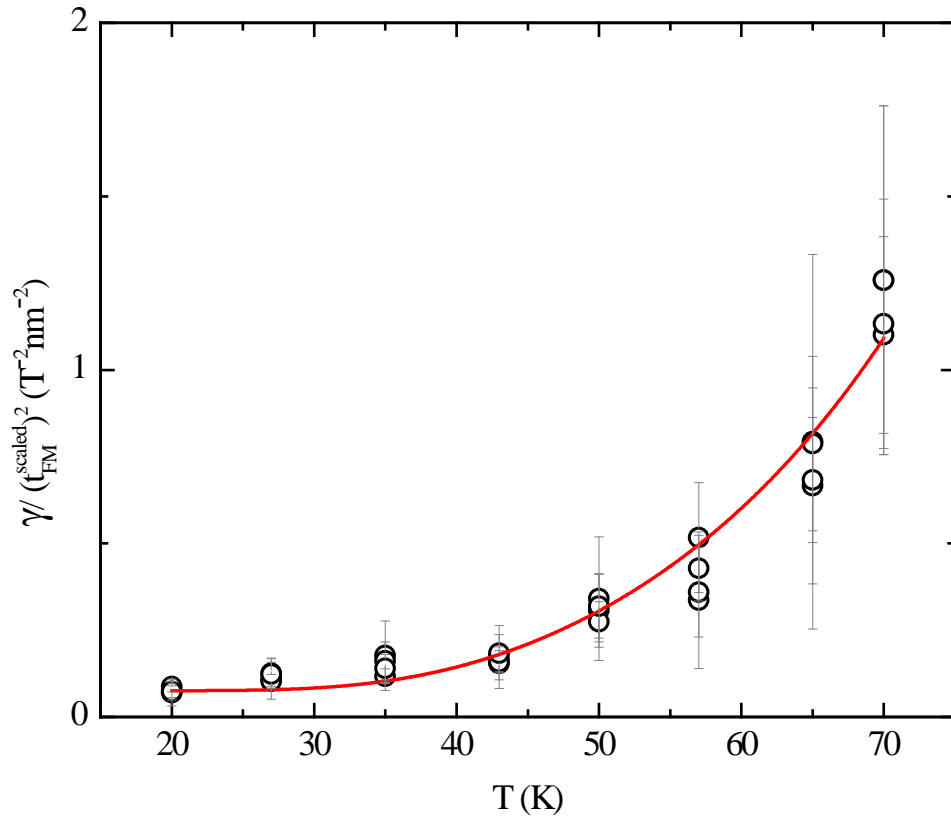


Figure 3.19. Scaling plot $\gamma / (t_{FM}^{scaled})^2$ vs. T . The line represents a best fit of the mean-field result for the temperature dependence of γ to the data (circles). The error bars reflect the maximum deviations of γ related to thickness fluctuations.

Note in addition that the $(t_{FM}^{scaled})^2$ -scaling of γ is a strong evidence for the validity of the underlying phenomenological theoretical approach. The latter is based on triggered relaxation of the pinning layer towards quasi-equilibrium. The dynamics of this triggered relaxation process is controlled via a discretized Landau-Khalatnikov equation

involving the free energy difference $\Delta F \propto (S_{AF}(n) - S_{AF}^e)^4$ between S_{AF}^e and $S_{AF}(n)$ for a given loop n . The functional form of the free energy involving the fourth power of the interface magnetizations gives rise to the functional form of the implicit Eq. (1-17) with the cubic term on the right hand side. Note, that only that particular cubic term on the right side of the expression of Eq. (1-17) provides $\gamma \propto (t_{FM}^{scaled})^2$. This is indeed a remarkable evidence for the underlying structure of the free energy.

In summary, we have studied scaling behavior of the exchange bias training effect on the FM film thickness and temperature in a CoO/Co-wedge heterostructure. The study is partially motivated by the observed entanglement between the coercivity of the FM film, its thickness dependence and its relation with the AF interface susceptibility. A possible change in the FM thickness onto the AF interface magnetization leaves, however, no fingerprint in the exchange bias training effect. This is evidenced by a detailed scaling analysis showing that each individual exchange bias field within a training sequence resembles the same well-known inverse thickness dependence on the FM film thickness. This finding implies, however, that the evolution of the AF interface magnetization is independent of the FM film thickness. Nevertheless, training of the absolute exchange bias fields shows a FM thickness dependence entering the corresponding theory in a non-trivial manner. Scaling behavior of the crucial fitting parameter involved in the latter provides unprecedented evidence for the underlying phenomenological approach based on discretized Landau-Khalatnikov dynamics.

CHAPTER 4

ANTIFERROMAGNETICALLY COUPLED HARD/SOFT FERROMAGNETIC BILAYERS

The hard/soft FM bilayers experience coupling through RKKY (Ruderman-Kittel-Kasuya-Yosida) interaction at their interface. In this chapter, I present experimental results on this interface coupling between hard and soft FM layers. I also present temperature dependent studies of the interface coupling phenomenon and its aging behavior. The latter is described with the help of a phenomenological theory based on Landau-Khalatnikov approach. Furthermore, I present dynamical enhancement of the soft layer hysteresis loop in the vicinity of the hard layer by increasing sweep rates of the applied magnetic field.

4.1 SPECIFIC SAMPLE PROPERTIES

It has been shown that the magnetic coupling at the interface between a ferromagnet and an antiferromagnet can generate exchange bias effect. The EB phenomenon was originally discovered more than 50 years ago by Meiklejohn and Bean.^{1,2} Since then the EB effect has been extensively observed in a vast variety of systems including AF/FM and FM/ferrimagnetic thin-film heterostructures, AF/FM core shell nanoparticles, FM precipitates in antiferromagnet and spin glass matrices, and spin

valves; however, the details of its origin is still under debate.^{20,105,171} Therefore, there is a need of an alternative system where not only microscopic details of the EB are understood but also a simple theory can be developed which can explain the phenomenon of EB and also its accompanying training effect.

Under these lines, we considered coupled bilayers of hard and soft FM films, very similar to exchange-spring magnets,^{172,173,174,175} that follow the strategy of conventional exchange bias.^{176,177} Here, the FM hard layer (HL) serves the purpose of the pinning layer, which is brought into a pre-conditioned state similar to the AM pinning layer. A FM soft layer (SL) is placed in the vicinity of HL that works as actual switchable pinned layer similar to the FM layer in conventional systems. To accomplish the effect of EB, both hard and soft layers need to be magnetically coupled. This coupling has to be strong enough to produce a considerable effect, but cannot be so strong that the individual character of each layer vanishes. Such an intermediate coupling strength can be realized by using the AF-interlayer exchange coupling.¹⁷⁸ This bilayer structure has the advantage that the switching field and temperature range is much more accessible in comparison to conventional exchange bias systems. Antiferromagnetically coupled HL/SL bilayers are not only important in magnetic recording technology but can also be used as model systems to study EB and its related effects.^{112,179,180} HL/SL systems have several advantages over conventional AF/FM systems. For example, a FM pinning layer provides unique experimental access to the change in its magnetization state. In addition, the dependence of the bias field on the pinning layer magnetization can be directly measured by simple magnetometry like AGFM.^{179,180} On the other hand, AF materials are naturally inert to applied magnetic fields which limit the control of the AF domain state.

Furthermore, setting the EB state typically requires a field-cooling procedure in AF/FM bilayers, which makes a high temperature processing necessary for room-temperature devices. The situation is different when the pinning layer couples strongly to an applied magnetic field as it does in HL/SL heterostructures.

In the HL/SL bilayer systems, the HL pins the magnetic SL through RKKY interface coupling and shifts its hysteresis loops along the magnetic field axis. The shift is quantified by the bias field, $\mu_0 H_B$. We label this shift as $\mu_0 H_B$ to distinguish it from conventional exchange bias, $\mu_0 H_{EB}$. In the case of AF coupling, $\mu_0 H_B$, is positive when the HL magnetization is set in a positive magnetization state and vice versa when the HL magnetization is negative. Moreover, the FM pinning layers provide unique experimental access to the change in their magnetization state and, in turn, reveal the dependence of the bias field on the pinning layer magnetization. Therefore, the cycle dependent evolution of the pinning layer magnetization can be unambiguously measured and its correlation with training of the bias field is clearly evidenced. The bias field training effect is defined here as an alteration of the bias field upon cycling the bilayer system through consecutive hysteresis loops of SL and is quantified by $\mu_0 H_B$ vs n , where n is the number of cycled SL loops. Training can be observed when the spin structure of the pinning layer (HL) is initially out of equilibrium and approaches the equilibrium spin configuration triggered via subsequent reversals of the pinned magnetization.

Recent attempts to measure the correlation between aging of the interface magnetization in an AF pinning layer and the training of the EB field in AF/FM heterostructures faced serious problems due to the smallness of the excess magnetic

moment in the AF pinning layer that gives rise to conventional EB.^{71,181} Also, in these EB systems, proportionality between the moment at the interface and the AF bulk magnetic moment is a faintly motivated assumption. The latter is far more reasonable in the case of a very thin FM pinning layer with a homogeneous spin structure along the normal of the film as demonstrated by the linearity of the effect. Recently, it is observed that a very tiny deviation from linearity can be expected.¹⁸²

This chapter presents results of the bias field and its training effect. We also present a theory of the training effect adapted to all FM bilayers, which shows excellent agreement with our experimental data [section 4.3]. Furthermore, we also show experimental results of the temperature dependence of the bias field training effect in consistent with the proposed phenomenological theory. The latter is developed with the help of discretized Landau-Khalatnikov approach [section 4.4]. Finally, the dynamical enhancement of the bias field and its training effect is presented [section 4.5] and the experimental results are well supported with the power law behavior above a quasi-static limit of sweeping rate of applied magnetic field.

4.2. SAMPLE DESCRIPTION AND MAGNETIC CHARACTERIZATION

The SL of the sample under investigation is a CoCr film of 3 nm thickness. It is exchange coupled with a magnetically hard CoPtCrB pinning layer of 15 nm thickness

via a Ru interlayer of thickness 0.7nm. This sample is prepared by using sputtering methodology. The details of the sample fabrication can be found elsewhere.^{179,180}

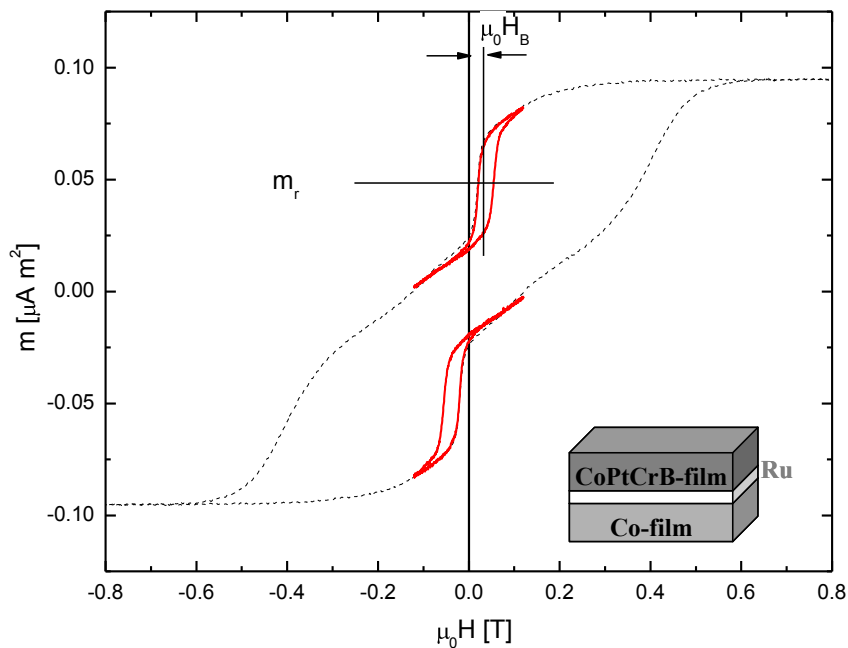


Figure 4.1. The dashed line shows the overall magnetic hysteresis m vs $\mu_0 H$. Thick solid red lines are low field minor loops after positive and negative saturation of the hard layer, respectively. The horizontal line visualizes magnetic remanence m_r for the upper soft loop, the vertical line indicates the shift of the soft layer loop along the field axis relative to $H=0$. The inset is a schematic of the sample.

The dotted line in Fig. 4.1 shows the overall magnetic hysteresis loops m vs. $\mu_0 H$, where m is the magnetic moment and H is the applied magnetic field. The measurements are done at room temperature with the help of AGFM. The inset shows a sketch of our sample. The shape of the overall loop reflects well separated switching fields of the HL and SL, respectively. Two minor loops in the first and third quadrant in Fig. 4.1 (solid red

lines) resemble the reversal of the SL. The SL loops shown in Fig. 4.1 have been measured within a field range $-100 \leq \mu_0 H \leq 100$ mT when the HL magnetization is closely below its saturation.

4.3. TRAINING EFFECT IN COUPLED HARD/SOFT BILAYERS

Similar to hysteresis loop shift of the ferromagnet in AF/FM bilayers, the SL also shows a horizontal loop shift along the magnetic field axis by an amount of $\mu_0 H_B$ as indicated by a vertical line in Fig 4.1. The SL also shifts significantly along the vertical direction by an amount of the remanent magnetic moment, m_r of the HL as described above. In contrast, no or insignificant vertical shift appear in the case of classical systems where the pinning layer (AF) magnetic moment, $m \approx 0$.^{177,183}

4.3.1. INITIALIZATION OF THE BIAS FIELD

HL/SL bilayer systems do not demand any field cooling procedure to generate bias field effect; however, an initial process is required to measure the SL without disturbing HL magnetization. The process contains applying large positive/negative magnetic fields to the bilayer heterostructure where both HL and SL saturate completely and which is followed by setting the HL state in a partially demagnetized condition. The

latter refers to the domain state of the HL that requires application of moderate negative/positive magnetic fields, respectively. This sets a starting point for measuring the bias field of the SL. Fig. 4.2 shows the above mentioned procedure in several schematics. They are depicting the evolution of the domain structures in the HL during typical experiments via arrows representing the local HL magnetization. These HL magnetization states in Fig 4.2 correspond to the initialization [(a) and (b)] of the measurement process and subsequent SL training cycles [(c) first cycle and (d) after large number of cycles].

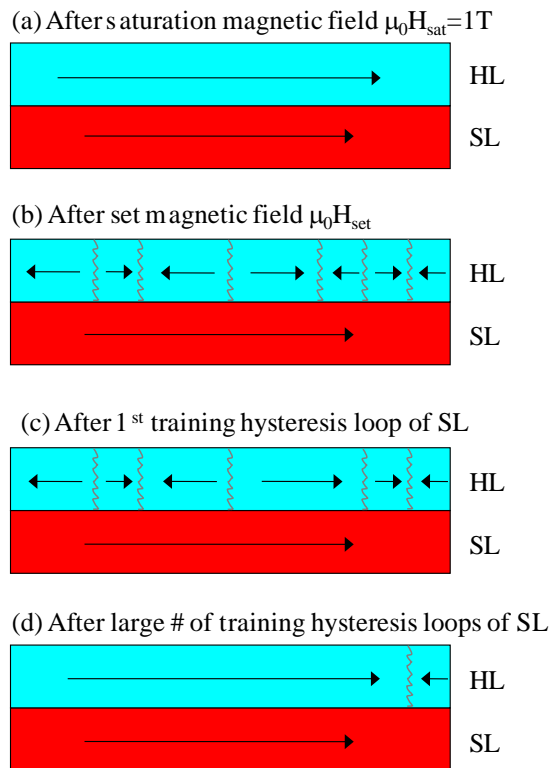


Figure 4.2. The schematic sketches the magnetic domain state of HL/SL heterostructure at different stages during the training cycle: (a) A strong magnetic field is applied on the bilayer that saturates the magnetization of both HL and SL in the direction of the applied magnetic field; (b) A moderate magnetic set field is applied in the opposite direction that creates HL domain state and initiate the starting point for measuring the bias field effect; (c) After the first magnetic reversal of the SL, the HL spins are dragged by back towards uniform magnetization of the HL; (d) After several hysteresis loops of the SL, the HL reaches to quasi-equilibrium state which has an increased magnetization in comparison to initial state.

4.3.2. THE BIAS FIELD TRAINING EFFECT IN SOFT FERROMAGNET

As mentioned above, the initialization process involves first saturation of both HL and SL magnetization aligned along a positive magnetic field. In the second step, a set field $-\mu_0 H_{sat} < \mu_0 H_{set} < \mu_0 H_{c1}$ is applied where $\mu_0 H_{c1}$ is the negative coercive field of the overall loop. This set field partially demagnetizes the HL and brings it in a domain state as shown in the schematic 4.2 (b). This partial HL demagnetization finalizes the initialization of the bias field training effect. Subsequently we measure the SL hysteresis loops in a magnetic field range of $0 < \mu_0 H < 140$ mT leaving the HL magnetization virtually unperturbed. Upon consecutive SL magnetization reversal, the HL interface spins are dragged back closer to the equilibrium spin configuration bringing the HL domain state closer to uniform HL magnetization. Therefore the HL quasi equilibrium which is reached in the limit of a large number of SL magnetization reversals has an increased magnetization with respect to the initial state of the training cycle. The schematics 4.2 (c) and (d) resemble the HL domain states after 1st and a large number n of SL hysteresis loops, respectively.

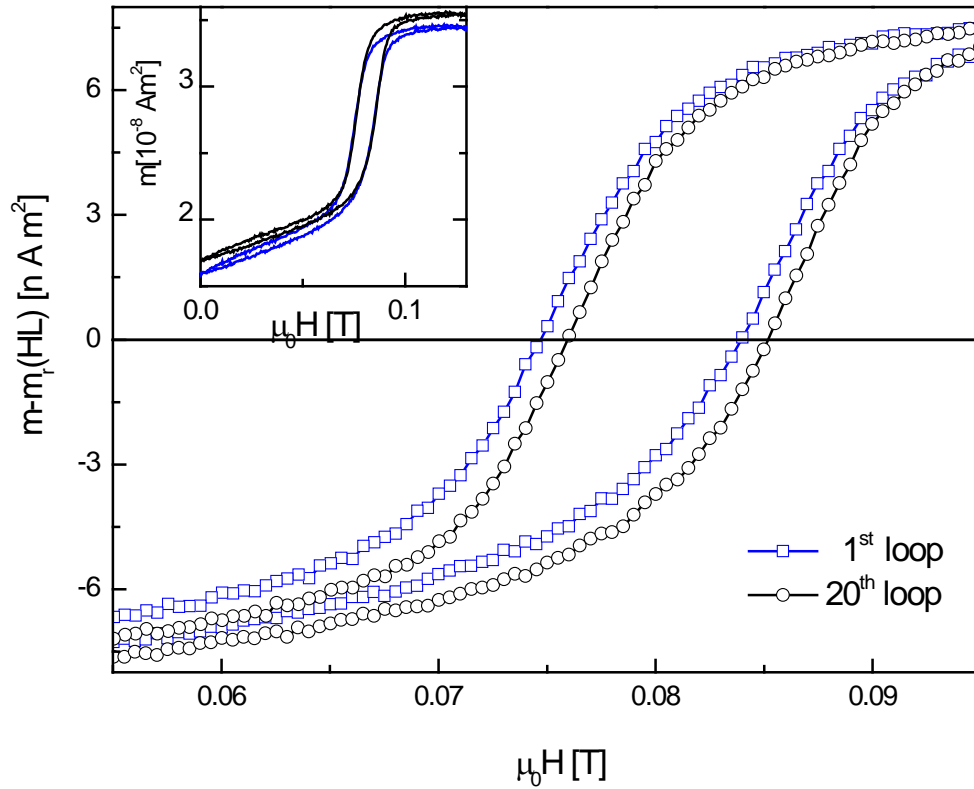


Figure 4.3. The first (squares) and 20th (circles) training hysteresis loops of the SL after saturating the whole bilayer at $\mu_0 H_{\text{sat}} = 0.8$ T and immediately followed by $\mu_0 H_{\text{set}} = -0.34$ T. The inset shows the SL loop shift along vertical axis.

Fig. 4.3 shows the 1st (squares) and 20th (circles) training hysteresis loops of the SL. All these measurements were performed after saturating the bilayer at $\mu_0 H_{\text{sat}} = 0.8$ T and subsequently partial demagnetization of pinning layer (HL) in the static set field of $\mu_0 H_{\text{set}} = -0.34$ T. The minor SL loops are measured in the magnetic fields of moderate strengths, $0 \leq \mu_0 H \leq 0.14$ T, which do not switch the HL. After subtracting m_r of HL, respectively, the first ($n = 1$, squares) and 20th ($n = 20$, circles) minor hysteresis loops of

the SL reveal a clear relative shift along the field axis as shown in Fig 4.3. The inset of the Fig 4.3 shows the raw curves of the SL before subtracting m_r of the HL. Initially the training effect is not visible in the raw data, however, after subtracting the background m_r values of the HL a significant training effect is apparent.

The procedure of analyzing data is slightly involved for getting the information of the bias fields of the SLs. I mention here how I obtain the bias field values from the raw hysteresis loops of the SL.

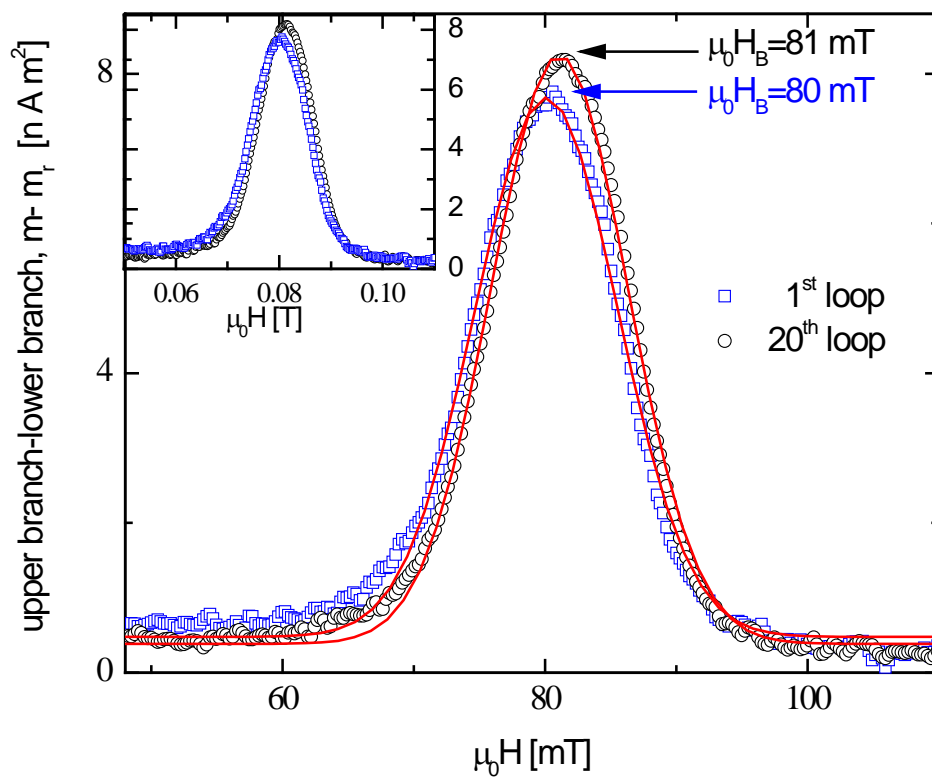


Figure 4.4. Gaussian type distribution of data points after subtracting the lower branch values from upper branch of the hysteresis loops of 1st (blue squares) and 20th (black circles) of the SL. The red lines are the fits of Gaussian function. Inset shows the raw data before Gaussian fits.

Initially I have separated up and down branches of the SL hysteresis loop. Then I subtracted lower branch values from upper branch which gives rise to a Gaussian type distribution of data points. Inset of Figure 4.4 shows this Gaussian distribution of data points for the 1st (squares) and 20th (circles) hysteresis loops of Fig 4.3. So I fitted the resulting data with a Gaussian function as shown in Fig 4.4 by red colored line. The peak value of this Gaussian function gives rise to the value of bias field. For instance, the Gaussian fits provide the values of the bias field for 1st and 20th hysteresis loops as $\mu_0 H_B = 80$ and 81 mT, respectively. This particular process is repeated for every loop in the training sequence and for at all temperatures to evaluate the values of bias fields.

Apparently, from the Fig. 4.5, the bias field experiences training through consecutive magnetization reversals of the SL and increases within the 20 subsequently cycled SL loops by about 1 mT. This training effect in $\mu_0 H_B$ is accompanied by the relaxation of the HL magnetization towards an increased equilibrium value. In particular, the shifts of the SL loops along the m and field axis are linearly correlated. In order to analyze the $\mu_0 H$ vs n dependence quantitatively we determine the bias field at each n value for a number of different starting conditions created by different fields $\mu_0 H_{\text{set}}$ applied to the HL. The results are displayed in Fig. 4.5.

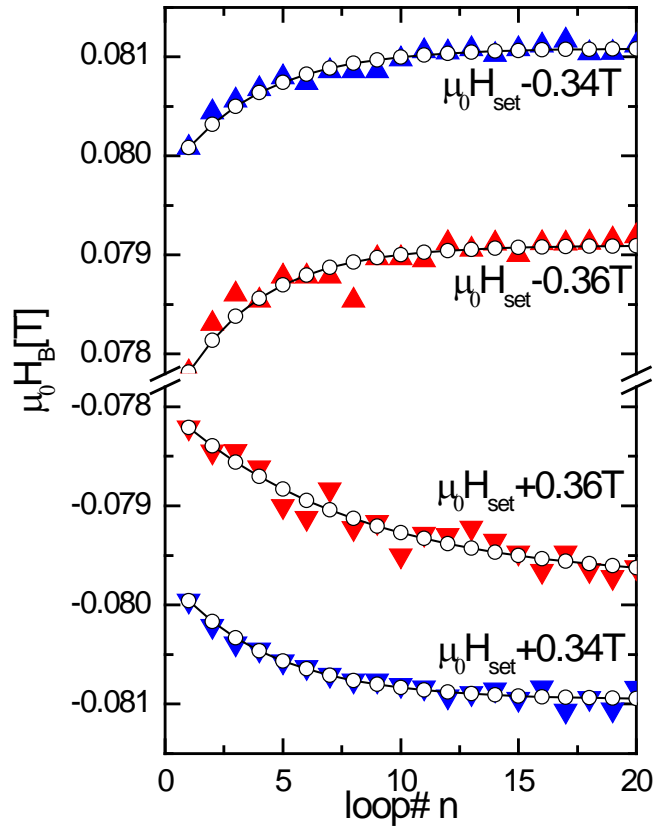


Figure 4.5. Training effect, $\mu_0 H_B$. vs n , of the HL-SL bilayer for set fields $\mu_0 H_{\text{set}} = \pm 0.36$ and ± 0.34 T after saturation in $\mu_0 H_{\text{sat}} = 0.8$ T for negative and $\mu_0 H_{\text{sat}} = -0.8$ T for positive set fields, respectively. Triangles are the experimental data measured for first 20 consecutive loops while lines with circles represent least-squares fits of Eq. (4.5) to the respective data sets. The lines are just eye-guiding.

Fig. 4.5 shows the training effect of the HL/SL bilayer for 4 different set fields $\mu_0 H_{\text{set}} = \pm 0.36$ and ± 0.34 T after saturation in $\mu_0 H = 0.8$ T, respectively. When saturating the bilayer in a positive (negative) magnetic field, a negative (positive) set field reduces (increases) the magnetization of the pinning layer. Subsequent SL hysteresis

loops will drag the HL back towards equilibrium corresponding to increased (reduced) magnetization. Triangles display the experimental $\mu_0 H_B$ vs n training data. The circles are the least-square fits of theoretical model of Eq. (4-5) developed based on Landau-Khalatnikov approach will be discussed later in section 4.3.5.

Similar to previous findings of conventional EB systems,⁹⁶ also here we observe that the loop-to-loop training effect is significant in the beginning of the training effect, *i.e.*, for low n values, and becomes substantially less pronounced for higher values of n . This also indicates that the related relaxation processes in the biasing HL occur predominantly during the first few reversals of the SL, while subsequent loops produce only minor changes. In accordance with the symmetry of the overall hysteresis loop (Fig. 4.1) identical absolute values but opposite signs of the saturation and set fields generates symmetrical results of $\mu_0 H_B$ vs n dependence with respect to $\mu_0 H_B = 0$. Note that the increasing absolute value of the set field decreases the absolute value of bias field. This simply reflects the fact that the absolute value of the HL magnetization is further reduced with higher magnitude of set field. At the same time, the higher magnitude of set field brings the HL away from equilibrium and, therefore, the intensity of the training effect increases as shown in Fig 4.4.

4.3.3. TRIGGERED TRAINING EFFECT BY REVERSAL OF THE FERROMAGNETIC SOFT LAYER

We know from AF/FM bilayers that the training is triggered by the cycled hysteresis loops of the pinned ferromagnet. To evidence that the training phenomenon allows for a universal description it is necessary to show experimentally that the training effect is indeed triggered by *only* the cycled SL hysteresis loops. In particular, we have to rule out the point that the change of $\mu_0 H_B$ reflects a continuous relaxation phenomenon depending on the time the HL is exposed to the applied magnetic field. In order to evidence the triggered nature of the training effect we study the change of the HL magnetization for 10 subsequent SL loops obtained for various field amplitudes $\mu_0 H_{\text{Amp}}$. The results are displayed Fig. 4.6.

Every individual set of 10 loops takes place in applied magnetic fields $0 \leq \mu_0 H \leq \mu_0 H_{\text{Amp}}$ after the sample has been initialized each time in an identical fashion through saturation of the bilayer in $\mu_0 H = 0.8$ T and partially demagnetized in a set field of $\mu_0 H_{\text{set}} = -0.34$ T. The squares in the Fig 4.6 represent the change in the HL magnetization between the first and 10th loop. In principle, we should measure the bias field of the SL; however, note that the SL does not completely reverse for $\mu_0 H_{\text{Amp}}$ fields smaller than its saturation field, so a meaningful bias field cannot be determined from the loop itself. On the other hand, due to the proportionality between the HL magnetization and $\mu_0 H_B$, we are able to determine the field cycling effect onto the bilayer system by simply measuring the remanent HL magnetization, m_r . The proportionality between m_r and $\mu_0 H_B$, also known from Ref. [179], is independently evidenced here.

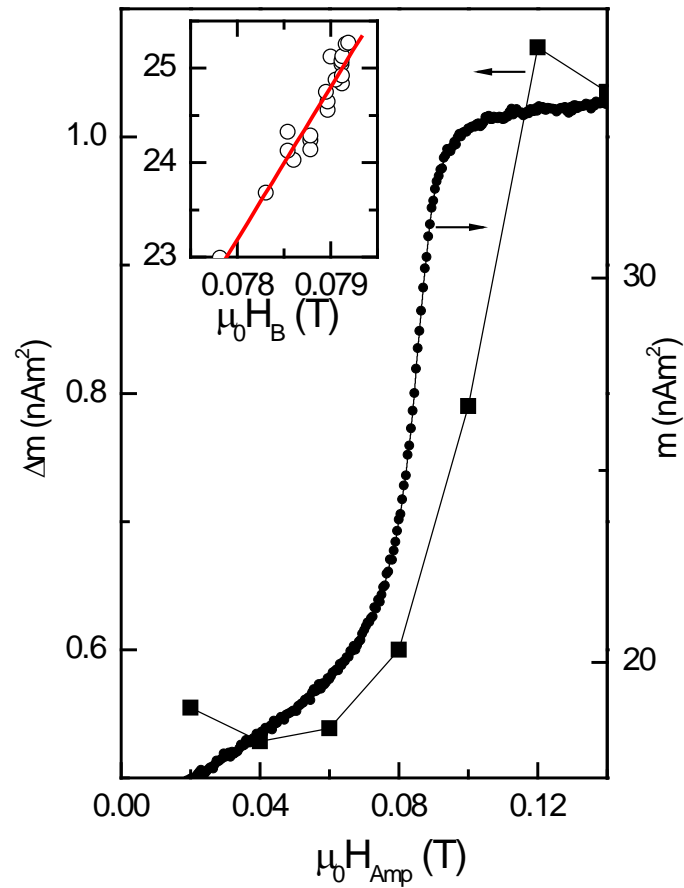


Figure 4.6. The change in the training effect (squares) for various field amplitudes $\mu_0 H_{\text{Amp}}$ vs. HL remanence magnetization ($\propto \mu_0 H_B$) in comparison to the left branch of the SL magnetic hysteresis loop. The inset (open circles) evidences the linear relation between the remanent magnetization and the bias field in our training experiments. The red colored line is the best linear fit to the data. Data is obtained from 20 consecutive loops after saturation at $\mu_0 H_{\text{sat}} = 0.8$ T and initialization in a set field of $\mu_0 H_{\text{set}} = -0.34$ T.

The inset of Fig. 4.6 shows as an example of the remanent magnetization $m(H=0)$ of the bilayer for 20 consecutive loops. The remanent magnetization is proportional to the HL magnetization due to uniform anti-parallel alignment of the SL in zero magnetic field. Each loop results in an individual value for the remanent magnetization and the bias field.

Clearly, within a small error bar, the expected linear dependence $m(H=0) \propto \mu_0 H_B$ is confirmed.

Therefore the change of the remanent magnetization $\Delta m = m(H = 0, n = 1) - m(H = 0, n = 10)$ taking place during a 10 loop training sequence in the field interval $0 \leq \mu_0 H \leq \mu_0 H_{Amp}$ can be used as a measure of the change of the bias field $\Delta H_B = H_B(H = 0, n = 1) - H_B(H = 0, n = 10)$. Fig. 4.6 (left frame) shows that Δm vs $\mu_0 H_{Amp}$ (squares) increases significantly at $\mu_0 H_{Amp} \approx 0.08$ T, simultaneous with the onset of magnetization reversal in the SL. This correlation between hysteretic behavior of the SL and the training effect is evidenced when comparing Δm vs $\mu_0 H_{Amp}$ with the up magnetization branch m vs $\mu_0 H$ of the hysteresis loop (solid circles, right frame). The constant value of Δm vs $\mu_0 H_{Amp}$ for field amplitudes $0.02 < \mu_0 H_{Amp} < 0.08$ T as well $\mu_0 H_{Amp} > 0.12$ T indicates that the training effect is not directly caused by the time and amplitude of the applied field, but triggered by the SL magnetization reversal. This result is in agreement with previous findings obtained by polarized neutron scattering, high resolution photoemission electron microscopy, and micromagnetic simulations.^{184,185}

It is general consensus that training of the EB is caused by the nonequilibrium nature of the spin structure in the pinning layer.^{66,74,87,89,163} Thus, the gradual decrease of $\mu_0 H_{EB/B}$ with increasing n is a fingerprint of rearrangements in the pinning layer spin structure towards an equilibrium configuration. These general assumptions are corroborated by our experimental observation that virtually no training effect is present in our samples if we start the minor loop cycling from a fully magnetized state of HL, *i.e.*,

beginning very close to the equilibrium configuration of the HL. Significant training effect is achieved only when a set field drives the HL out of saturation into a domain state. Consecutively cycled loops of the SL then drive the HL, in part, back towards saturation magnetization causing the training effect. This qualitative picture is for the first time confirmed by means of magnetometry. It is a conceptual advantage of all FM bilayer systems that the deviation of the HL magnetization from its equilibrium state can be measured via either $m_r(\text{HL})$ or the bias field. Moreover, the experimental results also provide an insight into the strength of the training effect and these details are discussed in the next section 4.3.4.

4.3.4. STRENGTH OF THE TRAINING EFFECT

Fig. 4.7 shows the experimentally measured size of the training effect, $|\mu_0 H_B(n=1) - \mu_0 H_B^e|$ vs. $|\mu_0 H_B(n=1)|$. Here $\mu_0 H_B^e$ denotes the equilibrium bias field in the limit of large n . From Fig 4.7, $|\mu_0 H_B(n=1) - \mu_0 H_B^e|$ increases with decreasing $|\mu_0 H_B(n=1)|$. According to proportionality between the HL magnetization and the bias field, the increases of $|\mu_0 H_B(n=1) - \mu_0 H_B^e|$ with decreasing bias field $\mu_0 H_B(n=1)$ evidences that the training requires a HL domain state that is not in equilibrium to allow for spin configurational rearrangements towards this very equilibrium state. The more the HL magnetization deviates from its equilibrium state of saturation the more pronounced is the training effect.

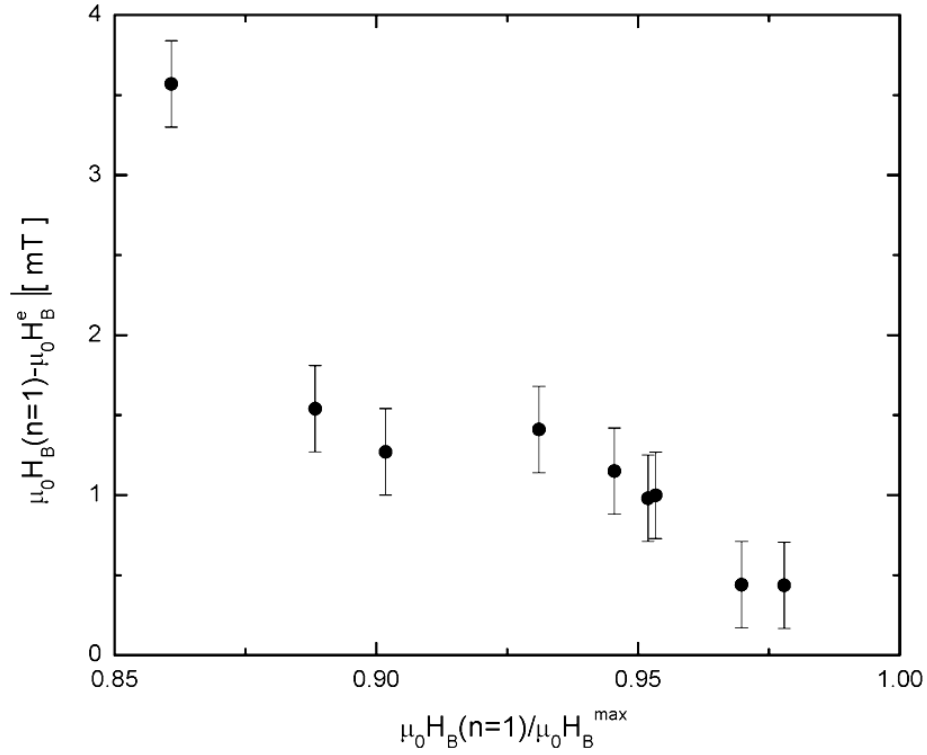


Figure 4.7. Dynamics of the $|\mu_0 H_B(n=1) - \mu_0 H_B^e|$ measured for various magnetization states of the HL. The HL magnetization at $n = 1$ is linearly correlated with the bias field $\mu_0 H_B(n=1)$. The maximum bias field $\mu_0 H_B^{\text{Amp}} \approx 0.084$ T is achieved when the HL is saturated and no training appears.

4.3.5. PHENOMENOLOGICAL THEORY OF THE BIAS FIELD TRAINING EFFECT IN ALL FERROMAGNETIC BILAYERS

In chapter 1, the training effect in conventional EB systems has been described by means of Landau-Khalatnikov approach, which allows the derivation of a sequence equation that determines $\mu_0 H_B(n+1)$ from its predecessor [Eq. 1-17].^{95,110} In the

framework of the physical picture here, I outline the analogous theoretical approach in order to calculate the training effect in all FM bilayer systems. Once again we start with Landau-Khalatnikov equation [Eq. (1-9)] which describes the time evolution of the interface magnetization, S , in the pinning HL. By now it is well accepted that the training, *i.e.*, relaxation in the pinning layer towards its equilibrium, is not a continuous process but rather discrete in time. Therefore, one can replace \dot{S} with $[S(n) - S(n+1)]/\tau$ where τ is characteristic time within the time of SL loop measured

$$\xi \left[\frac{S(n) - S(n+1)}{\tau} \right] = - \frac{\partial \Delta F}{\partial S} \quad (4-1)$$

where ΔF is the nonequilibrium free energy of the HL and ξ is a phenomenological damping constant.

Note that ΔF is here characterized by a single FM order parameter, S , unlike to conventional system. A harmonic approximation of ΔF in the vicinity of the equilibrium value, $S = S_e$ (dashed parabolas of Fig. 4.8) of the Landau free energy landscape of the double well type is essential to describe the triggered relaxation of pinning HL towards its quasi-equilibrium,

$$\Delta F \propto (S - S_e)^2 \quad (4-2)$$

Note that Eq. (4-2) is different from the free energy of the pinning AF in classical AF/FM system.

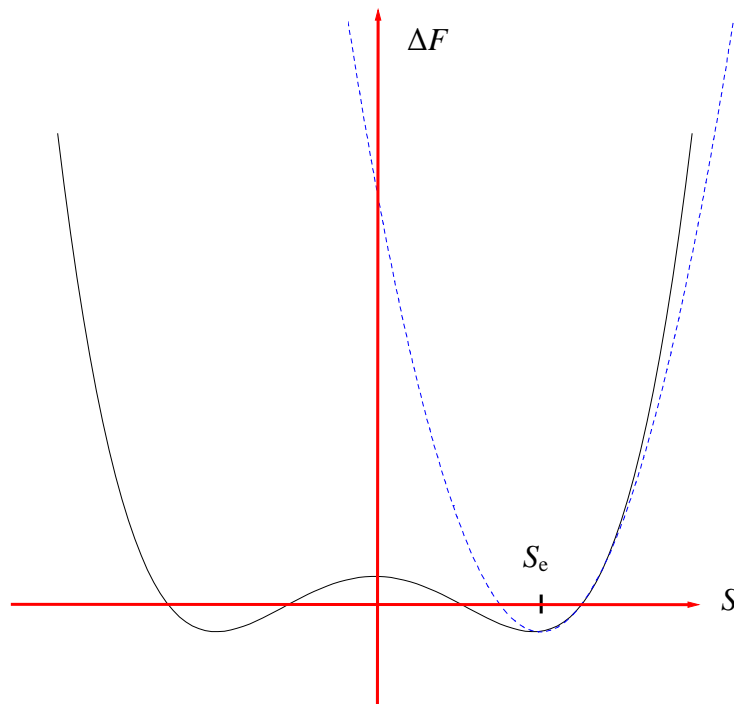


Figure 4.8. Landau-type free energy (solid line) of the pinning HL and the harmonic approximation around its equilibrium order parameter (*i.e.*, interface magnetization), $S=S_e$ (dashed blue color)

Now through the substitution of Eq. (4-2) into Eq. (4-1), one gets $S(n) - S(n+1) = -K[S(n) - S_e]$. Here K is a constant containing ξ , τ and the proportional constant involved in Eq. (4-2). After rearrangement, one obtains an implicit equation for the training effect in all FM bilayer systems

$$S(n+1) = (K+1)S(n) - KS_e$$

But we know that the interface magnetization $S(n)$ of the pinning HL is proportional to its remanent magnetization, m_r .^{179,180} Moreover, from the inset of Fig 4.6 we already know $m_r \propto \mu_0 H_B$. Therefore the above equation is modified to,

$$\mu_0 H_B(n+1) = (K+1)\mu_0 H_B(n) - K\mu_0 H_B^e. \quad (4-3)$$

However, closer inspection of Eq. (4-3) implies an explicit expression for $\mu_0 H_B(n)$,

$$\mu_0 H_B(n) = (K+1)^{n-1} \mu_0 H_1(n) - K\mu_0 H_B^e (K+1)^n \sum_{j=2}^n \left(\frac{1}{K+1} \right)^j \quad (4-4)$$

By taking advantage of the closed form of the sum of geometrical series, Eq. (4-4) becomes,

$$\mu_0 H_B(n) = (K+1)^{n-1} \left\{ \mu_0 H_B(n=1) - K\mu_0 H_B^e \left[\frac{(K+1)^{n+1} - 1}{K(K+1)^{n-1}} - (K+2) \right] \right\}. \quad (4-5)$$

Eq. (4-5) is an explicit expression of the training effect in all FM bilayer systems with two fitting parameters, $\mu_0 H_B^e$ and K . $\mu_0 H_B^e$ is the equilibrium bias field in the limit $n \rightarrow \infty$ and K is a phenomenological constant. Fig. 4.9 provides an intuitive understanding of the role of K for the characteristics of the training effect.

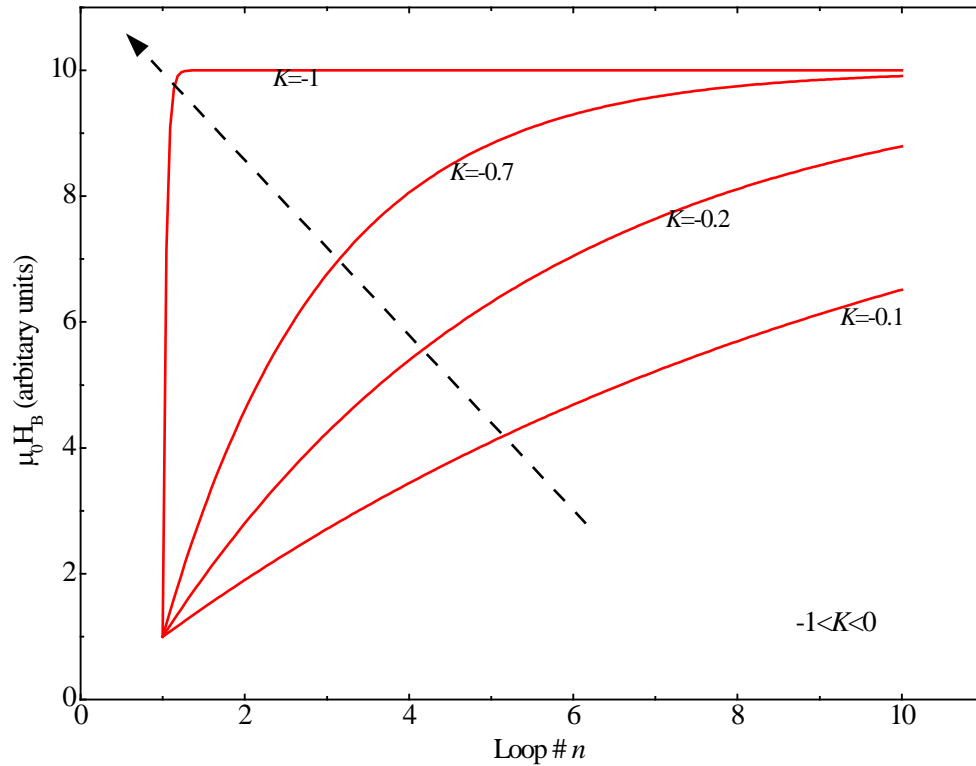


Figure 4.9. Simulated plots of Eq.(4-5) visualizing the role of K in the characteristics of $\mu_0 H_B$ vs. n . Value of K decrease from close to zero towards $K=-1$ in the direction of the arrow. Identical arbitrary values of the first and the equilibrium bias value are used for all simulated curves.

A family of curves is displayed in red color in Fig 4.9 where K is varied within the range $-1 \leq K \leq 0$. This interval defines the range of convergence for the geometrical series which is determined by transforming of the implicit sequence of Eq. (4-3) into the explicit Eq. (4-5). The value of K changes from 0 to -1 along the direction of displayed arrow. Inspection of Eq. (4-3) shows that $K=0$ yields $H_B(n+1) = H_B(n)$ which means no training at all, however, that does not imply that the bias field has to be

zero. On the other hand, $K=-1$ in turn yields $H_B(n+1) = H_B^e \forall n \geq 1$ which means a step-like change of the bias field between the first two points and zero training for $n > 2$. Therefore, it is clear from the Fig 4.9 that the rate of change of training effect is increasing with absolute value of K . Note that, however, K does not predict the magnitude of ΔH_B but rather shows the rate of change of training effect for given ΔH_B .

Eq. (4-5) is an explicit expression for training effect for all FM bilayers. Such an explicit expression is not achievable in case of traditional system where an implicit equation itself is much complicated. In the limit of $n \rightarrow \infty$, Eq. (4-5) will produce exponential behavior of the training effect. Subsequently I show here the math details of asymptotic behavior of Eq. (4-5).

In the limit of $n \rightarrow \infty$, $(K+1)^{n+1} \rightarrow 0$ due to $-1 \leq K \leq 0$. Therefore, Eq. (4-5) becomes

$$H_B(n) = (K+1)^{n-1} H_B(n=1) + H_B^e + KH_B^e(K+2)(K+1)^{n-1}.$$

After rearrangements, $H_B(n) = (K+1)^{n-1} [H_B(n=1) + KH_B^e(K+2)] + H_B^e$.

Above equation can be modified to $H_B(n) = e^{(n-1)\log(K+1)} \cdot [H_B(n=1) + KH_B^e(K+2)] + H_B^e$.

But for $n \rightarrow \infty$, it becomes $H_B(n) = e^{-n \cdot |\log(K+1)|} \cdot [H_B(n=1) + KH_B^e(K+2)] + H_B^e$.

Therefore, the asymptotic behavior of training effect in all FM magnetic bilayers is

$H_B(n \rightarrow \infty) \propto e^{-n \cdot |\log(K+1)|}$. Note that this asymptotic behavior is different from

$H_{EB}(n \rightarrow \infty) \propto 1/\sqrt{n}$ of AF/FM bilayers.

The circles in the Fig. 4.5 show the results of the least squares fits of Eq. (4-5) to the experimental data sets. Evidently, there is excellent agreement between the here derived theoretical expression and our experiments, validating our theoretical approach. In our analysis, K and the equilibrium bias field $\mu_0 H_B^e = \mu_0 H_B(n \rightarrow \infty)$ enter Eq. (4-5) as fitting parameters while $\mu_0 H_B(n = 1)$ is fixed as being the bias field of the first loop. The lines in Fig 4.5 are just eye guiding. Furthermore, it is remarkable that the parameter K varies only by about 25% around $K = -0.2$ throughout all fits indicating that K is virtually independent from the field initialization. Knowing the fact that K describes the characteristics of the training effect, further studies will stimulate in the direction of temperature dependence of K . This eventually provides insight into temperature dependence of behavior of the training effect. Furthermore, it is also interesting to know the evolution of K with the variation of thicknesses of both HL and SL.

Summarizing the results, I have shown that hard-soft FM bilayer systems contain prototypical properties for the fundamental understanding of exchange bias and demonstrated its corresponding training phenomenon in the systems. For the first time all FM bilayers unambiguously demonstrate that the deviations from equilibrium in the pinning layer are the driving force behind the exchange bias training effect. The theoretical approach of the training effect based on the discretized dynamical Landau Khalatnikov equation provides an excellent quantitative agreement with our experimental data which confirms the underlying physical picture of the training effect as a triggered relaxation mechanism towards the equilibrium state of the pinning layer.

4.4. TEMPERATURE DEPENDENCE OF THE TRAINING EFFECT

Numerous investigations have been done on the conventional EB training effect which focus for instance on the influence of temperature, AF and FM film thicknesses,^{55,111} dilution of the antiferromagnet.^{176,186} and interface roughness between antiferromagnet and ferromagnet.¹⁸⁷ The temperature dependence of the training effect is also studied in conventional AF/FM systems [section 3.1]. The theoretical description of the temperature dependence of the training effect in classical systems is exigent due to the non trivial relation between the AF order parameter and its magnetization. Nevertheless, the phenomenological theory based on the discretized Landau Khalatnikov approach is successfully able to show temperature dependence of the training effect in classical systems [chapter 3]. On the other hand, the temperature dependence of training effect in newly realized exchange bias systems of hard-soft FMs is still lacking. Therefore, in this section, I report a systematic study of the T -dependence of training effect in all FM bilayers. I also present a theory of the T -dependence of training effect in HL/SL bilayers which in fact shows an excellent agreement with our experimental results.

In all FM coupled systems training is initialized by partial demagnetization of the HL. Interestingly, and as an experimental big advantage, the HL magnetization can be isothermally tuned by a specific magnetic field protocol. It is given by initial saturation and subsequent demagnetization of the HL. Moreover, the T -dependence of the training effect is also expected in HL/SL systems due to the temperature dependence of the HL

domain state and its thermally assisted approach toward equilibrium on SL cycling. Moreover, the order parameter of the pinning HL is nothing but its magnetization that makes the theory of training effect very simple for all FM bilayers. Thus, coupled HL/SL heterostructures are intriguing systems to investigate various training related effects.

4.4.1. OVERALL HYSTERESIS LOOPS AT DIFFERENT TEMPERATURES

A similar sample of CoPtCrB (HL)/CoCr (SL) bilayer system is used for studies here. Fig. 4.10 shows the overall magnetic hysteresis loops m vs. $\mu_0 H$ at different temperatures $10\text{K} \leq T \leq 395\text{K}$ between $|\mu_0 H| \leq 1$ T. All magnetic results presented in this section were measured with the help of a SQUID magnetometer. Magnetic fields are applied within the easy anisotropy plane which is in-plane of the sample.

As expected, the overall hysteresis loop broadens with decreasing temperature since domain wall pinning is more effective when thermal activation is reduced.¹⁸⁸ Note that the HL magnetization did not reach full saturation during the overall loop at $T=10$ K. As a consequence overall loop shows a very small asymmetry and, and consistent with our training data, the SL magnetization reversal broadened for a partially demagnetized HL.

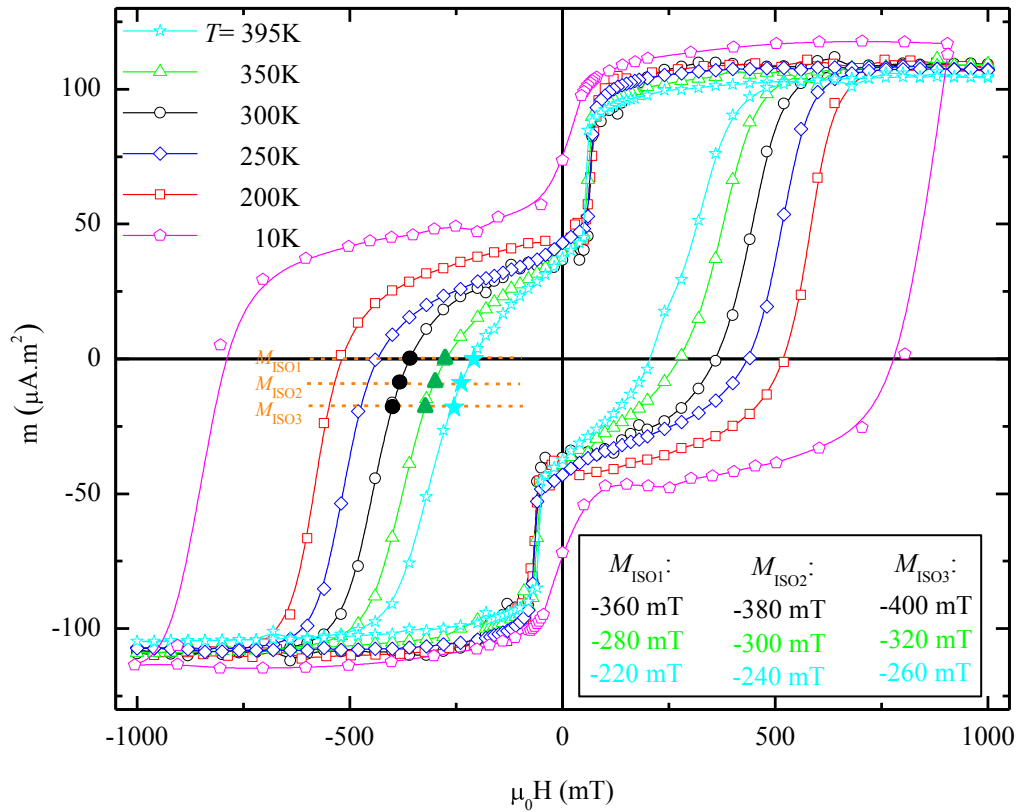


Figure 4.10. Overall magnetic hysteresis loops m vs. $\mu_0 H$ at different temperatures $T=395, 350, 300, 250, 200$ and 10 K. The three broken lines show the set fields producing iso-magnetic HL domain states M_{ISOj} with $j=1, 2$ and 3 .

In addition to overall loops, Fig 4.10 displays three horizontal dotted lines which are lines of isomagnetizations that are intercepting the overall hysteresis loops at $M_{ISO1}=0$, $M_{ISO2}=-9.0$, and $M_{ISO3}=-18.0$ nAm². These isomagnetization lines define our specific experimental protocols of training initializations. We group those initializations at temperatures $T=300, 350$ and 395 K together which belong to the same isomagnetization line. By doing so we obtain groups of data sets labeled by $j=1, 2, 3$. Different

temperatures within a group refer to various HL states initialized according to one of the isomagnetization lines $M_{\text{ISO}j}$. Fig. 4.10 allows to assign the set fields $\mu_0 H_{\text{set}} = -360, -280$ and -220mT for group 1 which give rise to $M_{\text{ISO}1} = 0$ at $T = 300, 350$ and 395K , respectively. Analogously $\mu_0 H_{\text{set}} = -380, -300$ and -240mT are the set fields for the initializations in group 2 ($M_{\text{ISO}2} = -9.0 \text{ nAm}^2$) and $\mu_0 H_{\text{set}} = -400, -320$ and -260mT correspond to group 3 ($M_{\text{ISO}3} = -18.0 \text{ nAm}^2$). Points $M_{\text{ISO}j}$ are displayed as solid symbols for $j = 1, 2, 3$. Choosing the set magnetic fields along the isomagnetization lines is an essential condition because our theoretical description requires the knowledge of the initial and the quasi-equilibrium magnetization states of the HL as important inputs. In order to get data points which allow for comparison it is mandatory to start with an identical initial magnetization state of the HL. Therefore, all training loops of the SL follow these different set fields after the bilayer has been saturated at $\mu_0 H = 1\text{T}$.

4.4.2. MINOR LOOP HYSTERESIS LOOPS AND ITS TRAINING EFFECT

The cycle dependent evolution of SL hysteresis loops reflecting typical training behavior of all FM bilayers are measured for $T = 395, 350$ and 300 K for all groups of $M_{\text{ISO}j}$ mentioned above and the corresponding results are shown in Fig. 4.11.

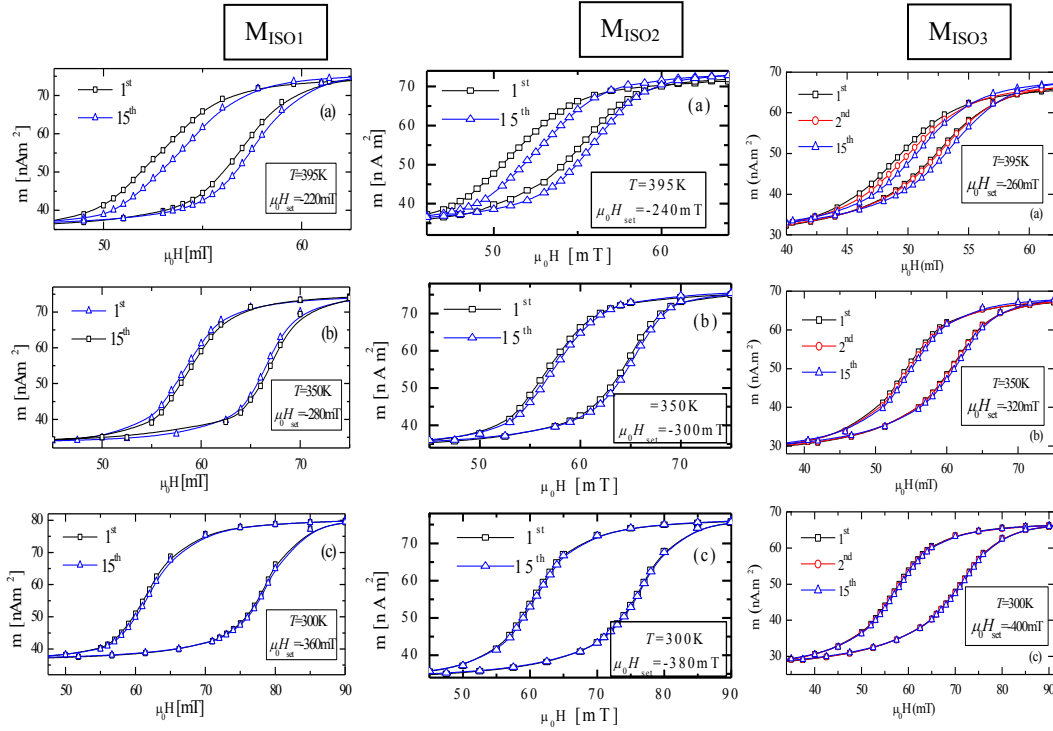


Figure 4.11. 1st (squares), 2nd (circles) and 15th (triangles) SL training hysteresis loops m vs. $\mu_0 H$ at three different temperatures $T=395$, 350 and 300 K for all isomagnetization M_{ISO_j} set fields after saturating the bilayer sample at $\mu_0 H_{\text{sat}} = 1$ T.

The first ($n=1$, squares), second ($n=2$, circles) and fifteenth ($n=15$, triangles) hysteresis loops of the SL reveal a clear cycle dependent relative shift along the field axis. The n -dependence is most pronounced for $T=395$ K. It can be quantified by the relative change of the bias field $\Delta H_B^{\text{max}} / H_B(n=1) := (H_B(n=15) - H_B(n=1)) / H_B(n=1)$ which is 2.0% at $T=395$ K, 1.5% at $T=350$ K, 0.6% at $T=300$ K for M_{ISO_3} , for example. Indeed we have measured SL hysteresis loops at $T < 200$ K but the training effect rapidly

drops down with decreasing temperature due to reduced thermal assistance of the triggered relaxation dynamics (not shown).

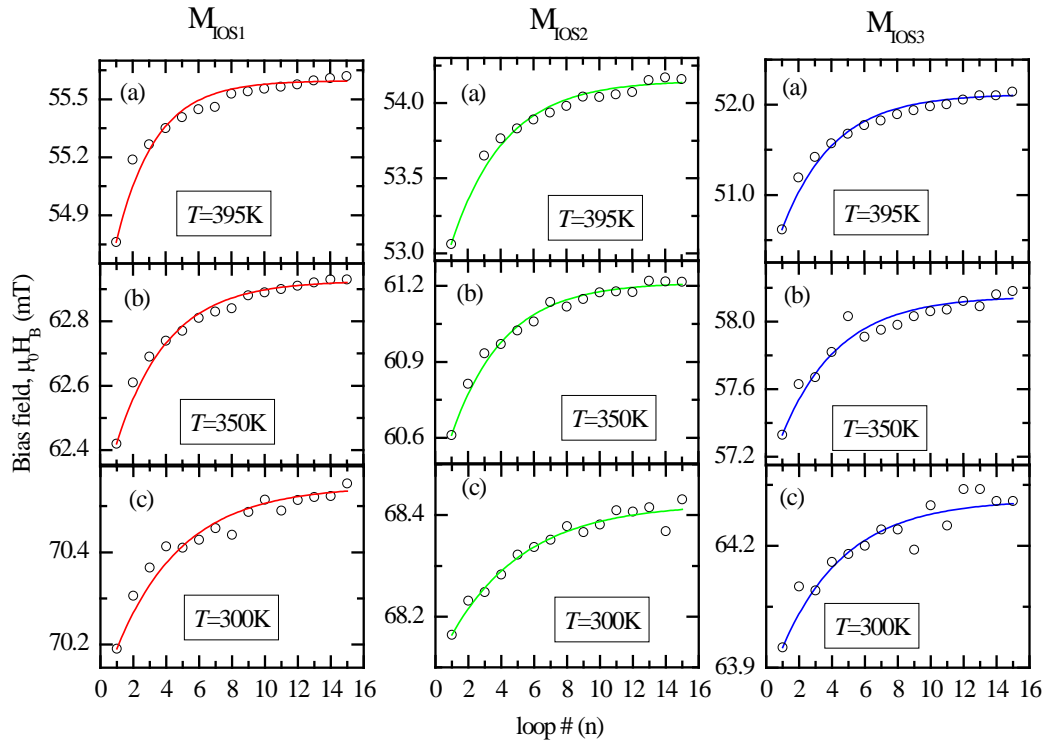


Figure 4.12. SL training effect $\mu_0 H_B$ vs. n at $T=395$, 350 and 300 K for initialization with isomagnetization M_{ISO1} , M_{ISO2} , M_{ISO3} set fields after saturating the bilayer sample in $\mu_0 H_{\text{sat}}=1$ T at different temperatures. Circles are experimental data while lines represent least-squares fits of Eq. (4-5) to the data sets.

Figure 4.12 shows the detailed analysis, $\mu_0 H_B$ vs. n , of the SL training loops at $T=300$, 350 and 395 K for M_{ISOj} initialization set fields. The n -dependence of $\mu_0 H_B$ reflects the tendency of the HL to approach its quasi equilibrium of increased magnetization on subsequently cycled SL loops. The circles are the experimental data and lines are the least-square fits of Eq. (4-5). It is observed that the change in $\mu_0 H_B$ is more pronounced

for lower n and it attains saturation for higher n . From the Fig. 4.12 it is also apparent that the strength of the training effect, $\left|(\mu_0 H_B(n=1) - \mu_0 H_B^e) / \mu_0 H_B(n=1)\right|$, is more pronounced for M_{ISO3} in comparison to M_{ISO1} , M_{ISO2} . Quantitatively, the strength of the training effect ≈ 3.017 for M_{ISO3} while M_{ISO1} has 1.519. Since M_{ISO3} brings the HL further away from equilibrium state than M_{ISO1} the strength of the training effect is also higher for M_{ISO3} .

4.4.3. INTRINSIC COERCIVITY OF THE SOFT MAGNETIC LAYER

Furthermore, I present enhancement of the intrinsic coercivity of the SL due to the neighboring HL. In the absence of the appropriate theory applicable to coercivity enhancement in the SL I considered a Landau-type free energy to derive the intrinsic coercivity. Fig. 4.13 shows the temperature dependence of the coercivity of the SL at $T=200, 250, 300, 350, 395$ K.

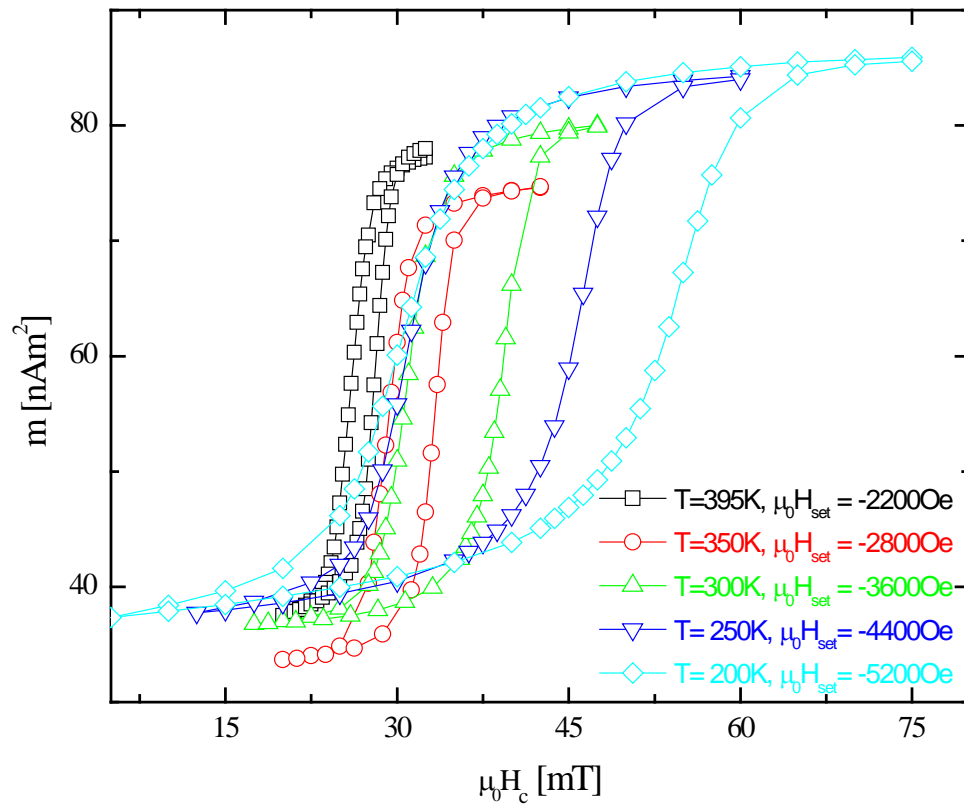


Figure 4.13. First SL hysteresis loops of training effect at $T=395, 350, 300, 250$ and 200 K for initialization with isomagnetization M_{ISO1} set fields after saturating the bilayer sample in $\mu_0 H_{\text{sat}}=1$ T.

Fig. 4.13 shows the SL hysteresis loops of the training effect at different temperatures $200 \text{ K} \leq T \leq 395 \text{ K}$. All these loops here follow the earlier mentioned experimental protocol of saturating the bilayer at $\mu_0 H_{\text{sat}}=1$ T and partially demagnetizing the HL. For the latter we use isomagnetization M_{ISO1} set fields. As expected the coercivity of the SL loop increases with decreasing temperature. The values of coercivity and the fit of a simple theoretical model are displayed in Fig 4.14.

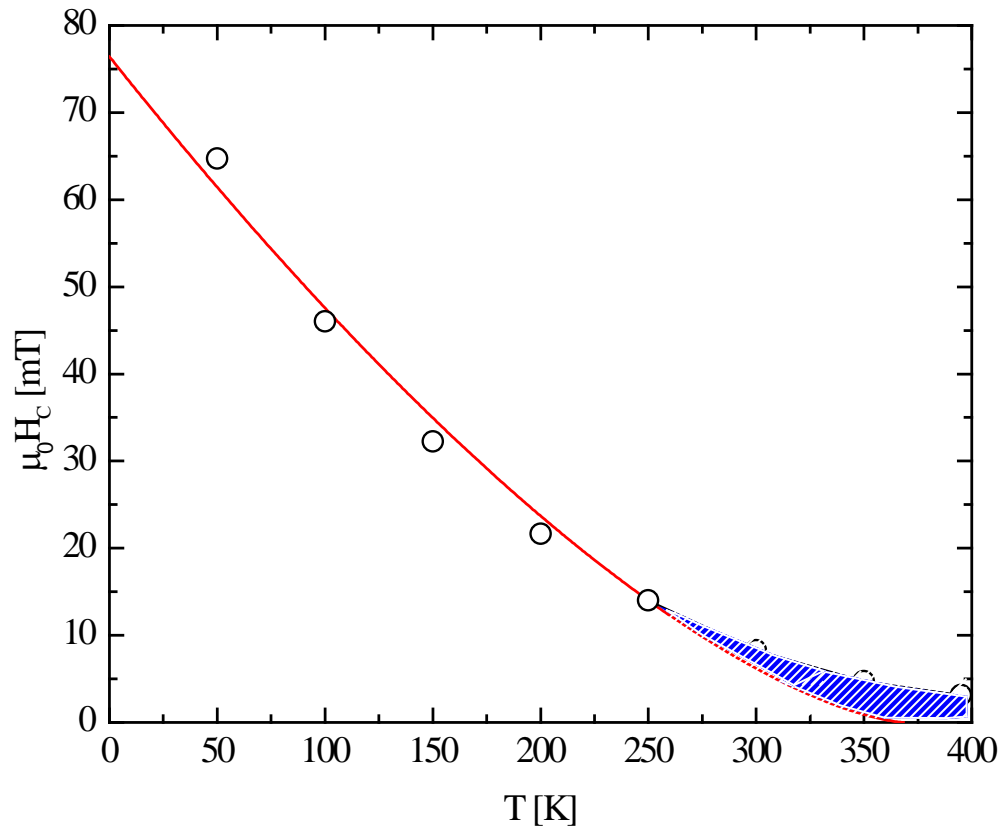


Figure 4.14. Open symbols are the coercivity values of SL in the vicinity of HL, while red colored curve is the fit of intrinsic coercivity by using Eq. (4-6)

The circles in Fig. 4.14 represent the coercivity values of a SL in the proximity of the HL. Note that the temperature evolution of the SL coercivity involves two different effects. The first one is the intrinsic coercivity of the SL at a given temperature and second one is coercivity broadening in the SL attained due to the coupling between SL and HL. The red curve in the Fig. 4.14 is a fit to the data by the subsequently shown naively derived expression for intrinsic coercivity of a ferromagnet [Eq. (4-6)]. The deviation of the data from the red curve shows likely effects of the coupling of HL on intrinsic coercivity of the SL as a function of temperature.

Here we obtain the qualitative description of the intrinsic coercivity and its temperature dependence of a FM by using Landau-type free energy in an applied magnetic field H ,¹⁸⁹

$$F = \frac{1}{2}aM^2 + \frac{1}{4}bM^4 - HM$$

where $a = a_0(T - T_C)$ and b are the Landau constants. Here T_C is the Curie temperature of the ferromagnet and $a_0 > 0$. The above equation is a series approximation of the free energy F that has one minimum for temperature $T > T_C$ ($a > 0$) and two minima for $T < T_C$ ($a < 0$). Note that the free energy is asymmetric around the origin because of zero applied magnetic field ($H \neq 0$).

The equilibrium requirement $\frac{dF}{dM} = 0$ leaves the condition on H as

$H = aM + bM^3$. The latter condition must be satisfied during the entire hysteresis loop.

Now we can plot H as function M to understand the behavior of magnetization, as shown in Fig. 4.15(a). The whole profile can be decomposed into two branches, first one $M > M_C$

and $M < -M_C$ where $\frac{d^2F}{dM^2} > 0$ and the second one is unstable central branch where

$\frac{d^2F}{dM^2} < 0$. The right branch starts from ∞ decreases down to $H = -H_C$. It ends at $H = -H_C$,

$M = M_C$ and the system immediately jumps to $H = -H_C$, $M = -M_C$ of the left branch. A similar phenomenon occurs for increasing fields.

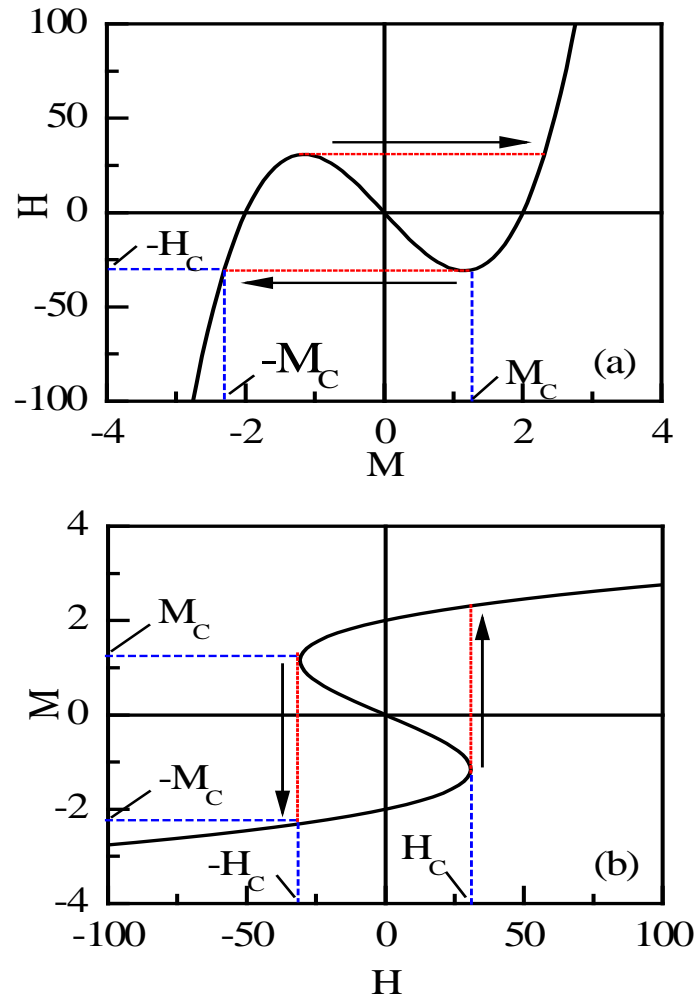


Figure 4.15. Magnetization response with applied magnetic field by minimizing free energy

Fig. 4.15(b) shows a plot of the magnetization M as a function of an applied field H . Though its derivation is based on very simplifying assumptions about the free energy, it actually shows many features of observed hysteresis loops. Two unstable points $H=H_C$, $M=-M_C$ and $H=-H_C$, $M=M_C$, where the magnetization reversal take place, are the points

where the two conditions, $\frac{dF}{dM}|_{H=H_c} = 0$ and $\frac{d^2F}{dM^2}|_{H=H_c} = 0$, must simultaneously hold.

These two conditions yield $H_c = aM_c + bM_c^3$ and $a + 3bM_c^2 = 0$. After some

rearrangements one obtains $H_c = \left(\frac{-4a^3}{27b}\right)^{1/2}$. With $a = a_0(T-T_C)$ one obtains for $T < T_C$,

the temperature dependence of the intrinsic coercivity of a FM,

$$H_c^{intr} = H_c^0 \left(1 - \frac{T}{T_C}\right)^{3/2} \quad (4-6)$$

Where $H_c^0 = \left(\frac{4a_0^3 T_C^3}{27b}\right)^{1/2}$ is the intrinsic coercivity at $T=0K$.

The fit in the fig. 4.14 lures to conclude that coupling between HL and SL contributes less to the temperature dependent overall coercivity in comparison to the intrinsic coercivity. Nevertheless, a surplus coercivity (see Fig 4.14 shaded region) due to the coupling seems to significantly bias the intrinsic coercivity of the SL above 250K. The resulting fit of Eq.(4-6) which considers only the intrinsic coercivity into account yields the values for coercivity of SL at $T=0$ K of 1528.5 Oe and a SL Curie temperature T_C of 369K. Similar effects may expect for HL coercivity due to the coupling with the SL.

4.4.4. THEORY OF TEMPERATURE DEPENDENCE OF THE TRAINING EFFECT IN ALL FERROMAGNETIC BILAYERS

It is the aim of the present chapter to show consistency in our phenomenological theory by fitting it to experimental data of the training effect. Particular emphasis lies on understanding of the temperature dependence of the rate of change of training effect, $\mu_0 H_B$ vs n , which up to now entered our theory as a free fitting parameter, K , only. Our Landau-type theory provides a functional form of the temperature dependence of this crucial parameter.

In the framework of the physical picture here, the training effect in all FM bilayers has been described theoretically by means of the discretized Landau-Khalatnikov dynamical equation [Eq. (4-1)]. Note that the ΔF involved in Eq. (4-1) quantifies the change in free energy when the HL magnetization M deviates from its quasi-equilibrium value M_e . The magnetization M plays the role of the order parameter allowing us to express the free energy in terms of Landau-type series expansions. As mentioned section 4.3.5, the overall HL magnetization M and interface magnetization S are proportional since $\partial M / \partial z = 0$ is a reasonable assumption for all positions (x, y) in the plane of the sample. The derivative $-\partial \Delta F / \partial S$ in Eq. (4-1) can be interpreted as a force that drives the HL domain state back towards the quasi equilibrium state of magnetization M_e . Hence, the LK equation is a discretized form of the equation of motion for S in the regime of over-critical damping. Since $\mu_0 H_B = c_1 S$ [as showed in section 4.3.3] and $M = c_2 S$ we express the free energy in terms of M and use later $\mu_0 H_B(n) = \frac{c_1}{c_2} M(n)$ with $c_{1,2} = \text{const.}$

In section 4.3.5, I have shown derivation the functional form $\mu_0 H_B = \mu_0 H_B(n)$ from Eq. (4-1) using the Landau-type free energy expansion in the vicinity of the quasi equilibrium magnetization, M_e , attained by the HL after a large number of SL hysteresis loops. It reads

$$F = F_0 + \frac{1}{2} \frac{\partial^2 F}{\partial M^2} \Big|_{M=M_e} (M - M_e)^2. \quad (4-7)$$

A straightforward result using Eq. (4-1), (4-7) and the proportionalities above, $\mu_0 H_B(n) = \frac{c_1}{c_2} M(n)$, is the implicit sequence of Eq. (4-3) and corresponding explicit expression of Eq. (4-5).

From the derivation it can be shown,

$$K = -\frac{\tau}{\xi} c_2^2 \frac{\partial^2 F}{\partial M^2} \Big|_{M=M_e} < 0 \quad (4-8)$$

The main objective of the present section is to extend our theoretical analysis of training effect by deriving an explicit temperature dependence of K . The K -values of latter function $K(T)$ entered the theory as a fitting parameter only. We use Eq. (4-5) to obtain these K -values for all of our training data $\mu_0 H_B$ vs n like those shown exemplarily in Fig. 4.12. Least squares fits of the function $K(T)$ to these K -values will evidence the consistency of the theory. Subsequently we outline the derivation of the function $K(T)$ from Eq. (4-8).

In order to obtain $K(T)$, we initially need to derive the temperature dependence of

$\left. \frac{\partial^2 F}{\partial M^2} \right|_{M=M_e}$. To do so, we compare Eq. (4-7) with the Landau expansion

$$F = F_0 + \frac{1}{2}aM^2 + \frac{1}{4}bM^4 - HM \quad (4-9)$$

in the vicinity of $M=0$ where $a = a_0(T - T_C)$, T_C is the Curie temperature of the HL and $a_0, b > 0$ are the constants. From Eq. (4-9) we obtain

$$\left. \frac{\partial^2 F}{\partial M^2} \right|_{M=M_e} = a + 3bM_e^2 \quad (4-10)$$

where M_e is the solution of $aM_e + bM_e^3 - H = 0$ derived from $\left. \frac{\partial F}{\partial M} \right|_{M=M_e} = 0$. Since the

magnetic fields applied during the training cycles are small in comparison to the HL coercive fields the Zeeman term in Eq. (4-9) is negligible and the equilibrium magnetization M_e can be expressed by the simple Landau expression $M_e = \sqrt{-a/b}$

allowing to simplify Eq. (4-10) which then reads $\left. \frac{\partial^2 F}{\partial M^2} \right|_{M=M_e} = 2bM_e^2 = -2a = 2a_0(T_C - T)$

. Substituting the latter expression into Eq. (4-8) we obtain

$$K = -\frac{\tau}{\xi} c_2^2 a_0 (T_C - T) \quad (4-11)$$

Note that the simple Landau expression away from T_C is not completely accurate. However, the temperature dependence of the damping constant, ξ , compensates this problem to a large extent, resulting in $K(T \rightarrow 0) \rightarrow 0$.

The damping constant is known to be temperature dependent in other ferroic systems like organic thin film ferroelectrics¹⁹⁰ having the functional form

$$\xi \propto \sqrt{T} \exp\left(\frac{2U}{kT}\right) \quad (4-12)$$

with U being an energy barrier. The latter has the microscopic interpretation of a dipole/spin-flip energy. Using mean-field arguments this energy is given by $U = \langle z J s^2 \rangle$ where z is the number of nearest neighbors, J is the exchange energy, s is the spin quantum number, and $\langle \dots \rangle$ denotes an average over the distribution of local configurations in the pinning layer alloy CoPtCrB. In mean field approximation¹⁹¹ U is related to T_C as $U = 3s^2 k_B T_C / (s(s+1))$. The Slater-Pauling (SP) curve, in particular the strong deviations from the SP curve for Co-alloys,¹⁹² is used to estimate an effective value of s for the alloy of CoPtCrB. Taking the strong suppression of the atomic magnetic moment in Co-alloys into account we use $s=1/2$ to obtain $U = k_B T_C$. Using this result of the energy barrier U and substituting Eq. (4-12) into Eq. (4-11) we obtain the temperature dependence of the crucial fitting parameter, K , involved Eq. (4-5)

$$K = -\frac{P}{\sqrt{T}} e^{-2T_C/T} (T_C - T), \quad (4-13)$$

where $P > 0$ is a fitting parameter of Eq. (4-13). Note that the Eq. (4-13) has two unknowns P and T_C . In the next section we evaluate the Curie temperature of HL, T_C through independent experimental procedure yielding Eq. (4-13) as one parameter fit to the K -values.

4.4.5. TEMPERATURE DEPENDENCE OF THE CHARACTERISTICS OF THE TRAINING EFFECT

The left axis of Fig. 4.16 shows the coercivity data $\mu_0 H_C$ vs. T of the HL. The coercivity values are obtained from the overall hysteresis loops displayed in Fig. 4.10. Note, however, that the visible HL coercivity, H_C^{broad} , in Fig 4.10 has contributions from the intrinsic HL coercivity, H_C , and from a coupling induced HL loop broadening as well. The values of H_C^{broad} are obtained from the overall loops after subtracting the SL magnetization. The correction with respect to the coupling induced broadening is a small but somewhat involved effect. Note that the H_C of the HL due to SL/HL coupling is given by the bias field created by the fully saturated SL. Thus the bias coming from the SL and affecting the HL coercivity has to be related to the bias onto the SL that a fully magnetized HL generates. It can be quantitatively written as $H_B^{HL} m_{HL} = H_B^{SL} m_{SL}$, where H_B^{HL} and H_B^{SL} are coupling induced coercivity broadening of HL and SL, while m_{HL} and m_{SL} are magnetization of HL and SL, respectively. The SL coupling contribution has to

be subtracted to get the genuine HL coercivity. This correction is done by using

$$H_C = H_C^{broad} - \left[H_B^{SL} m_{SL} / m_{HL} \right].$$

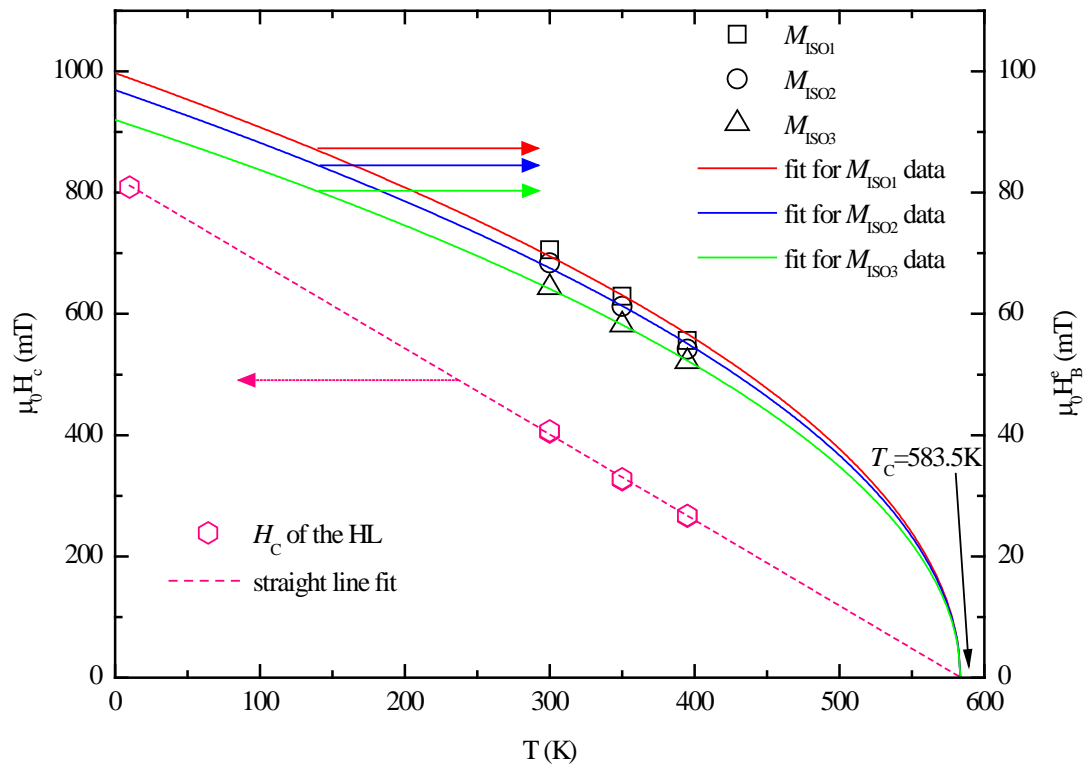


Figure 4.16. HL coercivity $\mu_0 H_C$ vs. T (left axis). Hexagons represent experimental data; the dotted line is an empirical linear best fit. Its extrapolation to $\mu_0 H_C = 0$ provides an estimate of the HL Curie temperature $T_C = 583.5\text{K}$. The right axis shows the equilibrium bias field $\mu_0 H_B^e$ vs. T for all three isomagnetization set fields, M_{ISOj} . Squares (M_{ISO1}), circles (M_{ISO2}) and triangles (M_{ISO3}) are the experimental data where lines are single parameter best fits of Eq. (4-14).

The hexagons in left of frame of Fig. 4.16 are experimental $\mu_0 H_C$ vs. T data. The corresponding dotted line is the best linear fit. Extrapolation down to $\mu_0 H_C = 0$ yields the HL Curie temperature $T_C = 583.5\text{K}$. The linear extrapolation is the best we can do in the

absence of a rigorous theory for $\mu_0 H_C$ vs. T . In fact from the section 4.3.3, a simple Landau expression $aM_e + bM_e^3 - H = 0$ predicts the non linear behavior of the intrinsic coercivity $H_C = \sqrt{\frac{-4[a_0(T - T_C)]^3}{27b}}$ which approaches the T -axis slower than the linear extrapolation implying a higher value of T_C [Eq. (4-6)]. However, the intrinsic coercivity considered in this expression is relevant for ideal ferromagnets but not the real ferromagnets of the present situation. Moreover, $T_C = 583.5$ K obtained from the linear extrapolation is strongly supported by the fits of $\mu_0 H_B^e$ vs. T as discussed follows.

The right axis of Fig. 4.16 shows the equilibrium bias fields $\mu_0 H_B^e$ vs. T for the initializations M_{ISO1} (squares), M_{ISO2} (circles) and M_{ISO3} (triangles). The lines represent single parameter fits of the function,

$$\mu_0 H_B^e(T) = \mu_0 H_B^e(T = 0) \sqrt{\frac{T_C - T}{T_C}}, \quad (4-14)$$

yielding $\mu_0 H_B^e(T = 0) = 99.73 \pm 0.97$, 96.93 ± 0.82 and 92.01 ± 0.17 mT for M_{ISO1} , M_{ISO2} and M_{ISO3} , respectively. Note that the successful fit of Eq. (4-14) reconfirms the applicability of the simple Landau expression for the temperature dependence of the HL magnetization which leads to Eq. (4-11). Moreover, Eq. (4-14) also confirms estimated value of T_C of the HL from Fig 4.16 [left frame].

Knowing the value of T_C of the HL from Fig. 4.16, we plot K vs. T for all K -values obtained from least-square fits of Eq. (4-5) to the experimental $\mu_0 H_B$ vs. n data of Fig. 4.12. The corresponding results of K vs. T are shown in Fig 4.17.

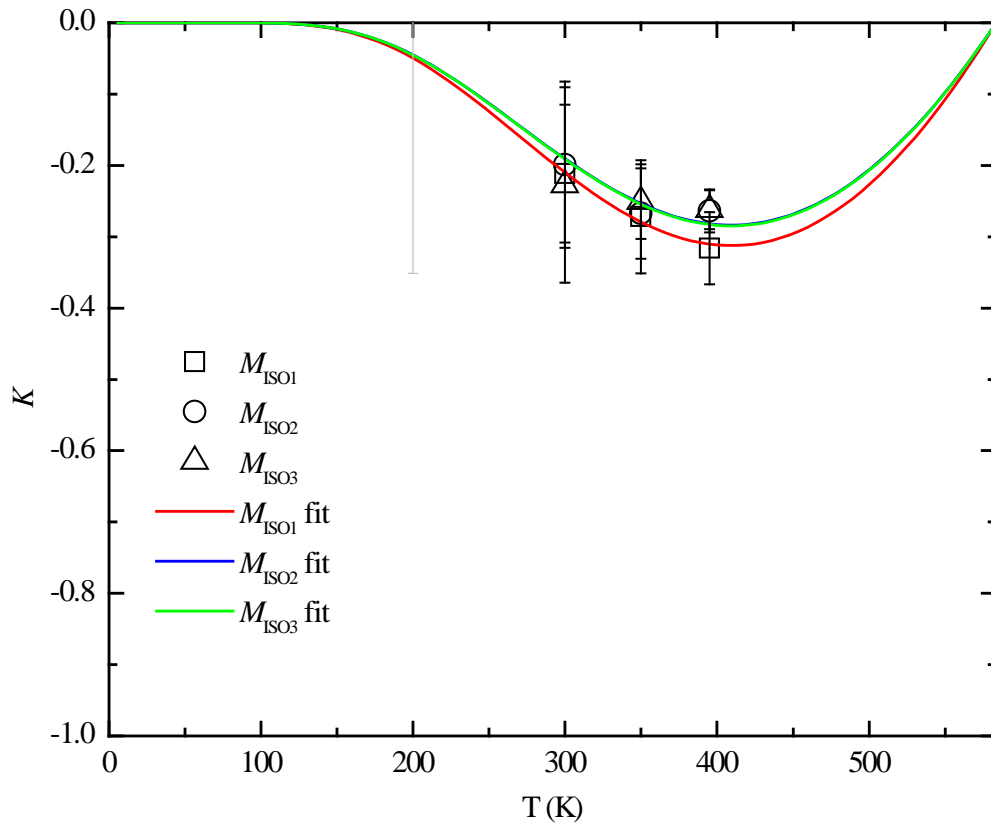


Figure 4.17. K vs. T for the three isomagnetization set fields. Initializations M_{ISO1} (squares), M_{ISO2} (circles) and M_{ISO3} (triangles) are the experimental data. Lines are single parameter best fits of Eq. (4-13). Representative error bars are shown for M_{ISO1} , M_{ISO2} , M_{ISO3} which are calculated from Eq. (4-16).

The experimental K -data in Fig. 4.17 originates from training initializations M_{ISO1} (squares), M_{ISO2} (circles) and M_{ISO3} (triangles). Lines represent the results of a best fits of

Eq. (4-13) to the respective data set where P is the single free fitting parameter with $P=0.626\pm 0.009$, 0.570 ± 0.023 , and $0.572\pm 0.0396 \text{ K}^{-1/2}$ for M_{ISO1} , M_{ISO2} and M_{ISO3} , respectively. The data of M_{ISO1} , M_{ISO2} and M_{ISO3} fall within the limits of error bars. The following discussion describes of how these error bars are obtained.

While the K -values shown in Fig. 4.17 are determined from best fits of Eq. (4-5) to respective training data. An alternative determination of optimized K -values is obtained from the expression

$$K = \frac{\sum_{n=1}^{N-1} (H_B(n) - H_B^e)(H_B(n+1) - H_B(n))}{\sum_{n=1}^{N-1} (H_B(n) - H_B^e)^2} \quad (4-15)$$

Here H_B^e is an input obtained from the fit of Eq. (4-5). Eq. (4-15) is from a least squares condition using Eq. (4-3). Expression (4-15) is used to calculate the standard deviation S_K of K from Gauss' law of error propagation which reads

$$S_K = \sqrt{\sum_{n=2}^{N-1} \left(\frac{\partial K}{\partial H_B(n)} \Delta H_B(n) \right)^2} \quad (4-16)$$

where $\Delta H_B(n)$ is the error in the bias field of the n^{th} training loop. The derivatives entering S_K are calculated from Eq. (4-15) and read

$$\frac{\partial K}{\partial H_B(n)} = \frac{(H_B(n-1) + H_B(n+1) - 2H_B(n))}{\sum_{n=1}^{N-1} (H_B(n) - H_B^e)^2} - 2K \frac{(H_B(n) - H_B^e)}{\sum_{n=1}^{N-1} (H_B(n) - H_B^e)^2}. \quad (4-17)$$

With $\Delta\mu_0 H_B(n) \approx 0.1 \text{ mT} \quad \forall n$ it is straight forward to numerically determine S_K . The results of this analysis are shown for all three isomagnetizations of M_{ISO1} , M_{ISO2} , M_{ISO3} in Fig. 4.17 as error bars. Note that the magnitude of the error bars increases with decreasing temperature. When applying the same analysis to the $T=200 \text{ K}$ data set where $\mu_0(H_B^e - H_B(1)) \approx 0.1 \text{ mT}$ is extremely small $S_K = 0.3$ in turn becomes even significantly larger than the theoretically expected value of $|K| = 0.05$. Note that this increase in the error bar takes place despite the fact that the absolute accuracy of the bias fields remains $\Delta\mu_0 H_B(n) \approx 0.1 \text{ mT}$. Hence it is obvious that any attempt to determine K -values at low temperatures where $\Delta H_B = H_B^e - H_B(1) \rightarrow 0$ will become experimentally difficult.

Intuitively $K(T \geq T_C) = 0$ has to be fulfilled because $H_B(n+1) = H_B^e = 0 \quad \forall n \geq 1$ at $T \geq T_C$ reflecting the absence of biasing and, hence, training effect. Similarly $K(T=0) = 0$ holds, however, it reflects the non trivial situation where a non-zero bias field can be accompanied by zero training effect. This means instead of zero bias field associated with zero pinning layer magnetization a non zero pinning layer magnetization can be frozen-in at $T=0$. Domain walls are pinned and the absence of thermal activation keeps the pinning layer in the initial domain state. In the framework of Eq. (4-5) this freezing behavior is reflected by a diverging damping constant [see Eq. (4.11)] which give rise to $K=0$. In addition, $K=0$ state at $T=0$ is approached with $dK/dT|_{T=0} = 0$ similar to the asymptotic behavior of equilibrium thermodynamic properties obeying the third law of thermodynamics.

It is hard to imagine any arbitrary “single” parameter fitting function which is consistent with the constraints $K(T=0)=0$, $dK/dT|_{T=0}=0$ and $K(T=T_C)=0$ providing the quality of the fits shown in Fig. 4.17. Moreover, the fitting parameters of Eq. (4-13) and Eq. (4-14) reflect the ratio $P_{ISO1}/P_{ISO2}=1.10 \approx \left(H_B^e(T=0, Iso1)/H_B^e(T=0, Iso2)\right)^2 = 1.06$ as expected from Eq. (4.8), (4.13) and the proportionality between H_B^e and M_e .

In summary, it has been demonstrated that in a far reaching analogy to AF/FM exchange bias heterolayers quantitative understanding of the temperature dependence of the training effect is achieved in all FM bilayers. Large training effects reflected by the parameter $-1 \leq K \leq 0$ require thermal activation allowing for triggered changes in the domain structure of the pinning layer but at the same time sufficient thermal stability of the pinning layer magnetization. This competition between thermal activation and stability creates maximum training effects at $T = T_C(\sqrt{41}-5)/2$. The successful modeling of the temperature dependence of the training effect in our all FM bilayer system confirms the consistent description of training behavior in the discretized Landau-Khalatnikov approach.

4.5. DYNAMIC ENHANCEMENT OF THE BIAS FIELD TRAINING EFFECT

In this section, we report on the dynamic enhancement of the training effect in exchange coupled bilayers of soft and hard FM materials. Dynamic enhancement is observed with increasing sweep rates of the applied magnetic field from quasi-static to the fully dynamic range. A generalized theory based upon triggered relaxation in the pinning layer is in excellent agreement with the enhanced training data which evidences once more the universality of our theoretical approach^{110,112} based on Landau-Khalatnikov dynamical equation.

More specifically, we show that the $\mu_0 H_B$ vs. n -dependence of the SL bias field depends on the sweep rate, $r_s = d\mu_0 H / dt$, of the SL hysteresis loops. In addition we show that the value of the equilibrium bias field, $\mu_0 H_B^e = \mu_0 H_B (n \rightarrow \infty)$, reflects the dynamic broadening of the SL hysteresis and follows a power law behavior with respect to the sweep rate. The dynamically altered training effect is quantitatively modeled by generalizing our recent theoretical approach and successfully fitted with our experimental data.

4.5.1. BROADENING OF THE SOFT LAYER HYSTERESIS

AGFM has been used to measure the minor loops in the field interval $0 \leq \mu_0 H \leq 140$ mT. The data sets are taken after saturating the bilayer in $\mu_0 H = 0.8$ T and subsequent partial demagnetization of the pinning layer in a static set field of $\mu_0 H_{set} = -0.31$ T. The results are shown in Fig. 4.18.

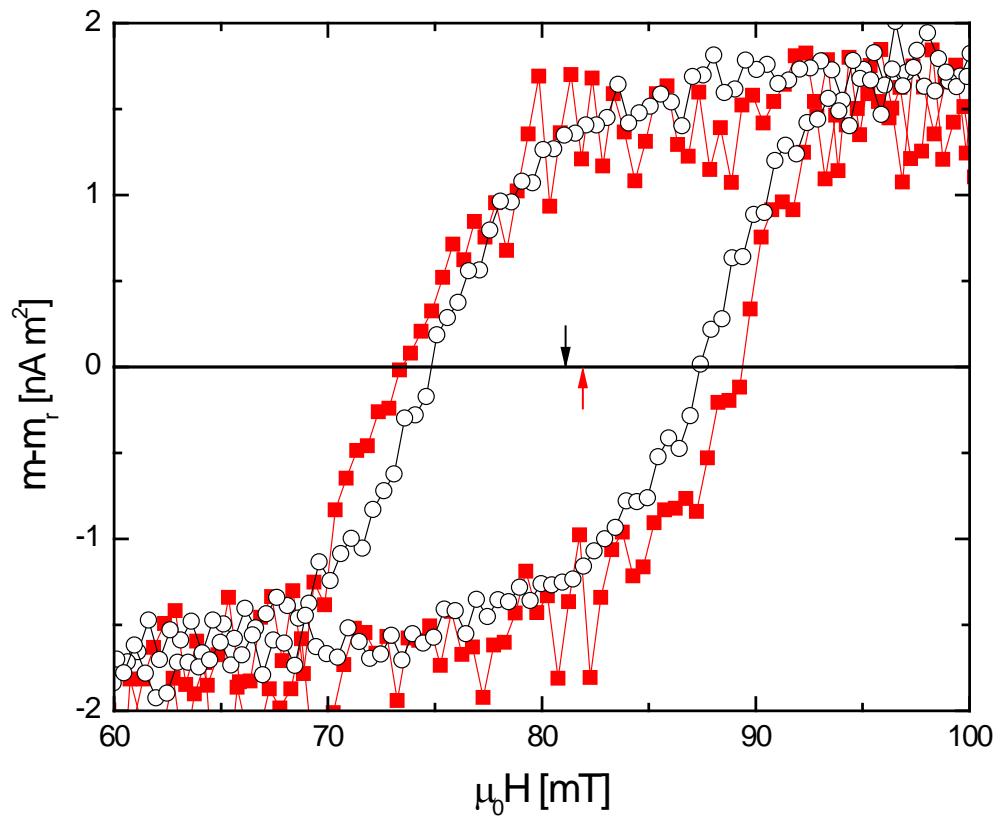


Figure 4.18. Dynamic broadening of the SL loop for sweep rates increasing from $r_s=0.2$ mT/s (circles) to $r_s=5$ mT/s (squares). The loop broadening is accompanied by a dynamical enhancement of the bias field as indicated by down ($r_s=0.2$ mT/s) and upwards ($r_s=5$ mT/s) pointing arrows.

Fig. 4.18 shows the dynamic broadening of the SL hysteresis when the sweep rate is increased from $r_s = 0.2$ mT/s (circles) to $r_s = 5$ mT/s (squares). The downwards and upwards pointing arrows mark the bias fields for $r_s = 0.2$ mT/s and $r_s = 5$ mT/s, respectively, indicating the correlation between dynamic loops broadening as well the increase of the bias field. Note that corresponding reference measurements with a Ni gauge sample show no sweep rate dependent broadening of the hysteresis. Therefore we confirm the observed fact as the dynamic broadening that is related to intrinsic behavior of the SL but not an experimental artifact.

4.5.2. ENHANCED TRAINING EFFECT WITH SWEEP RATES

The training effect, $\mu_0 H_B$ vs. n , is performed on SL of 20 subsequently measured minor hysteresis loops. All minor loops are measured in the field interval $0 \leq \mu_0 H \leq 140$ mT and the results are displayed in Fig. 4.19.

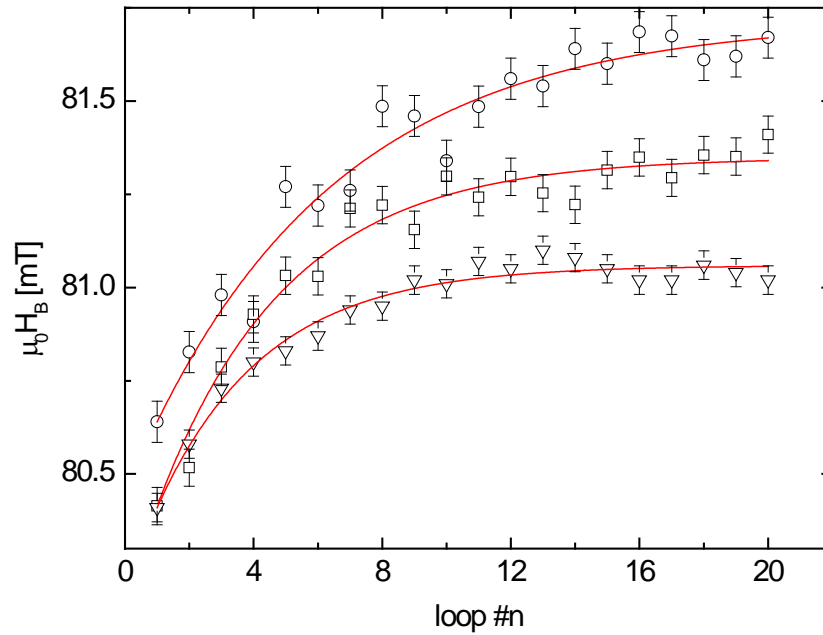


Figure 4.19. Training effect $\mu_0 H_B$ vs n of the HL-SL bilayer for various sweep rates $r_s = 5$ mT/s (circles), 1.67 mT/s (squares) and 1.0 mT/s (down triangles), respectively. The bars reflect the errors in deducing the bias fields from hysteresis loops. The initial magnetization state of the HL is set prior to each training sequence by a set field of $\mu_0 H_{\text{set}} = -0.31$ T after saturation in $\mu_0 H = 0.8$ T. Lines are best fits of Eq. (4-21) to the data.

Fig. 4.19 shows the training effect of the FM bilayer for various sweep rates $r_s = 5$ mT/s (circles), 1.67 mT/s (squares) and 1.0 mT/s (down triangles). Each $\mu_0 H_B$ vs. n data set shows the bias fields of 20 subsequently measured minor hysteresis loops of the SL. The data clearly show that the strength of the training effect increases with increasing sweep rate as well the increase in relaxation is spread out over more number of SL hysteresis loops. The lines are fits of theoretical model [Eq. (4-21)] which is subsequently outlined to describe the loop broadening in SL as well enhancement in the training effect.

4.5.3. THEORETICAL APPROACH

The triggered relaxation in the pinning HL is described by discretized Landau-Khalatnikov dynamical equation [Eq. (4-1)]. Discretization of LK equation is achieved by replacing the continuous change of the interface magnetization, \dot{S} , of the HL with a temporal average according to

$$\dot{S} \rightarrow \frac{1}{\tilde{\tau}} \int_{t_n}^{t_n+\tilde{\tau}} \dot{S} dt = \frac{S(t_n + \tilde{\tau}) - S(t_n)}{\tilde{\tau}} \quad (4-18)$$

where

$$\tilde{\tau} = \begin{cases} \tau & \text{if } \Delta t \gg \tau \\ \Delta t & \text{if } \Delta t \ll \tau \end{cases} \quad (4-19)$$

Here $\Delta t = 2\mu_0\Delta H_{\max} / r_s$ is the experimental time interval required for the measurement of SL hysteresis loop in the field range $0 \leq \mu_0 H \leq \mu_0\Delta H_{\max}$ (=140 mT). τ is the intrinsic time scale for non truncated relaxation of the pinning layer magnetization. The time interval between two subsequent loops is virtually free from relaxation and is, hence, not involved in Eq. (4-19). Note that the experimental finding of an increasing training effect with increasing sweep rate confirms that the training does not depend on the time the pinning layer is exposed to the external magnetic field. In fact the exposure time actually decreases with increasing r_s . Instead, as shown earlier (section 4.3.3, Fig

4.5) the training is a discontinuous process triggered by the SL hysteresis loop while relaxation is absent otherwise.

Note that the so far presented results on training effect in chapter 3 and chapter 4 are measured in quasi-static limit of low sweep rates. In this static regime the experimental time interval of an individual hysteresis loop is large enough to allow for triggered but subsequently unperturbed relaxation of S . This free relaxation of the pinning layer magnetization takes place on a characteristic time scale ($\Delta t \gg \tau$) such that $\tilde{\tau} \rightarrow \tau$. On the other hand, in the limit of fast magnetic field sweeps when Δt becomes smaller than characteristic time τ , truncation of the triggered relaxation process sets in which is expressed by $\tilde{\tau} \rightarrow \Delta t$.

The above description of the crossover from truncated to free relaxation of the pinning layer can be considered in the framework of a mechanical analogue of an “over-critically damped oscillator”. The effect of the SL hysteresis loop on the HL magnetization relaxation resembles a time dependent external driving force in this mechanical picture. The general solution of the differential equation of a damped driven oscillator requires the superposition of a transient exponential (free relaxation) and a stationary component (truncated). In the case of high sweep rates or fast varying forces the transient solution is virtually constant on the time scale Δt where the external force significantly changes. Since the weighting of the transient contribution decays exponentially for $\Delta t \rightarrow 0$ or high sweep rates, the crossover from $\tilde{\tau} \approx \tau$ to $\tilde{\tau} \approx \Delta t$ is given by

$$\tilde{\tau} = \tau \left(1 - e^{-\Delta t / \tau}\right), \quad (4-20)$$

where $\Delta t = 2\mu_0\Delta H_{\max}/r_s$. The crossover expression (4-20) obeys the above mentioned conditions of Eq. (4-19) which in fact reflects the key element of the dynamic generalization of our former quasi static approach outlined in section (4.3.5). Replacing the characteristic time constant τ by the dynamically generalized $\tilde{\tau}$ of Eq. 4-20) throughout the derivation of $\mu_0 H_B = \mu_0 H_B(n)$ yields (refer section 4.3.5)

$$\mu_0 H_B(n) = (\tilde{K} + 1)^{n-1} \left\{ \mu_0 H_B(n=1) - \mu_0 H_B^e \left[\frac{(\tilde{K} + 1)^{n+1} - 1}{\tilde{K}(\tilde{K} + 1)^{n-1}} - (\tilde{K} + 2) \right] \right\}. \quad (4-21)$$

Eq. (4-21) is identical to the quasi static expression of Eq. (4-5) when replacing the constant $K \propto \tau$ by $\tilde{K} \propto \tilde{\tau}$. Lines in Fig. 4.19 show the best fits of Eq. (4-21) to $\mu_0 H_B$ vs. n data using \tilde{K} and $\mu_0 H_B^e$ as fitting parameters.

4.5.4. SWEEP RATE DEPENDENCE OF THE CHARACTERISTICS OF THE TRAINING EFFECT AND EQUILIBRIUM BIAS FIELD

We furthermore investigated the sweep rate dependence of those crucial parameters, \tilde{K} vs. r_s and $\mu_0 H_B^e$ vs. r_s , involved in Eq. (4-21) and the results are presented Fig. 4.20.

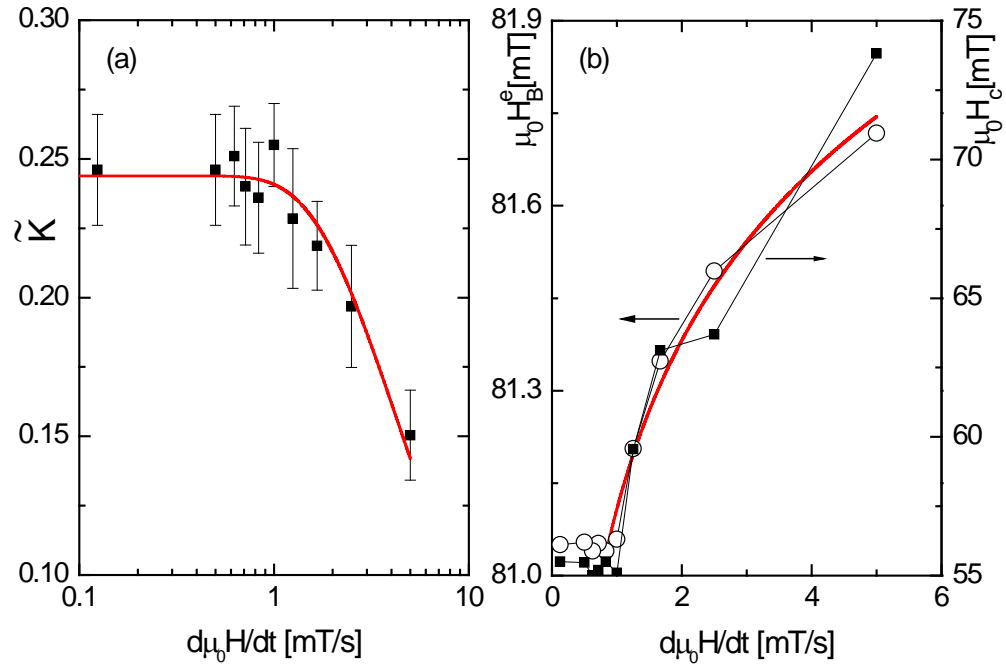


Figure 4.20. (a) Sweep rate dependence of the fit parameter \tilde{K} resulting from the fits shown in Fig. 4.17 and additional data sets (not shown). The bars reflect the errors resulting from a best fit using the Levenberg-Marquardt algorithm. The \tilde{K} vs. r_s data are in turn fitted to $\tilde{K} = c_1(1 - e^{-c_2/r_s})$ in accordance with Eq. (4-20). The line is the result of the best fit. (b) Sweep rate dependence of the fit parameter $\mu_0 H_B^e$ (circles, left frame) and the SL loop width $\mu_0 H_c = \mu_0(H_{c_2} - H_{c_1})/2$ (squares, right frame). The line is a best fit of the empirical power law $\mu_0 H_B^e = A[r_s - r_s(1 \text{ mT/s})]^\eta$ with $\eta = 3 \times 10^{-3}$ [Ref. 87].

In Fig. 4-20(a), the values of squares obtained from theoretical fit of Eq. (4-20) and error bars indicated here are the fixed inaccuracy involved in \tilde{K} . In accordance with Eq. (4-20) the line in Fig. 4.20(a) is the best fit of $\tilde{K} = c_1(1 - e^{-c_2/r_s})$, where the fitting parameter $c_1 = 0.244 \pm 0.003$ takes into account the proportionality between \tilde{K} and $\tilde{\tau}$ while $c_2 = 4.3 \pm 0.3$ mT/s accounts for the proportionality between Δt and the inverse

sweep rate. The two-parameter fit is in excellent agreement with the data confirming the overall approach and its dynamic generalization.

Fig. 4.20 (b) (circles, left frame) shows the sweep rate dependence of the fitting parameter $\mu_0 H_B^e$ obtained from best fits of Eq. (4-21) to the respective training data (see Fig 4.19). The squares in the right frame of Fig 4.20 shows the sweep rate dependence of the coercivity $\mu_0 H_c$ where $\mu_0 H_c = \mu_0 (H_{c_2} - H_{c_1})/2$ is the width of the SL loop determined by the intercepts $\mu_0 H_{c_{1,2}}$ of the loop $m - m_r$ vs. $\mu_0 H$ with the field axis. Clearly, there is a strong correlation between the bias field and the loop width. This type of correlation is a well-known phenomenon in EB systems.^{102,193,194} The origin of the sweep rate dependence of $\mu_0 H_B^e$ is therefore reduced to the dynamic broadening of the SL loop. The solid line in Fig. 4.20(b) represents an empirical power law fit suggested for AF/FM EB systems in Ref. [87]. The plateau like behavior of $\mu_0 H_B^e$ vs. r_s for $r_s < 1\text{mT/s}$ (see Fig. 4.20(b)) corresponds to the asymptotic approach $\tilde{K}(r_s < 1\text{mT/s}) \rightarrow 0.244$ (see Fig. 4.20(a)) indicating the onset of quasi-static behavior consistent throughout both data sets.

4.5.5. SWEEP RATE DYNAMICAL ENHANCEMENT IN AF/FM HETEROSYSTEM

Recently, the sweep rate dependence of the EB training has been studied in the antiferromagnetic/FM heterosystem $\text{Ni}_{81}\text{Fe}_{19}$ (6nm)/ $\text{Ir}_{22}\text{Mn}_{78}$ (2nm). By reanalyzing the

data presented in Ref. [87], we evidence the universality of the dynamic training delay effect as well as our data analysis methodology. Moreover, we show that the sweep rate dependence of the fitting parameters is consistent with the process of truncation quantified in Eq. (4-20).

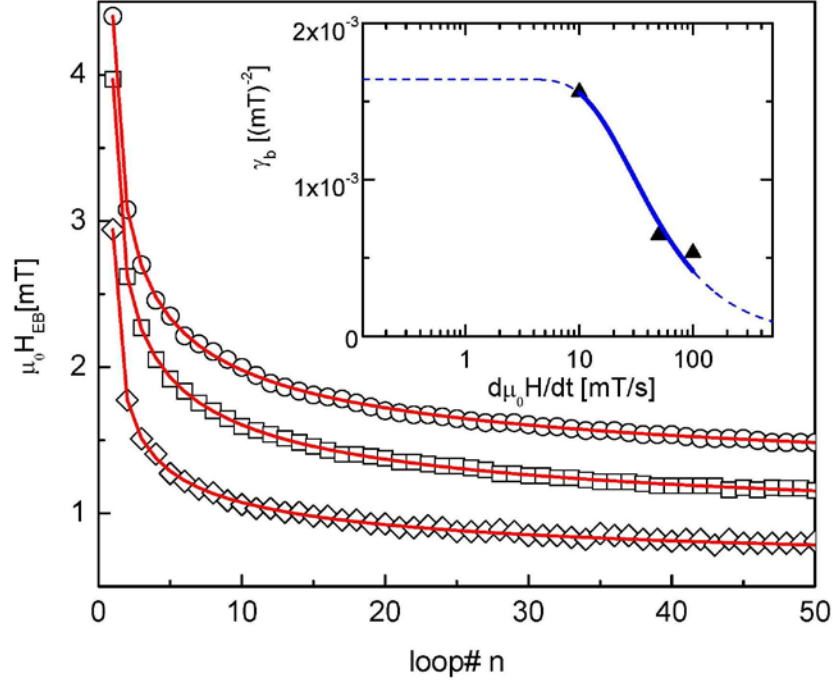


Figure 4.21. Training $\mu_0 H_B$ vs. n of a conventional AF/FM exchange bias heterostructures for various sweep rates $r_s = 10$ mT/s (rhombhedra), 50 mT/s (squares) and 100 mT/s (circles). Data (open symbols) are taken from Ref. [87]. Lines are the best fits of the sequence (4-22). Note that the lines have physical meaning only at integer values. The inset shows the sweep rate dependence of the fitting parameter γ_b . The solid line in turn is the best fit of $\gamma_b = c_b (1 - e^{-c_b/r_s})$ to the data γ_b vs. r_s . The dashed line is an extrapolation of the fit.

Open symbols in Fig. 4.21 show the experimental results obtained by Heiwan et al. for sweep rates $r_s = 10$ mT/s (rhombhedra), $r_s = 50$ mT/s (squares) and $r_s = 100$ mT/s (circles). Lines represent the best fits of our theoretical approach based on the discretized

LK-equation for AF/FM heterostructures. In addition to our basic approach of training effect for AF/FM bilayers as developed in Ref. [110,112], we extended here the free energy expansion with a correction of the leading term. By doing so we achieve virtually perfect fitting results for $1 \leq n \leq 50$ from

$$\mu_0 (H_{EB}(n+1) - H_{EB}(n)) = -\gamma_b \left(\mu_0 (H_{EB}(n) - H_{EB}^e) \right)^3 - \gamma_c \left(\mu_0 (H_{EB}(n) - H_{EB}^e) \right)^5 \quad (4-22)$$

The new parameter γ_c results from the higher order expansion of the free energy and hence $|\gamma_c| \ll |\gamma_b|$. Both, γ_b and γ_c are proportional to $\tilde{\tau} = \tilde{\tau}(r_s)$ giving rise to their respective sweep rate dependence in accordance with Eq. (4-20). The implicit sequence (4-22) is a straightforward refinement of our recent approach^{110,112} outlined in section (1.2.1) and evidenced for diverse exchange coupled systems.^{97,179} Note that Eq. (4-22) involves three fitting parameters and the identical number of free parameters is required for the power law description first introduced in Ref. [83]. However, the physically motivated Eq. (4-22) provides much better fitting results for all sweep rates and explains in a consistent manner the r_s -dependence of the fitting parameters. The inset of Fig. 4.20 shows data of γ_b obtained from Eq. (4-22) vs. r_s . The solid line is the best fit of Eq. (4-20) to the data points. The dashed line displays the extrapolated result of the fit towards the quasi static [left extrapolation] as well as the high sweep rate regime [right extrapolation]. The result is in accordance with the predicted exponential behavior of $\tilde{\tau} = \tilde{\tau}(r_s)$ [Eq. (4-20)].

Summarizing the story, we have shown enhancement in the bias field of soft-hard bilayers with the increase of sweep rate of the magnetic field. The increase of the bias

field is also associated with a dynamic broadening of the soft layer hysteresis. Both, the bias field increase and the SL loop broadening follow the same power law behavior above a quasi-static limit. Furthermore, the training effect is dynamically spread out with sweep rate. This effect is described here in the framework of a dynamically generalized theoretical approach, which is in excellent agreement with our experimental data. The analysis of the sweep rate dependence of the fitting parameters evidences in turn the key element of the dynamically generalized theory which is based on truncated relaxation of the pinning layer magnetization. We also demonstrate that the same generalization which models the dynamic enhancement of the training effect in FM bilayers also applies to conventional exchange bias systems when the free energy is adapted to the AF order of the pinning layer.

CHAPTER 5

COMPARISON BETWEEN AF/FM AND HARD/SOFT FERROMAGNETIC BILAYERS

In my thesis, I have presented two kinds of exchange coupling heterostructures: (i) AF/FM bilayers, and (ii) hard/soft FM bilayers. The interface coupling phenomena of the exchange bias and the biasing effect in all FM bilayers are successfully discussed in both CoO(AF)/Co(FM) and CoPtCrB(HL)/CoCr(SL) systems, respectively. Furthermore, the training effect is also studied in both systems with a special attention on its thermal evolution. Now, here in the conclusion part of my thesis, I will bring these two different systems under one umbrella and show the similarities and differences between them.

In both systems the pinning layer [AF and HL] is coupled with pinned layer [FM and SL] and shifts hysteresis loops of the latter along the magnetic field axis by an amount equal to the exchange bias [AF/FM] and bias field [HL/SL], respectively. However, in the latter case the hysteresis loop of the pinned SL also shifts along the vertical axis by an amount equivalent to remanent magnetization of the pinning HL. Furthermore, the pinning layers in both of these systems show significant changes in its interface magnetization due to spin configurational rearrangements generated by successively cycling the pinned layer through its magnetic hysteresis loop. This is referred as the training effect and it occurs only when the pinning layer is at a perturbed state which is away from its equilibrium condition. This non-equilibrium state of the AF

is achieved in AF/FM heterostructures by means of magnetic field-cooling procedure of the system from above Néel temperature of the antiferromagnet to a lower temperature. On the other hand, temperature cooling procedure is not required for HL/SL heterostructures. However, a definite set magnetic field needs to be applied on the HL to drag its magnetization away from its equilibrium state and, therefore, it initializes the bias field. Figure 5.1(a) depicts the comparison of AF/FM and HL/SL bilayers after exchange bias and bias field, respectively, have been initialized. Subsequently cycled hysteresis loops of pinned ferromagnet and SL trigger the spin configurational changes in the pinning layer which drive both antiferromagnet and HL closer towards perfect long range AF and FM order, respectively, as shown in Fig 5.1(b) and (c). This approach towards a new quasi-equilibrium spin configuration accompanied by decay (improvement) of the interface magnetization of antiferromagnet (HL) reducing (enhancing) the magnitude of exchange bias (bias field).

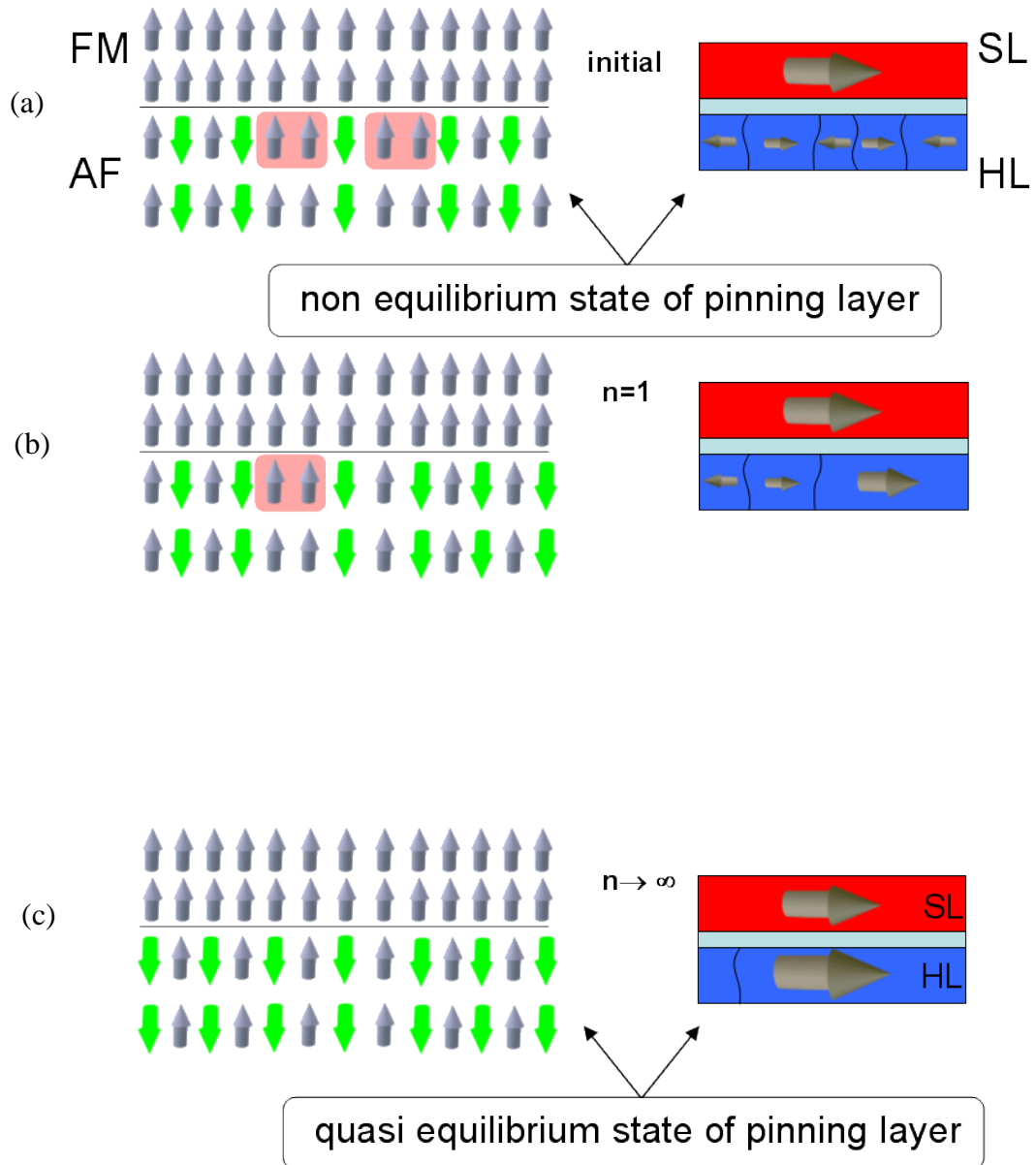


Figure 5.1. Comparison of the training effect in an AF/FM and a HL/SL heterostructures. The left column depicts three sketch of an AF/FM EB heterostructure after (a) initializing EB, (b) the first and (c) a very large number of hysteresis loops. The non equilibrium AF domain state carries magnetization to the interface (horizontal line). Neighboring spin pairs with non compensating moment contributing to S_{AF} are highlighted. The quasi equilibrium state reflects the asymptotic approach of nearly perfect AF long range order. S_{AF} is reduced and so is the EB field. The right column depicts sketches of an HL/SL heterostructure after (a) initializing a FM domain state, (b) the first SL hysteresis loop and (c) after a very large number of hysteresis loops. The non equilibrium FM domain state reduces the HL interface magnetization. The latter recovers on subsequent cycling when the domain state asymptotically approaches nearly perfect FM long range order. [Courtesy: Ref. [5]]

From the experimental point of view, the newly recognized HL/SL systems have vast supremacy over the conventional systems due to the FM nature of its pinning HL. The latter allows a characterization of its magnetization state by means of simple magnetometry. Therefore for the first time, we demonstrate the fact that the deviations from equilibrium in the pinning layer are indeed the driving force behind the training effect.

Both HL/SL and AF/FM bilayers provide particular fact that the relaxation in the pinning layer towards its equilibrium occurs *only* due to the triggered reversal of the pinned layer magnetization. It is also evidenced that the training effect is independent on the waiting time between two consecutive pinned layer hysteresis loops as well the amplitude of the applied magnetic field. This is true in general and applicable to all kinds of exchange bias systems and is undoubtedly evidenced for HL/SL systems in section 4.3.3. Therefore, we use discretized form of the Landau-Khalatnikov dynamical equation by replacing continuous time with time taken for the hysteresis loop of the pinned layer during the measure of training effect.

$$\frac{S_{AF/HL}(n+1) - S_{AF/HL}(n)}{\tau} = -\frac{1}{\xi} \frac{\partial \Delta F}{\partial S_{AF/HL}}$$

The above equation assists in obtaining quantitative description of training effect for both AF/FM [section 1.2.1] and HL/SL [section 4.3.5] systems.

In order to obtain an analytical expression for the training effect, the free energy, ΔF of the pinning layer is expanded in terms of its order parameter. In the case of AF/FM bilayers the free energy of antiferromagnet:

$$\Delta F_{AF} \propto (\eta - \eta_e)^2 \rightarrow \Delta F_{AF} \propto (S_{AF} - S_{AF}^e)^4.$$

Here η represents the order parameter, which is not proportional to interface magnetization of AF S_{AF} , but rather related in a very complex way, *i.e.* $\eta = f(S_{AF})$ as indicated by Eq. (3-5). In contrast, the free energy of HL in the case of HL/SL bilayers:

$$\Delta F_{HL} \propto (\eta - \eta_e)^2 \rightarrow \Delta F_{HL} \propto (S_{HL} - S_{HL}^e)^2.$$

Where S_{HL} represents interface magnetization (proportional to order parameter, η) of the HL. Figure 5.2 shows Landau type free energy landscape for both antiferromagnet and HL and corresponding spin and domain structures, respectively. Dotted red lines are the harmonic approximations in the vicinity of quasi-equilibrium order parameters of AF and HL, respectively.

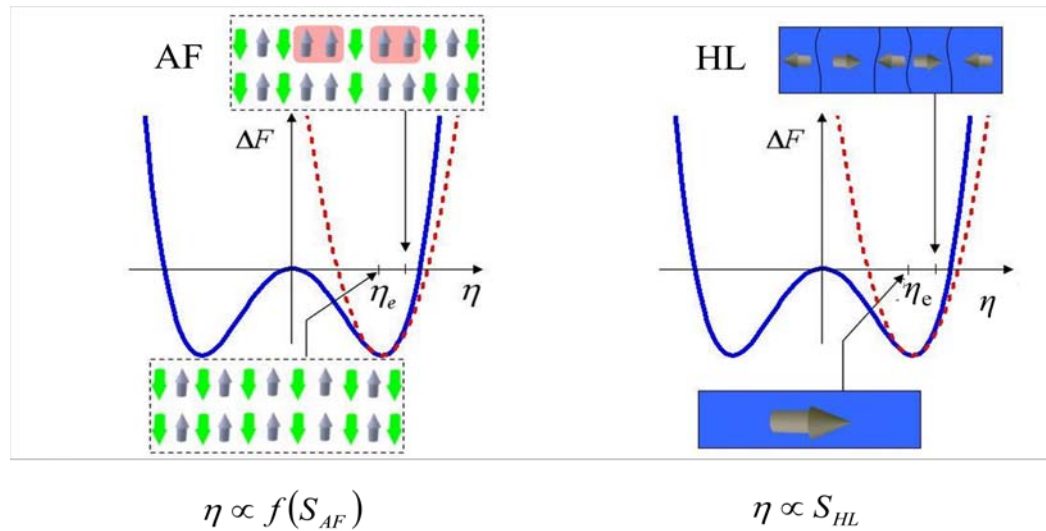


Figure 5.2. ΔF vs. η for AF (left graph) and the HL (right graph) pinning systems. Arrows assign sketches of the spin and domain structure of AF and HL non-equilibrium states (η) and equilibrium states (η_e). Dashed lines show harmonic approximations of the Landau free energy landscape. In case antiferromagnet, the order parameter η is a function of S_{AF} . On the other hand, η of the HL is directly proportional to S_{HL} . [Courtesy: [5]]

The involved relation between order parameter and interface magnetization of antiferromagnet generates an implicit expression [section 1.2.1], where EB of in-progress hysteresis loop of FM depends on its preceding value of EB. On the other hand, the direct proportionality between order parameter and interface magnetization of HL makes it trivial for getting an explicit expression for the training effect in HL/SL bilayers [section 4.3.5], where EB value of n^{th} training loop of SL depends on its 1st training loop.

More precisely, the implicit expression of training effect in AF/FM bilayers reads,

$$\mu_0(H_{EB}(n+1) - H_{EB}(n)) = -\gamma(\mu_0(H_{EB}(n) - H_{EB}^e))^3.$$

Here γ is the temperature-dependent fitting parameter. Note that γ has no upper limit, however, the lower limit is zero. In general, γ describes the characteristics of the training effect but not the strength of the training. However, for the step-like behavior $1/\sqrt{\gamma}$ represents the strength of the training, where $\gamma = \frac{1}{[\mu_0(H_{EB}(n=1) - H_{EB}^e)]^2}$. On the other

hand, the explicit expression of training effect in HL/SL bilayers reads,

$$\mu_0 H_B(n) = (K+1)^{n-1} \left\{ \mu_0 H_B(n=1) - K \mu_0 H_B^e \left[\frac{(K+1)^{n+1} - 1}{K(K+1)^{n-1}} - (K+2) \right] \right\}.$$

Here the fitting parameter K quantifies characteristics of the training effect in HL/SL bilayers. Note that the values of K are limited between -1 and 0. The lower limit of $K=-1$ represents the step-like behavior of the training effect, whereas the upper limit $K=0$

means absolutely no training effect. Note that, however, $K=0$ does not mean that the EB is zero. The values of K do not provide the information on strength of the training effect; rather it characterizes the decay rate of training effect through the consecutive hysteresis loops of SL. The experimental results and corresponding theoretical fits of above equations for the training effect in AF/FM and HL/SL bilayers are shown in Fig 5.3.

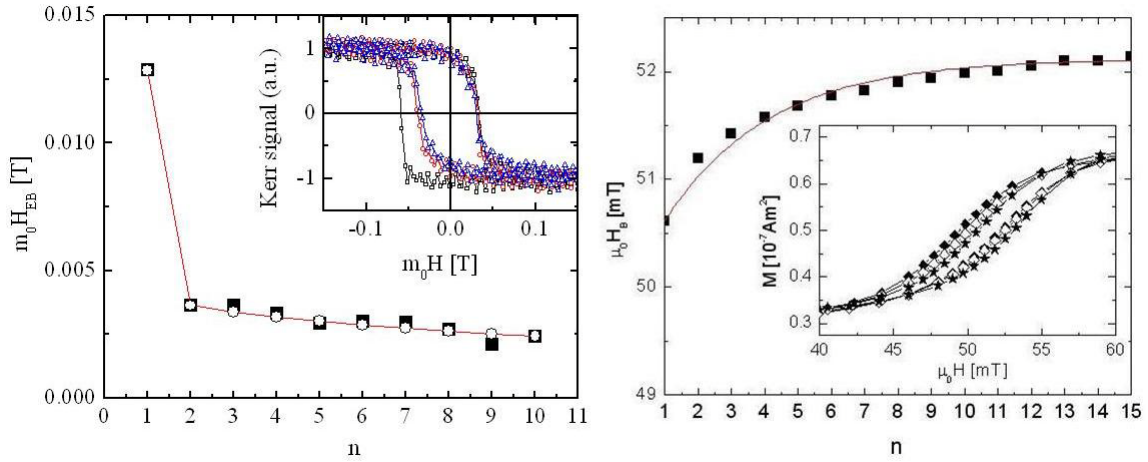


Figure 5.3. [Left frame] $\mu_0 H_{EB}$ vs. n of CoO/Co-wedge sample at Co thickness of 12nm. The solid squares are experimental data measured at $T= 50\text{K}$. Open circles connected with eye-guiding lines are results of a single parameter fit of Eq. (1-17). The inset shows the first (squares), second (circles) and the 10th (triangles) training hysteresis loops. [Right frame] $\mu_0 H_B$ vs. n , of CoPtCrB (15 nm)/Ru (0.7 nm)/ CoCr (3 nm). Solid squares are experimental data measured at $T= 395\text{K}$. The line represents a single parameter best fit of Eq. (4-5). The inset shows the first (solid diamonds), second (open diamonds) and the 15th (stars) hysteresis loop of the SL.

Furthermore, the power law behavior of $1/\sqrt{n}$ -type of training is achieved for the interface magnetization of the antiferromagnet in the limit of infinite number of hysteresis loops of ferromagnet. Conversely, exponential decay, $e^{-n|\ln(K+1)|}$, of interface magnetization of HL is observed for the asymptotic behavior in HL/SL bilayers.

I have also presented thermal evolution of the training effect in both AF/FM and HL/SL bilayer systems in terms of their characteristic decay rates, γ and K , of the training effect, respectively. In order to obtain an explicit expression of temperature dependence of γ , we have used mean-field theory which provides a relation between the primary and secondary order parameter, η to the magnetization m_{AF} of the AF [section 3.1.4]. The final expression for thermal evolution γ reads:

$$\gamma(T) = C \left(\frac{\eta_e(T) \tanh \left[\frac{T_B \eta_e(T)}{T} \right]}{T \left\{ T \left(1 + \cosh \left[\frac{2T_B \eta_e(T)}{T} \right] \right) - 2T_B \right\}} \right)^2.$$

Here C is phenomenological constant. In contrast, the temperature dependence of K is obtained from the simplest Landau expression which provides the relation between free energy of HL and its *only* order parameter m_{HL} [section 4.4.4]. The resulting expression of the thermal evolution of K follows:

$$K(T) = -\frac{P}{\sqrt{T}} e^{-2T_c/T} (T_c - T).$$

Here P is phenomenological constant. The validity of both these theoretical models is evidenced by the successful fitting to the experimental data as shown in the figure below.

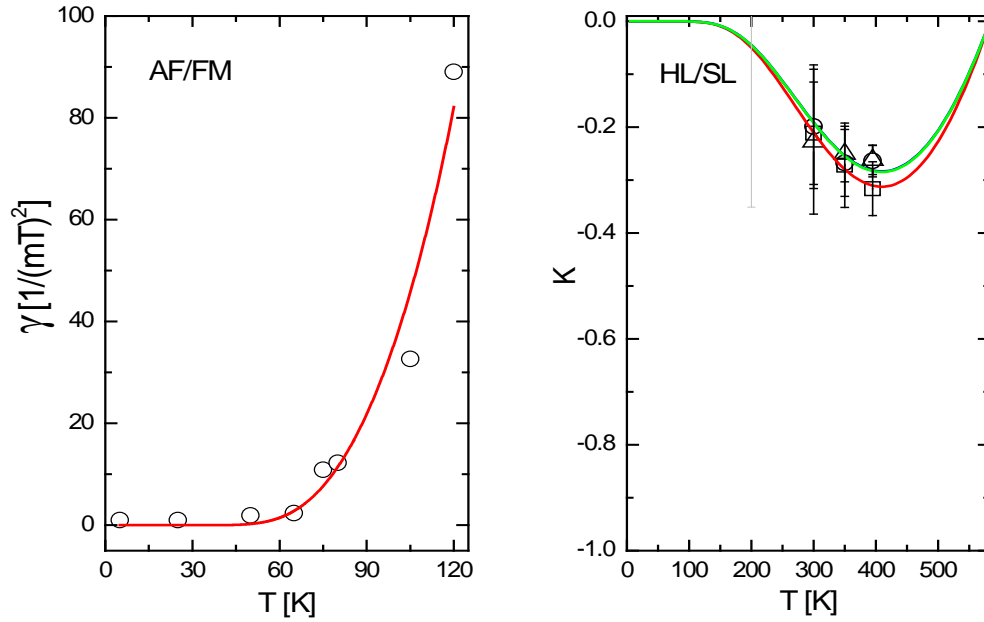


Figure 5.4. Comparison of temperature dependence of characteristic decay rates, γ and K , of training effect in AF/FM and HL/SL bilayers, respectively. Left frame: Circles are the γ -values obtained from fitting procedures of Eq. (1-17) to $\mu_0 H_{EB}$ vs n data for temperatures $5 \leq T \leq 120$ K. The line is a one parameter best fit of Eq. (3-11) to γ vs T . Right frame: K vs. T for the three isomagnetization set fields. Squares (M_{ISO1}), circles (M_{ISO2}) and triangles (M_{ISO3}) are the K -values obtained from fitting procedure of Eq. (4-5). Lines are single parameter best fits of Eq. (4-13).

The successful modeling of the temperature dependence of training effect in both AF/FM and HL/SL heterostructures confirm the consistent theoretical description of the training behavior based on the discretized Landau-Khalatnikov approach. The table below provides the list of comparison of AF/FM and HL/SL heterostructures.

AF/FM	HL/SL
Pinning layer is Antiferromagnet. Pinned layer is Ferromagnet.	Pinning layer is Hard Ferromagnet. Pinned layer is Soft Ferromagnet.
Magnetic field-cooling below Néel temperature of the antiferromagnet is required to set exchange bias.	Magnetic field-cooling is not required, to set bias field. However, an initial demagnetized state of HL is necessary.
Theoretical approach of training effect is not simple due to non trivial relation between order parameter and pinning layer interface magnetization S_{AF} .	Theoretical approach is somewhat simpler due to the direct proportionality between order parameter and pinning later interface magnetization S_{HL} .
Free energy of AF, $\Delta F_{AF} \propto (\eta - \eta_e)^2 \rightarrow \Delta F_{AF} \propto (S^{AF} - S_e^{AF})^4$	Free energy of HL, $\Delta F_{HL} \propto (\eta - \eta_e)^2 \rightarrow \Delta F_{HL} \propto (S^{HL} - S_e^{HL})^2$
Characteristic decay constant $\gamma = \frac{\mu_0(H_{EB}(n) - H_{EB}(n+1))}{(\mu_0(H_{EB}(n) - H_{EB}^e))^3} \geq 0$	Characteristic decay constant $-1 \leq K = \frac{\mu_0(H_B(n+1) - H_B(n))}{\mu_0(H_B(n) - H_B^e)} \leq 0$
The asymptotic behavior (within the limit $n \rightarrow \infty$): $H_{EB} \propto \frac{1}{\sqrt{n}}$	The asymptotic behavior (within the limit $n \rightarrow \infty$): $H_B \propto e^{-n \ln(K+1) }$
$\gamma(T)$ is derived by using mean field theory.	$K(T)$ is derived from Landau theory. Alternatively mean field theory can also be used.
Magnetic changes in pinning antiferromagnet cannot be easily measured during the training effect.	Simple magnetometer can be used to measure the magnetic changes in pinning HL during training effect.

Table 2. Comparison of AF/FM and HL/SL bilayers

CHAPTER 6

CONCLUSIONS

This thesis presents the experimental results of exchange bias training effect in two different systems of AF/FM [CoO/Co] and HL/SL [CoPtCrB/CoCr] heterostructures. Consecutively cycled hysteresis loops of pinned ferromagnet (and SL) trigger the spin configurational relaxation of the AF (and HL) interface magnetization towards their equilibrium. A phenomenological theory of training effect is also presented for both systems based on a discretized Landau-Khalatnikov equation that fits experimental results with convincing accuracy. The resulting fitting parameters from the respective phenomenological theories able to predict the characteristics of the training effect for both AF/FM and HL/SL systems. I have also shown that HL/SL bilayers are good exemplary coupling systems for demonstrating exchange bias and its corresponding training phenomenon due to its FM nature of the pinning HL.

A special emphasis is laid on thermal evolution of the training effect. I further extended above phenomenological ideas to derive temperature dependence of the training effect with particular attention on HL/SL bilayers. The resulting equations for the temperature dependence of the training effect shows excellent quantitative agreement with our experimental data, confirming the underlying phenomenological ideas based on Landau-Khalatnikov dynamical equation. The fitting parameters resulting here from theoretical fits to the experimental data of training effect at different temperatures produces temperature dependence of the characteristics of the training effect in both

systems. For AF/FM systems, the values of this fitting parameter increases with the increasing temperature implying small absolute training effects at high temperatures. On the other hand in case of HL/SL, the fitting parameter shows its extreme value at a temperature where the competition between thermal activation and stability in the pinning layer HL balances that correspond to maximum training effect. It is a future challenge to understand microscopic details of underlying phenomenological approach, however, it turns out that there is no simple unique microscopic theory for the exchange bias effect; training might be a universal property.

Moreover, I have also presented scaling behavior of the exchange bias training effect in CoO/Co-wedge sample. The detailed scaling analysis showing that each individual exchange bias field within a training sequence resembles the same well-known inverse thickness dependence on the FM film. This means a possible change in the FM film thickness evolves no effect in the AF interface magnetization.

In addition, I have also presented magnetoresistance data on the CoO/Co bilayer. The paramagnetic based magnetoresistance formula as a function of the applied magnetic field is modified for the exchange biased AF/FM systems, which produces excellent fits to the experimental data. Observed vertical asymmetry in magnetoresistance curves is associated to the exchange bias field. A power law is employed to fit the temperature dependence of exchange bias producing a significantly smaller value of the blocking temperature.

Furthermore, in HL/SL bilayers I have shown that the enhancement in the bias field and loop width of the SL with the increase of the sweep rate of the magnetic field.

The training effect is also dynamically spread out with the sweep rate. This effect is described here in the framework of a dynamically generalized theoretical approach, which is in excellent agreement with our experimental data. I also demonstrated that the same generalization of dynamic enhancement of the training effect in HL/SL bilayers also applies to conventional AF/FM exchange bias systems when the free energy is tailored to the antiferromagnetic pinning layer.

Finally, the successful application of a simple but powerful phenomenological description of the training effect to the several different systems evidence the universality of the underlying theory of training effect based Landau-Khalatnikov dynamical equation.

REFERENCES

-
- ¹ W. H. Meiklejohn, C. P. Bean, Phys. Rev. **102**, 1413 (1956).
- ² W. H. Meiklejohn, C. P. Bean, Phys. Rev. **105**, 904 (1957).
- ³ C. P. Bean, in *Structure and Properties of Thin Films*, edited by C. Neugebauer, J. Newkirk, and D. Vermilyea (Wiley, New York, 1959), P. 331.
- ⁴ Ch. Binek, J. Hardy, S. Polisetty, X. He, APS Journal (submitted).
- ⁵ J. Ping Liu, “*Nanoscale Magnetic Materials and Applications*”, book chapter by Ch. Binek, Springer, 2009. Edited by J. Ping Liu, Eric Fullerton, Oliver Gutfleisch, D. J. Sellmyer
- ⁶ A. Baruth, D. J. Keavney, J. D. Burton, K. Janicka, E. Y. Tsymbal, L. Yuan, S. H. Liou, and S. Adenwalla, Phys. Rev. B **74**, 054419 (2006).
- ⁷ Xi Chen, Ch. Binek, A. Hochstrat, W. Kleemann, Phys. Rev. B **65**, 012415 (2002).
- ⁸ A. Baruth and S. Adenwalla, submitted to Phys. Rev. B (2009).
- ⁹ I. Roshchin, O. Petravic, R. Morales, Z.-P. Li, X. Battle, and I. K. Schuller, Europhys. Lett. **71**, 297 (2005).
- ¹⁰ C. Leighton, J. Nogués, B. J. Jönsson-Åkerman, and Ivan K. Schuller, Phys. Rev. Lett. **84**, 3466 (2000).
- ¹¹ C. Hou, H. Fujiwara, and K. Zhang, Appl. Phys. Lett. **76**, 3974 (2000).
- ¹² T. Gredig, I. N. Krivorotov, P. Eames, and E. D. Dahlberg, App. Phys. Lett. **81**, 1270 (2002.)
- ¹³ E.P. Wohlfarth, Adv. Phys. **8**, 87 (1959).
- ¹⁴ H. Schmid, Cobalt **6**, 8 (1960).
- ¹⁵ F.S. Luborsky, Electro-Technology, 107 (Sept. 1962).
- ¹⁶ I.S. Jacobs, in: G.T. Rado, H. Suhl (Eds.), Magnetism, Academic Press, New York, 1963, p. 271.
- ¹⁷ A. Yelon, in: M.H. Francombe, R.W. Hoffman (Eds.), Physics of Thin Films, vol. 6, Academic Press, New York, 1971, p. 205
- ¹⁸ J.S. Kouvel, J. Phys. Chem. Sol. **24**, 795 (1963).
- ¹⁹ N.H. March, P. Lambin, F. Herman, J. Magn. Mater. **44**, 1 (1984).

-
- ²⁰ T.J. Moran, J.M. Gallego, I.K. Schuller, J. Appl. Phys. **78**, 1887 (1995)
- ²¹ A.E. Berkowitz, J.H. Greiner, J. Appl. Phys. **36**, 3330 (1965).
- ²² AF Properties: K. Fukamichi, J. Magn. Soc. Japan **21**, 1062 (1997).
- ²³ M. Takahashi, A. Yanai, S. Taguchi, T. Suzuki, Jpn. J. Appl. Phys. **19**, 1093 (1980).
- ²⁴ P.J. van der Zaag, R.M. Wolf, A.R. Ball, C. Bordel, L.F. Feiner, R. Jungblut, J. Magn. Magn. Mater. **148**, 346 (1995)
- ²⁵ W.C. Cain, M.H. Kryder, J. Appl. Phys. **67**, 5722 (1990).
- ²⁶ J. Nogués and I.K. Schuller, J. Magn. Magn. Mater. **192**, 203 (1999).
- ²⁷ A. Berkowitz and K. Takano, “*Exchange anisotropy- a review*” J. Magn. Magn. Mater. **200**, 552 (1999).
- ²⁸ M. Ali, P. Adie, C. H. Marrows, D. Greig, B. J. Hickey and R. L. Stamps, Nat. Mater. **6**, 70 (2007).
- ²⁹ Andrew Baruth, Ph.D. Thesis, Department of Physics and Astronomy, University of Nebraska, Lincoln, NE (2009).
- ³⁰ K. Takano, Ph.D. thesis, Physics Department, University of California at San Diego, San Diego, CA (1998).
- ³¹ Hugo Loosvelt, Ph.D. thesis, Department of Natuurkunde En Sterrenkunde, Katholieke Universiteit Leuven (2005).
- ³² Florin Radu, Ph.D. thesis, Ruhr-University Bochum (2005).
- ³³ Hongtao Shi, Department of Physics and Astronomy, West Virginia University (2002).
- ³⁴ Guolei Liu, Max-Planck-Institut für Mikrostrukturphysik, Germany (2003).
- ³⁵ Ch. Binek, “*Ising-type antiferromagnets: Model systems in statistical physics and the magnetism of exchange bias*” Springer Tracts in Modern Physics Vol. **196**, (Springer, Berlin, 2003).
- ³⁶ E. C. Stoner and E. P. Wohlfarth: Trans. R. Soc. (Lond.) A **240**, 599 (1948).
- ³⁷ J.oo-Von Kim, R. L. Stamps, B. V. Mc Grath and R. E. Camley, Phys. Rv. B **61**, 8888 (2000).
- ³⁸ C. Tsang, N. Heiman and K. Lee, J. Appl. Phys. **52**, 2471 (1981)
- ³⁹ A. P. Malozemoff, Phys. Rev. B **35**, 3679 (1987).
- ⁴⁰ S. Maat, K. Takano, S. S. P. Parkin, and E. E. Fullerton, Phys. Rev. Lett **87**, 087202 (2001).

-
- ⁴¹ A. Baruth and S. Adenwalla, *Phys. Rev. B* **78**, 174407 (2008).
- ⁴² G. Scholten, K. D. Usadel, and U. Nowak, *B* **71**, 064413 (2005).
- ⁴³ Vassil Skumryev, Stoyan Stoyanov, Yong Zhang, George Hadjipanayis, Dominique Givord & Josep Nogués, *Nature* **423**, 850-853 (19 June 2003)
- ⁴⁴ C. Leighton, H. Suhl, M. J. Pechan and R. Compton, J. Nogués, I. K. Schuller, *J. Appl. Phys.* **92**, 1483 (2002).
- ⁴⁵ Yves Henry, Stéphane Mangin, Thomas Hauet, and François Montaigne, *Phys. Rev. B* **73**, 134420 (2006).
- ⁴⁶ C.M. Park, K.A. Lee, D.G. Hwang, S.S. Lee, M.Y. Kim, M.Y. Kim, *J. Korean Phys. Soc.* **31**, 508 (1997).
- ⁴⁷ B. Kagerer, Ch. Binek, W. Kleemann, *J. Magn. Magn. Mater.* **217**, 139-146 (2000).
- ⁴⁸ J. Nogués, D. Ledermann, T. J. Moran, and I. K. Schuller, *Phys. Rev. Lett.* **76**, 4624 (1996).
- ⁴⁹ R. Ramirez, M. Kiwi, D. Lederman, *Bull. Am. Phys. Soc.* **42**, 445 (1997).
- ⁵⁰ N.C. Koon, *Phys. Rev. Lett.* **78**, 4865 (1997).
- ⁵¹ J. Nogués, C. Leighton and Ivan K. Schuller, *Phys. Rev. B* **61**, 1315 (2000).
- ⁵² T. L. Kirk, O. Hellwig, and Eric E. Fullerton, *Phys. Rev. B*, **65**, 224426 (2002).
- ⁵³ Z.Y. Liu and S. Adenwalla, *Phys. Rev. Lett.* **91**, 037207-1 (2003).
- ⁵⁴ Changjun Jiang, Desheng Xue, Xiaolong Fan, Dangwei Guo and Qingfang Liu, *Nanotechnology* **18**, 335703 (2007).
- ⁵⁵ M. Ali, C. H. Marrows, and B. J. Hickey, *Phys. Rev. B* **67**, 172405 (2003).
- ⁵⁶ J. S. Kouvel, *J. Phys. Chem. Solids* **21**, 57 (1961).
- ⁵⁷ L. Néel, *Ann. Phys. t.* **2**, 61 (1967).
- ⁵⁸ D. Mauri, H.C. Siegmann, P.S. Bagus, and E. Kay, *J. Appl. Phys.* **62**, 3047 (1987).
- ⁵⁹ A. P. Malozemoff, *Phys. Rev. B* **37**, 7673 (1988).
- ⁶⁰ T.C. Schulthess and W.H. Butler, *Phys. Rev. Lett.* **81**, 4516 (1998).
- ⁶¹ T. J. Moran, J. Nogués, D. Lederman, and I. K. Schuller, *Appl. Phys. Lett.* **72**, 617 (1998).
- ⁶² M. Kiwi, J. Mejia-Lopez, R. D. Portugal, and R. Ramirez, *Solid State Communications* **116**, 315 (2000).

-
- ⁶³ M. Kiwi, J. Magn. Magn. Mater. **243**, 584 (2001).
- ⁶⁴ A. R. Ball, J. G. Leenaerts, P. J. van der Zaag, K. A. Shaw, B. Singer, D. M. Lind, H. Frederikze, and M. Th. Rekveldt, Appl. Phys. Lett. **69**, 1489 (1996).
- ⁶⁵ M. D. Stiles and R. D. McMichael, Phys. Rev. B **59**, 3722 (1999).
- ⁶⁶ M. D. Stiles and R. D. McMichael, Phys. Rev. B **60**, 12950 (1999).
- ⁶⁷ M. D. Stiles and R. D. McMichael, Phys. Rev. B **63**, 064405 (2001).
- ⁶⁸ F. Y. Yang and C. L. Chien, Phys. Rev. Lett. **85**, 2597 (2000).
- ⁶⁹ K. Takano, R. H. Kodama, A.E Berkowitz, W. Cao, and G. Thomas, Phys. Rev. Lett. **79**, 1130 (1997).
- ⁷⁰ F. T. Parker, K. Takano, and A. E. Berkowitz, Phys. Rev. B **61**, 866 (2000).
- ⁷¹ H. Ohldag, A. Scholl, F. Nolting, E. Arenholz, S. Maat, A. T. Young, M. Carey, and J. Stöhr, Phys. Rev. Lett. **91**, 017203 (2003).
- ⁷² H. Ohldag, *Exchange coupling of Co and Fe on AF NiO investigated by dichroism X-ray absorption spectromicroscopy*, PhD thesis, Heinrich-Heine Universität Dusseldorf, Germany (2003).
- ⁷³ R. L. Stamps, J. Magn. Magn. Mat. **242-245**, 139 (2002).
- ⁷⁴ D. Suess, M. Kirschner, T. Schrefl, J. Fidler, R. L. Stamps, and J.-V. Kim, Phys. Rev. B **67**, 054419 (2003).
- ⁷⁵ P. Myltényi, M. Gierlings, J. Keller, B. Beschoten, G. Güntherodt, U. Nowak, and K. D. Usadel, Phys. Rev. Lett. **84**, 4224 (2000).
- ⁷⁶ U. Nowak, A. Misra, and K. D. Usadel, J. Magn. Magn. Mater. **240**, 243 (2002).
- ⁷⁷ U. Nowak, A. Misra, and K. D. Usadel, J. Appl. Phys. **89**, 7269 (2001).
- ⁷⁸ M. S. Lund, W. A. A. Macedo, K. Liu, J. Nogués, I. K. Schuller, and C. Leighton, Phys. Rev. B **66**, 054422 (2002).
- ⁷⁹ A. Misra, U. Nowak, and K. D. Usadel, J. Appl. Phys. **95**, 1357 (2004).
- ⁸⁰ M. Ali, C. H. Marrows, M. Al-Jawad, B. J. Hickey, A. Misra, U. Nowak, and K. D. Usadel, Phys. Rev. B **68**, 214420 (2003).
- ⁸¹ B. Beckmann, U. Nowak, and K. D. Usadel, Phys. Rev. Lett. **91**, 187201 (2003).
- ⁸² F. Radu, A. Westphalen, K. Theis-Bröhl, and H. Zabel, J. Phys.: Condens. Matter **18**:L29 (2006).

-
- ⁸³ D. Paccard, C. Schlenker, O. Massenet, R. Montmory, and A. Yelon, *Phys. Status Solidi* **16**, 301 (1966).
- ⁸⁴ C. Schlenker, S. S. P. Parkin, J. C. Scott, and K. Howard, *J. Magn. Magn. Mater.* **54**, 801 (1986).
- ⁸⁵ K. Zhang, T. Zhao, and M. Fujiwara, *J. Appl. Phys.* **89**, 6910 (2001).
- ⁸⁶ S. G. te Velthuis, A. Berger, G. P. Felcher, B. Hill, and E. Dahlberg, *J. Appl. Phys.* **87**, 5046 (2000).
- ⁸⁷ Heiwan Xi, R. M. White, S. Mao, Z. Gao, Z. Yang, and E. Murdock, *Phys. Rev. B* **64**, 184416 (2001).
- ⁸⁸ Haiwen Xi, S. Franzen, S. Mao, and R. M. White, *Phys. Rev. B* **75**, 014434 (2007).
- ⁸⁹ A. Hoffmann, *Phys. Rev. Lett.* **93**, 097203 (2004).
- ⁹⁰ U. Nowak, K. D. Usadel, J. Keller, P. Miltényi, B. Beschoten, and G. Güntherodt. *Phys. Rev. B.* **66**, 014430 (2002).
- ⁹¹ J. McCord, R. Mattheis, and R. Schäfer. *J. Appl. Phys.* **93**, 5491 (2003).
- ⁹² K. Temst, E. Popova, H. Loosvelt, M. J. Van Bael, S. Brems, Y. Bruynseraede, C. Van Haesendonck, H. Fritzsche, M. Gierlings, L. H. A. Leunissen, and R. Jonckheere. *J. Magn. Magn. Mater.*, **304**, 14 (2006).
- ⁹³ T. Gredig, I. N. Krivorotov, and E. Dan Dahlberg. *Phys. Rev. B.* **74**, 094431 (2006).
- ⁹⁴ F. Radu, S. K. Mishra, I. Zizak, A. I. Erko, H. A. Dürr, W. Eberhardt, G. Nowak, S. Buschhorn, H. Zabel, K. Zhernenkov, M. Wolff, D. Schmitz, E. Schierle, E. Dudzik, and R. Feyerherm, *Phys. Rev. B.* **79**, 184425 (2009).
- ⁹⁵ Ch. Binek, *Phys. Rev. B* **70**, 014421 (2004).
- ⁹⁶ A. Hochstrat, Ch. Binek, and W. Kleemann, *Phys. Rev. B* **66**, 092409 (2002).
- ⁹⁷ D. Niebieskikwiat, and M. B. Salamon, *Phys. Rev. B* **72**, 174422 (2005).
- ⁹⁸ G. Vizrik, S. Ducharme, V.M. Fridkin, and G. Yudin, *Phys. Rev. B* **68**, 094113 (2003).
- ⁹⁹ H. Haken, *Light*, Vol. 2 (North-Holland Physics Publishing, 1985), p. 314 ff.
- ¹⁰⁰ C. Schlenker, D. Paccard, *J. Phys.* **28**, 611 (1967).
- ¹⁰¹ A. Paul, T. Brückel, E. Kentzinger and U. Rücker, *J. Phys.: Condens. Matter*, **19**, 086229 (2007).
- ¹⁰² Yan-kun Tang, Young Sun, and Zhao-hua Cheng, *Phys. Rev. B* **73**, 174419 (2006).
- ¹⁰³ R. Ang, Y. P. Sun, X. Luo, C. Y. Hao, X. B. Zhu, and W. H. Song, *Appl. Phys. Lett.* **92**, 162508 (2008).

-
- ¹⁰⁴ S. Karmakar, S. Taran, E. Bose, and B. K. Chaudhuri, C. P. Sun, C. L. Huang, and H. D. Yang, *Phys. Rev. B* **77**, 144409 (2008).
- ¹⁰⁵ J. Ventura, J. P. Araujo, J. B. Sousa, A. Veloso, and P. P. Freitas, *Phys. Rev. B* **77**, 184404 (2008).
- ¹⁰⁶ M Patra, M Thakur, S Majumdar and S Giri, *J. Phys.: Condens. Matter* **21**, 236004 (2009).
- ¹⁰⁷ Shujuan Yuan, Kun Xu, Zhe Li, Liming Yu, Baojuan Kang, and Shixun Cao, *J. Appl. Phys.* **105**, 093910 (2009).
- ¹⁰⁸ Z. M Tian, S L Yuan, L Liu , S Y Yin, L C Jia, P Li, S X Huo and J Q Li, *J. Phys. D: Appl. Phys.* **42**, 035008 (2009).
- ¹⁰⁹ S. Polisetty, S. Sahoo, A. Berger, Ch. Binek, *Phys. Rev. B* **78**, 184426 (2008).
- ¹¹⁰ Ch. Binek, Xi He and S. Polisetty, *Phys. Rev. B* **72**, 054408 (2005).
- ¹¹¹ S. Polisetty, S. Sahoo, and Ch. Binek, *Phys. Rev. B* **76**, 184423 (2007).
- ¹¹² Ch. Binek, S. Polisetty, Xi He, and A. Berger, *Phys. Rev. Lett.* **96**, 067201 (2006).
- ¹¹³ S. Sahoo, S. Polisetty, Ch. Binek, and A. Berger, *J. Appl. Phys.* **101**, 053902 (2007).
- ¹¹⁴ Milton Ohring, *Materials Science of Thin Films*, Academic press, California (2002).
- ¹¹⁵ J.A. Thornton and D.W. Hoffman, *Thin Film Solids* **171**, 5 (1989).
- ¹¹⁶ J. Vossen and W. Kern, *Thin Film Processes*, Academic Press, New York (1978).
- ¹¹⁷ B.N. Chapman, *Flow Discharge Processes*, John Wiley and Sons, New York (1980).
- ¹¹⁸ <http://www.angstromsciences.com/technology/sputtering-technology/figure-/index.html>
- ¹¹⁹ Steven A. Michalski, Ph. D. thesis, University of Nebraska-Lincoln, 2007.
- ¹²⁰ A. Cho, "Film Deposition by Molecular Beam Techniques," *J. Vac. Sci. Tech* **8**, S31 (1971).
- ¹²¹ A. Cho, J. Arthur, "Molecular Beam Epitaxy" *Prog. Solid-State Chem.* **10**, 157 (1975).
- ¹²² Fernando Rinaldi, Annual Report 2002, Optoelectronics Department, University of Ulm.
- ¹²³ Crystal growth of materials for energy production and energy saving applications, R. Fornari, L. Sorba, Eds. (Edizioni ETS, Pisa, 2001).
- ¹²⁴ B.D. Cullity and S.R. Stock, *Elements of X-Ray Diffraction: Third Edition*, Prentice Hall, America (2001).

-
- ¹²⁵ N.W. Ashcroft, N.D. Mermin, *Solid State Physics*, Holt Rinehart & Winston (1976).
- ¹²⁶ Azároff, L. V.; R. Kaplow, N. Kato, R. J. Weiss, A. J. C. Wilson, R. A. Young, *X-ray diffraction*. McGraw-Hill (1974).
- ¹²⁷ B. H. Bransden, C. J. Joachain, “*Physics of atoms and molecules*”, 2nd edition, Pearson edu. (2004).
- ¹²⁸ J.Daillant, A.Gibaud, *X-Ray and Neutron Reflectivity: Principles and Applications*, Springer (1999).
- ¹²⁹ A. Gibaud and S. Hazra, *Current Science* **78**, 1467 (2000).
- ¹³⁰ http://www.almaden.ibm.com/st/scientific_services/materials_analysis/sxr/
- ¹³¹ P.J. Flanders, *J. Appl. Phys.* **63**, 3940 (1988).
- ¹³² <http://upload.wikimedia.org/wikipedia/commons/b/b2/MOKE.PNG>
- ¹³³ Z. Q. Qiu and S. D. Bader, *Rev. Sci. Instrum.* **71**, 1243 (2000).
- ¹³⁴ A. Berger, and M. R. Pufall, *Appl. Phys. Lett.* **71**, 965 (1997).
- ¹³⁵ V. Usov, S. Murphy, L. Seravalli, and I. V. Shvets, *Rev. Sci. Instrum.* **76**, 046102 (2005).
- ¹³⁶ J. R. Hampton, J.-L. Martínez-Albertos, and H. Abruña, *Rev. Sci. Instrum.* **73**, 3018 (2002).
- ¹³⁷ K. M. Poduska, and S. Morin, *Rev. Sci. Instrum.* **74**, 4723 (2003).
- ¹³⁸ D. A. Allwood, G. Xiong, M. D. Cooke, and R. P. Cowburn, *J. Phys. D: Appl. Phys.* **36**, 2175 (2003).
- ¹³⁹ T. Ishibashi, Z. Kuang, S. Yufune, T. Kawata, M. Oda, T. Tani, Y. Iimura, K. Sato, Y. Konishi, K. Akahane, X. Zhao, T. Hasegawa, *J. Appl. Phys.* **100**, 093903 (2006).
- ¹⁴⁰ J. Hamrle, J. Ferré, J. P. Jamet, V. Repain, G. Baudot, and S. Rousset *Phys. Rev. B* **67**, 155411 (2003).
- ¹⁴¹ A. V. Petukhov, A. Kirilyuk, and Th. Rasing, *Phys. Rev. B* **59**, 4211 (1999).
- ¹⁴² S. N. Jespersion and S. E. Schnatterly, *Rev. Sci. Instrum.* **40**, 761 (1969).
- ¹⁴³ P.Q. J. Nederpel and J. W. D. Martens, *Rev. Sci. Instrum.* **56**, 687 (1985).
- ¹⁴⁴ W. S. Kim, M. Aderholz, and W. Kleemann, *Meas. Sci. Technol.* **4**, 1275 (1993).
- ¹⁴⁵ S. Maat, L. Shen, C. Hou, H. Fujiwara, and G. J. Mankey, *J. Appl. Phys.* **85**, 1658 (1999).
- ¹⁴⁶ M. Farle, W. A. Lewis, and K. Baberschke, *Appl. Phys. Lett* **62**, 2728 (1993).

-
- ¹⁴⁷ M. N. Deeter and D. Sarid, IEEE Trans. Magn. **MAG-24**, 2470 (1988).
- ¹⁴⁸ S. Tanaka, Jap. J. Appl. Phys. **2**, 548 (1963).
- ¹⁴⁹ G. Arfken, *Mathematical Methods for Physicists*, 3rd ed. (Academic Press Orlando, FL, 1985).
- ¹⁵⁰ R. M. A. Azzam and N. M. Bashara, *Ellipsometry and Polarized Light*, (North Holland, Amsterdam, 1979).
- ¹⁵¹ S. Polisetty, J. Scheffler, S. Sahoo, Yi Wang, T. Mukherjee, Xi He, and Ch. Binek, Rev. Sci. Instru. **79**, 055107 (2008)
- ¹⁵² <http://www.wmi.badw.de/methods/squid.htm>.
- ¹⁵³ D. Ruelle, J. Stat. Phys. **95**, 393 (1999).
- ¹⁵⁴ S. Lübeck, Int. J. Mod. Phys. B **18**, 3977 (2004).
- ¹⁵⁵ D Predoi, V Kuncser, E Tronc, M Nogues, U Russo, G Principi and G Filoti, J. Phys.: Condens. Matter **15** 1797 (2003).
- ¹⁵⁶ W. T. Lee, S. G. E. te Velthuis, G. P. Felcher, F. Klose, T. Gredig, and E. D. Dahlberg, Phys. Rev. B **65**, 224417 (2002).
- ¹⁵⁷ F. Radu, M. Etzkorn, R. Siebrecht, T. Schmitte, K. Westerholt, and H. Zabel, Phys. Rev. B **67**, 134409 (2003).
- ¹⁵⁸ A. Z. Patashinskii and V. I. Pokrovskii, *Fluctuation Theory of Phase Transitions* (Pergamon, 1979).
- ¹⁵⁹ J. M. Kincaid and E. G. D. Cohen, Phys. Rep., Phys. Lett. **22**, 57 (1975).
- ¹⁶⁰ K. Seu, H. Huang, J. L. Showman, H. Showman, W. F. Egelhoff, Jr. and A. Reilly, J. Appl. Phys. **93**, 6611 (2003).
- ¹⁶¹ V. Baltz, J. Sort, S. Landis, B. Rodmacq, and B. Dieny, Phys. Rev. Lett. **94**, 117201 (2005).
- ¹⁶² G. Malinowski, M. Albrecht, I. L. Guhr, J. M. D. Coey, and S. van Dijken, Phys Rev. B **75**, 012413 (2007).
- ¹⁶³ S. Brems, D. Buntinx, K. Temst, C. Van Haesendonck, F. Radu, and H. Zabel, Phys. Rev. Lett. **95**, 157202 (2005).
- ¹⁶⁴ Ch. Binek, A. Hochstrat, and W. Kleemann, phys. stat. sol. (a) **189**, No. 2, 575 (2002).
- ¹⁶⁵ L. Smardz, phys. Stat. sol. (a) **181**, R7 (2000).
- ¹⁶⁶ F. Celestini and F. Mortessagne, cond-mat 08 Aug 2007.

-
- ¹⁶⁷ A. Stierle, A. Abromeit, N. Metoki, and H. Zabel, *J. Appl. Phys.* **73**, 4808 (1993).
- ¹⁶⁸ Th. Zeidler, F. Schreiber, H. Zabel, W. Donner, and N. Metoki, *Phys. Rev. B* **53**, 3256 (1996).
- ¹⁶⁹ R. Allenspach, M. Stampanoni, and A. Bischof, *Phys. Rev. Lett.* **65**, 3344 (1990).
- ¹⁷⁰ H. Shi and D. Lederman, *J. Appl. Phys.* **87**, 6095 (2000).
- ¹⁷¹ J. Nogués, D. Lederman, T. J. Moran, I. K. Shuller, and K. V. Rao, *Appl. Phys. Lett.* **68**, 3186 (1996).
- ¹⁷² I. S. Jiang, E. E. Fullerton, C. H. Sowers, A. Inomata, S. D. Bader, A. J. Shapiro, R. D. Shull, V.S. Gornakov and V. I. Nikitenko, *IEEE Trans. Magn.* **35**, 3229 (1999).
- ¹⁷³ M. Sorescu, A. Grabias, and M. Valeanu, *IEEE Trans. Magn.* **39**, 2959 (2003).
- ¹⁷⁴ E. E. Fullerton, J. S. Jiang, M. Grimsditch, C. H. Sowers, and S. D. Bader, *Phys. Rev. B.* **58**, 12193 (1998).
- ¹⁷⁵ J. E. Shield, J. Zhou, S. Aich, V.K. Ravindran, Ralph Skomski, and D. J. Sellmyer, *J. Appl. Phys.* **99**, 08B508 (2006).
- ¹⁷⁶ J. I. Hong, T. Leo, D. J. Smith, and A. E. Berkowitz, *Phys. Rev. Lett.* **96**, 117204 (2006).
- ¹⁷⁷ Ch. Binek, X. Chen, A. Hochstrat, W. Kleemann, *J. Magn. Magn. Mat* **240**, 257 (2002).
- ¹⁷⁸ P. Grünberg, R. Schreiber, Y. Pang, M. B. Brodsky, and H. Sowers, *Phys. Rev. Lett.* **57**, 2442 (1986).
- ¹⁷⁹ A. Berger, D. T. Margulies, and H. Do, *Appl. Phys. Lett* **85**, 1571 (2004).
- ¹⁸⁰ A. Berger, Ch. Binek, D. T. Margulies, A. Moser, and E. E. Fullerton, *Physica B* **372**, 168 (2006).
- ¹⁸¹ P. Kappenberger, S. Martin, Y. Pellmont, H. J. Hug, J. B. Kortright, O. Hellwig, and E. E. Fullerton, *Phys. Rev. Lett.* **91**, 267202 (2003).
- ¹⁸² A. Berger, O. Hovorka, G. Friedman, and E. E. Fullerton, *Phys. Rev. B* **78**, 224407 (2008).
- ¹⁸³ A. Hochstrat, Ch. Binek, X. Chen and W. Kleemann, *J. Magn. Magn. Mat.* **325**, 272 (2004)
- ¹⁸⁴ M. Toney, J. Borchers, K. O'Donovan, C. Majkrzak, D. Margulies, and Eric E. Fullerton, *Appl. Phys. Lett.* **86**, 162506 (2005).
- ¹⁸⁵ L. Thomas, J. Luning, A. Scholl, F. Nolting, S. Anders, J. Stohr, and S. Parkin, *Phys. Rev. Lett.* **84**, 3462 (2000).
- ¹⁸⁶ J. Keller, P. Miltényi, B. Beschoten, G. Güntherodt, U. Nowak, and K. D. Usadel, *Phys. Rev. B.* **66**, 014431 (2002).

-
- ¹⁸⁷ Jarosław Kanak, Tomasz Stobiecki, and Sebastiaan van Dijken, *IEEE Trans. Magn.* **44**, (2008).
- ¹⁸⁸ Xi Chen, O. Sichel Schmidt, W. Kleemann, O. Petravic, Ch. Binek, J. B. Sousa, S. Cardoso, P. P. Freitas, *Phys. Rev. Lett.* **89**, 137203 (2002).
- ¹⁸⁹ Giorgio Bertotti, “*Hysteresis in Magnetism*”, Academic Press, London, 1998.
- ¹⁹⁰ A. R. Massih and L. O. Jernkvist, *J. Phys. Chem. Solids* **65**, 1193 (2004).
- ¹⁹¹ H. E. Stanley, “*Introduction to phase transition and critical phenomena*”, Oxford University press, New York 1971.
- ¹⁹² R. M. Bozorth, *Phys. Rev.* **79**, 887 (1950).
- ¹⁹³ Pennec, Y. *et al.*, *Phys. Rev. B* **69**, 180402 (2004).
- ¹⁹⁴ J. Sort, B. Dieny, J. Nogués, *Phys. Rev. B* **72**, 104412 (2005).

PUBLICATIONS

1. Anisotropic magnetoresistance in exchange biased Co/CoO bilayer

S. Sahoo, S. Polisetty, Y. Wang, T. Mukherjee, X. He, S. S. Jaswal, and Ch. Binek (J. Appl. Phys, submitted).

2. 1D antiferromagnetic arrays of Ni magnetic nanoparticles

V. Bliznyuk, S. Singamaneni, S. Sahoo, S. Polisetty, X. He, Ch. Binek, Nanotechnology 20, 105606 (2009).

3. Temperature dependence of the training effect in exchange coupled all ferromagnetic bilayers

S. Polisetty, S. Sahoo, A. Berger, and Ch. Binek, Phys. Rev. B. 78, 184426 (2008).

4. Optimization of magneto-optical Kerr setup: Analyzing experimental assemblies using Jones matrix formalism

S. Polisetty, J. Scheffler, S. Sahoo, Y. Wang, T. Mukherjee, X. He, and Ch. Binek, Rev. Sci. Instrum.79, 055107 (2008).

5. Scaling behavior of the exchange-bias training effect

S. Polisetty, S. Sahoo, Ch. Binek, Phys. Rev. B. 76, 184423 (2007).

6. Ferroelectric control of magnetism in BaTiO₃/Fe heterostructures via interface strain coupling

S. Sahoo, *S. Polisetty*, C.G. Duan, S. S. Jaswal, E. Y. Tsybal, and Ch. Binek, *Phys. Rev. B.* 76, 092108 (2007).

7. Dynamic enhancement of the exchange bias training effect

S. Sahoo, *S. Polisetty*, Ch. Binek, and A. Berger, *J. Appl. Phys.* 101, 053902 (2007).

8. Nonextensivity in magnetic nanoparticle ensembles

Ch. Binek, *S. Polisetty*, X.He, T. Mukherjee, R. Rajesh, and J. Redepenning. *Phys. Review. B.* 74, 054432 (2006).

9. Exchange Bias Training Effect in Coupled All Ferromagnetic Bilayer Structures

Ch. Binek, *S. Polisetty*, X. He, and A. Berger, *Phys. Rev. Lett.* 96, 067021 (2006).

10. Temperature dependence of the training effect in a Co/CoO exchange-bias layer

Ch. Binek, X. He, and *S. Polisetty*, *Phys. Rev. B.* 72, 054408 (2005).